Synthesis and characterisation of molecular magnetic switches

Yemeli Tido, Eddy Weulersse

Synthesis and Characterisation of Molecular Magnetic Switches

Eddy Weulersse Yemeli Tido

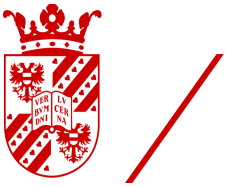

rijksuniversiteit groningen

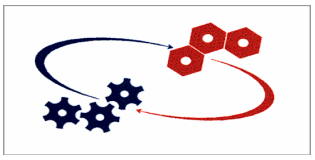

Stratingh Institute for Chemistry

The work described in this thesis has been carried out in the Molecular Inorganic Chemistry group – Stratingh Institute for Chemistry, University of Groningen, The Netherlands.

Cover design: Eddy W. T. Yemeli; artwork: Tania C. R. Guerrero.

Printed by Ipskamp Drukkers B.V., Enschede, The Netherlands

ISBN: 978-90-367-4352-5 (printed version)
ISBN: 978-90-367-4353-2 (digital version)

RIJKSUNIVERSITEIT GRONINGEN

Synthesis and Characterisation of Molecular Magnetic Switches

Proefschrift

ter verkrijging van het doctoraat in de
Wiskunde en Natuurwetenschappen
aan de Rijksuniversiteit Groningen
op gezag van de
Rector Magnificus, dr. F. Zwarts,
in het openbaar te verdedigen op
vrijdag 14 mei 2010
om 13.15 uur

door

Eddy Weulersse Yemeli Tido

geboren op 10 maart 1975
te Bamenda, Kameroen

Promotor: Prof. dr. T. T. M. Palstra

Copromotor: Dr. P. J. van Koningsbruggen

Beoordelingscommissie: Prof. dr. A. Hauser
Prof. dr. ir. P. H. M. van Loosdrecht
Prof. dr. R. Broer

Table of Contents

Abbreviations

B	Magnetic field
C_p	Molar heat capacity at constant pressure (J mol^{-1} K^{-1})
χ, χ_m	Magnetic susceptibility, molar magnetic susceptibility
D	Zero Field Splitting parameter (cm^{-1})
Δ, Dq	Ligand field strength, Cubic ligand Field Splitting
f, Θ_D	Recoilless fraction, Debye temperature
g	Landé factor (2.002 for a free electron)
G, H, S	Gibbs free energy, enthalpy, entropy (J)
γ_{HS}	High Spin fraction ($\gamma_{HS} = 1-\gamma_{LS}$)
k_B	Boltzmann Constant, 1.38066×10^{-23} J K^{-1} (0.69503877 cm^{-1} K^{-1})
K_{HL}	Relaxation constant (s^{-1}) (cm^3 mol^{-1})
μ_{eff}, μ_B	Effective magnetic moment, Bohr magneton
Γ	Interaction term
$\Gamma/2$	Half-line width
P, *E*	Pairing energy, Energy
QS, ΔE_Q and IS, δ	Quadrupole Splitting and Isomer Shift (mm s^{-1})
r	Average metal-to-ligand bond length distance (Å)
R	Gas constant, 8.314472 (J K^{-1} mol^{-1})
$T_{1/2}$	Transition Temperature
T, G	Tesla, gauss
ATR	Attenuated Total Reflection
DSC	Differential Scanning Calorimetry
EPR, ESR, EMR	Electron Paramagnetic Resonance, Electron Spin Resonance, Electron Magnetic Resonance
EXAFS	Extended X-Ray Absorption Fine Structure
FTIR, NIR	Fourier transforms Infra Red, near-Infra Red
HS, LS	High Spin, Low Spin
HT, LT, RT	High temperature, low temperature, room temperature
LD-LISC	Ligand-Driven Light-Induced Spin Changes

LIESST, LITH	Light Induced Excited Spin State Trapping, Light Induced Thermal Hysteresis
LMCT	Ligand Metal Charge Transfer
MS	Mass spectrum or Mössbauer spectrum
NMR	Nuclear Magnetic Resonance
ppm	parts per million
SCO, ST	Spin Crossover, Spin Transition
SQUID	Superconducting Quantum Interference Device
TGA	Thermal Gravimetric Analysis
UV, vis	Ultra Violet, Visible
XPS	X-Ray Photoelectron Spectroscopy
XRPD	X-ray powder diffraction
ZFC, FC	Zero-field cooled, field-cooled
ZFS	Zero Field Splitting
Ligands	
bpp1	2,6-di(pyrazol-1-yl)-pyridine
bpp2	2,6-di(pyrazol-1-yl)-pyrazine
Hpap	2-hydroxyphenyl-(2-pyridyl)-methaneimine
H_2ethpy	Pyridoxal 4-ethylthiosemicarbazone
H_2mthpy	Pyridoxal-4-methylthiosemicarbazone
H_2thpy	Pyridoxal thiosemicarbazone
H_2thpu	Pyruvic acid thiosemicarbazone
H_2thsa	Salicylaldehyde thiosemicarbazone
paptH	2-(Pyridin-2-yl-amino)-4-(pyridin-2-yl)thiazole
ptz	1-n-Propyl-tetrazole

Chapter I
Introduction and Objective

Synopsis

In this chapter we review the potential for the application of the spin crossover phenomenon in molecular electronics. An outline is presented of the principal features of electronic spin crossover. The development of the subject is traced and the various modes of manifestation of spin transitions are presented. The role of cooperativity in influencing solid state behaviour is considered. In addition, attention is directed to thiosemicarbazone Schiff base-type ligands and to 2,6-bis(pyrazole)-pyridine and its derivatives. The chapter also includes the objective and a general overview of this dissertation.

1.1 Introduction

1.1.1 Molecular Magnetic Switches

There is a rapidly growing interest in molecular magnetic materials sparked by their perceived technological importance for molecular electronics. Molecule-based switchable magnetic materials have the advantages above conventional magnets that they are transparent and can be tailor-made; thus they provide a unique tool for fine-tuning the physical properties. In addition, the study of the optical control of the magnetic behaviour of materials is a field of high current interest, where many of the mechanisms and possibilities are still to be explored and understood.

To understand how molecular switches work, we refer to a classical example of a two state-device; where transcription can either be “ON” or “OFF”. When the switch is closed, *i.e.*, at “ON” position, the current only flows in one direction at a particular voltage, and if that voltage is increased or decreased it turns “OFF” again making the switch reversible. In any case, the switch is a two-component system that is composed of the oxidized and reduced forms of a redox active molecule. The two states can also be isomers of an acid and its conjugate base or even of the complexed and uncomplexed forms of a receptor.[1-9]

Under these circumstances, the molecular bistability expressed by the spin crossover (SCO) behaviour became relevant. The change of the spin state in a SCO material, as illustrated in Figure 1.1, can undergo reversible switching cycles in a solid matrix generated by surrounding sources (temperature, pressure, light irradiation etc.).[10,11] As a direct consequence to these stimulus, the molecular magnetic switches produce outputs that may be, for instance, change in absorbance or in magnetic response. It then becomes achievable to connect a piece of information with each of the LS and HS states. When the input is applied, the output alternates from a low to a high value or vice-versa, depending on the logic convention positive or negative, respectively.[12] Such a switch, or logic gate, is a necessary computing component, used to represent ones and zeros, the binary language of digital computing. In fact, the spin transition phenomenon concedes the definition of a NOT gate, which is one of the three fundamental logic operations. It is good to remind that a NOT operator, outputs the exact opposite digital signal as what is input.[12] For example, pyrazoline derivatives execute NOT operations by transducing a chemical input into an optical output.[13,14] However, the increasing demands of broadland telecommunication and internet applications requires ultrafast speeds, lower power needs and inexpensive materials for the transmission capacity and communication

networks.[15] The current technology is based mainly on optical signals. It then becomes crucial to identify molecular switches able to provide an optical input/output transduction mechanism. Molecular magnetic switches, in such a context, are very promising candidates.[10]

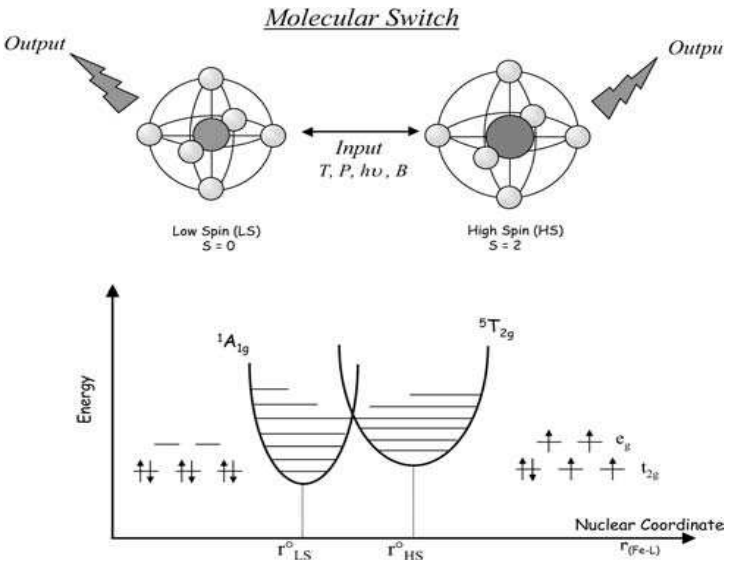

Figure 1.1. Molecular switch based on the Iron(II) Spin Crossover (SCO) phenomenon. The Fe^{2+} ion has six valence electrons occupying the 3d orbitals. The input stimulation, *i.e.*, temperature (*T*), light (*hυ*), pressure (*P*) and magnetic field (*B*), induces the transformation of one state into the other and determines the intensity of the output signals, *i.e.*, absorption, magnetic and volume changes. Taken from Létard.[16]

In opposition to the dynamic nature of a molecular switch, a bistable memory effect device represents a static component.[17] After undergoing the OFF-to-ON transition (as a molecular switch), the device remains in its ON state even after the triggering signal has been turned off, the state parameters having a hysteresis characteristic as a function of the triggering signal for changing states. If we consider the SCO phenomenon of an isolated complex with a relatively weak cooperative interaction, this condition is not reached. This is the course of a transition observed for a system in solution where essentially a Boltzmann distribution of the molecular states is involved. As a result, the spin crossover phenomenon is a continuous type (Figure 1.2). The input information is erased immediately after the triggering signal has ceased. Such a molecular component exhibits no static memory property. It is now well established that to obtain an electronic memory feature in a SCO material, the spin transition (ST) phenomenon must be accompanied by a hysteresis loop.[18]

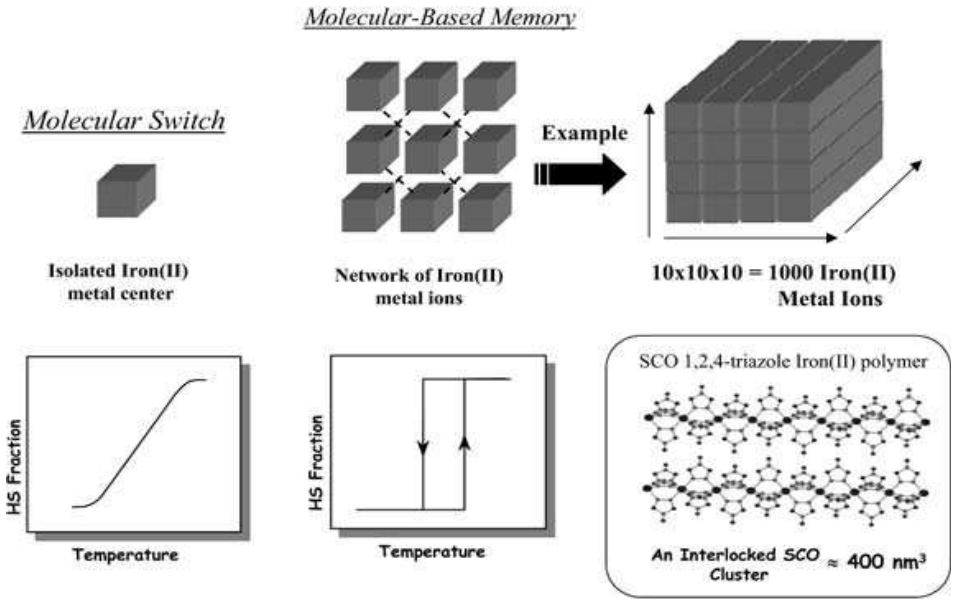

Figure 1.2. Schematic drawing of a gradual spin conversion recorded for a molecular switch involving an isolated iron(II) metal center and of a thermal hysteresis loop obtained for a strongly interlocked polynuclear iron(II) cluster. The structure of the polymeric 1,2,4-triazole iron(II) compounds is deduced from the EXAFS investigation.[19] (Taken from Létard[16]).

1.1.2 Background

1.1.2.1 Discovery of Spin Crossover Phenomenon and Ligand Field Strength

The phenomenon of spin crossover was discovered by Cambi and Szegö as part of a study on iron(III) tris(N,N-dialkyl-dithiocarbamato) complexes in the early 1930s, whose magnetic moments were shown to be temperature-dependent.[20,21] Their initial interpretation of this unusual magnetic behaviour was in terms of thermal equilibrium between two different magnetic isomers. The high temperature isomer having $\mu_{eff} = 5\ \mu_B$ and the low temperature isomer having $\mu_{eff} = 1\ \mu_B$.[21] This suggestion was only clarified 30 years later, when the physics behind spin-crossover was first elucidated.[22] The magnetic isomers of these compounds do not have different chemical structures, as had been proposed. Rather they reflect the ability of the same molecule to adopt one of two different electronic states, with different distributions of electrons in its frontier d orbitals.

In octahedral ligand fields, transition metal ions with $[Ar]3d^4$–$3d^7$ electronic configurations can be distinguished by different occupations of the antibonding e_g and the nonbonding t_{2g} d orbitals of the central metal ion. If the spin pairing energy *P*, is large compared to Δ (ligand field strength), the d electrons are arranged according to Hund's rule to give the maximum number of unpaired electrons. The complex is referred to as a

high-spin (HS). If the splitting of the d orbitals is large with respect to the pairing energy ($\Delta > P$), it is more favourable for electrons to pair in the t_{2g} level and the metal complex adopts the low-spin state (LS). (Figure 1.3, left). Most Cr(II), Mn(II), Mn(III), Fe(II), Fe(III), Co(II) and Co(III) complexes can be classified in one of these two families.

When the two interactions are comparable ($\Delta \approx P$), *i.e.*, close to the critical point (Δ_c) of the Tanabe-Sugano diagram,[23] an electron in the highest suborbital may transfer into the lowest suborbital and changes its spin direction in a controlled, detectable and reversible manner, by the applied action of temperature, pressure or light irradiation. This gives birth to a new family of complexes called spin crossover. Thus, the spin transition (ST) phenomenon corresponds to an intra-ionic transfer of electron between the t_{2g} and the e_g orbitals centered in the immediate environment of the metal ion (Figure 1.3).

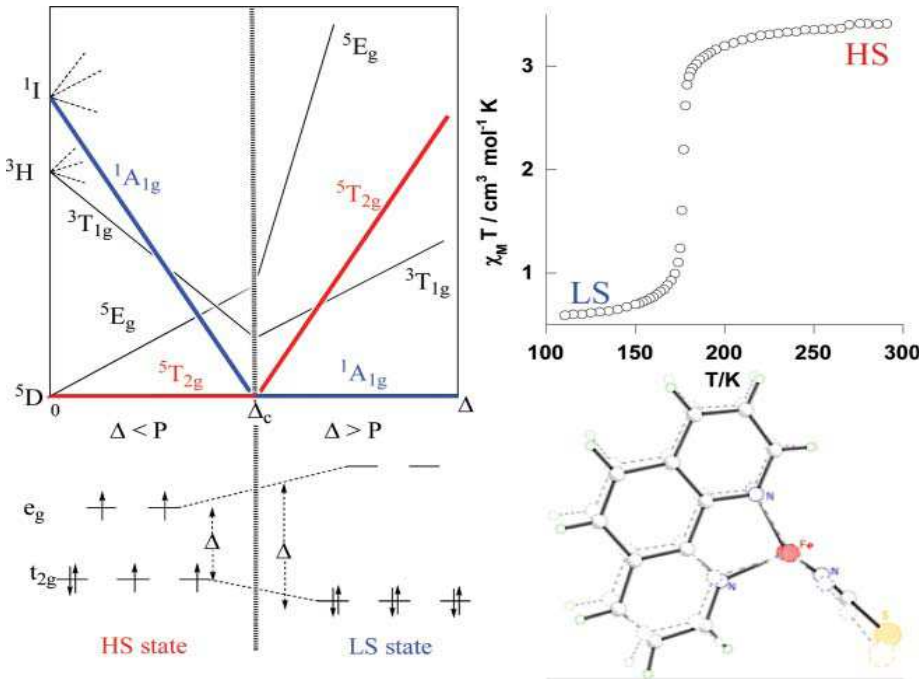

Figure 1.3. Simplified Tanabe–Sugano diagram illustrating the relative dependence of the HS and LS states and the corresponding electron distribution for the [Ar]3d^6 configuration on Δ (left). Overlay of the HS (dotted line) and LS (line) asymmetric unit of $[Fe(phen)_2(NCS)_2]$ and its magnetic behaviour (right). Taken from Real *et al.*[24]

1.1.2.2 Configurational Coordinate Diagram of the SCO Molecule

For each ground state, high or low spin, we can plot the energy as functions of: the average metal-to-ligand bond elongation, r, or the totally symmetric stretch vibration coordinates of the Born-Oppenheimer approximation.[25] For SCO complex

$[Fe(phen)_2(NCS)_2]$, $r_{LS} \approx 2.0$ Å and $r_{HS} \approx 2.2$ Å, which corresponds to a difference in metal-ligand bond length between the high- and low-spin state of $\Delta r \approx 0.2$ Å. This means that the minima of the two potential wells are displaced relative to each other, both vertically and horizontally, as depicted in Figure 1.4. The shift in zero-point energy depends essentially on the nature of the ligand. Based on such a diagram, we deduce the condition for the phenomenon of a thermal spin transition:

$$\Delta E_{HS} = E_{HS} - E_{LS} \approx k_B T \qquad (1.1)$$

In such case, only the $^1A_{1g}$ state is populated at low temperatures, however, an increase in temperature allows gradual population of the $^5T_{2g}$ state. Note that the energy difference between the ground states, HS and LS, is not experimentally accessible. Indeed, accessing the quintet excited state by absorption of light from the singlet ground state or vice versa is forbidden by the spin selection rules, and thus should be ruled out.

The condition on ΔE_{HL} allows to define the range of Δ values for which a spin-transition is expected.[26] Empirical studies have given the following values:

$$\Delta_{HS} = 10Dq^{HS} < 11000\,cm^{-1} \Rightarrow \quad HS\ complex$$

$$\left.\begin{aligned}\Delta_{HS} &= 10Dq^{HS} \simeq 11000 - 12500\,cm^{-1}\\ \Delta_{LS} &= 10Dq^{LS} \simeq 19000 - 22000\,cm^{-1}\end{aligned}\right\} \Rightarrow SCO\ complex$$

$$\Delta_{LS} = 10Dq^{LS} > 23000\,cm^{-1} \Rightarrow \quad LS\ complex$$

This diagram allows to reconsider the meaning of the Δ_c parameter of the Tanabe-Sugano diagram raised previously. Δ_c is the crossing point (described in Figure 1.3, left) and represents an unstable region where the transient species change the spin state at a distance r_c. This point of intersection has no physical reality, because it is not associated to any configurational states of the metal complex in equilibrium. The r_c value in turn, gives no indication of the difference between the zero-point energy and the ground states (HS and LS), and so for the possibility to observe a thermal spin transition. We only know that:

$\Delta_{HS} < \Delta_c < \Delta_{LS}$

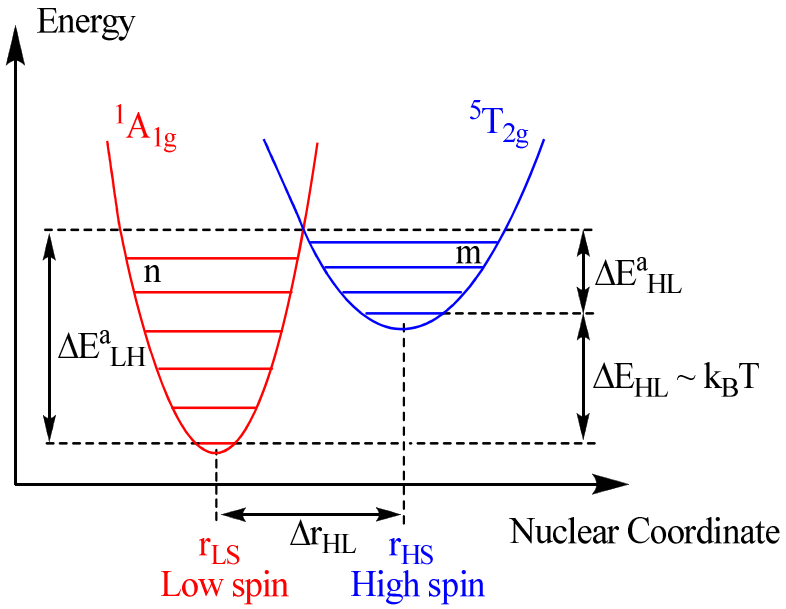

Figure 1.4. Adiabatic potentials for the high-spin and the low-spin state along with the most important reaction coordinate for spin crossover. Adapted from König.[27]

1.1.2.3 Photo-Conversion of Spin States and the Relaxation Process

The first example of photoinduced magnetization changes of spin state was observed by McGarvey and Lawthers in solution at around ambient temperature,[28] however, the resulting light-induced states were of the order of submicroseconds to microseconds. Following the pioneering discovery, Decurtins *et al*. observed photo-induced LS → HS transition of the iron(II) SCO compound $[Fe(ptz)_6][BF_4]_2$ in solid state at cryogenic temperature. Subsequently, the term "light-induced excited state spin trapping (LIESST)" was coined to describe this effect.[29,30] In fact, irradiating a crystal of $[Fe(ptz)_6](BF_4)_2$ at 10 K with green light (λ = 514.5 nm) into the spin allowed $^1A_1 \rightarrow {}^1T_1$ d–d absorption band gives access to a metastable state $^1T_1$ or to the intermediate state $^3T_1$ (if pumping with 980 nm) (Figure 1.5, left). The excited state $^1T_1$, rapidly decays through the intermediate state $^3T_1$ *via* double intersystem crossing to either return back to its original ground state $^1A_1$ or to reach the $^5T_2$ high spin ground state. Figure 1.5 (left) indicates the possibility of pumping the system back to the low-spin state by selectively irradiating with red light (λ = 820 nm), into the maximum of the $^5T_2 \rightarrow {}^5E$ band of the trapped high-spin compound.[32] However, the light-induced return to the low-spin state (reverse-LIESST) is not fully quantitative.

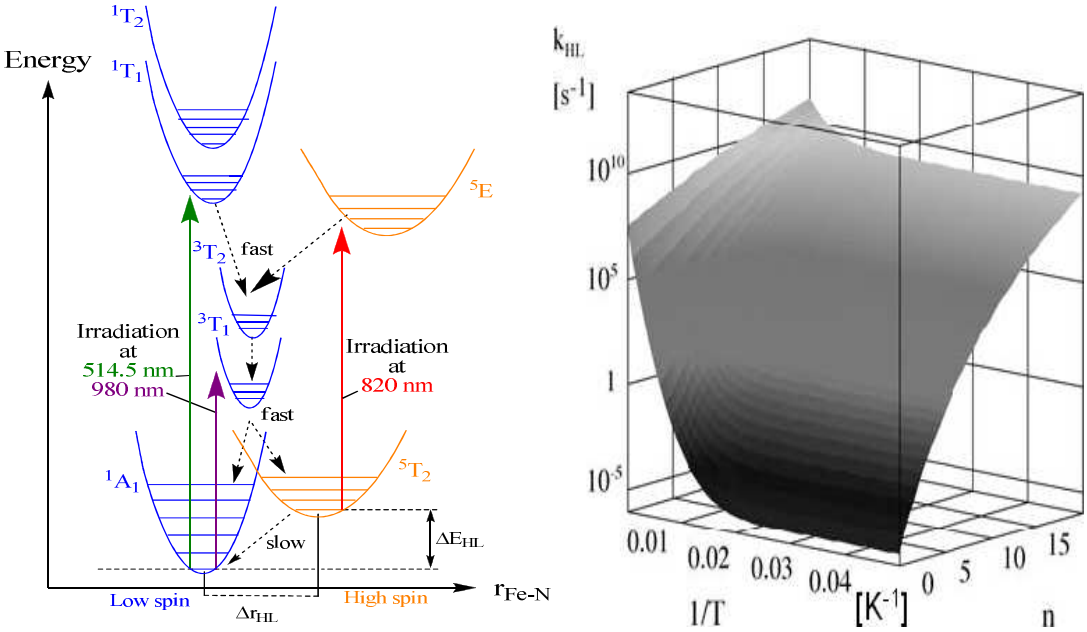

Figure 1.5. **(**Left) Electronic states for an Fe^{II} spin transition complex. The LIESST and reverse LIESST processes are both indicated. (Right) Dependence of the relaxation rate constants (K_{HL}) on the energy gap (n) and the inverse of temperature ($1/T$, in K^{-1}). Taken from Hauser.[31]

At temperatures above 100 K, in the so-called thermally activated region, the compound relaxes to the LS state from transient HS state via tunnelling.[33] A correlation between the life time of the metastable state and the $T_{1/2}$, was established by Hauser, and is known as the inverse energy gap law.[33] The energy gap between the high-spin and the low-spin state is given by ΔE_{HL} or $n = \Delta E_{HL}/\hbar\omega$. The calculated relaxation rate constants (K_{HL}) is a function of the temperature and the energy gap n ($n = \Delta E_{HL}/\hbar\omega$), the latter corresponds approximately to $0.02 \cdot T_{1/2}$ (Figure 1.5, right).[31]

The relaxation process curve is strongly influenced by the degree of cooperativity associated with the system.[34] For compounds which do not show any degree of cooperativity, the relaxation curves are always exponential, while those that do show cooperative phenomena, the relaxation curves exhibit a sigmoidal behaviour (see Figure 1.6a).[34] This non-exponential behaviour is characteristic of self-accelerating process and is mainly caused by the greater internal pressure induced by the LS state as compared to the HS state, which stabilizes the state with a smaller volume. Thus as γ_{LS} ($\gamma_{LS} = 1 - \gamma_{HS}$) grows ($\gamma_{LS}$ is the low spin fraction and γ_{HS} the high spin fraction), the stability of the LS state increases and the process is accelerated (Figure 1.6b).

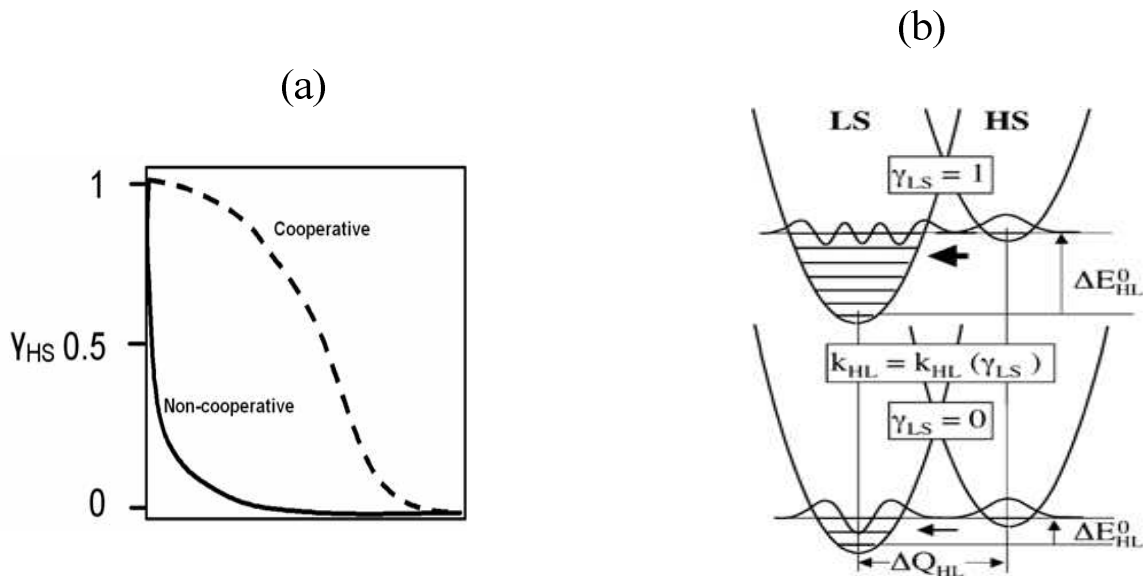

Figure 1.6. **(**a) Relaxation kinetics for the metastable high-spin state. Dashed line shows a sigmoidal curve while the full line shows an exponential decay. (b) Potential wells for the HS and LS states and their relative energies depending on the γ_{LS} value. Taken from Hauser.[35]

Although LIESST is unfavorable in SCO iron(III) systems, introduction of strong intermolecular interactions such as – π-stacks and hydrogen bonds afford cooperative spin interconversion with large thermal hysteresis and LIESST effects. The first LIESST effect in solid state was observed in $[Fe(pap)_2]ClO_4 \cdot H_2O$,[36] which exhibits an abrupt spin transition at $T_{1/2}\uparrow$ = 180 K and $T_{1/2}\downarrow$ = 165 K.

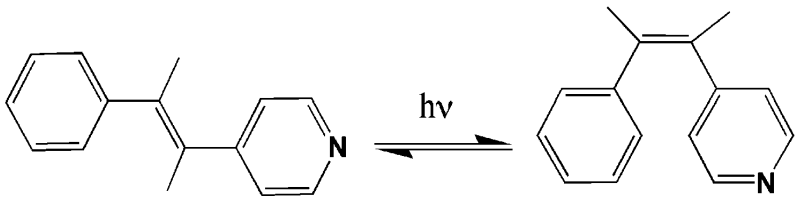

Scheme 1.1. *Trans* (left) – *cis* (right) isomerization in 1-phenyl-2-(4-pyridyl)ethane (stpy).

An introduction of potentially photo-isomerizable ligands into SCO iron(II) and iron(III) systems gives a different type of light induced SCO behaviour. This phenomenon is known as ligand-driven light-induced spin changes (LD-LISC),[37] and was first realized by Zarembowitch and co-workers. It relies on the principle that the photo-chemical perturbation of one or more ligands will result in a change of the ligand field sufficient to influence the magnetic behaviour of the complex. Let us assume that A and B are the

states of a metal complex before and after photochemical modification of the ligand, respectively. In order to observe the LD-LISC effect, A and B must have different magnetic behaviours. If A shows a thermal spin transition, and B maintains a high-spin form for example, irradiation into the complex at temperatures where A is LS, triggers a reversible spin state switching (Figure 1.7, left).

In practice, the first reaction implemented in order to observe a LD-LISC effect was based on *cis-trans* photo-isomerization of 1-phenyl-2-(4-pyridyl)ethane (stpy) (Scheme 1.1).[37] The following compounds [Fe(*trans*-stpy)$(NCS)_2$] and [Fe (*cis*-stpy)$(NCS)_2$] were synthesized. The first shows a spin transition centered around 108 K, while the second is completely high spin. Boillot *et al*. have been able to obtain a LD-LISC effect at room temperature in solution with the compound [Fe (t-msbpy) $(NCS)_2$] (t = msbpy-4-methyl-4'-trans-styryl-2, 2'-bipyridine).[38] Up till now, the phenomenon of LD-LISC has not been observed in solid state, because of the mechanical forces involved in the *cis–trans* conversion. However, a complex with a LD-LISC phenomenon has been successfully incorporated into a Langmuir-Blodgett film, opening new perspectives for practical applications.[39]

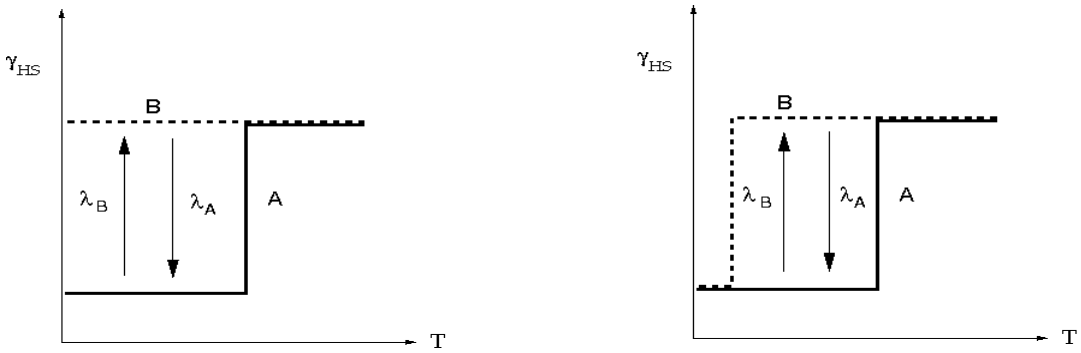

Figure 1.7. Schematic mechanism of the spin transition induced by isomerization of the ligand Taken from Zarembowitch *et al*.[37]

1.1.2.4 Spin Crossover and Cooperativity

In most cases, the spin crossover compounds in solid state do not follow a Boltzmann-type distribution. To explain we must take into account cooperativity effects, *i.e.*, interactions between molecules that switch. These interactions are essentially elastic, and cooperativity in spin transition systems depends on the ability of each molecule to propagate structural changes throughout the solid. Many models have been proposed to quantify cooperativity in spin crossover complexes.

Slichter and Drickamer[40] have proposed a macroscopic model based on regular solution theory, which implies a random distribution of molecules in the material.[41] The idea behind this model is to add an interaction term to the expression of the Gibbs free energy of the system:

$$G = \gamma_{HS} G_{HS} + (1-\gamma_{HS}) G_{LS} + TS_{mix} + \Gamma \gamma_{HS} (1-\gamma_{HS}) \quad (1.2)$$

Taking G_{LS} as the origin of the energies, we can write:

$$G = \gamma_{HS} \Delta H + RT \left(\gamma_{HS} \ln \gamma_{HS} + (1-\gamma_{HS}) \ln (1-\gamma_{HS}) - \gamma_{HS} \frac{\Delta S}{R} \right) + \Gamma \gamma_{HS} (1-\gamma_{HS}) \quad (1.3)$$

The equilibrium condition of the system is given by:

$$\left(\frac{\partial G}{\partial \gamma_{HS}} \right)_{P,T} = 0 \quad (1.4)$$

This leads to the following relationship:

$$\ln \left(\frac{1-\gamma_{HS}}{\gamma_{HS}} \right) = \left(\frac{\Delta H + \Gamma (1-2\gamma_{HS})}{RT} \right) - \frac{\Delta S}{R} \quad (1.5)$$

This equation is used to plot T as a function of γ_{HS}. Three cases may arise, as shown in Figure 1.8.

a) $\Gamma < 2RT_{1/2}$: In this case, $dT/d\gamma_{HS}$ is always positive regardless of γ_{HS}, and for each value of T corresponds a value of γ_{HS}. The transition is gradual without hysteresis.

b) $\Gamma = 2RT_{1/2}$: $dT/d\gamma_{HS}$ is positive and vanishes only for $dT/d\gamma_{HS} = 0.5$. The transition is abrupt when the temperature is close to $T_{1/2}$, but there is no hysteresis.

c) $\Gamma > 2RT_{1/2}$: This is a case where the spin transition has a hysteresis. However, $dT/d\gamma_{HS}$ vanishes by changing the sign for two different values, which we denote γ^{A}_{HS} and γ^{B}_{HS}, respectively at T_A and T_B. γ^{A}_{HS} is less than 0.5 and γ^{B}_{HS} above. Between these two temperatures is $dT/d\gamma_{HS}$ positive and negative elsewhere. In Figure 1.8, the XA and YB bifurcations correspond to minima of G, and the central part AB to maxima of G. On this region of the figure and at each temperature corresponds two separated values of γ_{HS}, one that minimizes G and the other that maximizes the free energy. Thus, when T increases to T_A, γ_{HS} changes abruptly from γ^{A}_{HS} to $\gamma^{A'}_{HS}$, to minimize the free energy of the system while tending to 1 if the temperature continues to rise. If the temperature then decreases, the HS fraction decreases as well to a γ^{B}_{HS} value, before suddenly shifts to $\gamma^{B'}_{HS}$ avoiding area where G is maximal, then tends to 0. The transition temperature is different from the previous one obtained during the rising of temperature, a hysteresis is therefore observed.

It is possible to find easily the parameter, Γ, by least-squares fittings of the magnetic susceptibility curves measured for SCO compounds. It then provides quantification of the cooperativity which allows to compare various systems among them with objective parameters.

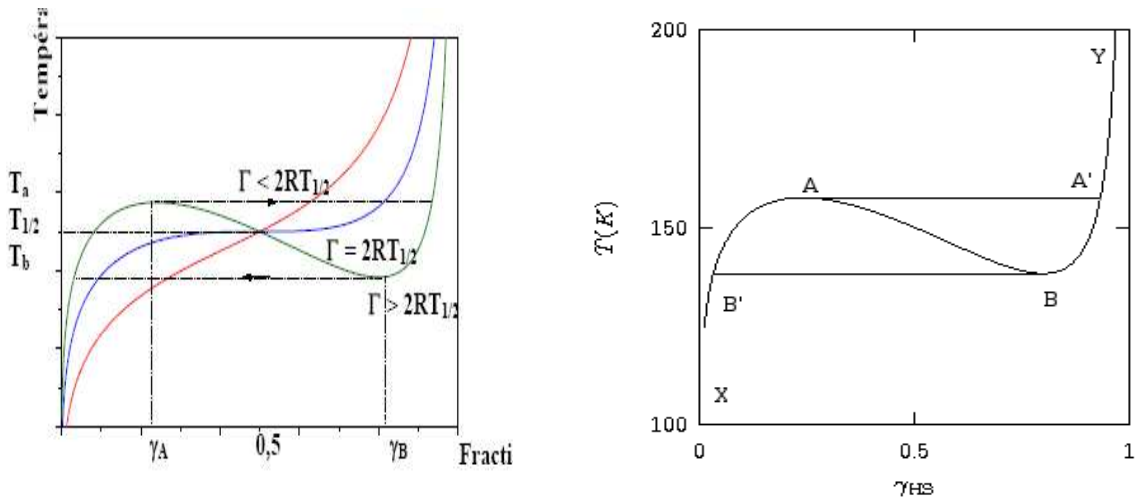

Figure 1.8. Variation of temperature, *T*, versus high-spin molar fraction, γ_{HS}: ΔH = 600 cm^{-1} and ΔS = 4 cm^{-1} K^{-1}. Taken from Kahn.[42]

1.1.2.5 Thiosemicarbazone – Schiff base-type Ligands

Because they possess a broad range of chemo-therapeutical and biological properties, thiosemicarbazones complexes are of great interest and are widely studied by many groups.[43-48] In this field, a particular attention was given to transition metal complexes of pyridoxal thiosemicarbazones derivatives, the pyridoxal moiety being a derivative of vitamin B6.[49] In another investigation area, the thiosemicarbazones ferric complexes are well-known to provide cooperative S =1/2 ↔ S = 5/2 spin-conversion processes, sometimes associated with a hysteresis effect,[50-53] whereas a majority of ferric systems exhibit thermally activated spin-equilibria.[54]

The coordination chemistry of thiosemicarbazones appeared to be very interesting from the point of view of both the number of metals forming complexes with them and the diversity of the ligand systems themselves (among them being also macrocyclic ones[55-59]) *i.e.*, their denticity, set of donor atoms, stabilization of various (less common) oxidation states of metals,[60,61] reactions of coordinated ligands,[59,62,63] *etc*. In solution thiosemicarbazones probably consist of an equilibrium mixture of thione (left) and thiol

(right) tautomers. Furthermore, it is possible to isolate complexes containing both tautomeric forms of the ligand (see chapters 3, 4 and 6).

Scheme 1.2. Proposed equilibrium in solution for thiosemicarbazones between the thione (left) and thiol (right) tautomers.

Pyridoxal thiosemicarbazones (H_2thpy) (Chart 1.1, left) form a special group of this ligand. First, because they can serve as models for studying a wide range of biological reactions which are catalyzed by enzymes;[64-66] second, because discontinuous spin transition associated to hysteresis loops were discovered for cationic ferric complexes of pyridoxal thiosemicarbazone derivatives.[67] This magnetic behaviour is exceptional and should be related to the analysis of the intermolecular interactions in the solid to be well understood.

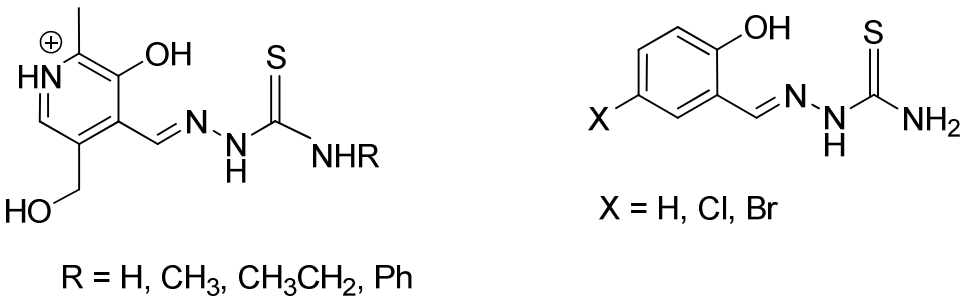

Chart 1.1. Structural formulas of pyridoxal-4R-thiosemicarbazone (H_2thpy), left and 5X-salicylaldehyde thiosemicarbazone (H_2thsa), right.

The common coordination mode of these ligands is presented in Chart 1.2. As can be seen, three ligators are engaged in coordination. Namely, the phenolic oxygen, the hydrazine nitrogen and the sulfur atom of the thioamide group. In each case, two metallocycles are formed: one six-membered (pyridoxilydene) and one five-membered (semicarbazide derivative). Furthermore the ligand can be coordinated either in neutral, monoanionic or dianionic forms. The monoanionic form is formed by deprotonation of the thiol form (Chart 1.2b). The dianionic form of ligand is formed by the additional deprotonation of the pyridine nitrogen (Chart 1.2c), *i.e.*, of the zwitterion, the existence of which is explained by the migration of the hydrogen atom from the phenolic OH group to

the heterocyclic nitrogen atom. In view of the mentioned deprotonation sequence, the form of the coordinated ligand will depend primarily on the pH and then on the nature of the metal ion.

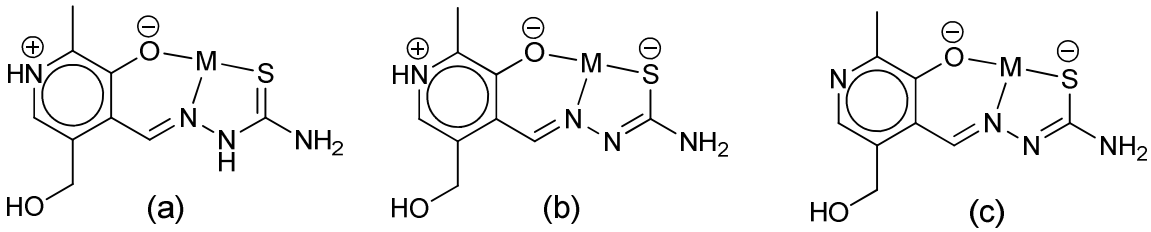

Chart 1.2. Coordination modes and ligand forms of H_2thpy (a, b, c).

When the carbonyl compound is salicylaldehyde or a substituted salicylaldehyde, the tridentates coordinate as the di-anionic groups shown in Chart 1.1 (right). The salts of the (anionic) bis(ligand) iron(III) complexes of this class of Schiff base anion (typically (cation^{+})[Fe(ligand^{2-})$_2$]$\cdot$nH_2O) frequently show spin crossover behaviour.

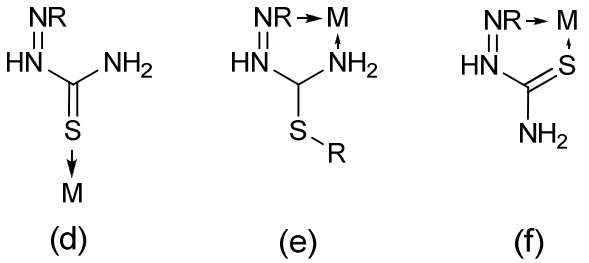

Chart 1.3. Coordination modes of thiosemicarbazide.

It has been shown[68] that the thiosemicarbazide molecule itself exists in the *trans* configuration (d), and while complexing in this configuration, it behaves as a monodentate ligand, bonding only through the sulfur atom. Gerbeleu *et al.*[69] have shown that bonding may also occur through the hydrazine nitrogen and the amide nitrogen (e) if the sulfur center is substituted. On reinvestigating the crystal structure of thiosemicarbazide hydrochloride, Coghi *et al.*[70] explained these conformational changes on the basis of protonated ↔ deprotonated isomeric forms and steric effects. In most of the complexes studied the thiosemicarbazone function coordinates to the metal ion in the *cis* configuration (f). In agreement with the above considerations, the most common stereochemistries encountered in thiosemicarbazone complexes are octahedral and five-coordinate.

1.1.2.6 2,6-bis(pyrazole)-pyridine Ligand and its Derivatives

During the last two decades, growing interest in the field of material chemistry has been focused on the synthetic design of organic high-spin molecules for use as novel magnetic materials. Conjugated radicals based on the bis(pyrazolyl)-pyridine core are very attractive in principle, since they per se combine optical, chelating and magnetic properties on a single molecular entity. Metal complex chemistry of 2,6-di(pyrazol-1-yl)-pyridine (bpp1) and 2,6-di(pyrazol-1-yl)-pyrazine (bpp2) ligands have been studied for some time.[71] The iron(II) complexes of these ligands have proved to be particularly fruitful, in that they undergo thermal spin-crossover transitions at accessible temperatures (typically 200–300 K), which are amenable to detailed study.[72-76] Materials that undergo spin-crossover near room temperature are of great current interest, because their thermochromism lends itself to a variety of applications in display and information storage devices.[77] Others have also found 2,6-dipyrazolylpyridine derivatives to be effective sensitisers for lanthanide ions, which have been incorporated into sensors for biological molecules.[78,79] On the other hand, it is worth mentioning that in both bis(pyrazolyl)-pyridine and bis(pyrazolyl)-pyrazine cores, the topological guidelines for intramolecular coupling for π-conjugated radicals cannot be applied because the presence of two pyrazolyl fragments (five membered ring) renders this system nonalternant.

Chart 1.4. Structures of 2,6-bis(pyrazol-1-yl)-pyridine (bpp1), left and 2,6-bis(pyrazol-1-yl)-pyrazine (bpp2), right.

1.2 Objective and Scope of the Thesis

The aim of the project is the design of new supramolecular systems based on transition metal fragments displaying switching behaviour with the objective of developing materials with novel (photo)physical properties for which several types of application may be envisaged.

The thesis is organized as follows:

- Chapter 1 is an introduction about the spin crossover phenomenon, the basic concepts and its application to molecular electronics. Based on this review, the scope and objective of the present work have been outlined.
- Chapter 2 briefly describes the experimental techniques employed for the analysis of materials and details synthetic protocols for obtaining the compounds.
- In chapters 3 and 4, we present iron(III) complexes with spin state changes above room temperature.

A systematic study on some ferric compounds of pyridoxal-N-substituted thiosemicarbazone ligands reveals that the occurrence of spin crossover behaviour in these systems is associated with the desolvation process.

- Chapters 5 and 6 study the photo-physical behaviour of new materials.

The research field of photomagnetism as applied to spin crossover systems, *i.e.* the study of a light-induced change of the magnetic properties of a material, began with the discovery of Light-Induced Excited Spin-State Trapping (LIESST).[26] This phenomenon involves the reversible switching between the diamagnetic low spin form and paramagnetic high spin state of Fe(II) spin crossover compounds under the influence of laser light of an appropriate wavelength. A recent important advance in the field of photo-physical properties is the discovery of the LIESST phenomenon for an Fe(III) derivative in the solid state.[35,80] This has been achieved by preventing the normally expected rapid relaxation from the metastable high spin to the low spin state through the introduction of strong intermolecular π-stacking interactions.

However, the general requirements for the observation of LIESST for Fe(III) are not yet understood, therefore, our approach is focused on the elucidation of the structural and electronic factors involved for observing the phenomenon. For this objective, Fe(III) materials are designed in which cooperative spin crossover – and an associated expected photo-physical behaviour – are attained by using 5X-salicylaldehyde thiosemicarbazone (X = Cl, Br) acting as chelating agents and, capable of promoting π-stacking interactions and hydrogen bonding. Such an approach is also motivated by the quasi-absence of Fe(III) LIESST spin transition materials in literature. In summary, it is anticipated that the present study may be a worthwhile contribution towards the elucidation of the Fe(III) LIESST mechanism.

- The design and preparation of double switches is discussed in chapter 7.

A route towards the novel challenge of preparing hybrid materials with a switching of properties is explored. The chemical approach that has been used to reach this goal consists of combining anionic component, cesium bis(salicylaldehyde thiosemicarbazonato) ferrate(III) tetrahydrate with cationic unit, bis[2,6-bis(pyrazol-1-yl)-pyridine] iron(II) diperchlorate, both have the potential to induce a SCO effect.

1.3 References

(1) Balzani, V.; Credi, A.; Raymo, F. M.; Stoddart, J. F. *Angew. Chem. Int. Ed.* **2000**, *39*, 3348.

(2) Fabbrizzi, I.; Licchelli, M.; Pallavicini, P. *Acc. Chem. Res.* **1999**, *32*, 846.

(3) Willner, I.; Katz, E. *Angew. Chem. Int. Ed*. **2000**, *39*, 1180.

(4) Irie, M. *Chem. Rev.* **2000**, *100*, 1685.

(5) Yokoyama, Y. *Chem. Rev.* **2000**, *100*, 1717.

(6) Berkovic, G.; Krongauz, V.; Weiss, V. *Chem. Rev.* **2000**, *100*, 1741.

(7) Feringa, B. L.; Van Delden, R. A.; Koumura, N.; Geertsema, E. M. *Chem. Rev.* **2000**, *100*, 1789.

(8) Feringa, B. L. *Acc. Chem. Soc.* **2001**, *101*, 504.

(9) Diederich, F. *Chem. Commun.* **2001**, 219.

(10) Gütlich, P.; Hauser, A.; Spiering, H. *Angew. Chem. Int. Ed. Engl*. **1994**, *33*, 2024.

(11) Bousseksou, A.; Negre, N.; Goiran, M.; Salmon, L.; Tuchagues, J.-P.; Boillot, M.-L.; Boukheddaden, K.; Varret, F. *Eur. Phys. J. B* **2000**, *13*, 451.

(12) Raymo, F. M. *Adv. Mater*. **2002**, *14*, 401.

(13) De Silva, A. P.; Gunaratne, O. N.; MCCoy, C. P. *Nature* **1993**, *42*, 364.

(14) De Silva, A. P.; De Silva, A. A.; Dissanavake, A. S.; Sandanayake, K. R. A. S. *J. Chem. Soc. Chem. Commun.* **1989**,1054.

(15) Special Issue on "Optical networking" *Bell Labs Tech. J.* **1994**, *4*, 3.

(16) Létard, J.-F.; Guionneau, P.; Goux-Capes, L. *Top. Curr. Chem*. **2004**, *235*, 221-249.

(17) Caroll, R. L.; Gorman, C. B. *Angew. Chem. Int. Ed. Eng.* **2002**, *41*, 4378.

(18) Kahn, O.; Launay, J. P. *Chemtronics* **1988**, *3*, 140.

(19) Kahn, O.; Codjovi, E. *Phil. Trans. R. Soc. Lond. A*. **1996**, *354*, 359.

(20) Cambi, L.; Szegö, L. Ber. **1931**, *10*, 2591.

(21) Cambi, L.; Szegö, L. Ber. **1933**, *66*, 656.

(22) Ewald, A.H.; Martin, R. L.; Ross, I. G.; White, A. H. *Proc. Roy. Soc. London Ser*. **1964**, *A 280*, 235.

(23) (a) Tanabe, Y.; Sugano, S. *J. Phys. Soc. Jpn.* **1954**, *9*, 753. (b) Tanabe, Y.; Sugano, S. *J. Phys. Soc. Jpn.* **1954**, *9*, 766.

(24) Real, J. A.; Gaspar, A. B.; Muñoz, M. C. *Dalton Trans*. **2005**, 2062-2079.

(25) Born, M.; Oppenheimer, R. *Annalen der Physik* **1927**, *84*, 457-484.

(26) Hauser, A. *J. Chem. Phys.*, **1991**, *94*, 2741.

(27) König, E. Struct. Bonding (Berlin) **1991**, *76*, 51.

(28) McGarvey, J. J.; Lawthers, I. *J. Chem. Soc., Chem. Commun.* **1982**, 906.

(29) (*a*) Decurtins, S.; Gütlich, P.; Köhler, C. P.; Spiering, H.; Hauser, A. *Chem. Phys. Lett.* **1984**, *139*, 1. (*b*) Decurtins, S.; Gütlich, P.; Hasselbach, K. M.; Spiering, H.; Hauser, A. *Inorg. Chem.* **1985**, *24*, 2174.

(30) Hauser, A.; Jeftić, J.; Romstedt, H.; Hinek, R.; Spiering, H. *Coord. Chem. Rev.* **1999**, *190–192*, 471.

(31) Hauser, A. Light-induced spin crossover and the high-spin -> low-spin relaxation. In *Spin Crossover in Transition Metal Compounds II, Topics in Current Chemistry*, Gütlich, P.; Goodwin, H. A., Eds. Springer: 2004; Vol. 234, pp 155-198.

(32) Hauser, A. *Chem. Phys. Lett*. **1986**, *124*, 543.

(33) Hauser, A.; Vef, A.; Adler, P.; *J. Chem. Phys.* **1991,** *95*, 8710-8717.

(34) Hauser, A.; Gütlich, P.; Spiering, H., *Inorg. Chem.* **1986,** *25*, 4245-4248.

(35) Hauser, A. *Comments Inorg. Chem.* **1995**, *17*, 17.

(36) Hayami, S.; Gu, Z. Z.; Shiro, M.; Einaga, Y.; Fujishima, A.; Sato, O. *J. Am. Chem. Soc.* **2000**, *122*, 7126.

(37) Roux, C.; Zarembowitch, J.; Gallois, B.; Granier, T.; Claude, R. *Inorg. Chem.* **1994**, *33*, 2273.

(38) Boillot, M. L.; Sour, A.; Delhaès, P.; Mingotaud, C.; Soyer, H. *Coord. Chem. Rev.* **1999**, *190–192*, 47.

(39) Soyer, H.; Mingotaud, C.; Boillot, M.-L.; Delhaès, P. *Langmuir* **1998**, *14*, 5890.

(40) Slichter, C. P.; Drickamer, H. G. *J. Chem. Phys.* **1972**, *56*, 2142.

(41) Fisher, D. C.; Drickamer, H. G. *J. Chem. Phys.* **1971**, *54*, 4825.

(42) Kahn, O. *Molecular Magnetism*; Wiley - VCH, 1993.

(43) Padhye, S.; Kauffman, G. B. *Coord. Chem. Rev*. **1985**, *63*, 127.

(44) Richardson, D. R. *Crit. Rev. Onc. Hemat*. **2002**, *42*, 267.

(45) Afrasiabi, Z.; Sinn, E.; Lin, W. S.; Ma, Y. F.; Campana, C.; Padhye, S. *J. Inorg. Biochem.* **2005**, *99*, 1526.

(46) Belicchi Ferrari, M.; Bisceglie, F.; Casoli, C.; Durot, S.; Morgenstern-Badarau, I.; Pelosi, G.; Pilotti, G.; Pinelli, E.; Tarasconi, P. *J. Med. Chem*. **2005**, *48*, 1671.

(47) West, D. X.; Padhye, S. B.; Sonawane, P. B. *Struct. Bond.* **1991**, *76*, 1.

(48) West, D. X.; Liberta, A. E.; Padhye, S. B.; Chikate, R. C.; Sonawane, P. B.; Kumbhar, A. S.; Yerande, R. G. *Coord. Chem. Rev.* **1993**, *123*, 49.

(49) (a) Belicchi Ferrari, M.; Fava Gasparri, G.; Leoparti, E.; Pelizzi, C.; Tarasconi, P.; Tosi, G. J. *Chem. Soc., Dalton Trans*. **1986**, 2455. (b) Belicchi Ferrari, M.; Gasparri Fava, G.; Pelizzi, P. Tarasconi, G. Tosi, *J. Chem. Soc., Dalton Trans*. **1987**, 227. (c) M. Belicchi Ferrari, C.; Gasparri Fava, G.; Lanfranchi, M.; Pelizzi, C.; Tarasconi, P. *J. Chem. Soc., Dalton Trans.* **1991**, 1951. (d) Belicchi Ferrari, M.; Gasparri Fava, G.; Tarasconi, P.; Albertini, R.; Pinelli, S.; Starcich, R. *J. Inorg. Biochem*. **1994**, *53*, 13. (e) Belicchi Ferrari,

M.; Gasparri Fava, G.; Pelosi, G.; Rodriguez-Argüelles, M. C.; Tarasconi, P. *J. Chem. Soc., Dalton Trans*. **1995**, 3035. (f) Belicchi Ferrari, M.; Gasparri Fava, G.; Pelizzi, C.; Pelosi, G.; Tarasconi, P. *Inorg. Chim. Acta* **1998**, *269*, 297. (g) Belicchi Ferrari, M.; Gasparri Fava, G.; Pelosi, G.; Tarasconi, P. Polyhedron **2000**, *19*, 1895. (h) Belicchi Ferrari, M.; Bisceglie, F.; Leporati, E.; Pelosi, G.; Tarasconi, P. *Bull. Chem. Soc. Jpn* **2002**, *75*, 781.

(50) Zelentsov, V. V. *Sov. Sci. Rev. B, Chem*. **1987**, *10*, 485. (b) Zelentsov, V. V. *Sov. J. Coord Chem.* **1992**, 18, 787.

(51) Timken, M. D.; Wilson, S. R.; Hendrickson, D. N. *Inorg. Chem*. **1985**, *24*, 3450.

(52) Gupta, N. S.; Mohan, M.; Jha, N. K.; Antholine, W. E. *Inorg. Chim. Acta* **1991**, *184*, 13.

(53) (a) Floquet, S.; Guillou, N.; Négrier, P.; Rivière, E.; Boillot, M.-L. *New J. Chem*. **2006**, *30* 1621. (b) Floquet, S.; Boillot, M.-L.; Rivière, E.; Varret, F.; Boukheddaden, K.; Morineau, D.; Négrier, P. *New J. Chem*. **2003**, *27*, 341.

(54) van Koningsbruggen, P. J.; Maeda, Y.; Oshio, H. in *Spin Crossover in Transition Metal Compounds I, Topics in Current Chemistry*, eds. P. Gütlich and H. A. Goodwin, Springer, Berlin, 2004, vol. 233, 259-324.

(55) Arion, V.; Revenko, M.; Gradinaru, J.; Simonov, Yu.; Kravtsov, V.; Gerbeleu, N.; Saint-Aman, E.; Adams, F. *Rev. Inorg. Chem.* **2001**, *21*, 1.

(56) Leovac, V. M.; Češljević, V. I. *Coordination Chemistry of Isothiosemicarbazide and It's Derivatives*, Faculty of Science, Novi Sad, 2002 (in Serbian).

(57) Chandra, S.; Sangeetika, X. *Spectrochim. Acta A* **2004**, *60*, 147.

(58) Singh, N. K.; Srivastava, A.; Sodhi, A.; Ranjan, P. *Trans. Met. Chem.* **2000**, *25*, 133.

(59) Gerbeleu, N. V.; Arion, V. B.; Burgess, J. *Template Synthesis of Macrocyclic Compounds*, Wiley-VCH, Weinheim, 1999.

(60) Leovac, V. M.; Jovanović, Lj. S.; Češljević, V. I.; Bjelica, L. J.; Ević, N. J. *Polyhedron* **1992**, 11, 1029.

(61) Knof, U.; Weyhermuller, T.; Wolter, T.; Weighardt, K. *J. Chem. Soc. Chem. Commun.* **1993**, 726.

(62) Češljević, V. I.; Leovac, V. M. *J. Serb. Chem. Soc.* **1994**, *59*, 13.

(63) Arion, V.; Weighardt, K.; Weyhermuller, T.; Bill, E.; Leovac, V. M.; Rufinska, A. *Inorg. Chem.* **1997**, *36*, 661.

(64) Holm, R. H. *Complexes of Vitamin B6* in *Inorganic Biochemistry*, G. B. Eichhorn, Ed., Elsevier, Amsterdam, 1975.

(65) Dolphin, D.; Poulson, R.; Avramovic, O. Eds., *Vitamin B-6 Pyridoxal Phosphate: Chemical, Biochemical and Medical Aspects,* Part A, Wiley, New York, 1986.

(66) Aoki, K.; Yamazaki, H. *J. Chem. Soc. Chem. Commun.* **1980**, 363.

(67) Mohan, M.; Madhuranath, P. H.; Kumar, A.; Kumar, M.; Jha, N. K. *Inorg. Chem.* **1989**, *28*, 96.

(68) (a) Domiano, P.; Gasparri Fava, G.; Nardelli, M.; Sgarabotto, P. *Acta Crystallogr*. **1969**, *25B*, 343. (b) Andreetti, G. D.; Domiano, P.; Fava, G.; Nardelli, M.; Sgarabotto, P. *Acta Crystallogr*. **1970**, *B26*, 1005.

(69) Gerbeleu, N. V.; Revenko, M. D.; Leovats, V. M.; *Russ. J. Inorg. Chem.* **1977**, *22*, 1009.

(70) Coghi, L.; Lanfredi, A. M. M.; Tiripicchio, A. J. Chem. Sot., Perkin Trans. **1976**, *2*, 1808.

(71) Halcrow, M. A. *Coord. Chem. Rev*. **2005**, *249*, 2880.

(72) (a) Holland, J. M.; McAllister, J. A.; Lu, Z.; Kilner, C. A.; Thornton-Pett, M.; Halcrow, M. A. *Chem. Commun.* **2001**, 577. (b) Holland, J. M.; McAllister, J. A.; Kilner, C. A.; Thornton-Pett, M.; Bridgeman, A. J.; Halcrow, M. A. *J. Chem. Soc., Dalton Trans.* **2002**, 548. (c) Money, V. A.; Evans, I. R.; Halcrow, M. A.; Goeta, A. E.; Howard, J. A. K. *Chem. Commun.* **2003**, 158.

(73) (a) Holland, J. M.; Barrett, S. A.; Kilner, C. A.; Halcrow, M. A. *Inorg. Chem. Commun.* **2002**, *5*, 328. (b) Elhaïk, J.; Kilner, C. A.; Halcrow, M. A. *CrystEngComm*. **2005**, *7*, 151.

(74) (a) Elhaïk, J.; Money, V. A.; Barrett, S. A.; Kilner, C. A.; Radosavljevic Evans, I.; Halcrow, M. A. *Dalton Trans*. **2003**, 2053. (b) Money, V. A.; Elhaïk, J.; Evans, I. R.; Halcrow, M. A.; Howard, J. A. K. *Dalton Trans.* **2004**, 65. (c) Money, V. A.; Evans, I. R.; Elhaïk, J.; Halcrow, M. A.; Howard, J. A. K. *Acta Crystallogr*. **2004**, *B60*, 41.

(75) Money, V. A.; Elhaïk, J.; Halcrow, M. A.; Howard, J. A. K. *Dalton Trans.* **2004**, 1516.

(76) Carbonera, C.; Costa, J. S.; Money, V. A.; Elhaïk, J.; Howard, J. A. K.; Halcrow, M. A.; Létard, J.-F. *Dalton Trans.* **2006**, 3058.

(77) Spin Crossover in Transition Metal Compounds I–III; Gütlich, P., Goodwin, H. A., Eds.; Topics in Current Chemistry; 2004; Vols. 233–235.

(78) (a) Rodríguez-Ubis, J. C.; Sedano, R.; Barrosso, G.; Juanes, O.; Brunet, E. *Helv. Chim. Acta* **1997**, 80, 86 and 621 (correction). (b) Yuan, J.; Wang, G.; Majima, K.; Matsumoto, K. *Anal. Chem.* **2001**, *73*, 1869. (c) Brunet, E.; Juanes, O.; Sedano, R.; Rodríguez-Ubis, J. C. *Photochem. Photobiol. Sci.* **2002**, *1*, 613. (d) Yuan, J.; Tan, M.; Wang, G. J. Lumin. **2004**, *106*, 91.

(79) (a) Sueda, S.; Yuan, J.; Matsumoto, K. *Bioconjugate Chem.* **2002**, *13*, 200. (b) Ye, Z.; Tan, M.; Wang, G.; Yuan, J. *Anal. Chem.* **2004**, *76*, 513. (c) Ye, Z.; Tan, M.; Wang, G.; Yuan, J. *Talanta* **2005**, *65*, 206. (d) González-Martínez, M. A.; Penalva, J.; Rodríguez-Urbis, J. C.; Brunet, E.; Maquieira, A.; Puchades, R. *Anal. Bioanal. Chem.* **2006**, *384*, 1540.

(80) Juhász, G.; Hayami, S.; Sato, O.; Maeda, Y. *Chem. Phys. Lett*. **2002**, *364*, 164.

Chapter II
General Overview of the Analytical Techniques and Synthesis

Synopsis

This chapter presents the general experimental details of the studies presented in this dissertation. It begins with a brief description of the experimental setup and parameters for each of the techniques used. Relevant review articles for each method are listed and reference to later chapters in the dissertation is given where appropriate. The chapter subsequently presents the procedures for the synthesis of all the materials studied in this thesis. In most cases, the compounds were synthesized according to previously reported methods, with slight variations to increase the size and quality of the crystals.

2.1 Introduction

This chapter starts with a brief description of the various physical techniques used during the research project to characterize the compounds synthesized. In the first part, some standard techniques used for a general characterization of the different materials are presented. A more general description of the single crystal X-ray structure determinations carried out on the different compounds is then presented. This is followed by an explanation of the synthesis and characterizations of all the materials used during the thesis. This part is subdivided in two sections, ligands and complexes, which in turn are divided into two sections, thiosemicarbazone-based compounds and pyrazole-based compounds.

2.2 General Laboratory Techniques

Elemental Analysis. (C, H, N, S) was carried out at the Microanalytical Department of the University of Groningen, using the Euro EA Elemental Analyzer from the EuroVector Instrument and Software Company. The iron content was determined at the service central d'analyse, CNRS, Echangeur de Solaize – Chemin du Canal (France). During CHNS-analysis approximately 2 mg of sample is accurately weighed on a 6-digit analytical scale. With air sensitive organo-metals the weighing is performed in a glove box under argon. The tin sample-cups are placed in an autosampler, here the air is washed out with helium and the analysis cycle is started. Aided by the exothermal burning of tin and the dosed addition of oxygen the sample is completely burned at 1700-1800°C. Further oxidation of the sample is supported by a tube with Tungstenoxide (WoO_3) catalyst that provides oxygen.

$$C_xH_xN_xS_x + O_2 \rightarrow xCO_2 + xH_2O + xNO_x + xSO_x \qquad (2.1)$$

After oxidation the gasses are reduced by a very pure Copper catalyst inside the same tube as the Tungsten catalyst is in.

$$xNO_x + xSO_x \rightarrow xN_2 + xSO_2 \qquad (2.2)$$

The gasses are reduced to CO_2, H_2O, N_2 and SO_2. These gasses are then separated via an online GC method with a 'poropak QS' column at 80°C and measured with thermal conductivity detection (TCD). 'CalladuisTM' software draws and integrates the chromatogram. The integrated peak height is converted to a very exact percentage of one of the mentioned elements using for example acetanilide as a standard.

The result is used as a quality check for the produced compound.

Beside these applications the EuroEA3000-CHNS0analyser is also used for measuring proteins and for measuring C,N,S and O isotopes when coupled to an IRMS-analyser.

UV-Visible-NIR. UV/vis absorption spectrum (accuracy ± 2 nm) was recorded using a HP8453 diode array spectrophotometer or a JASCO V570 UV/vis-NIR spectrophotometer equipped with an integrating sphere for solid state measurements (JASCOISN470), using the diffuse reflectance technique, with $BaSO_4$ as a reference. A sample holder mounted on a Dewar and in thermal contact with the refrigerant through a copper rod was used to perform measurements at temperatures around 100 K. The spectral range used was 200 – 2000 nm. All samples, crystalline or powder were powdered when placed in the sample holder.

FTIR Spectroscopy. Infrared spectroscopy is a technique based on the vibrations of the atoms of a molecule. An infrared spectrum is commonly obtained by passing infrared radiations through a sample and determining what fraction of the incident radiation is absorbed at a particular energy. The energy at which any peak in an absorption spectrum appears corresponds to the frequency of a vibration of a part of a sample molecule. The preferred format for presenting spectral data for qualitative analysis is in the percentage transmittance format. This format provides the best dynamic range for both weak and intense bands. For a good transmission IR spectrum of a solid or a liquid, a sample should not be thicker than 10 μm. For thicker samples a very popular technique called Attenuated Total Reflection (ATR) is used.

Room temperature infrared spectra were recorded on Interspec 200-X FT-IR spectrometer in the 4000 and 400 cm^{-1} spectral range, using KBr-mulled tablets (spectral resolution of 1 cm^{-1}).

NMR. ^1H NMR spectra were recorded in DMSO-d_6 for thiosemicarbazone based-ligands and in $CDCl_3$ using a Varian VXR 300 spectrometer with TMS as standard.

Mass Spectrometer. Routine EI+ spectra were measured with the MS route JMS-600H sector mass spectrometer (JEOL).

Thermogravimetric Measurements. Thermogravimetric measurements were carried out using a Perkin Elmer TGA7 apparatus in the temperature range 298 – 773 K under inert atmosphere (N_2) with 5 K/min heating rate.

2.2.1 Single Crystal X-Ray Diffraction and Structure Solution

Crystallographic data and numerical details on data collection and refinement for all the compounds are summarized in the first table of their corresponding chapters. All data collections were performed on a Bruker SMART APEX CCD diffractometer (Platform with full three-circle goniometer), equipped with a 4K CCD detector set 60.0 mm from the crystal. Intensity measurements were performed using graphite monochromated Mo-K$\bar{\alpha}$ radiation from a sealed ceramic diffraction tube (SIEMENS). Suitable crystals were mounted on top of a glass fiber, aligned and cooled to 100(1) K using the Bruker KRYOFLEX low-temperature device. Data integration and global cell refinement was performed with the program SAINT,[1] intensity data were corrected for Lorentz and polarisation effects, scale variation, for decay and absorption: a multi-scan absorption correction was applied, based on the intensities of symmetry-related reflections measured at different angular settings (SADABS),[2] and reduced to F_o^2. The program suite SAINTPLUS was used for space group determination (XPREP).[1]

All structures were solved by direct methods using the program SIR2004,[3] Patterson methods and extension of the model was accomplished by direct methods applied to difference structure factors using the program DIRDIF.[4,5] All non hydrogen atoms were refined anisotropically. Hydrogen atoms were refined using the riding model.

The positional and anisotropic displacement parameters for the non-hydrogen atoms and isotropic displacement parameters for hydrogen atoms were refined on F^2 with full-matrix least-squares procedures minimizing the function $Q = \sum_h[w(|(F_o^2) - k(F_c^2)|)^2]$, where $w = 1/[\sigma^2(F_o^2) + (aP)^2 + bP]$, $P = [\max(F_o^2,0) + 2F_c^2]/3$, F_0 and F_c are the observed and calculated structure factor amplitudes. Neutral atom scattering factors and anomalous dispersion corrections were taken from International Tables for Crystallography.[6,7] All refinement calculations and graphics were performed on a HP XW6200 (Intel XEON 3.2 Ghz) / Debian-Linux computer at the University of Groningen with the program packages SHELXL[8,9] (least-square refinements), a locally modified version of the program PLUTO[10,11] (preparation of illustrations) and PLATON [12,13] package (checking the final results for missed symmetry with the MISSYM option, solvent accessible voids with the SOLV option, calculation of geometric data and the ORTEP[12,13] illustrations).

2.2.2 X-Ray Powder Diffraction Measurements

In this study, the XRPD measurements were carried out using Bruker D8 and Huber G670 diffractometers. The Bruker D8 diffractometer operates using Bragg-Brentano geometry, Cu Kα radiation and an energy-dispersive solid-state detector. This setup was used both for routine phase analysis and for crystal structure refinement. Typical scans for phase analysis were carried out with a step-width of 0.02 degrees (2θ) and with a counting time of 1 second per step; the data were examined using the Powdercell software. For structural refinement typical scans were performed with a step-width of 0.02 degrees (2θ) and a counting time of 4 seconds per step; the data were analyzed using the GSAS software package with the EXPGUI interface.[14,15] The Huber G670 diffractometer was used to collect variable temperature XRPD data. This setup uses Mo-Kα radiation and a G670 Guinier camera comprised of a curved imaging plate as a replacement for photographic film. The linear detector allows rapid data collection. Measurement at low temperature was performed using a closed-cycle refrigerator system supplied by Helix Technology Corporation (8200 compressor). The diffraction patterns cover an angular range from 0 to 100 degrees 2θ with data at intervals of 0.005 degrees 2θ. An exposure time of 30 minutes was used for each measurement.

2.2.3 X-Ray Photoelectron Spectroscopy (XPS) Measurements

For the XPS measurements Aluminum foil was used as substrate. The hybrid molecular switch powder samples were dispersed in dimethylformamide and after short stirring, a small drop of the suspension was left to dry in air on the substrate. The samples were introduced through a load look system into an SSX-100 (Surface Science Instruments) photoelectron spectrometer with a monochromatic Al Kα X-ray source (hν = 1486.6 eV). The base pressure in the spectrometer during the measurements was $2 \cdot 10^{-10}$ mbar. The photoelectron take off angle was 37 ^{o}. The energy resolution was set to 1.4 eV. Sample charging was compensated for by directing an electron flood gun supplying 0.1 eV kinetic energy electrons onto the sample and covering the sample holder with a Ta grid. Since molecular magnetic switches are insulating compounds, XPS binding energies have to be referenced to an internal reference of the sample. The sulfur 2p signal at 163.9 eV (thioamide group) was chosen for this purpose. The XP spectra showed no X-ray induced changes. Spectral analysis included Shirley background subtraction,[16] and peak

deconvolution employing Gaussian functions, in a least squares curve-fitting program (WinSpec) developed at the LISE, University of Namur, Belgium.

2.2.4 Electron Paramagnetic Resonance (EPR)

Electron Paramagnetic Resonance (EPR), also known as Electron Spin Resonance (ESR) or Electron Magnetic Resonance (EMR), is a magnetic resonance method formally related to NMR, Nuclear Magnetic Resonance. It is used to study paramagnetic materials, those containing unpaired electrons. Materials which have unpaired electrons include free radicals, donor and acceptor impurities in semiconductors and metal ions in crystals. Most other chemical compounds have an even number of electrons with all electrons paired. In the case of EPR, the magnetic moments arise from electrons rather than nuclei.

In an EPR experiment the sample is placed in a strong magnetic field and irradiated with photons (electromagnetic radiation) in the microwave range (ν = 3 – 95 GHz). With EPR we measure energy separations between spin states of an unpaired electron in the environment of other magnetic species (usually nuclei) and the external magnetic field, *B*. In the simple case of a free electron, the spin, and the magnetic moment associated with it, is quantized parallel or antiparallel to the external field. Irradiation with photons satisfying the resonance condition, $\Delta E = h\nu$, can induce transitions between the levels. An EPR spectrometer accomplishes resonance by using a fixed frequency, ν, while sweeping the magnetic field. A typical experiment utilizes microwave frequencies of roughly 9 GHz which for organic radicals give resonances at magnetic fields of about 300 mT or 3 kG. Commonly EPR spectra are presented as first or second derivatives. With the move to more advanced experiments, it has become possible to considerably extend the frequency range, allowing the use of higher magnetic fields and yielding higher sensitivity and better spectral resolution. More detailed information can be found in literature.[17-19]

Complementary to Mössbauer measurements, EPR was used to identify the oxidation and spin states of iron ions present in the iron complexes described in this dissertation.
The EPR measurements were performed in the range 77 - 420 K with an X-band Bruker ESP 300e spectrometer equipped with a variable temperature accessory from Oxford Instruments. The crystals are mounted on a small Perspex sample holder to allow their

orientation with respect to the magnetic field. The microwave frequency is measured with a Systron Donner frequency counter.

2.2.5 Magnetic Measurements

All of the magnetization measurements described in this thesis were performed using a Quantum Design MPMS7 magnetometer. This system is equipped with a SQUID (superconducting quantum interference device), which is a very sensitive device for measuring magnetic fields and is based on superconducting loops containing Josephson junctions. The basic components of a SQUID magnetometer typically consist of the following: a superconducting magnet, a superconducting detection coil (pick-up coil), a SQUID and a superconducting magnetic shield. The magnetic signal of the sample is obtained via the superconducting pick-up coil which is connected to the SQUID device, located away from the sample in a liquid helium bath. This device acts as a magnetic flux-to-voltage converter. When the sample is moved up and down it produces an alternating magnetic flux in the pick-up coil which leads to an alternating output voltage in the SQUID device. This voltage is then amplified and read out by the magnetometer electronics. The output signal is proportional to the magnetic moment of the sample which can be magnetized by a magnetic field produced by the superconducting magnet. The MPMS7 operates at temperatures between 2 and 400 K and at magnetic fields of up to 7 T. The sensitivity of the magnetometer is 10^{-7} emu in reciprocating sample oscillation mode. The sample was inserted into a gelatin capsule, which has a weak diamagnetic signal. In order to avoid movement of the sample during the measurement, the capsule was filled with cotton. The capsule was then placed in a plastic straw and attached to the MPMS sample probe using tape. It is important to check that the straw is attached properly so that it does not break loose during the measurement. The samples were measured in a particular magnetic field after cooling either in the absence of a magnetic field (zero-field cooled, ZFC) or in the measurement field (field-cooled, FC). More information on this analytical method can be found in literature.[20,21]

2.2.6 Mössbauer Spectroscopy

^{57}Fe Mössbauer spectra (MS) were collected at various sample temperatures using a constant acceleration spectrometer equipped with a ^{57}Co(Rh) source kept at room temperature (RT). For the low temperature measurements a liquid N_2 bath cryostat (Oxford) was used to cool the samples. The calibration of the spectrometer was done

using metallic α-Fe at RT and all isomer shift (IS) values are given relative to this standard.

Details about the theory and application of Mössbauer spectroscopy can be found in literature.[22-24]

2.2.7 Differential Scanning Calorimetry

Differential Scanning Calorimetry (DSC) means the measurement of the change of the difference in the heat flow rate to the sample and to a reference sample while they are subjected to a controlled temperature program. In the event that a transition occurs in the sample, however, thermal energy is added to or subtracted from the sample or reference containers in order to maintain both sample and reference at the same temperature. Because this energy input is precisely equivalent in magnitude to the energy absorbed or evolved in the particular transition, a recording of this balancing energy yields a direct calorimetric measurement of the transition energy. It should even be mentioned, that heat flow only flows if there is a temperature difference present. In other words, a non-zero heat flow rate difference implies always a temperature difference between the sample and the reference and their surroundings and a change of the heat flow rate difference implies a change of the temperature as well.

The heat flow has been recorded using a DSC 2920 MDSC of TA-Instruments with 1, 2, 5 and 10 K/min scan rates in the temperature range of 188 – 343 K.

Heat capacity measurements were performed with a Q1000 MDSC of TA-Instruments in the modulated mode. Heating rate was 2 K/min, amplitude 0.5 K and period 60 s. The heat capacity constant was calibrated using sapphire, details of the thermodynamic calibration are given elsewhere.[25] For heat capacity determination reported in chapter 3, samples were equilibrated at 233 K, heated to 313 K for the low temperature phase and to 423 K for the high temperature phase.

2.2.8 Photomagnetic Experiments

Photomagnetic measurements were performed using a HL-2000-FSHA halogen lamp (Ocean Optics) as a light source. The lamp output was filtered to a narrow-band spectrum (approximately 25 nm) centered around 530 nm using a set of linear variable high-pass and low-pass filters (LVF-HL, Ocean Optics). The excitation light was coupled into the optical fiber (Superguide G UV-VIS, Fiberguide Industries) of a Fiber Optic Sample Holder (FOSH, Quantum Design) mounted in a Quantum Design MPMS-XL

SQUID magnetometer. The power density at the sample surface was adjusted to appproximately 0.25 mW mm^{-2}. Samples, consisting of one Single crystal (~ 15 mg) or powders (~13 mg), were placed in the transparent sample cup of the FOSH for the photomagnetic experiments. For the LIESST experiment, the sample was slowly cooled down to 10 K in the dark. Next, the magnetic field was set to 0.1 T and the excitation light switched on, during which the evolution of the magnetic moment was monitored. After saturation of the material in the high spin state was achieved (~100 min.), the light was switched off and the temperature was cycled up to 300 K and back down to 10 K, at a rate of 0.3 K min^{-1}. The relaxation temperature of the light induced high spin state, T(LIESST), was established by the corresponding feature in the $\partial\chi_M T/\partial T$ versus T curve. For the LITH experiment, the sample was cooled to 130 K, after which the light and magnetic field (0.1 T) were switched on. Next, the magnetism of the material was monitored during thermal cycling down to 10 K and back up to 135 K, at a rate of 0.3 K min^{-1}.

2.3. Ligands Synthesis

2.3.1 Synthesis of Thiosemicarbazone based Ligands

2.3.1.1 Pyridoxal-4R-thiosemicarbazone hydrochloride (R = H, CH_3, CH_3CH_2)

General experimental procedure for the synthesis of pyridoxal-4R-thiosemicabazone hydrochloride.

All pyridoxal-4R-thiosemicarbazone hydrochloride were synthesized according to a modification of the procedure described in literature.[26,27]

49 mmol of pyridoxal hydrochloride (99%) was dissolved in 80 mL of water with constant stirring, and was added to 49 mmol of the corresponding thiosemicarbazide (97%) also dissolved in 40 mL of water. The mixture was refluxed for 120 minutes. Whereafter the resultant solution was cooled to room temperature, the solvent was removed under reduced pressure and a deep yellow solid precipitated. The material was then recrystallized in a mixture of solvent (water/ethanol) and kept at room temperature for 24 hours. Yellow needle-like crystals were isolated by filtration, washed with water and dried in vacuo for two days.

Pyridoxal thiosemicarbazone hydrochloride (H_2thpy·HCl). The synthesis of H_2thpy·HCl follows exactly the general procedure described above. Yield: 12.83 g (46.40 mmol, 94.5%). Mp: 212 °C. Anal. Calcd for $C_9H_{13}N_4O_2S$·HCl: C, 39.06; H, 4.73; N, 20.25; S, 11.58. Found: C, 39.08; H, 4.74; N, 20.07; S, 11.60. H_2thpy·HCl is soluble in

water, ethanol, but scarcely dissolves in acetone, chloroform and methanol, even at elevated temperatures. ^{1}H NMR (300 MHz, DMSO-d_6) δ(ppm): 10.46 (1H, br s, NH-3), 9.29 (1H, br s, OH py), 8.56 (1H, s, HC=N), 8.33 - 8.10 (2H, br s, NH_2), 7.96 (1H, s, py), 5.26 (1H, t, OH), 4.87 (2H, s, py CH_2O) and 1.74 (3H, s, CH_3 py).MS (ionization mode: EI+) m/z (%): 196 (7), 165 (100), 150 (41), 119 (11), 77 (22) and 60 (17). IR (cm^{-1}, KBr): 3294 (NH), 3164 (OH), 2773 (NH^+), 1641 (CN), 1572 (py), 1369 (OH), 1256 (NN), 1185 (CN) and 1017 (CS).

Pyridoxal-4-methylthiosemicarbazone hydrochloride (H_2mthpy·HCl). The synthesis of H_2mthpy·HCl follows exactly the general procedure described above. Yield: 9.0 g (30.98 mmol, 63%). Mp: 228 °C. Anal. Calcd for $C_{10}H_{14}N_4O_2S$·HCl: C, 41.31; H, 5.20; N, 19.27; S, 11.03. Found: C, 41.30; H, 5.18; N, 19.10; S, 11.11. H_2mthpy·HCl is soluble in water, ethanol, but scarcely dissolves in acetone, chloroform and methanol, even at elevated temperatures. ^{1}H NMR (300 MHz, DMSO-d_6) δ (ppm): 11.40 (s, br, 1H, OH py), 9.93 (s, br, 1H, NH-2), 8.59 (m, 2H, py CHN + NH-4), 7.93 (s, 1H, py), 5.29 (t, 1H, OH), 4.56 (d, 2H, py CH_2O), 2.99 (d, 3H, CH_3N), 2.42 (s, 3H, CH_3 py). MS (ionisation mode: EI+) m/z (%): 254 (98), 165 (100), 150 (27), 116 (7), 74 (31), 57 (39). IR (cm^{-1}, KBr): 3197.9 (br), 2963.1 (w), 2921.4 (w), 2850.8 (w), 1615.2 (m), 1558.0 (vs), 1471.6 (m), 1396.2 (m), 1305.9 (vs), 1259.7 (m), 1236.9 (m), 1197.7 (s), 1043.6 (s), 1000.2 (vs), 859.3 (v), 770.0 (s), 948.2 (w), 859.3 (m), 770.3 (m), 667.6 (s), 589.2(s).

Pyridoxal 4-ethylthiosemicarbazone hydrochloride (H_2ethpy·HCl). The synthesis of H_2ethpy·HCl follows exactly the general procedure described above. Yield: 13.41 g (44.18 mmol, 89.6%). Mp: 214 °C. Anal. Calcd for $C_{11}H_{16}N_4O_2S$·HCl: C, 43.35; H, 5.62; N, 18.38; S, 10.52. Found: C, 43.23; H, 5.73; N, 18.11; S, 10.43. H_2ethpy·HCl is soluble in water, ethanol, but scarcely dissolves in acetone, chloroform and methanol, even at elevated temperatures. ^{1}H NMR (300 MHz, DMSO-d_6) δ(ppm): 12.01 (1H, br, NH-2), 8.67 (1H, br s, OH py), 8.51 (2H, s, py CHN + NH-4), 8.18 (1H, s, py), 5.28 (1H, t, OH), 4.75 (2H, s, py CH_2O), 2.59 (2H, s, CH_2), 1.74 (3H, s, CH_3 py) and 1.14 (3H, t, CH_3 CH_3CH_2N). MS (ionization mode: EI+) m/z (%): 165 (80), 149 (42), 120 (9), 103 (14), 88 (10) and 60 (23). IR (cm^{-1}, KBr): 3262 (NH), 3148 (OH), 2923 and 2852 (CH), 2759 (NH^+), 1622 (CN), 1581 (py), 1328 (OH), 1258 (NN), 1196 CN) and 1017 (CS).

Pyridoxal-4R-thiosemicarbazone monohydrate (R = H, CH_3).

In a typical procedure, a mixture of pyridoxal hydrochloride (98.0 mmol) and triethylamine (8.9 mmol) in dichloromethane (200 mL) was stirred at RT for 24 h under

an inert atmosphere of dry nitrogen. The triethylamine hydrochloride salt formed during this reaction is soluble while the solid obtained was filtered off, washed with dichloromethane (3 × 15 mL) and recrystallized from a water-acetone solution and dried under vaccuum for 24 hours to give pyridoxal of its free form. Thereafter, a mixture containing pyridoxal free hydrochloride (0.061 mol) and 4-methyl-3-thiosemicarbazide(61.0 mmol) in ethanol solution on constant stirring was refluxed at 60 ^{o}C for about 4 hours during which time the reaction mixture turned into a yellow solid. The solid was washed with diethyl ether (3 × 30 mL) and dried under vacuum for 24 hours to give pyridoxal-4-methylthiosemicarbazone monohydrate (H_2mthpy·H_2O)

Pyridoxal thiosemicarbazone monohydrate (H_2thpy·H_2O). The synthesis of H_2thpy·H_2O follows exactly the general procedure described above Yield: 10.87 g (42.13 mmol, 92.8%). Mp: 226 °C. Anal. Calcd for $C_9H_{12}N_4O_2S·H_2O$: C, 42.01; H, 5.09; N, 21.78; S, 12.46. Found: C, 43.49; H, 5.06; N, 21.43; S, 12.97. H_2thpy·H_2O is soluble in DMSO, DMF but not in water, ethanol and methanol, even at elevated temperatures. ^{1}H NMR (300 MHz, DMSO-d_6) δ(ppm): 11.60 (1H, br s, NH-3), 9.65 (1H, br s, OH py), 8.57 (2H, s, py CHN + NH-4), 7.99 (1H, s, py), 5.25 (1H, s, OH), 4.57 (2H, s, py CH_2O) and 1.76 (3H, s, CH_3 py). MS (ionization mode: EI+) m/z (%): 206 (7), 165 (100), 150 (41), 120 (12), 77 (23) and 60 (16). IR (cm^{-1}, KBr): 1616 (CN), 1520 (py), 1381 (OH), 1100 (NN) and 1035 (CS).

Pyridoxal-4-methylthiosemicarbazone monohydrate (H_2mthpy·H_2O). The synthesis of H_2mthpy·H_2O follows exactly the general procedure described above Yield: 10.15 g (37.32 mmol, 68.2%). Mp: 228 °C. Anal. Calcd for $C_{10}H_{14}N_4O_2S·H_2O$: C, 44.11; H, 5.92; N, 20.57; S, 11.77. Found: C, 44.60; H, 5.85; N, 20.58; S, 12.07. H_2mthpy·H_2O is soluble in DMSO, DMF and insoluble in water, ethanol and acetone, even at elevated temperatures. ^{1}H NMR (300 MHz, DMSO-d_6) δ (ppm): 11.60 (1H, br s, NH-2), 9.93 (1H, br s, OH py), 8.56 (2H, s, py CHN + NH-4), 7.98 (1H, s, py), 5.26 (1H, t, OH), 4.56 (2H, d, py CH_2O), 2.99 (3H, s, CH_3N) and 1.75 (3H, s, CH_3 py). MS (ionization mode: EI+) m/z (%): 180 (17), 165 (100), 150 (26), 105 (21), 74 (39) and 57 (37). IR (cm^{-1}, KBr): 3375 (NH), 2953 and 2919 (CH), 2849 (NH^+), 1629 (CN), 1550 (py), 1385 (OH), 1260 (NN) and 1044 (CS).

2.3.1.2 5X-salicylaldehyde thiosemicarbazone (X = H, Cl, Br).

All 5X-salicylaldehyde thiosemicarbazone were synthesized according to the procedure described in literature.[28,29]

49 mmol of the corresponding salicylaldehyde (99%) was dissolved in 80 mL of ethanol with constant stirring, and was added to 49 mmol of thiosemicarbazide (97%) dissolved in 40 mL of ethanol. The mixture was refluxed for 120 minutes. After the mixture was cooled to room temperature, a white solid was isolated by filtration, washed with ether and dried in vacuo for two days. Yield: 70 – 90 %.

2.3.2 Synthesis of Pyrazole based Ligands

General synthetic procedure for the preparation of the pyrazole-based ligands.

The synthesis of 2,6-bis(pyrazol-1-yl)pyridine (bbp1) and 2,6-bis(pyrazol-1-yl)pyrazine (bbp2) ligands have been performed following the procedure developed by Braum et al..[30] A 500 mL flask was purged with nitrogen and filled with sodium hydride (60% pure in mineral oil), (6 g, 150 mmol). The NaH was washed trice with pentane, by using a syringe. After removal of pentane by evaporation, dry THF (200 mL) was added and the stirred suspension was cooled in ice. Pyrazole (14.2 g, 208 mmol) was added portions-wise (there was evolution of H_2 and heat). To the clear solution, 2,6-dibromopyridine/2,6-dibromopyrazine (12.36 g, 52 mmol) was added. After reflux for 5 days, the mixture was poured into 2 L of ice-water. The solid was collected, washed with water and dried in vacuum to give 11.2 g (100%) of product. Mp: 138 ^{o}C.

2.4 Synthesis of the Coordination Compounds

Numbers in bold correspond to the numbers that the compounds will have in the thesis.

2.4.1 Thiosemicarbazone-based Complexes

2.4.1.1 Pyridoxal-4R-thiosemicarbazone-based complexes (R = H, CH_3, CH_3CH_2).

[Fe(Hthpy)(thpy)]·CH_3OH·$3H_2O$ (1). About 20 mL of concentrated ammonia was added to a mixture of pyridoxalthiosemicarbazone·HCl (0.55 g, 2 mmol) in 20 mL of water and $Fe(CH_3C_6H_4SO_3)_3 \cdot 6H_2O$ (0.68 g, 1 mmol) in 20 mL of methanol on constant stirring. The resulting dark green solution was stirred and heated mildly up to 40 ^{o}C for about 15 minutes, before approximately 2 g of NH_4Cl salt was added. The final solution was stirred for 10 minutes and allowed to stand at room temperature for five days. The dark green microcrystals were isolated by filtration, washed with methanol and

diethylether, and dried in a well ventilated space for 24 hours. Yield: 0.43 g (0.69 mmol, 68.8%). Mp: >280 °C. Anal. Calcd for $C_{19}H_{31}N_8O_8S_2Fe$: C, 36.84; H, 5.04; N, 18.09; S, 10.35. Found: C, 35.58; H, 4.80; N, 18.02; S, 10.23. The complex is soluble in DMSO and DMF. IR (cm^{-1}, KBr): 3409 and 3311 (NH), 1624 (CN), 1494 and 1465 (py), 1386 and 1370 (OH), 1261 and 1210 (NN), 1007 (CS).

[Fe(Hmthpy)(mthpy)]·2H_2O (2). A solution of $Fe(NO_3)_3·9H_2O$ (0.40 g, 1 mmol) in 15 mL of water, was added dropwise to a mixture of concentrated ammonia (20 mL) and pyridoxal-4-methylthiosemicarbazone·HCl (0.58 g, 2 mmol) in 20 mL of water on constant stirring. The resulting dark green solution was stirred and heated mildly up to 40 ^oC for about 10 minutes whereafter approximately 2 g of NH_4Cl salt was added. The final solution was stirred for 10 minutes and allowed to stand at room temperature for three days. The dark green microcrystals were isolated by filtration, washed with water and diethylether, and dried in a well ventilated space for 24 hours. Yield: 0.32 g (0.54 mmol, 54.1%). Mp: >280 °C. Anal. Calcd for $C_{20}H_{29}N_8O_6S_2Fe$: C, 40.21; H, 4.89; N, 18.75; S, 10.73. Found: C, 39.30; H, 4.99; N, 18.42; S, 10.57. The complex is soluble in DMSO and DMF. IR (cm^{-1}, KBr): 1509 (py), 1393 and 1364 (OH), 1252 and 1207 (NN), 1018 (CS).

[Fe(Hthpy)$_2$]$(SO_4)_{1/2}$· 3.5H_2O (3). To a methanolic slurry of pyridoxalthiosemicarbazone hydrochloride, H_2thpy·HCl (0.55 g, 2 mmol) on constant stirring, was added a solution of $Fe_2(SO_4)_3·5H_2O$ (0.49 g, 1 mmol) in 20 mL of methanol. The resulting brown solution was stirred and heated mildly up to 40 ^oC for about half an hour before being allowed to stand at room temperature for 2 days. The dark brown microcrystals were isolated by filtration, washed with methanol and diethylether, and dried in a well ventilated space for 24 hours. Yield: 0.29 g (0.45 mmol, 44.7%). Mp: >280 °C. Anal. Calcd for $C_{18}H_{29}FeN_8O_{9.5}S_{2.5}$: C, 33.49; H, 4.53; N, 17.36; S, 12.42. Found: C, 33.46; H, 4.63; N, 16.99; S, 12.51. The complex is readily soluble in methanol and sparingly soluble in water. IR (cm^{-1}, KBr): 1612 (CN), 1577 (py), 1381 (OH), 1247 (NN) and 1206, 1130, 998 and 605 (SO_4).

[Fe(Hthpy)$_2$]NO_3·3H_2O (4). To a water slurry of recrystallized pyridoxal thiosemicarbazone monohydrate, H_2thpy·H_2O (2.68 g, 10.37 mmol) on constant stirring, was added a solution of $Fe(NO_3)_3·9H_2O$ (2.09 g, 5.19 mmol) in 20 mL of water resulting in a dark red solution. The final mixture was stirred and heated mildly up to 40 ^oC for about 15 minutes, before allowed to stand at room temperature for five days. The dark red microcrystals were isolated by filtration, washed with methanol and

diethylether, and dried in a well ventilated space for 24 hours. Yield: 2.10 g (3.23 mmol, 62.3%). Mp: >280 °C. Anal. Calcd for $C_{18}H_{28}FeN_9O_{10}S_2$: C, 33.24; H, 4.34; N, 19.38; S, 9.86. Found: C, 32.91; H, 4.27; N, 19.37; S, 10.06. The complex is readily soluble in methanol and sparingly soluble in water. IR (cm^{-1}, KBr): 3457 (NH), 2895 (CH), 1620 (CN), 1464 (py), 1383 (NO_3), 1318 (OH), 1250 (NN), 1029 (CS) and 618 (NO_3).

$[Fe(H_2mthpy)_2](CH_3C_6H_4SO_3)_3 \cdot CH_3CH_2OH$ (5). To an ethanolic slurry of recrystallized pyridoxal-4-methylthiosemicarbazone monohydrate, $H_2mthpy \cdot H_2O$ (1.41 g, 5.19 mmol) on constant stirring, was added a solution of $Fe(CH_3C_6H_4SO_3)_3 \cdot 6H_2O$ (1.76 g, 2.59 mmol) in 30 mL of ethanol resulting in a dark brown solution. The final mixture was stirred and heated mildly up to 40 ^oC for about 20 minutes and allowed to stand at room temperature for at least one week. The dark brown microcrystals were isolated by filtration, washed with ethanol and diethylether, and dried in a well ventilated space for 24 hours. Yield: 0.95 g (0.85 mmol, 32.8%). Mp: >280 °C. Anal. Calcd for $C_{43}H_{55}FeN_8O_{14}S_5$: C, 45.95; H, 4.93; N, 9.97; S, 14.26. Found: C, 45.13; H, 4.84; N, 10.28; S, 14.12. The complex is readily soluble in water and sparingly soluble in methanol. IR (cm^{-1}, KBr): 1617 (CN), 1496 (py), 1382 (OH), 1210 (NN),1168 and 1122 (SO_3), 1009 (CS) and 568 (SO_3).

$[Fe(Hethpy)(ethpy)] \cdot 8H_2O$ (6). A solution of $Fe(NO_3)_3 \cdot 9H_2O$ (1.05 g, 2.59 mmol) in 20 mL of water, was added dropwise to a mixture of concentrated ammonia (40 mL) and pyridoxal-4-ethylthiosemicarbazone hydrochloride, $H_2ethpy \cdot HCl$ (1.58 g, 5.19 mmol) in 40 mL of water on constant stirring. The resulting dark green solution was stirred and heated mildly up to 40 ^oC for about 10 minutes whereafter approximately 3 g of NH_4Cl salt was added. The final solution was stirred for 10 minutes and allowed to stand at room temperature for a period of one week. The dark green microcrystals were isolated by filtration, washed with water and dried in a well ventilated space for 24 hours. Yield: 1.02 g (1.39 mmol, 53.6%). Mp: >280 °C. Anal. Calcd for $C_{22}H_{45}FeN_8O_{12}S_2$: C, 36.02; H, 6.18; N, 15.27; S, 8.74%). Found: C, 35.94; H, 5.79; N, 15.00; S, 8.90. The complex is soluble in DMSO, DMF and pyridine. IR (cm^{-1}, KBr): 1636 (CN), 1543 (py), 1364 (OH), 1261 (NN), 1252.0 (w), 1206.9 (m), 1169.7 (m) and 1028 (CS).

2.4.1.2 5X-salicylaldehyde thiosemicarbazone-based complexes (X = H, Cl, Br).

All 5X-salicylaldehyde thiosemicarbazone-based complexes were synthesized according to the procedure described in literature.[31-33]

[Fe(Hthsa)(thsa)]·H_2O (7). Yield: 1.54 g (3.35 mmol, 67.01%). Mp: >280 °C. Anal. Calcd for $C_{16}H_{17}N_6O_3S_2Fe$: C, 41.66; H, 3.71; N, 18.22; S, 13.90; Fe, 12.11. Found: C, 41.63; H, 3.72; N, 18.09; S, 13.94; Fe, 11.94. The complex is soluble in DMSO, DMF and less soluble in methanol. IR (cm^{-1}, KBr): 3403 and 3239 (NH), 3134 (NH), 3045 (CH), 1597 and 1541 (ring), 1336 and 1303 (CO), 1207 and 1156 (NN), 1036 (CS) and 757 (CH).

[Fe(Hth5Clsa)(th5Clsa)]·H_2O (8). Yield: 0.44 g (0.83 mmol, 46.49%). Mp: >280 °C. Anal. Calcd for $C_{16}H_{15}Cl_2N_6O_3S_2Fe$: C, 36.25; H, 2.85; Cl, 13.37; N, 15.85; S, 12.09; Fe, 10.53. Found: C, 36.23; H, 2.87; Cl, 13.47; N, 15.76; S, 11.79; Fe, 10.32. The complex is soluble in DMSO, DMF and less soluble in methanol. IR (cm^{-1}, KBr): 3460, 3412 and 3264 (NH), 3161(CCl), 1611 (CN), 1536 and 1466 (ring), 1319 and 819 (CO), 1297 and 1191 (NN).

[Fe(Hth5Brsa)(th5Brsa)]·$(H_2O)_{1/2}$ (9). Yield: 0.71 g (1.16 mmol, 64.70%). Mp: >280 °C. Anal. Calcd for $C_{16}H_{14}Br_2N_6O_{2.5}S_2Fe$: C, 31.50; H, 2.31; Br, 26.19; N, 13.77; S, 10.51; Fe, 9.15. Found: C, 31.41; H, 2.48; Br, 26.17; N, 13.73; S, 10.25; Fe, 8.32. The complex is soluble in DMSO, DMF and less soluble in methanol. IR (cm^{-1}, KBr): 3448 3403 and 3239 (NH), 3134 (CBr), 2925 and 2851 (CH), 1617 and 1610 (CN), 1576 and 1560 (ring), 1393 and 1364 (OH), 1296 and 1190 (NN) and 820 (CH).

Cs[Fe$(thsa)_2$]·$4H_2O$ (11). A solution of $FeCl_3·6H_2O$ (1.02 g, 3.76 mmol) in 30 mL of water, was added dropwise to a mixture of $Cs(OH)·H_2O$ (2.56 g, 15.06 mmol) and salicylaldehyde thiosemicarbazone (1.47 g, 7.56 mmol) in 60 mL of water on constant stirring. The resulting dark green solution was stirred and heated up to 80 ^oC for about 30 minutes. The final solution was filtered and allowed to stand at room temperature for five days. The dark green microcrystals were isolated by filtration, washed with water and diethylether, and dried in a well ventilated space for 24 hours. Yield: 0.61 g (0.94 mmol, 24.83%). Mp: >280 °C. Anal. Calcd for $C_{16}H_{22}N_6O_6S_2CsFe$: C, 29.69; H, 3.43; N, 12.98; S, 9.91. Found: C, 29.61; H, 3.32; N, 12.74; S, 10.01. The complex is soluble in water, methanol and actonitrile. IR (cm^{-1}, KBr): 3576 (H_2O), 3328 and 3209 (NH), 1641 (CN), 1593 and 1580 (ring), 1322 and 954 (CO), 1210 and 1154 (NN), 1036 (CS) and 763 (CH).

2.4.2 Pyrazole-based Complexes

CAUTION: while we have experienced no difficulty in handling the ClO_4^- salts in this study, metal-organic perchlorates are potentially explosive and should be handled with due care in small quantities!!

$[Fe(bpp2)_2](ClO_4)_2 \cdot MeCN$ (10). A solution of $Fe(ClO_4)_2 \cdot 6H_2O$ (0.512 g, 1.4×10^{-3} mol) and bpp2 (0.60 g, 2.8×10^{-3} mol) in acetone (50 mL) was stirred at room temperature for 15 min. The resultant brown solution was filtered and concentrated to *ca.* 1/3 of its original volume, whereupon a yellow precipitate formed. Following overnight storage at -30 ^oC, the product was filtered and washed sequentially with cold MeCN and Et_2O. Recrystallization from MeCN/Et_2O yielded red brown parallelepiped crystals. Yield: 0.59 g, (0.819 mmol, 58.4%). Mp: >280 °C. Anal. Calcd for $C_{22}H_{19}Cl_2N_{13}O_8Fe$: C, 36.69; H, 2.66; N, 25.28. Found: C, 36.25; H, 2.56; N, 24.55. The complex is soluble in acetone, acetonitrile and sparingly soluble in methanol. IR (cm^{-1}, KBr): 3121 (NH), 3075 (CH), 2937 and 2816 (CH), 2259 (CN), 1560, 1528 and 1461 (py), 1122, 1097, 1075 and 1052 (ClO_4).

$[Fe(bpp1)_2](ClO_4)_2$ (12). To a solution of $Fe(ClO_4)_2 \cdot 6H_2O$ (0.52 g, 1.44 mmol) in acetonitrile (50 mL) was added 2,6-bis(pyrazol-1-yl)-pyridine (0.60 g, 2.88 mmol), and the mixture was stirred. Slow diffusion of diethyl ether into this solution yielded yellow block crystals. Yield: 0.80 g (1.18 mmol, 82.42%). Mp: >280 °C. Anal. Calcd for $C_{22}H_{18}Cl_2N_{10}O_8Fe$: C, 39.02; H, 2.68; N, 20.68. Found: C, 38.80; H, 2.64; N, 20.19. The complex is soluble in acetone, acetonitrile and sparingly soluble in methanol. IR (cm^{-1}, KBr): 3130 (NH), 3088 (CH), 2914 and 2812 (CH), 1624, 1592, 1528, 1499, 1478, 1404, 1344 and 1312 (py), 1106, 1053 and 1018 (ClO_4).

2.4.3 Hybrid Molecular Switch Complex

$[Fe^{III}(thsa)_2]_2[Fe^{II}(bpp1)_2] \cdot CH_3OH \cdot 4H_2O$ (13). A solution containing microcrystals of $[Fe(bpp1)_2](ClO_4)_2$ (0.68 g, 0.001 mmol) in 40 mL of methanol was added to a suspension of $Cs[Fe(thsa)_2] \cdot 4H_2O$ (1.30 g, 0.002 mmol) in 60 mL of water. The resulting dark solution was heated up to 100 ^oC and stirred for about 1 h, during which time a black precipitate is formed. The final solution was filtered and the resulting precipitate was collected, washed with water and dried in a well ventilated space for 24 hours. Yield: 0.90 g (0.61 mmol, 61.10%). Mp: >280 °C. Anal. Calcd for $C_{55}H_{58}N_{22}O_9S_4Fe_3$: C, 45.03; H, 3.98; N, 21.01; S, 8.74; Fe, 11.42. Found: C, 44.57; H, 3.63; N, 20.93; S, 8.77; Fe, 11.32. The complex is soluble in DMF and DMSO. IR (cm^{-1}, KBr): 3418 and 3254 (NH),

1609 (CN), 1541 (ring), 1475 and 1437 (py), 1335 and 936 (CO), 1207 and 1155 (NN), 1036 (CS) and 758 (CH).

2.5 References

(1) *SMART, SAINTPLUS* and *XPREP, Area Detector Control and integration Software, Smart Apex Software Reference Manuals;* Bruker Analytical X-ray instruments Inc.: Madison, WI, 2000.

(2) Sheldrick, G. M. *SADBAS version 2.03, Multi-scan absorption correction program*; University of Göttingen: Göttingen, Germany, 2001.

(3) SIR2004: Burla, M. C.; Caliandro, R.; Camalli, M.; Carrozzini, B.; Cascarano, G. L.; De Caro, L.; Giacovazzo, C.; Polidori, G.; Spagna, R. *J. Appl. Cryst.* **2005**, *38*, 381-388.

(4) Beurskens, P. T.; Beurskens, G.; de Gelder, R.; García-Granda, S.; Gould, R. O.; Israël, R.; Smits, J. M. M. The *DIRDIF*-99 *program system*; Crystallography Laboratory, University of Nijmegen: Nijmegen, The Netherlands, 1999.

(5) Beurskens, P. T.; Beurskens, G.; Gelder, R.; Smits, J. M. M. de; García-Granda, S.; Gould, R. O. The *DIRDIF*-07 *program system*; Crystallography Laboratory, University of Nijmegen: Nijmegen, The Netherlands, 2007.

(6) Wilson, A. J. C., Ed.; *International Tables for Crystallography*; Kluwer Academic Publishers: Dordrecht, The Netherlands, 1992; Vol. C.

(7) Hahn, T., Ed.; *International Tables for Crystallography*; Space-group symmetry, Kluwer Academic Publishers: Dordrecht, The Netherlands, 1983; Vol. A.

(8) Bondi, A. *J. Phys. Chem.* **1964**, *68*, 441.

(9) Sheldrick, G. M. *SHELXL-97, Program for the refinement of crystal structures*; University of Göttingen: Göttingen, Germany, 1997.

(10) Meetsma, A. *PLUTO, Molecular graphics program, Version of March 2006*; University of Groningen: Groningen, The Netherlands, 2006.

(11) Meetsma, A. *PLUTO, Molecular graphics program, Version of March 2008;* University of Groningen: Groningen, The Netherlands, 2008.

(12) a) Spek, A. L. *PLATON, Program for the automated analysis of molecular geometry (A Multipurpose Crystallographic Tool), Version of February 2006*; University of Utrecht: Utrecht, The Netherlands, 2006. b) Spek, A. L. *J. Appl. Crystallogr.* **2003**, *36*, 7.

(13) a) Spek, A. L. *PLATON, Program for the automated analysis of molecular geometry* (*A Multipurpose Crystallographic Tool*), Version of March 2008; University of Utrecht: Utrecht, The Netherlands, 2008. b) Spek, A. L. *J. Appl. Cryst.* **2003**, *36*, 7.

(14) Larson, A. C.; Von Dreele, R. B. *General Structure Analysis System (GSAS)*, Los Alamos National Laboratory Report LAUR 86-748 (2000).

(15) Toby, B. H. *EXPGUI, A graphical user interface for GSAS, J. Appl. Cryst.* **2001**, *34*, 210-213.

(16) Shirley, D. A. *Phys. Rev. B.* **1972**, *5*, 4709.

(17) Lebedev, Y. S. Very-high-field EPR and its applications, *Appl. Magn. Reson.* **1994**, *7*, 339–362.

(18) Earle, K. A.; Tipikin, D. S.; Freed, J. H. Far-infrared electron-paramagnetic-resonance spectrometer utilizing a quasioptical reflection bridge, *Rev. Sci. Instrum.* **1996**, *67*, 2502–2513.

(19) Fuchs, M. R.; Prisner, T. F.; Möbius, K. A high-field/high-frequency heterodyne induction-mode electron paramagnetic resonance spectrometer operating at 360 GHz, *Rev. Sci. Instrum.* **1999**, *70*, 3681–3683.

(20) Mabbs, F.E.; Machin, D.J. In *Magnetism and Transition Metal Complexes*; Chapman and Hall: London, 1973.

(21) Boča, R. In *Theoretical Foundations of Molecular Magnetism; Current Methods in Inorg. Chemistry*, Elsevier: Amsterdam, 1999; Vol 1.

(22) Trautwein, A. X.; Bill, E.; Bominaar, E. L.; Winkler, H. *A thorough overview on spin-Hamiltonian parameters and Mössbauer spectroscopy with a lot of examples of spin-coupled systems*; Struct. Bonding **1991**, *78*, 1.

(23) Parish, R.V. In *NMR, NQR, EPR, and Mössbauer Spectroscopy in Inorganic Chemistry* (Ellis Horwood series in inorganic chemistry); Ellis Horwood Ltd, 1991.

(24) Long, G. J. In *Mössbauer Spectroscopy Applied to Inorganic Chemistry (Modern Inorganic Chemistry)*; Kluwer Academic Publishers.

(25) Höhne, G. W. H.; Hemminger, W. F.; Flammersheim, H. J. *Differential Scanning Calorimetry*; 2nd ed.; Springer: Berlin, 2003; p 298.

(26) Belicchi Ferrari, M.; Fava Gasparri, G.; Leporati, E.; Pelizzi, C.; Tarasconi, P.; Tosi, G. *J. Chem. Soc. Dalton Trans.* **1986**, 2455.

(27) Belicchi Ferrari, M.; Bisceglie, F.; Leporati, E.; Pelosi, G.; Tarasconi, P. *Bull. Chem. Soc. Jpn.* **2002**, *75*, 781.

(28) Freund, M.; Schander, A. *Ber. Drsch. Chem. Ges.* **1902**, *35*, 2602.

(29) (a) Al-Karawi, J. A. M.; Clegg, W.; Harrington, R. W.; Henderson, R. A. *Dalton Trans.* **2009**, 564-570. (b) Chikate, R. C.; Padhye, S. B. *Polyhedron* **2005**, *24*, 1689-1700.

(30) (a) Downard, A. J.; Honey, G. E.; Steel, P. J. *Inorg. Chem.* **1991**, *30*, 3733. (b) Jameson, D. L.; Goldsby, K. A. *J. Org. Chem.* **1990**, *55*, 4992.

(31) Ryabova, N. A.; Ponomarev, V. I.; Atovmyan, L. O.; Zelentsov, V. V.; Shipilov, V. I. *Koordinats. Khimiya* **1978**, *4*, 119.

(32) Ryabova, N. A.; Ponomarev, V. I.; Zelentsov, V. V.; Atovmyan, L. O. *Kristallografiya* **1981**, *26*, 101.

(33) Ryabova, N. A.; Ponomarev, V. I.; Zelentsov, V. V.; Shipilov, V. I.; Atovmyan, L. O. *Zh. Strukt. Khim.* **1981**, *22*, 111.

Chapter III

Neutral Fe(III) Complexes of Pyridoxal-4R-Thiosemicarbazone with Desolvation-Induced Spin-State Transformation above Room Temperature

Synopsis

The preparation and characterization of two new neutral ferric complexes with desolvation induced discontinuous spin-state transformations above room temperature are reported. The compounds, $[Fe(Hthpy)(thpy)]\cdot CH_3OH\cdot 3H_2O$ (**1**) and $[Fe(Hmthpy)(mthpy)]\cdot 2H_2O$ (**2**), are low spin at room temperature and below, whereas their non-solvated forms are high spin exhibiting zero field splitting. In these complexes, Hthpy, Hmthpy, and thpy, mthpy are the deprotonated forms of pyridoxal - thiosemicarbazone and –methylthiosemicarbazone respectively; each is an ONS tridentate ligand. The discontinuous spin-state transformation is accompanied by liberation of solvate molecules. This is evidenced also from DSC analysis.[1]

[1] A part of this chapter has been published: Yemeli Tido, E. W.; Alberda van Ekenstein, G. O. R.; Meetsma, A.; van Koningsbruggen, P. J. *Inorg. Chem.* **2008**, *47*, 143.

3.1 Introduction

Octahedral transition metal complexes with the configuration $3d^4$, $3d^5$, $3d^6$ and $3d^7$ only for specific ligands can exhibit spin-crossover behaviour when the energy difference between the low-spin and high-spin states is in the range of kT.[1-4] Since this requirement is very restrictive, only a few classes of transition metal complexes featuring low-spin ↔ high-spin equilibria are well documented. For instance, the monomeric iron(III) complexes with tridentate O,N,S-thiosemicarbazone ligands were the first representatives of a large class of chelates which can exhibit the S = 5/2 ↔ S = 1/2 spin transition at attainable temperatures.[5] Following the pioneering synthesis and characterization of the neutral complex of this family of Schiff base type ligands,[6,7] Timken *et al.*[8] determined the crystal structure of [Cr(Hthpu)(thpu)]·H_2O, (where Hthpu and thpu are the singly and doubly deprotonated forms of pyruvic acid thiosemicarbazone) and showed that the room temperature X-ray powder diffraction pattern is isostructural to that of [Fe(Hthpu)(thpu)]·H_2O. The iron type of its nonhydrated form, showed an abrupt transition with associated thermal hysteresis ($T_{1/2}\downarrow$ = 225 K and $T_{1/2}\uparrow$ = 235 K). Further study [9] showed photoswitchable behaviour at low temperature (T = 5 K) albeit with low photoefficiency (about 2 %). It is worth noting, however, that its powder diffraction diagram was not isostructural to either of the hydrated materials, due to the significant role that water molecules play in forming the extensive hydrogen bonding network found in the chromium structure. Afterwards, Belicchi *et al.*[10] reported the crystal structure of [Co^{III}(HL)(L)]·4.5H_2O, where HL and L are the mono- and di-anionic form of pyridoxal thiosemicarbazone. Despite the good structural determination of the molecular compound, its synthesis involves some intriguing features. First, because the starting material was a Co^{II} salt and secondly, the pH range referred to, did not correspond with literature, in view of the deprotonation sequence, of pyridoxal-N-substituted thiosemicarbazone.[11-13]

In addition, literature presents metal complexes of various terdentate X-semicarbazones (X = S, Se),[14-20] with the ligand attached to the central metal ion in two different deprotonated forms, but the structural features of the complexes remain unclear as these have not been reported. In any case, the reason that has been put forward to explain this unusual nature of the inequivalency of the ligands, is the different tautomeric forms one can find the chelate in in solution, but the pH at which those compounds are formed is often overlooked. With pyridoxal-N-substituted thiosemicarbazone the

situation is somewhat different because the inequivalent ligands are all of the thiol form. In this work, we describe the synthesis and structural characterization of two new neutral iron(III) complexes of pyridoxal-N-substituted thiosemicarbazonato, bringing about the pH range of formation of these complexes. Moreover, the low and high temperature magnetic behaviour is revealed even for the nonhydrated ones. To monitor the spin state change, ^{57}Fe Mössbauer spectroscopy has been used. The data on the heat capacities of compounds are given.

3.2 Results and Discussion

3.2.1 Influence of pH on the Synthesis[2]

Many chemical transformations are sensitive to the presence of protons. Therefore, knowledge of the pH value, especially of the complex solution is important in order to decide about its possible application. Because pH is dependent on activity, a property which cannot be measured easily or predicted theoretically, it is difficult to determine an accurate value for the pH of a solution. However, we carried out a pH study by recording daily the pH of the complex solution until microcrystals were obtained. For this purpose H_2thpy.HCl was dissolved in an ammonia/water (1/1) mixture, and a methanolic solution of $Fe(CH_3C_6H_4SO_3)_3 \cdot 6H_2O$ was subsequently added to this. On the other hand, H_2mthpy·HCl was dissolved in an ammonia/water (1/1) mixture to which an acqueous solution of $Fe(NO_3)_3 \cdot 9H_2O$ was added. Testing revealed that the optimal base to be used was concentrated ammonia, even though experiments revealed that triethylamine could also be used, but in that case it takes several weeks to obtain crystals. It was found that stronger bases (NaOH, KOH) were not suitable for this purpose since no crystals were grown from such solutions. The optimum pH range was defined as follows [9.0 – 11.5]. In most cases, crystals suitable for single crystal X-ray purpose came from solutions with a pH between 10.40 and 10.70, otherwise they formed microcrystalline powders. The deprotonation sequence and pK_a constants of the ligands are known from previous studies.[11-13] An addition of iron(III) salts influence predominantly the pH of the basic solution, but not to such an extent that it switches to a neutral or an acidic pH range. In the present study, the ligand binds to the metal ion in two inequivalent thiol forms, the mono-deprotonated which is known to have a pK_a equal to 7.9 and the di-deprotonated which is obtained from $pK_a \geq 11.2$. The complex solution

[2] See chapter 2 for details on the experimental procedures and recipes for compounds presented in this chapter

can therefore be regarded as a non-classical buffer solution due to the fact that it was not possible to go beyond the previously defined pH interval by subsequently adding the base or increasing its concentration. As it is known already from pyruvic acid- and salicylaldehyde-X-semicarbazone (X = S, Se),[6,7,19,21,22] this neutral-type of compound is obtained by simply reacting metal salts and the ligands all dissolved in methanol, ethanol or a mixture of each with water. Adding a base (soft or strong) leads in general to the anionic form of the complex,[20,23,24] *i.e.* the doubly deprotonated ligand is attached to metal ion yielding $[M^{III}(L)_2]^-$ entities. Contrary to this expectation, the complex with the twice deprotonated ligand was not possible to obtain with pyridoxal-N-substituted thiosemicarbazone hydrochloride, because of the strong stability of the intermediate compound. Accordingly, the cationic compound ($[M^{III}(HL)_2]$) could not be prepared; an attempt generally leads to the decomposition of the material when using various strategies. In all, when the intermediate compound ($[M^{III}(HL)(L)]$) is formed in a neutral or a weak acidic media, subsequent deprotonation is possible whereas, if it is a basic medium, further deprotonation will lead to unsuccessful results.

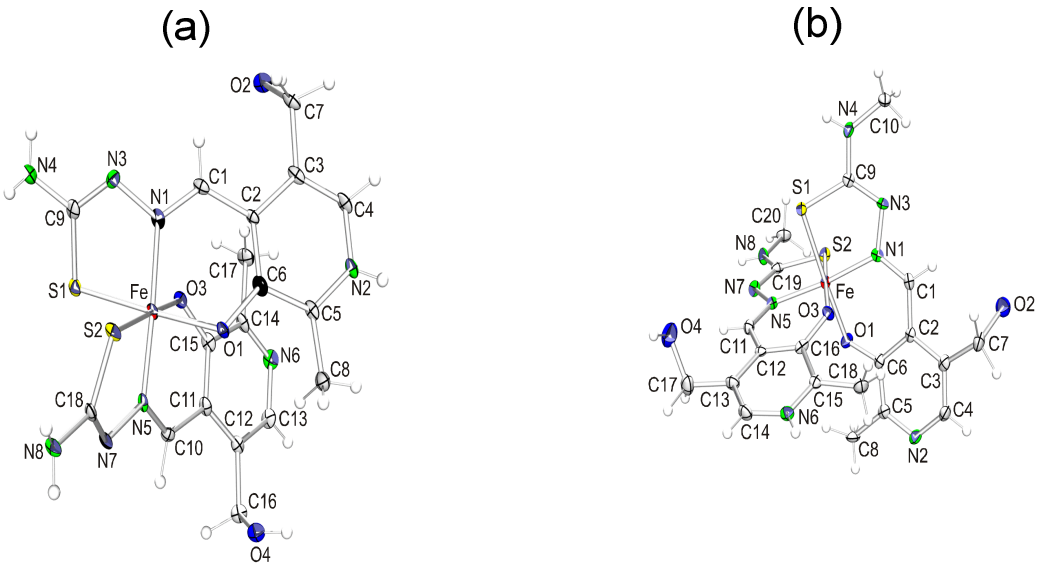

Figure 3.1. A perspective view (ORTEP drawing) of: (a) $[Fe(Hthpy)(thpy)]\cdot CH_3OH\cdot 3H_2O$ and (b) $[Fe(Hmthpy)(mthpy)]\cdot 2H_2O$ molecule with atom labeling. Non-hydrogen atoms are represented by thermal ellipsoids with 50% probability level.

3.2.2 Molecular Structures Description

A perspective view of the molecular structure of the compounds is illustrated by the ORTEP[25] drawings in Figure 3.1. The packing of the molecules is presented in the respective unit cells and is displayed in Figure 3.2. Crystal data and numerical details on data collection and refinement are given in Table 3.1. Relevant information on bond lengths and angles is given in Table 3.2.

Table 3.1 Crystal Data and Refinement Details of the Structure Determination of [Fe(Hthpy)(thpy)]·CH_3OH·$3H_2O$ (**1**) and [Fe(Hmthpy)(mthpy)]·$2H_2O$ (**2**)

Compound	**1**	**2**
Formula	$C_{19}H_{31}FeN_8O_8S_2$	$C_{20}H_{29}FeN_8O_6S_2$
Formula weight ($g.mol^{-1}$)	619.48	597.48
Crystal system	triclinic	monoclinic
Space group	$P\bar{1}$	$P2_1/c$
Crystal colour	dark green	dark green
Crystal description	platelet-shaped	platelet-shaped
Crystal dimensions (mm)	0.27 x 0.23 x 0.07	0.35 x 0.11 x 0.03
a, (Å)	10.701(2)	11.599(1)
b, (Å)	10.846(2)	24.273(2)
c, (Å)	11.910(2)	9.0649(9)
α, (deg)	83.347(3)	
β, (deg)	83.896(3)	107.589(2)
γ, (deg)	68.914(3)	
Volume ($Å^3$)	1278.0(4)	2432.8(4)
Z	2	4
c / a	1.1130	0.7815
D_{calc} ($g.cm^{-3}$)	1.610	1.631
Temperature (K)	100(1)	100(1)
Radiation (Å)	0.71073	0.71073
μ (Mo Kα) (cm^{-1})	8.15	8.47
F(000)	646	1224
Number of unique data	4874	4599
Number of data with $[F_o \geq 4.0\ \sigma\ (F_o)]$	3702	3454
$R(F)$[a]	0.0560	0.0522
$wR(F^2)$[b]	0.1424	0.1194
GOF on F^2	1.041	1.050
$\Delta_\rho$max, $\Delta_\rho$min / $e.Å^{-3}$	-0.9, 1.6(1)	-0.46, 0.60(9)

[a] $R(F) = \sum(||F_o| - |F_c||) / \sum|F_o|$ for $F_o > 4.0\ \sigma\ (F_o)$ for observed reflections

[b] $wR(F^2) = [\sum[w(F_o^2 - F_c^2)^2] / \sum[w(F_o^2)^2]]^{1/2}$ for all data

Compound **1** crystallizes in the triclinic space group $P\bar{1}$ with $Z = 2$. The asymmetric unit consists of one formula unit with no atom at a special position. The triclinic system contains two iron complexes, two highly disordered methanol solvate molecules and six water solvate molecules. Compound **2** crystallizes in the monoclinic space group $P2_1/c$ with $Z = 4$. Its asymmetric unit consists of one formula unit without an atom at a special position. The unit cell contains four iron complexes and eight water molecules. The moieties of **1** and of **2** are linked by hydrogen bonds forming an infinite three- dimensional network along the base vectors respectively. In both compounds, the Fe(III) atom is coordinated by two inequivalent tridentate O,N,S-ligands, with the formation of a distorted $FeS_2N_2O_2$ octahedron. The donor atoms are located in mutually normal planes, the S and O atoms being at the *cis*- and N at the *trans*-positions. The singly deprotonated ligand is in its zwitterionic form whereas, the doubly deprotonated does not possess any hydrogen at the pyridine nitrogen. Protonation is evident from the values of the C4-N2-C5 and C14-N6-C15 of the pyridyl angles of 121.2(4)^o and of 124.4(4)^o for **1** and **2** respectively, which have significantly increased with respect to the C13-N6-C14 and C4-N2-C5 angles of 119.2(3)^o and of 118.4(3)^o for their corresponding non protonated analogues. This structural difference is easily seen from the C-N bond distances about the pyridyl nitrogen, which are equal for the protonated nitrogen and meaningfully different for their non-protonated homologous. One major motivation for this study is to characterize the structural differences between the two ligands and determine whether a change of the N-substituent on the ligand part, may have some effects on the geometry of the complex.

The chemical inequivalency of the mono- and di-anionic ligands, is characterized by the intramolecular distances tabulated in Table 3.2. As expected, the C-S bond length for the singly deprotonated form is slightly shorter than that of the doubly deprotonated ligand (S1-C9 = 1.726(4) Å, S2-C18 = 1.738(4) Å for **1** and S1-C9 = 1.755(4) Å, S2-C19 = 1.730(4) Å for **2**). In both cases, they appear to be substantially longer than those observed in the free ligand pyridoxalthiosemicarbazone (C-S = 1.70(1) Å)[26] and pyridoxal-4-methylthiosemicarbazone hydrochloride (C-S = 1.669(5) Å).[27] The longer C-S distance is therefore a consequence of the chelate of its thiol form being attached to the metal ion. This thiol form is also identified by noting that the hydrazinic nitrogens (N3, N7) are not bonded to any hydrogen atom and having a C-N distance which is within the range found for C=N double bonds. However, the bond lengths of the hydrazinic nitrogen to carbon are equal to its adjacent C-N bond lengths for the mono-

deprotonated ligand, but considerably different for the di-deprotonated counterparts. The question of whether the equivalency is a result of electron delocalization within the entire thiosemicarbazone moiety and whether this difference would be related to the basicity of the two types of nitrogen atoms cannot be answered at present.

X-ray structural data of Fe(III) bis-ligand compounds of the dianion of R-salicylaldehyde thiosemicarbazone reveal that the Fe-S, Fe-O and Fe-N distances typically are of the order of 2.44 Å, 1.96 Å and 2.12 Å for high spin Fe(III), whereas they are 2.23 Å, 1.94 Å and 1.96 Å for low spin Fe(III), severally.[28] Comparison with these iron ligand bond lengths indicates that the Fe(III) ion is in the low spin state in the present compounds at 100(1) K.

The major difference between these two compounds resides in the substituent at the terminal N position. Moreover, the C-N and N-N bond distances about the azomethine nitrogens (N1, N5) are also indicative. For complex **1**, these distances are equal for the two inequivalent complexing agents, which is not the case observed for complex **2**, though the difference is sufficiently small. This is related to the planarity of the ligands in the Fe(III) compounds. Thus, the octahedron formed in **1** is less distorted compared to that formed in complex **2**. This is in agreement with the N1 – Fe – N5 bond angles of 176.60(14) for **1** and of 173.49(13) for **2**, respectively.

The packing of the molecules in the unit cell as viewed along the three dimensional axes is shown in Figure 3.2. The molecules of both compounds are held together by N–H---O, N–H---S, O–H---S, O–H---N and O–H---O hydrogen bonds. A summary of the hydrogen-bond dimensions is given in Table 3.3. The most striking ones are those formed in complex **2** which will be described in detail.

One of the H_2O molecules, O5 forms two short O–H---O hydrogen bonds as a donor, one to O6 with an O5---O6 distance of 2.689(6) Å and another to O4 while it acts as an acceptor with the O4---O5 separation of 2.611(5) Å. The third hydrogen-bond involves N7 as an acceptor, and has a normal contact with a O5–N7 distance of 2.821(5) Å. The result is the triangular configuration adopted by this water molecule, linking to N/O atoms at all its apexes.

The second H_2O solvate molecule, O6, forms one weak and one normal O–H---N contacts to the hydrazinic-N3 and pyridine-N2 nitrogen respectively. The O6---N3 distance of 2.952(6) is a hydrogen bond. This O6–H26---N3 hydrogen bond together with the O6–H26'---N2 contact links the molecules in the *a* direction.

Table 3.2 Selected Bond Lengths (Å) and Bond Angles (deg) for [Fe(Hthpy)(thpy)]·CH_3OH·$3H_2O$ (**1**) and [Fe(Hmthpy)(mthpy)]·$2H_2O$ (**2**). Standard deviations in the last decimal place are given in parentheses.

	1	**2**		**1**	**2**
Fe – S1	2.2508(14)	2.2453(11)	S1 – Fe – S2	88.38(5)	90.97(4)
Fe – S2	2.2549(13)	2.2471(11)	S1 – Fe – O1	176.83(10)	176.74(9)
Fe – O1	1.939(3)	1.904(3)	S1 – Fe – O3	90.02(10)	94.40(8)
Fe – O3	1.930(3)	1.912(3)	S1 – Fe – N1	84.99(11)	84.95(9)
Fe – N1	1.917(4)	1.940(4)	S1 – Fe – N5	92.91(11)	88.75(9)
Fe – N5	1.916(4)	1.926(4)	S2 – Fe – O1	94.46(10)	86.36(8)
S1 – C9	1.726(4)	1.755(4)	S2 – Fe – O3	176.64(8)	174.63(8)
S2 – C18	1.738(4)		S2 – Fe – N1	92.56(10)	95.66(9)
S2 – C19		1.730(4)			
O1 – C6	1.315(4)	1.319(4)	S2 – Fe – N5	84.7(1)	86.04(9)
O3 – C15	1.321(5)		O1 – Fe – O3	87.22(13)	88.27(11)
O3 – C16		1.303(4)			
N3 – C9	1.330(5)	1.305(5)	O1 – Fe – N1	93.47(13)	93.46(11)
N4 – C9	1.339(6)	1.348(5)	O1 – Fe – N5	88.76(13)	92.93(12)
N7– C18	1.316(5)		O3 – Fe – N1	90.25(13)	84.54(11)
N8 – C18	1.361(5)				
N7 – C19		1.322(5)	O3 – Fe – N5	92.43(12)	94.35(11)
N8 – C19		1.334(5)			
N2 – C4	1.341(6)	1.346(6)	N1 – Fe – N5	176.60(14)	173.49(13)
N2 – C5	1.345(5)	1.317(5)	C13 –N6– C14	119.2(3)	
N6 – C13	1.349(6)		C4 – N2 – C5	121.2(4)	118.4(3)
N6 – C14	1.326(6)	1.347(6)	C14 –N6- C15		124.3(4)
N6 – C15		1.333(5)			
N1 – N3	1.403(5)	1.408(4)			
N1 – C1	1.299(5)	1.284(5)			
N5 – N7	1.400(5)	1.380(4)			
N5 – C10	1.296(5)				
N5 – C11		1.302(5)			

Table 3.3 Geometry of Intra- and Intermolecular Hydrogen Bonds for [Fe(Hthpy)(thpy)]·CH_3OH·$3H_2O$ (**1**) and [Fe(Hmthpy)(mthpy)]·$2H_2O$ (**2**) Standard deviations in the last decimal place are given in parentheses.

D–H---A	D–H (Å)	H---A (Å)	D---A (Å)	D–H---A (°)
		Compound **1**		
O4–H24---O5[b]	0.84(10)	2.08(10)	2.838(5)	151(9)
N2–H25---O7[a]	0.82(12)	2.02(12)	2.831(7)	168(12)
N4–H26---O2[c]	0.86(6)	2.08(6)	2.918(6)	166(6)
N8–H27---O4[d]	0.80(5)	2.29(5)	3.074(5)	167(5)
N8–H27'---O1[d]	0.88(5)	2.33(5)	3.100(5)	146(4)
O5–H51---O6	0.86(7)	1.92(7)	2.768(6)	171(6)
O5–H51'---O4[e]	0.86(9)	2.10(9)	2.817(5)	141(8)
O6–H61---O3	0.85(5)	2.08(5)	2.926(6)	172(6)
O6–H61'---O8B	0.86(5)	2.00(6)	2.856(11)	175(6)
O7–H71---O8A[f]	0.91(4)	2.23(8)	2.807(13)	121(7)
O7–H71'---O5	0.87(4)	2.10(5)	2.919(6)	158(5)
		Compound **2**		
O2–H22---S2[a']	1.29(14)	2.33(15)	3.565(3)	159(10)
O4–H24---O5[b']	1.05(7)	1.60(7)	2.611(5)	159(6)
O5–H25---O6	1.03(6)	1.66(6)	2.689(6)	177(6)
O5–H25'---N7	0.95(7)	1.88(7)	2.821(5)	168(6)
O6–H26---N3[b]	0.76(9)	2.37(10)	2.952(6)	134(9)
O6–H26'---N2[c']	0.79(7)	2.00(7)	2.766(5)	165(7)
N4–H34---O3[d']	0.80(5)	2.30(4)	3.081(4)	166(4)
N6–H36---S1[e']	0.82(4)	2.49(4)	3.312(4)	175(3)
N8–H38---O2[f']	0.79(5)	2.24(5)	2.928(5)	147(4)

Atoms marked with a letter are generated by the symmetry operations: a = 1-x,1-y,-z; b = 1+x,y,z; c = -x,2-y,-z; d = 1-x,2-y,1-z; e = 1-x,1-y,1-z; f = -x,1-y,-z; a' = -x,-y,-z; b'= x,1/2-y,1/2+z; c'= 1-x,-y,-z; d'= x,1/2-y,1/2+z; e'= x,y,-1+z; f'= 1+x,y,1+z

Although the O–H---S hydrogen bond is rare, our value of 3.565(3) Å for the O2–S2 distance is longer than the other reported cases,[29] the range for the hydrogen bonding being 3.21 – 3.37 Å . However, the H22---S2 contact of 2.33(15) Å is definitely less than the van der Waals contact of 2.6 Å. The slight shortening of the H22---S2 distance together with the satisfactory O2–H22---S2 angle of 159(10)^o leads us to suggest that this

contact is a very weak O–H---S hydrogen bond. The protonated nitrogen of the pyridine ring forms one weak N–H---S hydrogen to S1 with an N6---S1 distance of 3.312(4) Å. The result is the linking of the molecules along the *c* direction. The nitrogen at the terminal N position also forms hydrogen bonds with oxygen atoms. One CH_3NH group, N4, forms a short N–H---O contact to O3. The N4---O3 distance of 3.081(4) Å is a hydrogen bond with a satisfactory N–H---O angle of 166(4)^o. The second CH_3NH group, N8, form a normal contact of 2.928(5) Å to O2, the result is that it links the molecules along the *ac* plane.

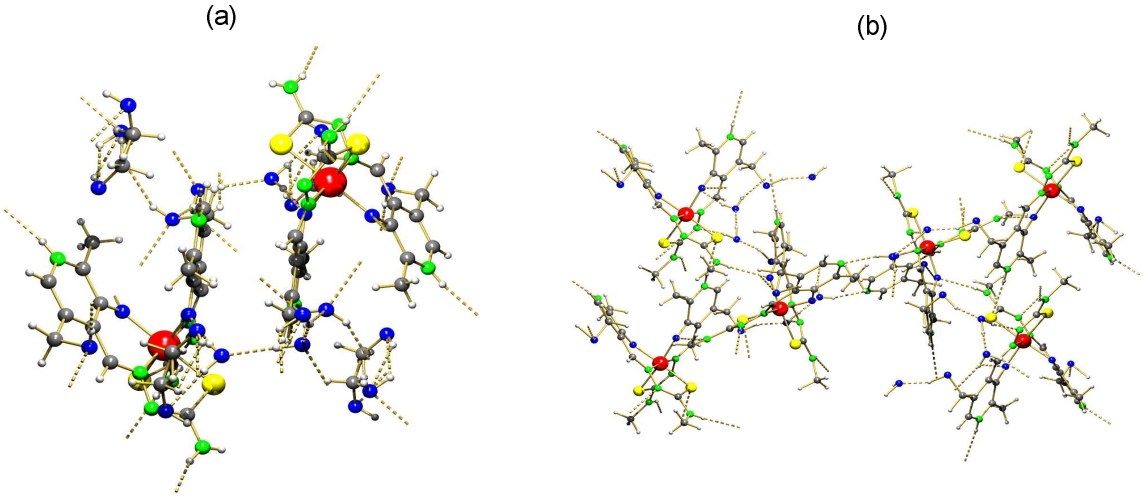

Figure 3.2. Packing arrangement as displayed in the unit cell. (a) $[Fe(Hthpy)(thpy)]\cdot CH_3OH\cdot 3H_2O$ and (b) $[Fe(Hmthpy)(mthpy)]\cdot 2H_2O$. Hydrogen bonds are shown as single dotted lines.

The result of the hydrogen bonding is a spider's web-like structure formed by O–H---O and O–H---N hydrogen bonds extending in the base vector. The spider's webs are linked together by weak O–H---S, N–H---O and N–H---S hydrogen bonds.

3.2.3 Magnetic and Thermal Studies

Low temperature measurements. The low temperature DSC curves of **1** and **2** show no thermal anomalies in heating and cooling mode respectively, pointing out the absence of a phase transition in this temperature range. This result correlates well with the dependent temperature magnetic data recorded from 5 up to 300 K. No change of spin state is observed in both compounds during heating and cooling. Thus, **1** and **2** remain low spin.

Thermogravimetric results. The observed weight loss corresponding to the first inflexion in the thermograms of both compounds were compared (Figure 3.3) with those calculated on the basis of possible decomposition of the expelled moieties. In the present study, the TGA profile consists of two well defined stages. On heating between 84 and 130 ^{o}C, the complexes liberate solvate molecules. The theoretical weight loss for this step is 13.89 % for **1** and 6.03 % for **2**. The experimental losses of weight are 13.20 % and 6.29 % for **1** and **2** respectively, which are very close to the theoretical values. Here the compounds are completely devoid of lattice solvent molecules. Then the curves showed a straight line which did not change even on heating up to 224 ^{o}C indicating that there is no further change in weight.

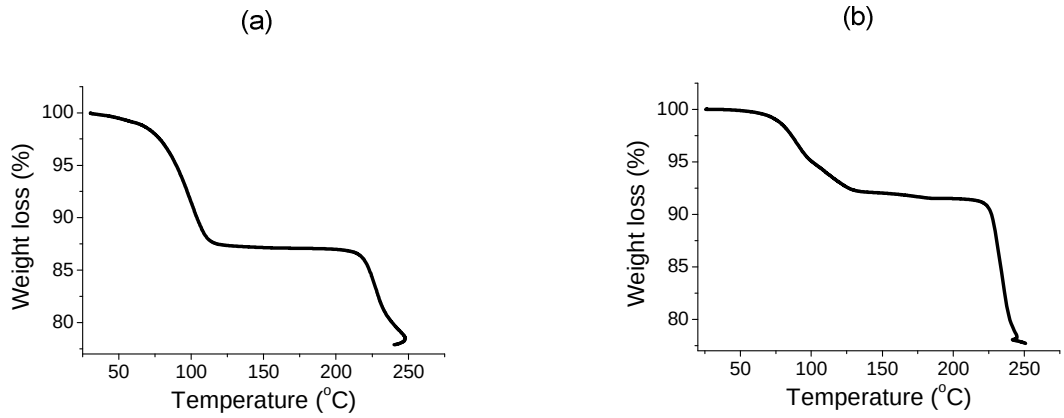

Figure 3.3. TGA curves of: (a) [Fe(Hthpy)(thpy)]·CH_3OH·$3H_2O$ and (b) [Fe(Hmthpy)(mthpy)]·$2H_2O$.

Finally, the last step of decomposition starts from around 224 ^{o}C and continues even beyond 250 ^{o}C involving decomposition of the compounds.

High temperature measurements. The high temperature DSC curves as displayed in Figure 3.4, were measured in agreement with the TGA results. For **2**, the curve show an endothermic feature accompanied with a broad shoulder in the first heating from room temperature up to 180 ^{o}C. As it is reported in literature,[30,31] the shoulder belongs to the desorption of solvate molecules, while the spin state change corresponds with the peak.

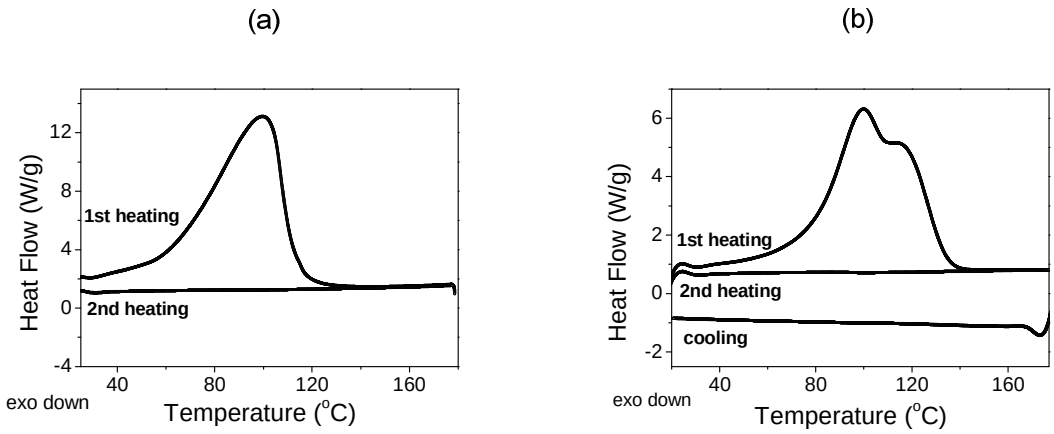

Figure 3.4. High temperature (20 – 180 °C) part of the DSC curves. (a) for $[Fe(Hthpy)(thpy)]\cdot CH_3OH\cdot 3H_2O$. (b) for $[Fe(Hmthpy)(mthpy)]\cdot 2H_2O$.

This peak is totally absent in the second heating curve when it was measured immediately after cooling down to room temperature, without allowing the compound a possible rehydration, since the rehydration process was not possible under these experimental conditions. Similar behaviour is observed for **1**; however the curve shows no shoulder and is rounded at the top. Thus, we suggest that after switching to a new phase, the compounds do not undergo any further phase transition involving a change in spin state. This result is supported by the high temperature (200 – 380 K) magnetic behaviour of **1** and **2**, displayed in Figure 3.5. Evidently, the product of the magnetic susceptibility and the temperature, $\chi_m T$, of **1** and **2** exhibit significant temperature dependence. In both cases, the compounds remain in their low spin state up till 350 K for **1** and 360 K for **2**, before changing abruptly to the high spin state. Because ^{57}Fe Mössbauer spectroscopic shows the spin state, liberation of solvent molecules thus accompanies the interconversion of Fe(III) spin states, which has further been monitored by ^{57}Fe Mössbauer spectroscopy. On the other hand, the $\chi_m T$ vs T plots for the non-solvated compounds as viewed in Figure 3.5 (triangle) are more pronounced. After treating samples in an oven at 453 K for about two hours, the value of $\chi_m T$ varies from 3.59 cm^3 K mol^{-1} at 300 K to 1.42 cm^3 K mol^{-1} at 5 K for **1**, and from 3.63 cm^3 K mol^{-1} at 300 K to 2.99 cm^3 K mol^{-1} at 5 K for **2**. The product of the magnetic susceptibility and the temperature clearly shows a plateau equal to 3.59 cm^3 K mol^{-1} for **1**, and to 3.63 cm^3 K mol^{-1} for **2**, between 50 – 300 K, which is close to the expected value of 4.38 cm^3 mol^{-1} K for a sextuplet high spin state (S = 5/2). Below 20 K, $\chi_m T$ drops rather abruptly, reflecting

the large zero-field splitting (ZFS) of the ground state which is usual *e.g.* in high-spin Fe(III) porphyrins.[32,33] The data were fitted using the following equation:

$$\chi_m = \frac{Ng^2\beta^2}{4kT}\left[\frac{0.14 + 5.12\,e^{-3.23X} + 23.85\,e^{-6.83X}}{1 + e^{-3.23X} + e^{-6.83X}}\right] \qquad (3.1)$$

Where, $X = D/kT$, D is the zero-field splitting parameter, g is the Landé factor and the other symbols have their usual meanings. Equation (3.1) is the theoretical equation for the magnetic susceptibility resulting from the axial and rhombic zero-field splitting for an $S = 5/2$ ion.[34] The best fit between 5 and 300 K has been obtained with the parameters D = 0.899(9) cm^{-1} and g = 2.002(9) with a coefficient of determination(COD), R^2 = 0.996 and a reduced χ^2 of 0.0005 for **1**, D = 0.223(1) cm^{-1} and g = 2.0009(2) with a coefficient of determination (COD), R^2 = 0.997 and a reduced χ^2 of 0.00002 for **2**. Reduced χ^2 measures the appropriateness of the fits and it is obtained from the following function:

$$\chi^2 = \left[\left(\sum(\chi_{obs}T - \chi_{calc}T)^2 / \chi_{obs}T\right)^2\right] \qquad (3.2)$$

Where $\chi_{obs}T$ and $\chi_{calc}T$ are the observed and calculated product of the magnetic susceptibility and the temperature respectively.

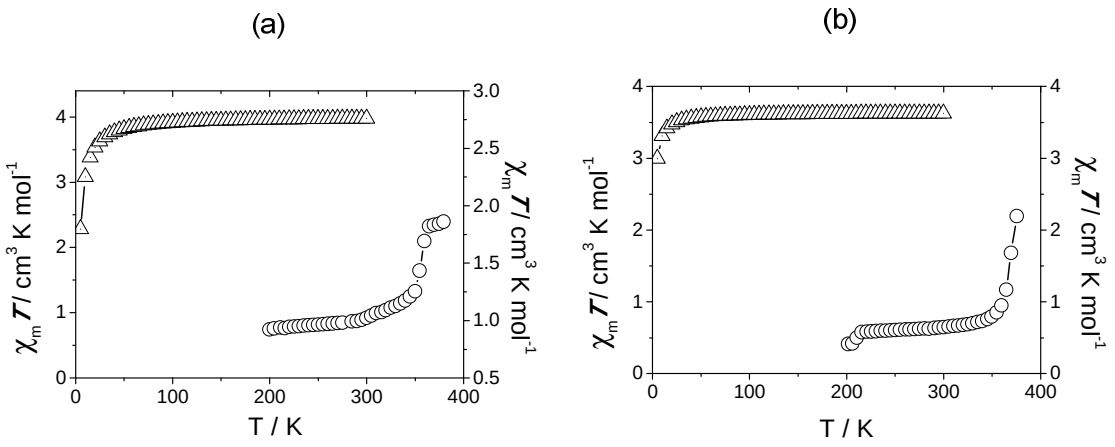

Figure 3.5. Variable-temperature of the magnetic susceptibility and the temperature for: (a) [Fe(Hthpy)(thpy)]·CH_3OH·$3H_2O$ and (b) [Fe(Hmthpy)(mthpy)]·$2H_2O$. Samples were first heated from 200 – 380 K (○) before being placed in an oven for 2 hours at 497 K. After removal of solvent molecules, $\chi_m T$ vs. T plot was measured from 5 – 300 K (Δ). The parameters obtained from the fit are discussed in the text.

3.2.4 Mössbauer and EPR Spectroscopy

^{57}Fe Mössbauer spectra (see Figure 3.6b) have been recorded at various temperatures in the range 293 – 425 K on a sample of **2** obtained as a crystalline powder. Apart from 293 and 340 K where only one doublet signal is observed, at other temperatures, two doublet signals are obtained, one with a large quadrupole splitting ($\Delta E_Q \approx 2.53$ mm·s^{-1}) centered at an isomeric shift of ca. 0.11 – 0.13 mm·s^{-1}, which is ascribed to Fe^{III} ions in the LS state and the other one with a small ΔE_Q (≈ 0.73 mm·s^{-1}) centered at an isomeric shift of ca. 0.29 – 0.40 mm·s^{-1}, which is ascribed to Fe^{III} ions in the HS state. The results of the fitting of these spectra are gathered in Table 3.4. The variation of the relative fraction of both doublets with temperature confirms the presence of a spin-state change in **2**. Nevertheless, Mössbauer data centre the crossover at a higher value, *i.e.* around 360 K, and indicate a more gradual and incomplete spin state change than observed in magnetic measurements (see Figure 3.5b). A 47 % of the iron centres present are still in the LS state at 425 K (see Table 3.4)

Table 3.4 ^{57}Fe Mössbauer Spectral Parameters of [Fe(H_2mthpy)(mthpy)]·2H_2O above RT with ΔE_Q the quadrupole splitting and δ the isomer shift (relative to metallic iron).

	low-spin state			high-spin state			
T (K)	δ (mm s^{-1})	ΔE_Q (mm s^{-1})	Γ/2 (mm s^{-1})	δ (mm s^{-1})	ΔE_Q (mm s^{-1})	Γ/2 (mm s^{-1})	A_{HS}/A_{tot} (%)
293	0.15(28)	2.65(57)	0.14(45)	-	-	-	-
340	0.13(13)	2.64(26)	0.14(21)	-	-	-	-
360	0.13(36)	2.64(73)	0.15(60)	0.34(31)	0.77(54)	0.29(47)	25.8(28)
380	0.15(40)	2.54(82)	0.16(75)	0.37(36)	0.83(66)	0.47(78)	39.9(45)
400	0.11(69)	2.40(14)	0.18(13)	0.33(26)	0.68(45)	0.38(52)	51.8(34)
425	0.12(50)	2.32(11)	0.19(94)	0.29(17)	0.62(30)	0.37(38)	52.9(25)

The observed X-band EPR signal strongly depended on the temperature, which affects not only its intensity but also its shape. At higher temperatures, for example at T = 360 K, a weak expanded spectrum is detected including the signals in the magnetic field B = 3150 G and a trace of other ones with the resonant field B = 1280 G. On cooling, the intensity of the signal with B = 3150 G started to increase. This signal dominated over the initial spectrum (see Figure 3.6a). We interpreted this signal as related to the low spin (LS) Fe(III) complexes (t_{2g}^5, S = 1/2), while the weak spectrum observed at 360 K was considered to include signals from the Fe(III) complexes in the high spin (HS) state

($t_{2g}^3e_g^2$, S = 5/2). This result corroborates well with that obtained from ^{57}Fe Mössbauer spectroscopy. The small intensity of the EPR spectrum of HS complexes recorded as the first derivative of the absorption signal should not be surprising. The observed spectrum depends on the relative values of radiofrequency quantum *hν* and *D*- and *E*-fine structure parameters.[23] When $h\nu \geq D, E$ and the individual linewidths are broadened due to dipole–dipole interactions between the magnetic neighbours (they can be additionally broadened when these interactions are comparable with exchange interactions between HS complexes) the spectrum can be hardly detectable, especially for a powder sample.

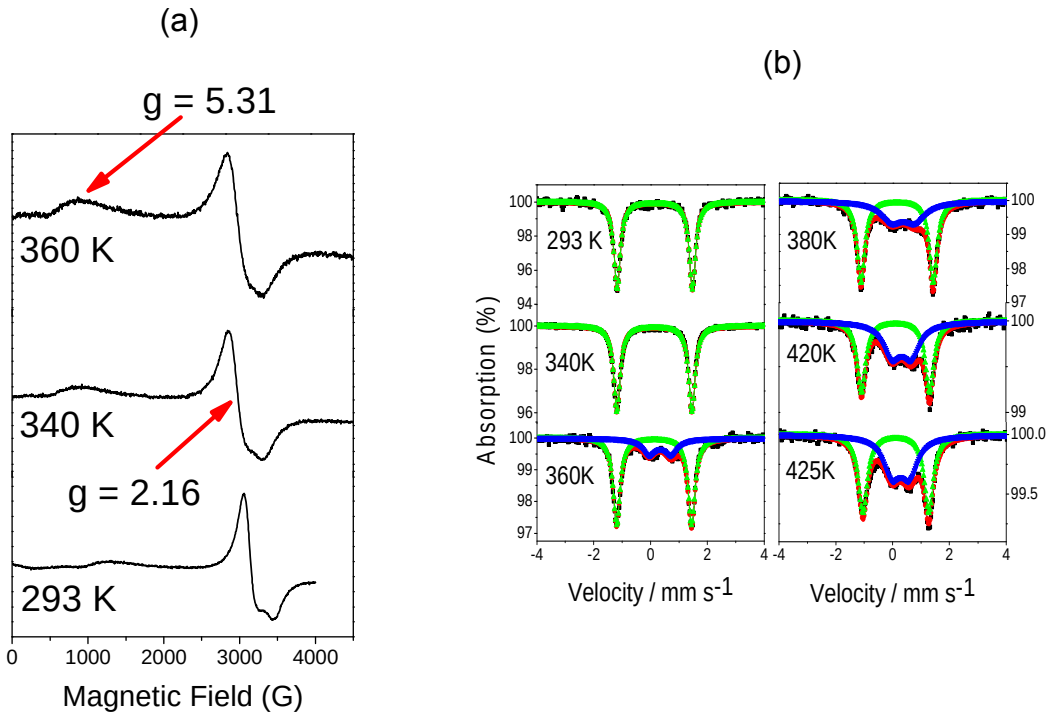

Figure 3.6. (a) Variable-temperature X-band EPR spectrum and (b) temperature dependent ^{57}Fe Mössbauer spectrum for [Fe(Hmthpy)(mthpy)]·2H_2O above room temperature. The green lines represent the LS fraction and the blue ones, the HS fraction.

3.2.5 Heat Capacity

The heat capacity is a thermodynamically well defined quantity and opens the way to determine thermodynamically potential functions.[35] In order to calculate the enthalpy and entropy changes connected with the spin transition of both complexes, the magnetic contribution to the heat capacity was evaluated by subtracting from the experimentally measured quantities, the contributions arising from the lattice vibrations.[36]

Table 3.5 Experimental Molar Heat Capacities of the LS Phase and HS Phase for Fe(Hthpy)(thpy)]·CH_3OH·$3H_2O$ (**1)** and [Fe(Hmthpy)(mthpy)]·$2H_2O$ (**2)**.

	low-spin phase			high-spin phase	
	1	**2**		**1**	**2**
T (K)	C_p ($J\ mol^{-1}\ K^{-1}$)	C_p ($J\ mol^{-1}\ K^{-1}$)	T (K)	C_p ($J\ mol^{-1}\ K^{-1}$)	C_p ($J\ mol^{-1}\ K^{-1}$)
232.95	738.400	630.912	413.03	787.112	924.828
238.00	739.598	639.296	418.33	805.400	944.704
242.94	741.701	647.300	422.68	820.796	961.390
248.00	744.811	655.347	427.98	840.025	982.173
252.96	748.798	663.038	432.97	858.601	1002.196
258.00	753.800	670.669	437.96	877.635	1022.662
262.95	759.646	677.983	442.95	897.126	1043.569
268.00	766.564	685.260	447.94	917.076	1064.918
273.05	774.445	692.351	453.07	938.063	1087.326
278.04	783.178	699.176	458.77	961.949	1112.772
283.04	792.872	705.831	463.13	980.623	1132.625
288.01	803.442	712.266	468.23	1002.910	1156.276
293.03	815.066	718.582	472.97	1024.053	1178.671
298.06	827.668	724.727	478.04	1047.125	1203.066
303.02	841.029	730.605	483.02	1070.247	1227.473
308.03	855.468	736.360	488.00	1093.826	1252.319
312.94	870.539	741.823	493.06	1118.250	1278.016

A comparison of the experimental heat capacities of the LS and HS phase in the vicinity of the peak for [Fe(Hthpy)(thpy)]·CH_3OH·$3H_2O$ (**1)** and [Fe(Hmthpy)(mthpy)]·$2H_2O$ (**2)** are given in Table 3.5. It is evident from an examination of this table that there are lattice contributions to the heat capacity of both compounds, otherwise one would expect to have the same values of heat capacity in LS phase of **1** and **2** as well as in the HS phase respectively. In Table 3.1 is listed, the formula weights, the lattice constants *a*, *b* and *c*, the axial ratio *c/a* and the volume per unit cell (Z = 2 for **1** and Z = 4 for **2**) of compounds. The variation in structural parameters is not large, although evidently large enough so that thermal properties of the lattice are not identical for both complexes. Another remark from Table 3.5 is on the values of the heat capacity of compound **1** in the HS state. At the beginning of this phase, the heat capacity data are even smaller compared to those of the LS phase in the immediate vicinity of the transition peak. By extrapolating, one can affirm that, the values have achieved a maximum, and then drop to a minimum before start to increase with increasing temperature in the HS phase. Similar behaviour has already been reported in the literature,[37-42] and it was proven from ^{57}Fe

Mössbauer spectroscopy analysis that this drop in heat capacity values in the HS state shows the presence of LS fraction in the phase. It disappears just at the temperature where the values of the heat capacity become larger.[42]

3.3 Comments and Conclusions

Since the very first studies the crucial influence of crystal solvent molecules on the spin crossover behaviour has been recognized. In spite of this fact, there are very few systematic investigations devoted to this issue. Compounds under study are typical examples which show the effect of solvent molecules on the spin state change occurrence. The presence of those in the crystal lattice stabilizes the low spin state up till room temperature before an abrupt change of spin state takes place when solvate molecules are released as the temperature is increased. In fact, this loss of solvent molecules causes an irreversible spin state transformation. A similar observation has already been reported in the literature.[43,44] The temperature interval where this transformation occurs, corresponds rightly to that where the solvated species change to the non-solvated ones. Hydrogen bonding also seems to play a significant role in changes in SCO behaviour accompanying desolvation process.[45] Solvated species result in a stabilization of the LS state, through hydrogen bonding of solvent molecules with the ligand. Since the ferric thiosemicarbazone are unique among ferric spin crossover solids in that they possess an abundance of potential sites for intermolecular hydrogen-bonding interactions,[46,47] the loss of these solvent molecules results in the breaking of such an interaction and completely modifies the relatively strong stability of the monomeric units in the solid state.

In conclusion, we have succeeded in synthesizing two new neutral ferric complexes of pyridoxal –thiosemicarbazone and –methylthiosemicarbazone, respectively solvated, and structural characterizing the differences between the two ligands (Hthpy, Hmthpy and thpy, mthpy). We have also demonstrated that thermal spin-state transformation is triggered by the desolvation process as well as by the destruction of the intermolecular hydrogen bonding networks.

3.4 References

(1) Gütlich, P.; Hauser, A.; Spiering, H. *Angew. Chem.* **1994**, *106***,** 2109; *Angew. Chem., Int. Ed. Engl*. **1994**, *33*, 2024.

(2) Gütlich, P. *Struct. Bonding* (*Berlin*) **1981**, *44*, 83.

(3) Kahn, O. *Molecular Magnetism*; WILEY-VCH: New York, 1993; Chapter 4, p 53 ff.

(4) Goodwin, H. A. *Coord. Chem. Rev*. **1976**, *18*, 293.

(5) (a) Zelentsov, V. V. *Russ. J. Coord. Chem*. (*Engl. Transl*.) **2003**, *29*, 425. (b) Zelentsov, V. V. *Sov. Sci. Rev., B. Chem*. **1987**, *10*, 485. (c) Kogan, V.A.; Zelentsov, V.V.; Larin, G.M.; Lukov, V.V. *Kompleksy Perekhodnykh Metallov s Gidrazonami: Fiziko-khimicheskie Svoistva i Stroenie* (*Complexes of Transition Metals with Hydrazones: Physiochemical Properties and Structure*); Nauka: Moscow, 1990; p 85.

(6) Ablov, A. V.; Gerbeleu, N. V. *Russ. J. Inorg. Chem*. **1965**, *10*, 33.

(7) Ablov, A. V.; Gerbeleu, N. V. *Russ. J. Inorg. Chem*. **1970**, *15*, 952.

(8) Timken, M. D.; Wilson, S. R.; Hendrickson, D. N. *Inorg. Chem*. **1985**, *24*, 3450.

(9) Hayami, S.; Hashiguchi, K.; Inoue, K.; Maeda, Y. *J. Nucl. Radiochem. Sci*. **2004**, *5*, N1.

(10) Belicchi Ferrari, M.; Fava, G.G.; Lanfranchi, M.; Pelizzi, C.; Tarasconi, P. *J. Chem. Soc., Dalton Trans*. **1991**, 1951.

(11) Leovac, V. M.; Jevtovic, V. S.; Jovanovic, L. S.; Bogdanovic, G. A. *J. Serb. Chem. Soc*. **2005**, *70*, 393.

(12) Bendito, D. P.; Valcárcel, M. *Afinidad* **1980**, *37*, 123.

(13) Ballesteros, L.; Bendito, D. P. *Mikrochim Acta* **1986**, *I*, 123.

(14) Ablov, A. V.; Goldanskii, V. I.; Turta, K. I.; Stukan, R. A.; Zelentsov, V. V.; Ivanov, E. V.; Gerbeleu, N. V. *Dokl. Phys. Chem. (Engl. Transl.)* **1971**, *196*, 134.

(15) Ablov, A. V.; Gerbeleu, N. V. *Russ. J. Inorg. Chem.* **1964**, *9*, 1260.

(16) Ablov, A. V.; Bologa, O. A. *Russ. J. Inorg. Chem.* **1977**, *22*, 127.

(17) Bologa, O. A.; Belichuk, N. I.; Ablov, A. V. *Russ. J. Inorg. Chem.* **1978**, *23*, 1036.

(18) Zelentsov, V. V.; Larin, G. M.; Ivanov, E. V.; Gerbeleu, N. V.; Ablov, A. G. *Theor. Exp. Chem. (Engl. Transl.)* **1971**, *7*, 648.

(19) Belicchi Ferrari, M.; Fava, G. G.; Pelosi, G.; Rodriguez-Argüelles, M. C.; Tarasconi, P. *J. Chem. Soc., Dalton Trans*. **1995**, 3035.

(20) Jovanovic, L. S.; Jevtovic, V. S.; Leovac, V. M.; Bjelica, L. J. *J. Serb. Chem. Soc.* **2005**, *70*, 187.

(21) Negryatse, N. Y.; Ablov, A. V.; Gerbeleu, N. V. *Russ. J. Inorg. Chem.* **1972**, *17*, 65.

(22) Ablov, A. V.; Gerbeleu N. V.; Romanov, A. M. *Russ. J. Inorg. Chem.* **1968**, *13*, 1558.

(23) Zelentsov, V. V.; Yablokov, Y. V.; Jablokow, M. A. A.; Krupska, A.; Mrozinski, J.;

Ulanov, V. A. *Chem. Phys*. **2004**, *301*, 15.

(24) Floquet, S.; Boillot, M.-L.; Rivière, E.; Varret, F.; Boukheddaden, K.; Morineau, D.; Négrier, P. *New J. Chem*. **2003**, *27*, 341.

(25) (a) Spek, A. L. *PLATON, Program for the Automated Analysis of Molecular Geometry (A Multipurpose Crystallographic Tool), Version of February 2006*; University of Utrecht: Utrecht, The Netherlands, 2006. (b) Spek, A. L. *J. Appl. Crystallogr*. **2003**, *36*, 7.

(26) Belicchi Ferrari, M.; Fava Gasparri, G.; Leporati, E.; Pelizzi, C.; Tarasconi, P.; Tosi, G. *J. Chem. Soc., Dalton Trans*. **1986**, 2455.

(27) Abram, U.; Ortner, K.; Gust, R.; Sommer, K. *J. Chem. Soc., Dalton Trans*. **2000**, 735.

(28) Zelentsov, V. V. In *V.I. Spitsyn*; 6th *ed*.; *Advances in Inorganic Chemistry*: MIR Publishers, 1983; p 122.

(29) *Conformation of Biopolymers*; Academic Press: New York, 1967; Vol. 2, p 607.

(30) Papánková, B.; Vrbová, M.; Boca, R.; Simon, P.; Falk, K.; Miehe, G.; Fuess, H. *J. Therm. Anal. Calorim*. **2002**, *67*, 721.

(31) Bocá, R.; Linert, W. *Monatsh. Chem*. **2003**, *134*, 199.

(32) Mitra, S. In *Iron Porphyrins*; Lever, A. B. P., Gray, H., Eds.; Addison-Wesley: Reading, MA, 1983; Part II, p 1.

(33) Mazzanti, M.; Marchon, J. C.; Wojaczyski, J.; Wolowiec, S.; -Granzynski, L. L.; Shang, M.; Scheidt, W. R. *Inorg. Chem*. **1998**, *37*, 2476.

(34) Chen, C.-H.; Lee, Y.-Y.; Liau, B.-C.; Elango, S.; Chen, J.-H.; Hsieh, H.-Y.; Liao, F.-L.; Wang, S.-L.; Hwang, L.-P. *J. Chem. Soc., Dalton Trans.* **2002**, 3001.

(35) Höhne, G. W. H.; Hemminger, W. F.; Flammersheim, H. J. *Differential Scanning Calorimetry*; 2nd ed.; Springer: Berlin, 2003; p 298.

(36) Stout, J. W.; Catalano, E. *J. Chem. Phys*. **1955**, *23*, 2013.

(37) (a) Nakamoto, T.; Bhattacharjee, A.; Sorai, M. *Bull. Chem. Soc. Jpn.* **2004**, *77*, 921. (b) Sorai, M. *Bull. Chem. Soc. Jpn*. **2001**, *74*, 2223.

(38) Mocala, K.; Navrostsky, A.; Sherman, D. M. *Phys. Chem. Miner*. **1992**, *19*, 88.

(39) Sorai, M.; Seki, S. *J. Phys. Soc. Jpn*. **1972**, *32*, 382.

(40) Sorai, M.; Seki, S. *J. Phys. Chem. Solids* **1974**, *35*, 555.

(41) Boo, W. O. J.; Stout, J. W. *J. Chem. Phys.* **1976**, *65*, 3929.

(42) Nakamoto, T.; Tan, Z.-C.; Sorai, M. *Inorg. Chem.* **2001**, 40, 3805.

(43) (a) Zhang, W.; Zhao, F.; Liu, T.; Yuan, M.; Wang, Z.-M.; Gao, S. *Inorg. Chem.* **2007**, *46*, 2541. (b) Codjovi, E.; Sommier, L.; Khan, O.; Jay, C. *New J. Chem.* **1996**, *20*, 503. (c) Garcia, Y.; van Koningsbruggen, P. J.; Codjovi, E.; Lapouyade, R.; Khan, O.; Rabardel, L. *J. Mater. Chem.* **1997**, *7*, 857. (d) van Koningsbruggen, P. J.; Garcia, Y.; Codjovi, E.; Lapouyade, R.; Khan, O.; Fournes, L.; Rabardel, L. *J. Mater. Chem.* **1997**, *7*,

2069. (e) Garcia, Y.; van Koningsbruggen, P. J.; Lapouyade, R.; Fournes, L.; Rabardel, L.; Khan, O.; Ksenofontov, V.; Levchenko, G.; Gütlich, P. *Chem. Mater.* **1998**, *10*, 2426. (f) Hayami, S.; Gu, Z.-Z.; Yoshiki, H.; Fujishima, A.; Sato, O. *J. Am. Chem. Soc.* **2001**, *123*, 11644. (g) Roubeau, O.; Haasnoot, J. G.; Codjovi, E.; Varret, F.; Reedijk, J. *Chem. Mater.* **2002**, *14*, 2559.

(44) Fukukai, T.; Yabe, K.; Ogawa, Y.; Matsumoto, N.; Mrozinski, J. *Bull. Chem. Soc. Jpn.* **2005**, *78*, 1484.

(45) (a) Gütlich, P.; Goodwin, H. A. *Top. Curr. Chem.* **2004**, *233*, 1–47. (b) Greenaway, A. M.; Sinn, E. *J. Am. Chem. Soc.* **1978**, *100*, 8080.

(46) Mathew, M.; Palenik, G. J. *J. Am. Chem. Soc.* **1969**, *91*, 6310.

(47) Mathew, M.; Palenik, G**.** *J. Inorg. Chim. Acta* **1971**, *5*, 349.

Chapter IV

Tuning of the Charge in Octahedral Ferric Complexes based on Pyridoxal-N-substituted Thiosemicarbazone Ligands

Synopsis

Depending upon preparative conditions (especially pH), a series of octahedral ferric complexes based on pyridoxal-N-substituted thiosemicarbazone is synthesized. Both the degree of deprotonation of the ligand and the charge of the metal complex vary; the magnetic properties of these four compounds are discussed and compared.[1]

[1] A part of this chapter has been published: Yemeli Tido, E. W.; Faulmann, C.; Roswanda, R.; Meetsma, A.; van Koningsbruggen, P. J. *Dalton Trans.* **2010**, *39*, 1643-1651.

4.1 Introduction

Thiosemicarbazones and their metal complexes continue to attract considerable interest because of their reported antineoplastic, antitumour, antiviral and antimalarial activity.[1-8] In addition, their Fe(III) complexes derivatives may exhibit unusual thermal magnetic behaviour.[9] The recent literature[1] shows that this general class of ligands exhibits a wide range of stereochemistries in complexation with transition metal ions; few of these metal compounds have been adequately investigated. A variety of functional groups have been attached to the thiosemicarbazone entity in order to modify the physical, chemical and/or biological properties of the resulting metal complexes.[10] The substitution includes among others: (i) changing the point of attachment of the thiosemicarbazone moiety in the parent aldehyde or ketone; (ii) substitution at the terminal N^4 position; and (iii) variation of the parent aldehyde or ketone. It is well known that depending on the appropriate coordination atoms (O,N,X, where X = N,O, S, Se), the ligand can bind to the connectors (metal ions) either in its neutral, monoanionic or dianionic form.[11,12] This also derives from the fact that in solution, thiosemicarbazone consists of an equilibrium mixture of thione and thiol tautomers. In this regard, our attention is directed to the design of pyridoxal semi-, thiosemi-, and isothiosemicarbazones which can adopt the above-mentioned forms and is especially crucial to the preparation of desirable compound by selecting the suitable synthetic procedure.

However, to the best of our knowledge, no study has been devoted to such synthetic variations. Therefore depending upon preparative conditions, especially the pH of the reaction medium, the complex unit can be neutral, monocationic, tricationic and even be monoanionic. Up to now, most investigations on metal pyridoxal-4R-thiosemicarbazone complexes have involved uncharged mono(ligand) and/or charged bis(ligand). So, data on the complexes containing neutral bis(ligand) metal compounds is really lacking. It is worth noting that octahedral ferric complexes of pyridoxal-4R-thiosemicarbazone ligands (R = H, Ph) are (well)known to exhibit cooperative $S = 1/2 \leftrightarrow S = 5/2$ spin-crossover associated with thermal hysteresis loops,[13] whereas expectedly in a majority of other transition metal systems involving this ligand so far known, either the HS or the LS prevails.[11] In general, Fe(III) spin crossover behaviour is related to many factors such as; counter anion, solvate molecules, intermolecular interactions or hydrogen

bonding network which mediate the intercentre communication in the solid.[14-17] Recent work carried out on ferrous complexes bearing imidazole-type ligand evidenced that the spin state of the metal center can also be tuned through the protonation state of the ligand,[18] as this may influence the ligand field strength about the metal ion. Considering these features, our report aims on varying the charge of the metal complex by essentially maintaining the same geometry around the central atom, and thereby, tuning the spin state of the metal ion. For this purpose, we designed and characterized four novel Fe(III) compounds:$[Fe(Hthpy)_2](SO_4)_{1/2}\cdot 3.5H_2O$ (**3)**, $[Fe(Hthpy)_2]NO_3\cdot 3H_2O$ (**4)**, $[Fe(H_2mthpy)_2](CH_3C_6H_4SO_3)_3\cdot CH_3CH_2OH$ (**5)** and $[Fe(Hethpy)(ethpy)]\cdot 8H_2O$ (**6)**, (H_2thpy = pyridoxalthiosemicarbazone, H_2mthpy = pyridoxal-4-methylthiosemicarbazone, H_2ethpy = pyridoxal-4-ethylthiosemicarbazone); where rather unprecedentedly both, the degree of deprotonation of the ligand and the charge of the metal complex vary; we also discuss and compare their magnetic properties.

4.2 Results and Discussion

4.2.1 Synthesis[2]

The pyridoxal-N-substituted thiosemicarbazone hydrochloride derivatives (scheme 4.1) were prepared according to a procedure described in literature [19] employing the condensation reaction of the corresponding thiosemicarbazide derivative and 3-hydroxy-5-(hydroxymethyl)-2-methyl-4-pyridinecarbaldehyde. Previously, these compounds have been prepared by refluxing the reaction mixture in ethanol.[13] The use of water as a reaction medium proves to be much more effective at generating the desired compounds in crystalline form but produces smaller yield and requires recrystallization.[20] Nevertheless, this type of Schiff-base, pyridoxal-N-substituted thiosemicarbazone hydrochloride salts are Brønsted-Lowry acid, and treatment with a mild base such as triethylamine is sufficient to afford the corresponding pyridoxal-N-substituted thiosemicarbazone monohydrate within 24 hours in essentially quantitative yield (Scheme 4.1); (additional experiments showed that stronger bases such as NaOH, KOH were not suitable for this purpose). These ligands have been prepared previously, though in an entirely different manner.[21] As the resulting compounds are insoluble in nonprotic solvents, the triethylammonium chloride ($Et_3N\cdot HCl$) formed can be easily removed by washing the residue with dichloromethane. Recrystallization of the products from water–

[2] See chapter 2 for details on the experimental procedures and recipes for compounds presented in this chapter

ethanol at room temperature afforded the products in pure, chloride-free form. Absence of chloride impurities was established in the first instance by a negative test reaction with aqueous $AgNO_3$ and then by elemental analysis.

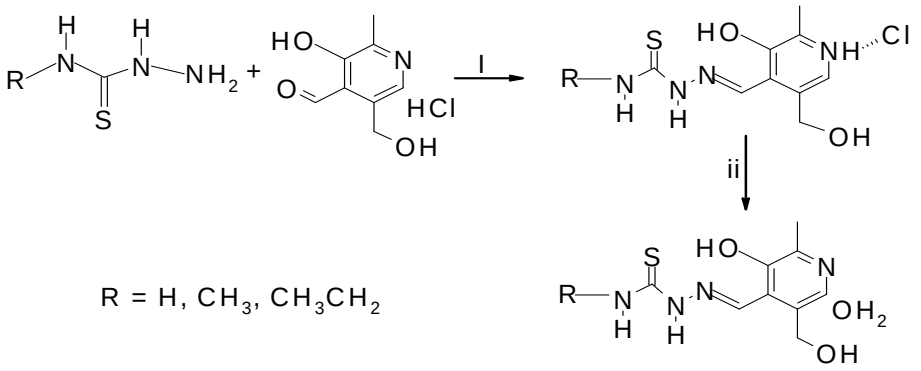

i = 4 h refluxing in EtOH; ii = $Et_3N + CH_2Cl_2$, overnight stirring.

Scheme 4.1. Synthesis of pyridoxal-N-substituted thiosemicarbazone monohydrate.

In DMSO-d_6, the ^1H NMR spectra undergo only minor changes on conversion of the pyridoxal-N-substituted thiosemicarbazone hydrochloride form to the monohydrate derivatives. However, the IR spectra of the hydrochloride free form (Figure 4.1b) clearly differ from those with hydrochloride (Figure 4.1a). The hydrochloride form contains weak/medium absorptions in the range 2700–2850 cm^{-1}, which have been assigned to N–H---Cl vibrations. In the monohydrate these vibrational bands are no longer observed, providing further evidence that chloride is no longer present. Although OH and NH units are still present in the hydrochloride free form, its interaction with the H_2O molecules appears to have changed considerably, accordingly, most of the bands in the 2500–3500 cm^{-1} region of the IR spectrum have disappeared.

This class of ligands can be complexed to transition metal ions by several routes and in three different forms. Metallation with alkali reagents can be accomplished using NH_3 or Et_3N to generate the desired salts. Several structurally characterized examples have already been reported.[22-27] Reaction of pyridoxal-N-substituted thiosemicarbazone hydrochloride and iron(III) sulfate pentahydrate in methanolic solution produces the monoanionic coordination complex with two monodeprotonated ligands. The same charge of the metal complex is obtained with its iron(III) chloride salts but the ligated mono(ligand) is of its neutral form.[28] On the other hand, addition of concentrated ammonia at room temperature to a solution containing pyridoxal-N-substituted thiosemicarbazone hydrochloride on constant stirring leads to the neutralisation of HCl

and the deprotonation of the chelate in solution. Thus, dropwise addition of a solution containing the appropriate iron(III) salt results in dark green solution (the pH of the reaction mixture should not be below 10.40 or exceed 10.70), followed by filtration and slow evaporation at room temperature, gives the analytically pure paramagnetic complex in good yield. If an excess of ammonia solution is added, no further deprotonation is observed. However, the metal compound is neutral and the ligand binds to the metal ion in two inequivalent forms: the singly and the doubly deprotonated form, suggesting the formation of a very stable compound.

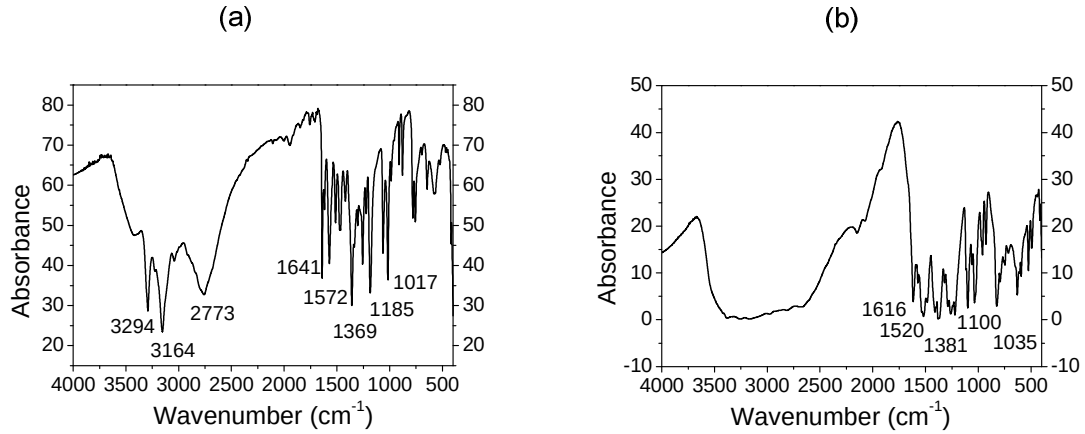

Figure 4.1. KBr pellets IR spectra of: (a) pyridoxalthiosemicarbazone hydrochloride (H_2thpy·HCl) and (b) pyridoxalthiosemicarbazone monohydrate (H_2thpy·H_2O).

Once HCl has been removed, the ligands can be used directly with suitable metal precursors such as iron(III) nitrate nanohydrate or iron(III) *p*-toluenesulfonate hexahydrate in metathesis reactions in water or ethanol respectively. In the first case of complexation, the charge of metal complex is +1 and the two ligated ligands are singly deprotonated while in the second case, the resulting charge is +3 and the two ligated ligands are of its uncharged form. These results demonstrate that factors such as the nature of the iron(III) salt, pH and as well as the substituent at the terminal N^4 position of the thiosemicarbazone moiety play an important role during the synthesis.

4.2.2 Description of Structures

X-ray structural analysis of **3** and **4** reveals that they adopt a monoclinic in unit cell, with different space groups, constructed from a unique 1-D basic subunit ($[Fe(Hthpy)_2]^+$). The asymmetric unit of **3** consists of eight moieties: a cationic Fe-

complex, a half of a sulfate anion, with S at special position: ·2· (two fold axis parallel the *b*-axis), and six solvate water molecules, of which five are partially occupied. In contrast, that of **4** consists of five moieties: a cationic Fe-complex, a nitrate anion, and three water solvate molecules, with no atom at a special position. Though complex **6** is isomorphic to **3**, it is not built up from the same subunits. Its asymmetric unit contains nine moieties: a neutral Fe-complex and eight water solvate molecules. In each case, these entities are linked by hydrogen bonds,[29-31] forming an infinite three-dimensional network along the crystal axes. On the other hand, **5** crystallizes in the triclinic space group *P*$\bar{1}$. The asymmetric unit contains five entities: a tricationic Fe-complex, three tosylate anions and one ethanol solvate molecule, with no atom at a special position. The entities are linked by hydrogen bonds,[29-31] forming an infinite one-dimensional chain along the vector [001]. The molecular structures and the packing arrangement are illustrated in Figures 4.2 – 4.5. Relevant bond lengths and angles are given beneath the corresponding figures. Crystallographic data and numerical details on data collection and refinement for compounds **3** – **6** are summarized in Table 4.1.

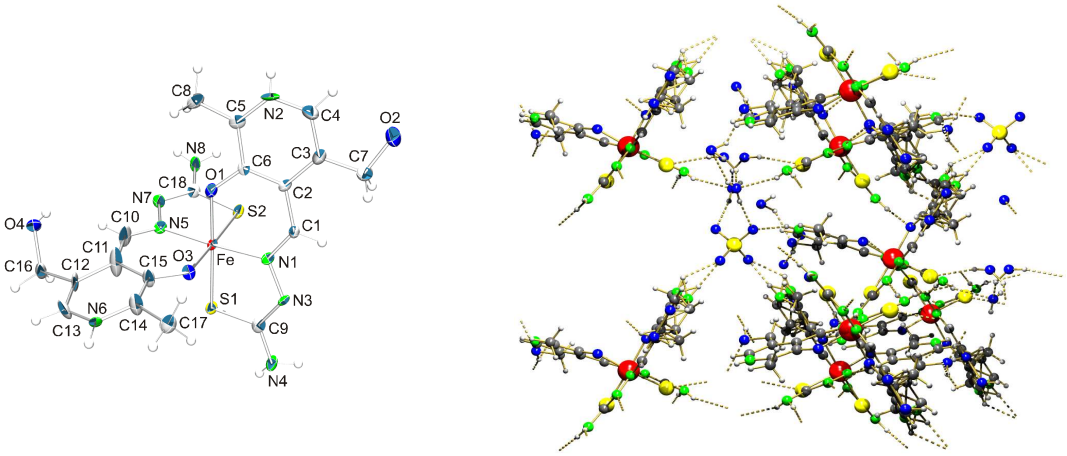

Figure 4.2. X-ray structure of **3** showing the coordination environment (thermal ellipsoids at the 70% probability level) along the *c* axis, illustrating the molecular packing and hydrogen-bonding scheme. Water molecules, and sulfate anions are omitted for clarity. Selected bond length (Å) and angle ranges (º). Standard deviations in the last decimal place are given in parentheses. Fe – S1, 2.2222(19); Fe – S2, 2.204(2); Fe – O1, 1.884(5); Fe – O3, 1.962(5); Fe – N1, 1.926(5); Fe – N5, 1.929(5); S1 – C9, 1.741(7); S2 – C18, 1.734(7); S1 – Fe – S2, 94.58(7); S1 – Fe – O1, 176.33(17); S1 – Fe – N1, 86.83(18); S2 – Fe – O1, 89.07(16); S2 – Fe – N1, 88.59(19); O1 – Fe – O3, 87.4(2); O1 – Fe – N1, 93.7(2); N1 – Fe – N5, 175.4(3); C4 – N2 – C5, 125.4(8); C13a –N6a– C14, 125.5(13).

Table 4.1 Crystallographic Data and Structure Refinement Results for **3**, **4**, **5** and **6**

Compound	**3**	**4**	**5**	**6**
Formula	$C_{18}H_{29}FeN_8O_{9.5}S_{2.5}$	$C_{18}H_{28}FeN_9O_{10}S_2$	$C_{43}H_{55}FeN_8O_{14}S_5$	$C_{22}H_{45}FeN_8O_{12}S_2$
Formula weight / g.mol^{-1}	645.49	650.45	1124.10	733.62
Crystal system	monoclinic	monoclinic	triclinic	monoclinic
Space group	*C*2/*c*	$P2_1/c$	$P\bar{1}$	*C*2/*c*
Crystal colour	dark-brown	dark-red	dark-brown	dark-green
Crystal description	platelet-shaped	block	platelet	platelet-shaped
Crystal dimensions /mm	0.39 x 0.27 x 0.10	0.47 x 0.39 x 0.28	0.47 x 0.34 x 0.17	0.47 x 0.41 x 0.07
a /Å	27.416(2)	9.3807(6)	12.7197(4)	24.778(4)
b /Å	12.2927(8)	19.045(1)	14.0994(4)	11.6118(19)
c /Å	17.230(1)	15.885(1)	15.8183(4)	25.799(4)
α / º			95.1230(10)	
β / º	106.167(1)	107.057(1)	113.2920(10)	116.310(2)
γ / º			92.9670(10)	
V /Å^3	5577.2(6)	2713.1(3)	2583.47(13)	6653.9(18)
Z	8	4	2	8
ρ_{calcd} / g.cm^{-3}	1.537	1.592	1.445	1.465
T / *K*	100(1)	100(1)	293(2)	100(1)
λ /Å	0.71073	0.71073	0.71073	0.71073
μ / cm^{-1}	7.9	7.78	5.64	6.47
F(000)	2680	1348	1174	3096
Total data	21093	24468	100918	25391
Unique data	5471	6727	11037	6762
R_{int}	0.0553	0.0225	0.0347	0.0614
$R(F)$[a]	0.0903	0.0302	0.0574	0.0709
$wR(F^2)$[b]	0.2056	0.0745	0.1623	0.1847
GOF on F^2	1.290	1.060	1.095	1.097
$\Delta_\rho$max, $\Delta_\rho$min / e.Å^{-3}	0.8, -0.6(1)	0.44, -0.27(6)	1.139, -1.127	0.91, -0.57(11)

[a] $R(F) = \sum (||F_o| - |F_c||) / \sum |F_o|$ for $F_o > 4.0\ \sigma\ (F_o)$ for observed reflections.

[b] $wR(F^2) = [\sum [w(F_o^2 - F_c^2)^2] / \sum [w(F_o^2)^2]]^{1/2}$ for all data.

In these four compounds, the Fe(III) atom is coordinated by two tridentate O,N,S-ligands, with the formation of a distorted $FeS_2N_2O_2$ octahedron. The donor atoms are located in mutually normal planes, the S and O atoms being at the cis-positions and N at the trans-positions. Particularly, the binding of the ligand involving the formation of two metallocycles: a five-membered thiosemicarbazide S,N-chelate ring together with a six-membered pyridoxilydene N,O-chelate ring, appears to be associated with a severe deviation from planarity of the iron-ligand framework. The angle between the least-squares planes through these five-membered and six-membered rings is approximately 6.83(5)^o. In **5**, pyridoxal-4-methylthiosemicarbazone appears to be of its neutral zwitterionic form, *i.e.* it is deprotonated at the phenolic oxygens O1, O3 whereas it is

protonated at the pyridine N4, N8 and the hydrazinic N2, N6 nitrogen. Protonation of N4, N8 is evident from the value of the C6–N4–C7 and C16–N8–C17 pyridyl angle of 124.6(5)^{o} and 124.8(4)^{o} which have significantly increased with respect to the C–N–C angle of about 120^{o} that could be expected for a non-protonated pyridyl-N. In addition, protonation of N2, N6 is in line with the ligand being of the thione form, *i.e.* having typical short C2 = S1, C12 = S2 distances of 1.718(4), 1.713(4) Å and adjacent carbon–nitrogen bond lengths which are typical for a single bond (C2–N2 = 1.338(4) Å, C12–N6 = 1.332(5) Å). These bond distances are in agreement with the literature values.[21,22]

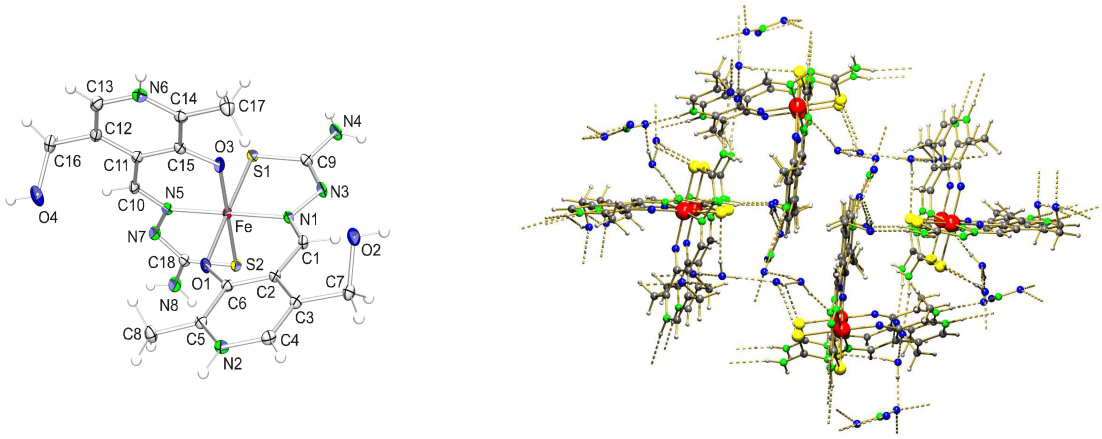

Figure 4.3. X-ray structure of **4** showing the coordination environment (thermal ellipsoids at the 50% probability level) along the *a* axis, illustrating the molecular packing and hydrogen-bonding scheme. Water molecules, and nitrate anions are omitted for clarity. Selected bond length (Å) and angle ranges (º). Standard deviations in the last decimal place are given in parentheses. Fe – S1, 2.2620(4); Fe – S2, 2.2489(4); Fe – O1, 1.9234(11); Fe – O3, 1.9101(11); Fe – N1, 1.9377(13); Fe – N5, 1.9415(13); S1 – C9, 1.7459(16); S2 – C18, 1.7445(16); S1 – Fe – S2, 88.40(1); S1 – Fe – O1, 178.94(3); S1 – Fe – N1, 85.65(4); S2 – Fe – O1, 90.93(3); S2 – Fe – N1, 95.90(4); O1 – Fe – O3, 89.55(4); O1 – Fe – N1, 93.60(5); N1 – Fe – N5, 177.75(5); C4 – N2 – C5, 124.03(13); C13 –N6– C14, 124.34(14).

In **3** and **4**, pyridoxalthiosemicarbazone binds in its monoanionic form to the metal ion, *i.e.* the nitrogen of the pyridine ring bears a proton whereas that of the hydrazinic nitrogen does not possess any hydrogen; several additional structural features to characterize the ligand form of **3** and **4** can be obtained from the bond distances and angles listed underneath the corresponding figures. In contrast to **3**, **4** and **5** whose ligands are equally bonded to iron, complex **6** is formed with two inequivalent forms of

the ligand. Both ligands are obtained by sequentially deprotonating neutral pyridoxal-4-ethylthiosemicarbazone. The singly deprotonated ligand ($Hethpy^-$) possesses a hydrogen atom bound to the N1 nitrogen atom, whereas no such hydrogen atom is found at the N5 position of the doubly deprotonated form ($ethpy^{2-}$). Specific structural differences between the singly and doubly deprotonated ligands, as well as differences in the manner in which each binds to the iron center, are illustrated in Figure 4.5. As expected from electrostatic considerations, the dianionic ligand is not more tightly bound to the iron ion than is the monoanionic chelate. This is because, although they are in two different oxidation states, still the two chelates remain in the thiol form. However, it is worth noting that this structural difference is easily seen from the angle about the pyridyl nitrogen which is 118.3(4)^o for the dianionic form and of 123.0(5)^o for the monoanionic ligand. It is also interesting to notice that the C-N bond distances about the pyridyl nitrogen, are almost equal for the protonated nitrogen and meaningfully different for their nonprotonated homologue.

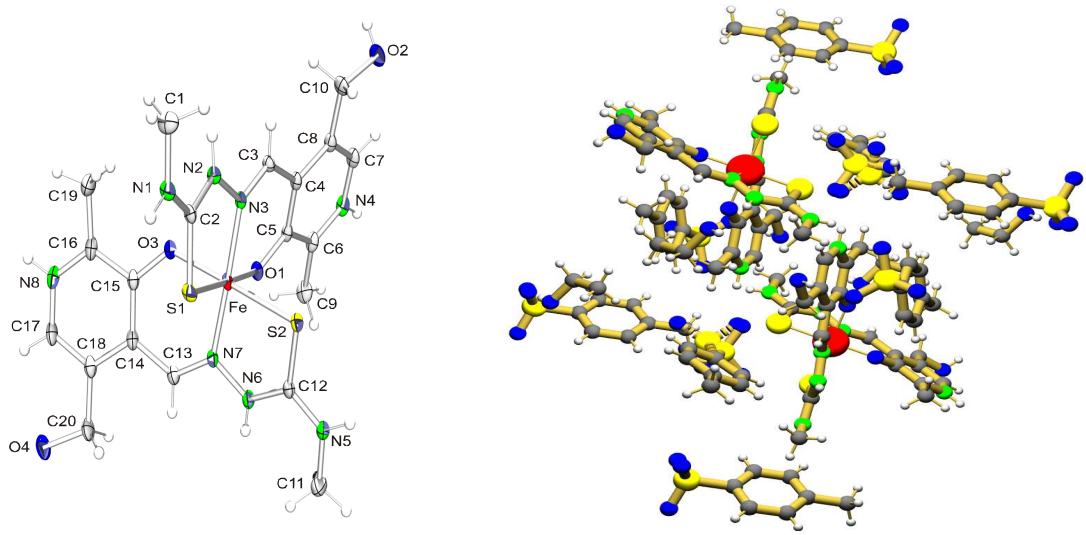

Figure 4.4. X-ray structure of **5** showing the coordination environment (thermal ellipsoids at the 20% probability level) along the *a* axis, illustrating the molecular packing. Ethanol molecule, and *p*-toluenesulfonate anions are omitted for clarity. Selected bond length (Å) and angle ranges (^{o}). Standard deviations in the last decimal place are given in parentheses. Fe – S1, 2.2545(10); Fe – S2, 2.2635(10); Fe – O1, 1.917(2); Fe – O3, 1.913(3); Fe – N3, 1.915(3); Fe – N7, 1.907(3); S1 – C2, 1.718(4); S2 – C12, 1.712(4); S1 – Fe – S2, 90.78(4); S1 – Fe – O1, 178.58(9); S1 – Fe – N3, 86.58(8); S2 – Fe – O1, 89.54(8); S2 – Fe – N3, 96.49(9); O1 – Fe – O3, 90.37(11); O1 – Fe – N3, 92.01(11); N3 – Fe – N7, 176.14(13); C6 – N4 – C7, 124.8(3); C16 –N8– C17, 124.6(4).

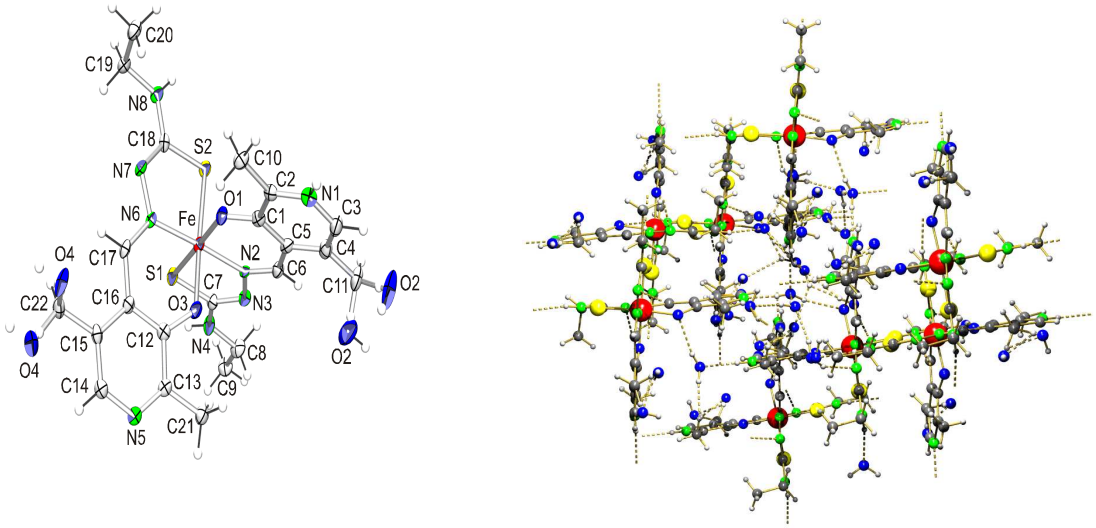

Figure 4.5. X-ray structure of **6** showing the coordination environment (thermal ellipsoids at the 50% probability level) along the *a* axis, illustrating the molecular packing and hydrogen-bonding scheme. Water molecules are omitted for clarity. Selected bond length (Å) and angle ranges (º). Standard deviations in the last decimal place are given in parentheses. Fe – S1, 2.2241(15); Fe – S2, 2.2326(14); Fe – O1, 1.932(3); Fe – O3, 1.912(3); Fe – N2, 1.930(4); Fe – N6, 1.924(4); S1 – C7, 1.754(6); S2 – C18, 1.761(6); S1 – Fe – S2, 92.49(5); S1 – Fe – O1, 177.86(12); S1 – Fe – N2, 86.83(12); S2 – Fe – O1, 88.60(11); S2 – Fe – N2, 95.58(12); O1 – Fe – O3, 87.59(15); O1 – Fe – N2, 94.90(16); N2 – Fe – N6, 177.51(16); C2 – N1 – C3, 123.0(5); C13 –N5– C14, 118.3(4).

X-ray structural data of Fe(III) bis-ligand compounds of the dianion of R-salicylaldehyde thiosemicarbazone reveal that the Fe–S, Fe–O and Fe–N distances typically are of the order of 2.44 Å, 1.96 Å and 2.12 Å for high spin Fe(III), severally, whereas these are 2.23 Å, 1.94 Å and 1.96 Å for low spin Fe(III), severally.[32] Comparison with these iron ligand bond lengths indicates that the Fe(III) ion is in the low spin state in the studied complexes. Figures 4.2 – 4.5 illustrate the molecular packing and hydrogen-bonding scheme in the unit cell along the three-dimensional axis. The molecules of compounds **3** – **6** are held together by N–H---O, N–H---S, O–H---S, O–H---N, and O–H---O hydrogen bonds. A summary of the hydrogen-bond dimensions is given in Table 4.2.

Table 4.2 Geometry of selected Intra- and Intermolecular Hydrogen Bonds (Å,°) for **3**, **4** and **6**. Standard deviations in the last decimal place are given in parentheses.

D–H---A	D–H (Å)	H---A (Å)	D---A (Å)	D–H---A (°)
		Compound **3**		
O7–H31---O9	0.59(19)	2.36(18)	2.900(19)	153(19)
O11–H35---O7	1.09(14)	1.52(13)	2.491(15)	145(12)
N2–H22---O5[b]	0.70(9)	2.14(8)	2.783(10)	154(9)
N4–H24'---O7[c]	0.74(8)	2.27(8)	2.967(12)	159(8)
O7–H31---O5[b]	0.82(12)	1.97(12)	2.783(11)	170(14)
O9–H33---O2[d]	1.2(2)	2.09(18)	2.753(18)	113(12)
O11–H35'---S1[e]	0.87(16)	2.40(17)	3.253(14)	166(12)
N6A–H61---O6[f]	0.88	2.12	2.816(15)	136
		Compound **4**		
N4–H34---O2[l]	0.85(2)	2.13(2)	2.9470(18)	159.6(18)
O8–H28---N7	0.88(3)	1.99(3)	2.8487(19)	167(3)
N6–H36---O5[i]	0.82(2)	2.08(2)	2.8819(19)	167(2)
O2–H22---O9[i]	0.83(2)	1.91(2)	2.7357(18)	172(2)
O9–H29---O10[j]	0.77(2)	2.01(2)	2.7750(18)	173(2)
O8–H28'---O6[k]	0.84(3)	1.95(3)	2.7815(18)	171(2)
N6–H36---O7[i]	0.82(2)	2.50(2)	3.1477(18)	137.3(18)
O9– H29'---S2[l]	0.83(3)	2.52(2)	3.3216(13)	165(2)
O10–H210---O8	0.83(2)	1.92(2)	2.733(2)	167(2)
		Compound **6**		
N1–H1---O36[c]	0.83(5)	1.95(5)	2.769(6)	176(6)
O33–H33---N3[b]	0.84(4)	2.12(5)	2.941(7)	165(5)
O33–H33'--O34[b]	0.84(3)	2.33(2)	3.129(8)	158(4)
O34–H34---O33[b]	0.84(4)	2.57(3)	3.129(8)	125(5)
O35–H35---N7[f]	0.84(3)	2.08(4)	2.861(6)	154(5)
O35–H35'---O38[f]	0.84(4)	1.92(4)	2.745(6)	168(4)
O38–H38'--O32[c]	0.84(4)	1.92(4)	2.754(7)	170(5)
O36–H36'---N5[c]	0.84(5)	1.85(5)	2.670(6)	168(5)
O37–H37---O35[c]	0.84(4)	1.95(4)	2.786(6)	172(4)

Atoms marked with a letter are generated by the symmetry operations: b = -x, y, 1/2-z; c = 1/2-x, -1/2+y, 1/2-z; d = x,1-y,1/2+z; e = -1/2+x, 1/2+y, z; f = 1/2-x, 1/2+y, 1/2-z; i = 1+x, 1/2-y, -1/2+z; j = 1-x, -y, 1-z; k = 1-x, -1/2+y, 1/2-z; l = x, 1/2-y, 1/2+z.

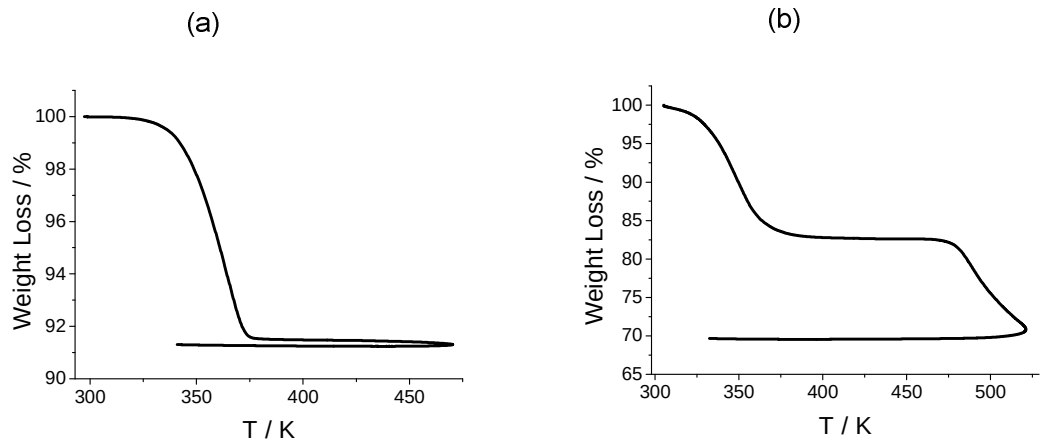

Figure 4.6. Thermal Gravimetric Analysis curves of: (a) $[Fe(Hthpy)_2](SO_4)_{0.5}\cdot 3.5H_2O$ and (b) $[Fe(Hethpy)(ethpy)]\cdot 8H_2O$.

4.2.3 Thermogravimetric analysis

The observed percentage weight loss corresponding to the first inflexion in the thermograms of both compounds were compared (Figures 4.6a and 4.6b) with those calculated on the basis of possible decomposition of the expelled moieties. In the present study, the TGA profile consists of two well defined stages. On heating between 357 and 403 K, the complexes liberate solvate molecules. The theoretical weight loss for this step is 9.76 % for **3** and 19.63 % for **6**. The experimental losses of weight are 8.60 % and 17.73 % for **3** and **6** respectively, which are very close to the theoretical values. Here the compounds are completely devoid of lattice solvent molecules. Then the curves showed a straight line which did not change even on heating up to 497 K indicating that there is no further change in weight. Finally, the last step of decomposition starts from around 497 K and continues even beyond 523 K involving decomposition of the compounds.

4.2.4 Magnetic Properties

Figure 4.7b shows the thermal variation (heating and cooling modes) of the effective magnetic moment, μ_{eff} of **6**. From 2 to 300 K, a roughly constant μ_{eff} equal to 1.85 μ_B is observed. This value is in agreement with the presence of 100 % of the Fe(III) cations in the LS state, as was already deduced from X-ray diffraction. Upon heating above 300 K, μ_{eff} increases to reach a value of 3.87 μ_B at 400 K. It is somewhat smaller than the expected "spin-only" value for one Fe(III) HS per formula unit. On cooling subsequently the sample below 400 K, a constant μ_{eff} value of ~3.6 μ_B is obtained, which is close to that observed at 400 K. Clearly, **6** is changing its configuration from the LS

state to the HS state during dehydration. TGA measurements show weight loss in this temperature range. Thus, after annealing the sample in the TGA up to 497 K (in order to get rid of water molecules), the anhydrous material was then placed in the squid magnetometer.

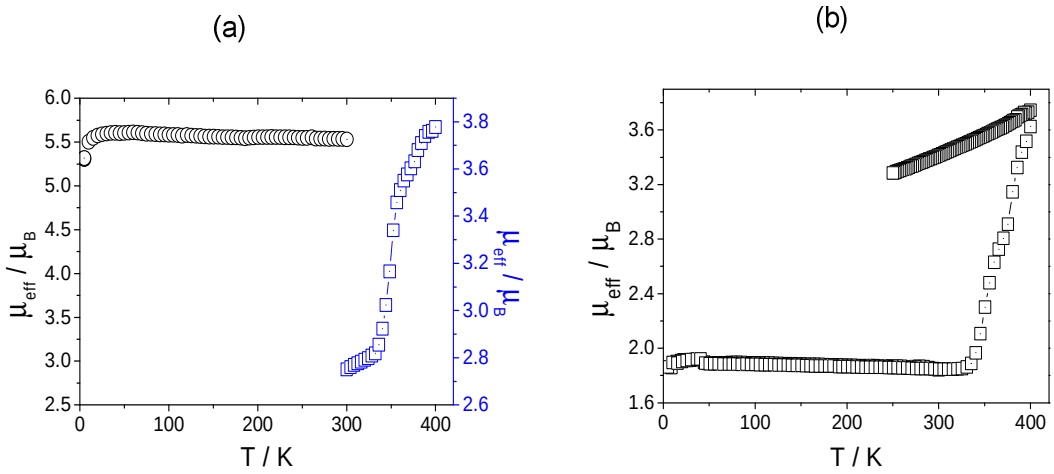

Figure 4.7. Magnetic behaviour of: (a) $[Fe(Hthpy)_2](SO_4)_{0.5}\cdot 3.5H_2O$ in the form of μ_{eff} vs temperature plots. The sample was first warmed from 300 to 400 K (□) before being placed in an oven at 497 K for 2 h. After removal of solvent molecules, μ_{eff} was then measured from 5 to 300 K (○), and (b) $[Fe(Hethpy)(ethpy)]\cdot 8H_2O$ in the form of μ_{eff} vs temperature plots. The sample was warmed from 2 to 400 K (□) and then cooled from 400 to 250 K (□), at a rate of 2 K min^{-1}.

The recorded temperature dependence of the effective magnetic moment yielded a constant value of 5.52 μ_B that did not change during the warming and cooling runs (100 – 220 K), respectively. As a consequence, complex **6** is HS after being transformed completely to an anhydrous material ([Fe(Hethpy)(ethpy)]). Complex **3** exhibits similar behaviour (Figure 4.7a), with the only exception that below room temperature, the effective magnetic moment is slightly higher than the spin only value expected for Fe(III) low spin. In contrast to **3** and **6**, compound **4** is low spin; even when heating from 200 to 400 K, the effective magnetic moment remains constant and equal to: μ_{eff} = 2.06 μ_B. Crystallographic studies at both 100 K and room temperature revealed the same crystal structure. Variable X-band EPR spectra above room temperature do not show any signal related to the high-spin form.

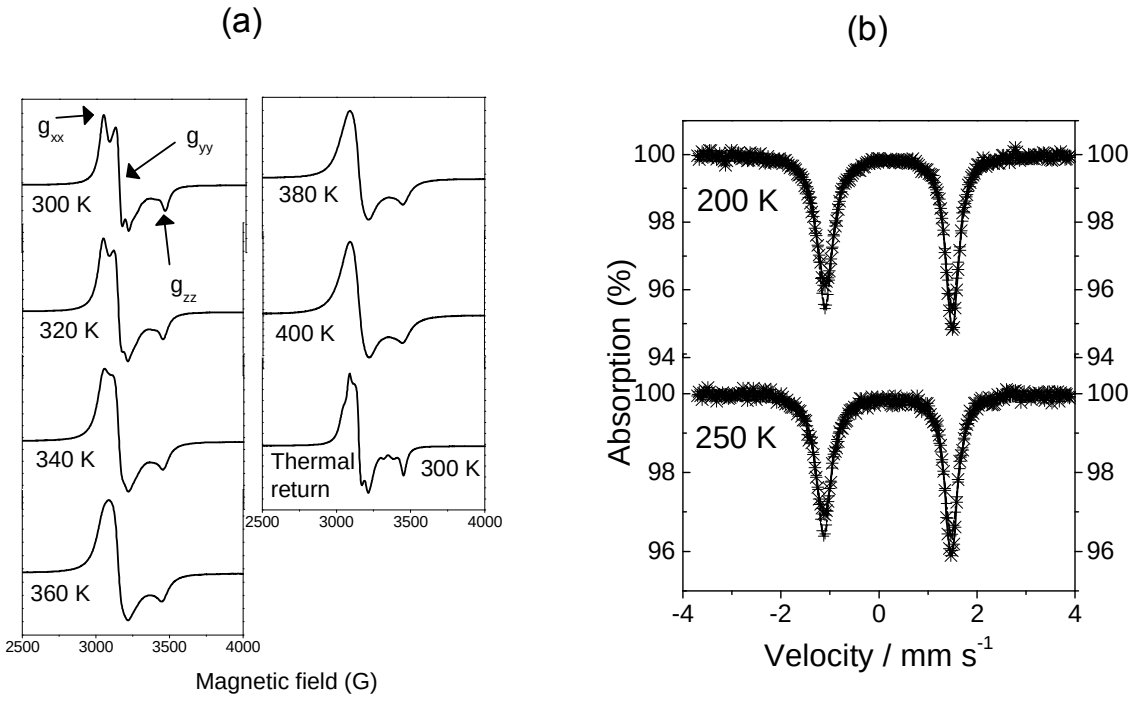

Figure 4.8. (a) Temperature dependence X-band spectrum above RT with microwave frequency 9.510743 GHz and (b) ^{57}Fe Mössbauer spectra at 200 and 250 K of $[Fe(H_2mthpy)_2](CH_3C_6H_4SO_3)_3 \cdot CH_3CH_2OH$.

Table 4.3 ^{57}Fe Mössbauer Spectral Parameters of $[Fe(H_2mthpy)_2](CH_3C_6H_4SO_3)_3 \cdot CH_3CH_2OH$ at 200 and 250 K, with ΔE_Q the quadrupole splitting and IS the isomer shift (relative to metallic iron).

	IS mm s^{-1}	ΔE_Q mm s^{-1}	$\Gamma/2$ mm s^{-1}	LS fraction %
250 K	0.18(37)	2.60(74)	0.18(61)	100
			χ^2 = 1.46	
200 K	0.19(25)	2.59(51)	0.18(42)	100
			χ^2 = 2.57	

The solid state X-band EPR spectrum recorded on a polycrystalline sample at 300 K (Figure 4.8a) for **5**, shows a typical spectrum for low spin iron(III) ion in a rhombic symmetry with g_{xx} = 2.23, g_{yy} = 2.15, and g_{zz} = 1.96. Similar signals were reported earlier for the Fe(III) center in a spin equilibrium system.[33,34] The temperature dependence of the EPR signal observed above room temperature is strongly influenced by the temperature, which affects not only its intensity, but also its shape. Upon heating, the rhombic signal slowly changes to an axial anisotropic signal from 360 to 400 K, with $g_\perp$ = 2.15 and $g_\parallel$ = 1.96 and hence is typical for LS iron(III) center.[35] Rapid cooling down to

300 K experiment has been carried out with the objective to determine whether the compound was affected during heating. On performing this experiment, it appears that the spectrum recovered its anisotropic rhombic symmetry but with less intense g_{xx} signal. ^{57}Fe Mössbauer spectra of **5** recorded at 200 and 250 K consist of a single asymmetric quadrupole-split doublet as shown in Figure 4.8b. The spectra were least-squares fitted with Lorentzian lines and the resulting isomer shift (IS) and quadrupole splitting parameters (ΔE_Q) are listed in Table 4.3. The magnitudes of IS and ΔE_Q are comparable to those observed for well characterized pure S = 1/2 spin systems. In fact, LS iron(III) compounds have IS values in the range of 0.05 – 0.20 mm.s^{-1} and relatively large ΔE_Q values of 1.9 – 3.0 mm.s^{-1}.[36] This conclusion is supported by the effective magnetic moment and the EPR spectra recorded at/around the same temperatures.

4.2.5 Comparative Study

The above results give compelling evidence of the role played by solvent molecules in the magnetic properties of the different complexes. It is clear that the magnetism of these salts is very sensitive to their solvate molecules and in other cases to the counterion, which is able to form hydrogen bonds. For instance, in a monocationic compound like **3** and **4**, where the ligand substitution and its degree of deprotonation are identical, their magnetic behaviour is completely different. **3** is showing an abrupt transition upon release of its cocrystallized water molecules, whereas **4** remains in the LS state even after loosing its water molecules. Consequently, the variation of anion from SO_4^{2-} to NO_3^- associated with this cationic spin crossover system, result to the extent that the spin crossover, SCO, behaviour is no longer observed. The influence of the anion for instance was noted for salts of $[Co(terpy)_2]^{2+}$ [37] and for iron(II) in salts of $[Fe(paptH)_2]^{2+}$ [38] and of $[Fe(pic)_3]^{2+}$.[39] If we replace the substituent at the terminal N^4 position of the thiosemicarbazone moiety by a methyl group and change the size of the counterion (from sulfate and nitrate anions to tosylate anion), we obtained a tricationic complex. As expected, although changes occurred on the lattice phonon distribution resulting from different crystal packing geometry and strength of the intermolecular forces, the iron(III) center is LS. Hence, modification does not bring about major fundamental changes in the nature of the transition or on the ligand field strength. On the order hand, in a neutral species like **6**, where the ligand is bound to the metal ion in two inequivalent forms, the transition occurs upon release of water molecules and breaking of the hydrogen bonding interactions. This phenomenon is irreversible and probably modifies completely the

crystal lattice stacking interactions. There are many other similar examples in the literature.[40-42] Whatever the rationale for the effects, it is clear that the magnetic properties of the four compounds are the same up till room temperature before behaving differently above room temperature upon release of their solvent molecules.

4.3 Conclusions

A new family of octahedral ferric complexes based on pyridoxal-N-substituted thiosemicarbazone, including two monocationic complexes $[Fe(Hthpy)_2](SO_4)_{1/2}\cdot 3.5H_2O$ (**3**), $[Fe(Hthpy)_2]NO_3\cdot 3H_2O$ (**4**), one tricationic complex, $[Fe(H_2mthpy)_2](CH_3C_6H_4SO_3)_3\cdot CH_3CH_2OH$ (**5**), and a neutral complex, $[Fe(Hethpy)(ethpy)]\cdot 8H_2O$ (**6**), has been characterized and extensively investigated. The coordination chemistry of iron(III) so far reported reveals that this ligand system yields stable Fe(III) complexes of the uncharged monoligand and/or charged bisligands metal compound.[1] Within each degree of deprotonation, the ligands which afford SCO are further limited because the ligand field in a SCO compound should be close to the crossover point of the Tanabe-Sugano diagram.[43] In fact, the ligand environments which induce SCO are limited to $FeO_2N_2S_2$ octahedron. Therefore, it should be stressed that the present pyridoxal attached to three thiosemicarbazide groups provides an ONS donor set able to bind the central atom in a versatile form and thus stabilize a remarkable variety of charge of the iron(III) complex, as described in this study. Among the materials in this family, $[Fe(Hthpy)_2](SO_4)_{1/2}\cdot 3.5H_2O$ (**3**) and $[Fe(Hethpy)(ethpy)]\cdot 8H_2O$ (**6**) assume appealing infinite three dimensional hydrogen bonding network in their crystal lattice. The degree of deprotonation and the substituent effect of the methyl and ethyl groups at the terminal thiosemicarbazone chain allow fine-tuning of the charge of metal complex and SCO behaviour of this type of molecular system.

4.4 References

(1) (a) Campbell, M. J. M. *Coord. Chem. Rev.* **1975**, *15*, 279. (b) Padhye, S. B.; Kauffman, G. *Coord. Chem. Rev.* **1985**, *63*, 127.

(2) West, D. X.; Padhye, S. B.; Sonawane, P. B. *Struct. Bonding (Berlin, Ger.)* **1991**, *76*, 1.

(3) West, D. X.; Liberta, A. E.; Padhye, S. B.; Chikate, R. C.; Sonawane, P. B.; Kumbhar, A. S.; Yerande, R. G. *Coord. Chem. Rev.* **1993**, *123*, 49.

(4) Casas, J. S.; Garcia-Tasende, M. S.; Sordo, J.*Coord. Chem. Rev.* **2000**, *209*, 197.

(5) Smith, D. R. *Coord. Chem. Rev.* **1997**, *164*, 575.

(6) Quiroga, A. G.; Ranninger, C. N. *Coord. Chem. Rev.* **2004**, *248*, 119.

(7) Klayman, D. L.; Scovill, J. P.; Bartosevich, J. F.; Mason, C. J. *J. Med. Chem.* **1979**, *22*, 367.

(8) Shipman, C.; Smith, Jr., S. H.; Drach, J. C.; Klayman, D. L. *Antiviral Res.* **1986**, *6*, 197.

(9) (a) Zelentsov, V. V. *Russ. J. Coord. Chem.* (*Engl. Transl*.) **2003**, *29*, 425. (b) Zelentsov, V. V. *Russ. J. Coord. Chem.* **1992**, *18*, 787. (c) Zelentsov, V. V. *Sov. Sci. Rev. B. Chem.* **1987**, *10*, 485. (d) Kogan, V. A.; Zelentsov, V. V.; Larin, G. M.; Lukov, V. V. *Kompleksy Perekhodnykh Metallov s Gidrazonami: Fiziko-khimicheskie Svoistva i Stroenie* (*Complexes of Transition Metals with Hydrazones: Physiochemical Properties and Structure*); Nauka: Moscow, 1990; p 85.

(10) van Koningsbruggen, P. J.; Maeda Y.; Oshio, H. *Top. Curr. Chem.*, **2004**, *233*, 259.

(11) Leovac, V. M.; Jevtovic, V. S.; Jovanovic, L. S.; Bogdanovic, G. A. *J. Serb. Chem. Soc.* **2005**, *70*, 393.

(12) Jovanovic, L. S.; Jevtovic, V. S.; Leovac, V. M.; Bjelica, L. J. *J. Serb. Chem. Soc.* **2005**, *70*, 187.

(13) (a) Mohan, M.; Madhuranath, P. H.; Kumar, A.; Kumar, M.; Jha, N. K. *Inorg. Chem.* **1989**, *28*, 96. (b) Gupta, N. S.; Mohan, M.; Jha, N. K.; Antholine, W. E. *Inorg. Chim. Acta* **1991**, *184*, 13.

(14) Sams, J. R.; Tsin, T. B. *J. Chem. Soc., Dalton Trans.* **1976**, 488.

(15) Sams, J. R.; Tsin, T. B.; *Inorg. Chem.* **1976**, *15*, 1544.

(16) Baker, A. T.; Goodwin, H. A. *Aust. J. Chem.* **1977**, *30*, 771.

(17) Boča, R.; Baran, P.; Dlháň, L.; Fuess, H.; Haase, W.; Renz, F.; Linert, W.; Svoboda, I.; Werner, R. *Inorg. Chim. Acta* **1997**, *260*, 129.

(18) Ikuta, Y.; Ooidemizu, M.; Yamahata, Y.; Yamada, M.; Osa, S.; Matsumoto, N.; Iilima, S.; Sunatsuki, Y.; Kojima, M.; Dahan, F.; Tuchagues, J.-P. *Inorg. Chem.* **2003**, *42*, 7001.

(19) Belicchi Ferrari, M.; Fava Gasparri, G.; Leporati, E.; Pelizzi, C.; Tarasconi, P.; Tosi, G. *J. Chem. Soc., Dalton Trans.* **1986**, 2455.

(20) Yemeli Tido, E. W.; Vertelman, E. J. M.; Meetsma, A.; van Koningsbruggen, P. J.; *Inorg. Chim. Acta* **2007**, *360*, 3896.

(21) Belicchi Ferrari, M.; Bisceglie, F.; Leporati, E.; Pelosi, G.; Tarasconi, P. *Bull. Chem. Soc. Jpn.* **2002**, *75*, 781.

(22) Abram, U.; Ortner, K.; Gust, R.; Sommer, K. *J. Chem. Soc., Dalton Trans.* **2000**, 735.

(23) Yemeli Tido, E. W.; Alberda van Ekenstein, G. O. R.; Meetsma, A.; van Koningsbruggen, P. J. *Inorg. Chem.* **2008**, *47*, 143.

(24) Belicchi Ferrari, M.; Fava, G. G.; Lanfranchi, M.; Pelizzi, C.; Tarasconi, P. *J. Chem. Soc., Dalton Trans.* **1991**, 1951.

(25) Belicchi Ferrari, M.; Fava, G. G.; Pelosi, G.; Rodriguez-Argüelles, M. C.; Tarasconi, P. *J. Chem. Soc., Dalton Trans.* **1995**, 3035.

(26) Belicchi Ferrari, M.; Bisceglie, F.; Pelosi, G.; Tarasconi, P.; Albertini, R.; Dall'Aglio, P. P.; Pinelli, S.; Bergamo, A.; Sava, G. *J. Inorg. Biochem.* **2004**, *98*, 301.

(27) Belicchi Ferrari, M.; Gasparri Fava, G.; Pelizzi, C.; Tarasconi, P.; Tosi, G. *J. Chem. Soc., Dalton trans.* **1987**, 227.

(28) Jevtovic, V. S.; Jovanovic, L. S.; Leovac, V. M.; Bjelica, L. J. *J. Serb. Chem. Soc.* **2003**, *68*, 929.

(29) Berkovitch-Yellin, Z.; Leiserowitz, L. *Acta Cryst.* **1984**, *B40*, 159-165.

(30) Steiner, Th. *Cryst. Rev.* **1996**, *6*, 1-57.

(31) Jeffrey, G. A.; Maluszynska, M.; Mitra, J. *Int. J. Biol. Macromol.* **1985**, *7*, 336-348

(32) Zelentsov, V. V. In *Advances in Inorganic Chemistry, 6th ed.*; Spitsyn, V.I., Ed., MIR Publishers 1983; p 122.

(33) (a) Nihei, M.; Shiga, T.; Maeda, Y.; Oshio, H. *Coord. Chem. Rev.* **2007**, *251*, 2606. (b) Oshio, H.; Maeda, Y.; Takashima, Y. *Inorg. Chem.* **1983**, *22*, 2684. (c) Golding, R. M. *Mol. Phys.* **1967**, *12*, 13.

(34) Kennedy, B. J.; Murray, K. S.; Zwack, P. R.; Homborg, H.; Kalz, W. *Inorg. Chem.* **1986**, *25*, 2539.

(35) (a) Timken, M. D.; Hendrickson, D. N.; Sinn, E. *Inorg. Chem.* **1985**, *24*, 3947. (b) Shongwe, M. S.; Al-Rashdi, B. A.; Adams, H.; Morris, M. J.; Mikuriya, M.; Hearne, G. R. *Inorg. Chem.* **2007**, *46*, 9558.

(36) Hayami, S.; Gu, Z. Z.; Yoshiki, H.; Fujishima, A.; Sato, O. *J. Am. Chem. Soc.* **2001**, *123*, 11644.

(37) Hogg, R.; Wilkins, R. G. *J. Chem. Soc.* **1962**, 341.

(38) Sylva, R. N.; Goodwin, H. A. *Aust. J. Chem.* **1967**, *20*, 479.

(39) (a) Renovitch, G. A.; Baker, W. A. *J. Am. Chem. Soc.* **1967**, 89, 6377. (b) Sorai, M.; Ensling, J.; Gütlich, P. *Chem. Phys.* **1976**, *18*, 199. (c) Spiering, H.; Meissner, E.; Köppen, H.; Müller, E.W.; Gütlich, P. *Chem. Phys.* **1982**, *68*, 65.

(40) (a) Giménez-López, M. C.; Clemente-León, M.; Coronado, E.; Romero, F. M.; Shova, S.; Tuchages, J.-P. *Eur. J. Inorg. Chem.* **2005**, 2783-2787. (b) Clemente-León, M.; Coronado, E.; Giménez-López, M. C.; Romero, F. M. *Inorg. Chem.* **2007**, *46*, 11266.

(41) Greenaway, A. M.; Sinn, E. *J. Am. Chem. Soc.* **1978**, *100*, 8080.

(42) Sugiyarto, K. H.; Craig, D. C.; Rae, A. D.; Goodwin, H. A. *Aust. J. Chem.* **1993**, *46*, 1269.

(43) (a) Tanabe, Y.; Sugano, S. *J. Phys. Soc. Jpn.* **1954**, *9*, 753. (b) Tanabe, Y.; Sugano, S. *J. Phys. Soc. Jpn.* **1954**, *9*, 766.

Chapter V

Thermal and Optical Switching of the Spin State in $[Fe(bpp2)_2](ClO_4)_2 \cdot MeCN$ System [bpp2 = 2,6-bis(pyrazol-1-yl)-pyrazine]

Synopsis

The spin-crossover compound $[Fe(bpp2)_2](ClO_4)_2 \cdot MeCN$ shows spin-transition properties, independently induced by temperature and light, with hysteretic thermal transitions at $T_{1/2}\uparrow$ = 231 K and $T_{1/2}\downarrow$ = 221 K, respectively, setting an hysteresis width ΔT of 10 K. Examination of the photomagnetic behavior of single crystals under continuous wave (λ = 530 nm) irradiation demonstrates the occurrence of both Light-Induced Excited Spin State Trapping (LIESST) and Light Induced Thermal Hysteresis (LITH) phenomena in this material. Besides, a thermochromic effect in the crystal is observed, with the crystals becoming darker on going from the high- to the low-spin state.

5.1 Introduction

Magnetic molecules are a new class of fascinating materials with great potential for information storage and data processing.[1-4] Systems exhibiting physical bistability that is reversibly tuneable by external perturbations can be obtained from octahedral transition metal complexes with $[Ar]3d^4–3d^7$ electronic configuration. For instance, when the energy difference between the high-spin and low-spin states is of the order of magnitude of the thermal energy (k_BT), a temperature modification can cause a transfer of electron between the highest suborbital (e_g) and the lowest suborbital (t_{2g}) by changing its spin direction. The so-called spin-crossover solids are text-book examples of inorganic systems that are (well)-known to exhibit light-induced spin-state switching phenomena under the influence of laser light of an appropriate wavelength. The most extensively studied SCO compounds by photo-irradiation are iron(II)-based complexes. In many cases, the resulting light-induced states are comparatively long-lived. This phenomenon is known as the LIESST effect (Light-Induced Excited Spin State Trapping).[5] The photoexcitation process involves, either a metal to ligand charge transfer, or d-d transitions. For typical Fe^{2+} compound ($[Fe(ptz)_6](BF_4)_2$), absorption bands for the LS→HS process are located around ~300 nm (Metal Ligand Charge Transfer) and, 500 and 550 nm (d-d) respectively.[6] The reverse process (HS→LS) occurs by irradiation at ~830 nm, albeit with low photoefficiency, due to branching ratio of 4:1 for the direct and return processes, respectively.[7] The switching of such compounds proceeds through excited states; the population mechanism of quintet state after irradiation into the MLCT band in the case with pyridine type ligands has been identified as a simple $^1MLCT→^3MLCT→^5T$ cascade from the initially excited state.[8] For irradiation into the d-d bands, the mechanism is not fully established yet. Besides, there is indirect evidence from quantum yield determinations that the low-lying triplet d-d states play a role. Light irradiation has proven extremely useful in the study of such processes.[8-12]

Previously, Money *et al*. investigated the crystal structures of the spin crossover systems, $[Fe(C_{10}H_8N_6)_2](BF_4)_2$ and $[Fe(C_{10}H_8N_6)_2](ClO_4)_2$, and their temperature dependences using X-ray powder diffraction techniques.[13-15] Their results indicate that these compounds crystallize into phases that can be closely approximated by a simple monoclinic structure with a doubling of the crystallographic *a* axis, on undergoing the spin transition. Such structural changes would significantly alter the thermodynamics of the LIESST relaxation, if it could be generated by photoexcitation.[16] Moreover, the

compounds were reported to exhibit the LIESST phenomenon quantitatively; forming long-lived trapped HS states at cryogenic temperatures.[17] The thermal stability of these trapped states closely follows an empirical linear relation (between the thermal spin transition temperature, $T_{1/2}$, and the thermal stability of the photochemically generated high-spin state, T(LIESST)) that had been proposed earlier for iron(II) complexes of tridentate nitrogen-donor ligands.[18] By elucidating the relationship between the chemical structure of a LIESST complex, and the lifetime of its photogenerated excited state, one may ultimately be able to design and tune these photoswitchable compounds to allow for higher operating temperatures.[19] With the objective to clarify these structural features seen in the powder samples suitable for phase change, we attempted to isolate single crystals out of the reported complexes. Though our effort leads us to the solvated species, $[Fe^{II}(bpp2)_2](ClO_4)_2 \cdot MeCN$, the interesting results discussed herein provide a detailed account of our investigation. We show how optical and structural studies could be combined to elucidate the origin of the complex behavior of the title compound.

5.2 Results and Discussion

5.2.1 Structural Description[1]

The crystallographic structure of the title compound was solved in both the high-spin (293 K) and low-spin (100 K) states. The temperature was raised to 293 K after measurement at 100 K of the previous crystal, but at this temperature, the sample gives smeared reflections spots, so another crystal was searched. Upon lowering the temperature, the structural parameters changed, but no modification of the structure type was observed. The space group $P2_1/c$ was found to be identical in both the high-spin (HS) and low-spin (LS) states, though the lattice parameters varied noticeably (Table 5.1). Selected bond lengths and angles are summarized in Table 5.2.

The iron(II) ion has a distorted octahedral geometry and is bound equatorially to two ligands through three of the ligand's six N donor sets, similar to the coordination environment in $[Fe(C_{10}H_8N_6)_2](BF_4)_2 \cdot 3CH_3NO_2$, $[Fe(C_{10}H_8N_6)_2](BF_4)_2$ and $[Fe(C_{10}H_8N_6)_2](ClO_4)_2$.[13-15] The asymmetric unit consists of four moieties: a cationic Fe-complex, two perchlorate anions and an acetonitrile solvate molecule.

[1] See chapter 2 for details on the experimental procedures and recipes for the compound presented in this chapter

Table 5.1 Crystal Data and Refinement Details of the Structure Determination of $[Fe(bpp2)_2](ClO_4)_2 \cdot CH_3CN$ at 100 and 293 K

Formula	$C_{22}H_{19}Cl_2FeN_{13}O_8$	$C_{22}H_{19}Cl_2FeN_{13}O_8$
Formula weight ($g.mol^{-1}$)	720.23	720.23
Crystal system	monoclinic	monoclinic
Space group	$P2_1/c$	$P2_1/c$
Crystal colour	brown	brown
Crystal description	parallelepiped	parallelepiped
Crystal dimensions (mm)	0.44 x 0.37 x 0.19	0.52 x 0.47 x 0.29
a, (Å)	17.364(4)	17.05(2)
b, (Å)	16.626(4)	16.92(2)
c, (Å)	9.789(3)	10.206(13)
β, (deg)	102.190(4)	100.565(18)
Volume ($Å^3$)	2762.3(13)	2901(6)
Z	4	4
D_{calc} ($g.cm^{-3}$)	1.732	1.649
Temperature (K)	100(1)	293(1)
Radiation (Å)	0.71073	0.71073
μ (Mo Kα) (cm^{-1})	8.15	7.76
F(000)	1464	1464
Number of unique data	5429	5470
Number of data with $[F_o \geq 4.0\ \sigma\ (F_o)]$	3440	2854
$R(F)$[a]	0.0427	0.0576
$wR(F^2)$[b]	0.1099	0.1842
GOF on F^2	0.970	0.932
$\Delta_\rho max$, $\Delta_\rho min$ / $e.Å^{-3}$	-0.50, 0.61(10)	-0.56, 0.44(9)

[a] $R(F) = \sum (||F_o| - |F_c||) / \sum |F_o|$ for $F_o > 4.0\ \sigma\ (F_o)$ for observed reflections.

[b] $wR(F^2) = [\sum [w(F_o^2 - F_c^2)^2] / \sum [w(F_o^2)^2]]^{1/2}$ for all data.

A perspective view of the molecular compound and its packing arrangement in the HS state (293 K) is displayed in Figure 5.1. The Fe–N bond lengths in the crystal at 293 K are consistent with a high-spin Fe(II) ion, lying within the range 2.121(4) – 2.209(4) Å. In contrast at 100 K, the Fe–N bond lengths have shortened to 1.893(3) – 2.010(3) Å, and are characteristic of a low-spin Fe(II) centre.[20-22] The difference between the average Fe–N distances at 293 and 100 K is 0.208(7) Å, which is a typical value for a spin-state transition involving an Fe(II) complex with a hexa-nitrogen donor set.[23,24] There are four coordination bonds from N atoms in the pyrazole rings and two from N atoms in the pyrazine rings. The largest extent of changes in the Fe–N{pyrazine} bond elongations suggests that the pyrazine is a stronger π-acceptor than the pyrazole. In addition, the 12 angles subtended at the metal ion by adjacent donor atoms lie in the

range 73 – 122^{o} in the predominantly high spin state, whereas these are closer to regular octahedral values (80 – 106^{o}) in the low spin form.

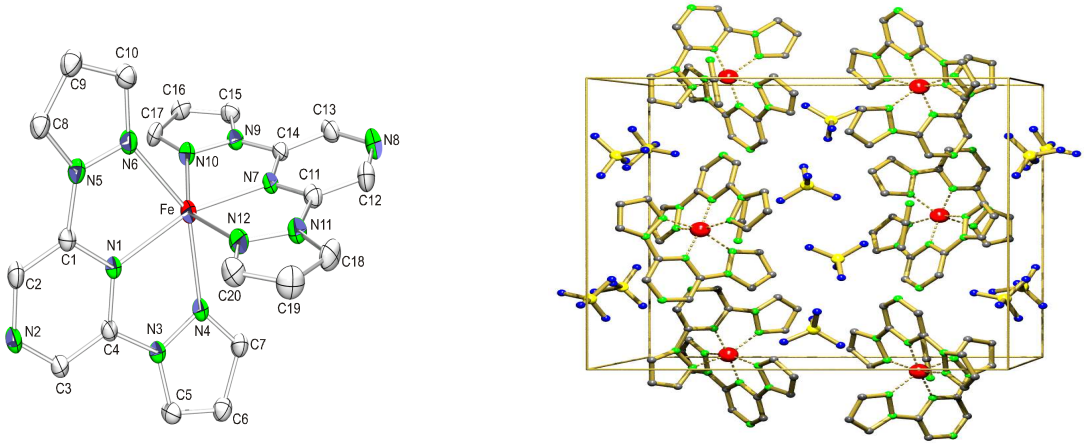

Figure 5.1. A perspective view (ORTEP drawing) of $[Fe(bpp2)_2](ClO_4)_2 \cdot CH_3CN$ complex at 293 K, with atom labeling and packing arrangement of the unit cell. Atoms are represented by thermal ellipsoids with 20% probability level. Hydogen atoms, acetonitrile molecule, and perchlorate anions are omitted for clarity.

From the packing diagram, it appears that the molecules are arranged in a parallel form to make a chain and the chain is supported by the offset, slipped π stacking interactions between the bpp2, *i.e.*, a pyrazole of one moiety and a pyrazine ring of the other neighbouring one (Figure 5.1). The distances of the nearest neighbours at 293 K (3.291 Å) being a little longer as compared with those at 100 K (3.216 Å). This stacking mode between the bpp2 is contrast to the face to face manner as found in $[\{Cu(\mu\text{-bpypz})(CH_3OH)_2\}_2]Cl_2 \cdot H_2O$ system,[25] and also different from that of the Cr–Fe complex[26] where there are the pyridyl–pyridyl as well as the pyrazolate(CH)–pyrazolate(CH) π stacking interactions. It is worth mentioning that the presence of acetonitrile solvate molecules in the crystal lattice has had no or very little effect on the stiffness of the cage complex or the twisting motion between the ligand around the metal atom. The relative ligand field strengths at the Fe ion in the high- and low-spin forms can be estimated from the crystallographic data using equation (5.1), where r_{HS} and r_{LS} are respectively, the average Fe–N bond lengths in the high-spin and low-spin forms of the complex.[24]

$$\frac{10Dq^{LS}}{10Dq^{HS}} = \left(\frac{r_{HS}}{r_{LS}} \right)^6 \tag{5.1}$$

From the X-ray data at 293 and 100 K, this equation gives a ratio of 1.84(1), which is substantially greater than the value of 1.74 that is typically observed for spin crossover compounds.[24] Deviations from this anticipated value may arise if a sample contains mixtures of HS and LS Fe ions at the temperatures examined.[27] This is believed not to be the case here, since the magnetic measurements described below demonstrate that at both temperatures essentially all Fe ions in the sample are in the same spin-state.[28] We therefore suggest that this anomalous ratio might reflect the strongly axial nature of the coordination sphere in the complex, so that the averaged Fe-N bond lengths do not provide an accurate description of 10*Dq*.

Table 5.2 Selected Bond Lengths (Å) and Bond Angles (deg) for $[Fe(bpp2)_2](ClO_4)_2 \cdot CH_3CN$ at 100 and 293 K. Standard deviations in the last decimal place are given in parentheses.

	100 K	293 K		100 K	293 K
Fe – N1	1.893(3)	2.121(4)	N1 – Fe – N4	79.91(12)	72.86(13)
Fe – N4	1.984(3)	2.209(4)	N1 – Fe – N7	174.03(13)	164.35(13)
Fe – N6	2.010(3)	2.181(4)	N1 – Fe – N10	100.45(12)	110.74(13)
Fe – N7	1.900(3)	2.122(4)	N4 – Fe – N6	159.35(11)	146.12(13)
Fe – N10	1.984(3)	2.178(5)	N4 – Fe – N10	92.61(12)	97.57(13)
Fe – N12	1.978(3)	2.186(5)	N6 – Fe – N7	106.52(12)	122.02(13)

5.2.2 Magnetic and Thermal Properties

Magnetic Measurements. The magnetic behavior of $[Fe^{II}(bpp2)_2](ClO_4)_2 \cdot MeCN$ is shown in Figure 5.2a and expressed in the form of a $\chi_m T$ versus T curve, where χ_m stands for the molar magnetic susceptibility and T the temperature. At room temperature, $\chi_m T$ is equal to 3.41 cm^3 K mol^{-1}, which is in the range of values expected for HS Fe^{II} ions, and below 200 K it is in the range of LS Fe^{II} ions. The transition is of first-order nature, with a 10 K wide thermal hysteresis: $T_{1/2}\downarrow$ = 221 K, $T_{1/2}\uparrow$ = 231 K, with the latter in good agreement with X-ray data. The steep and narrow hysteresis loop confirms the presence of cooperative interactions in a well-crystallized system. The effect of acetonitrile solvent molecules on the crystal field energy is likely to be responsible for the slightly high transition temperature and wide thermal hysteresis of the title compound.

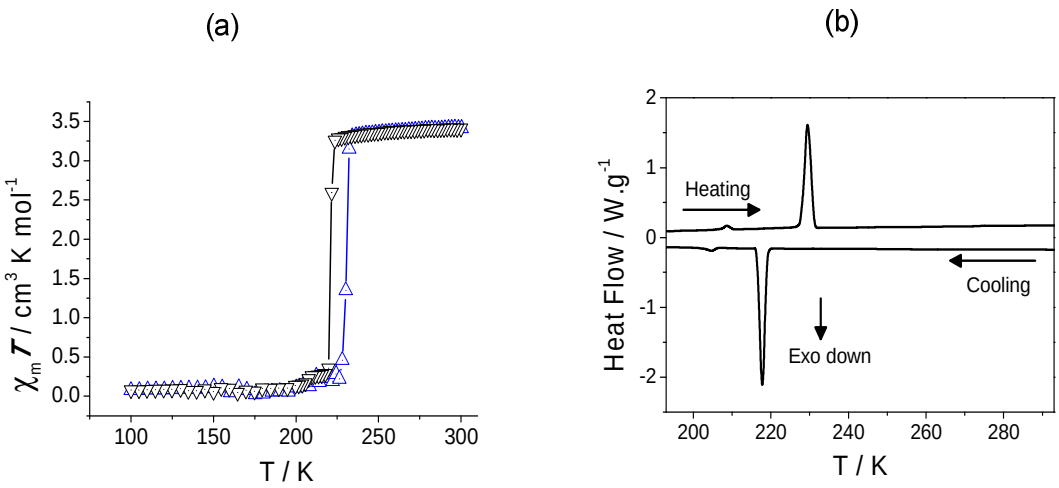

Figure 5.2. Temperature dependence of: (a) the molar magnetic susceptibility ($\chi_m T$) for $[Fe(bpp2)_2](ClO_4)_2 \cdot CH_3CN$, as obtained in successive warming (Δ) and cooling (∇) runs; and (b) the corresponding heat flow curves, obtained through differential scanning calorimetry. Heating and cooling branches are represented by full lines respectively.

Table 5.3 Molar Experimental Heat Capacities for $[Fe(bpp2)_2](ClO_4)_2 \cdot CH_3CN$

T (K)	C_p (J mol^{-1} K^{-1})
193.18	509.92
203.16	553.43
213.16	573.81
223.16	596.99
233.16	595.77
243.16	609.39
253.16	622.93
273.16	652.02
283.16	670.53
293.16	688.54
303.16	707.91
313.16	723.83
323.16	743.28

DSC Measurements. The Differential Scanning Calorimetric (DSC) measurements carried out in the 188-293 K temperature range, basically confirm the magnetic investigation (see above). For the title compound, a smooth line has been interpolated from the values in the normal regions, below 225 K and above 232 K. The heat capacity due to the transition has been deduced after subtraction of this baseline. The extracted temperature dependence of the molar heat capacity, C_p, in the warming and cooling

directions, respectively, for $[Fe^{II}(bpp2)_2](ClO_4)_2 \cdot MeCN$ are given in Table 5.3. $T_c\uparrow$ and $T_c\downarrow$ were determined as the temperatures for which $\partial C_p/\partial T$ is maximum and found as $T_c\downarrow$ = 218 K and $T_c\uparrow$ = 229 K. These values are in good agreement with those extracted from the $\chi_m T$ vs T plots: $T_{1/2}\downarrow$ = 221 K and $T_{1/2}\uparrow$= 231 K, discrepancies occur presumably as a result of a thermal lag of the device. These calorimetric results also confirm the presence of hysteresis with a width of 11 K. Estimates of the molar enthalpy and entropy changes associated with the thermal spin transition (based on DSC curves), yielded: ΔH = [(10.8 – 11.3) ± 0.3] kJ mol^{-1} and ΔS = [(46.9 – 51.7) ± 1.3] J mol^{-1} K^{-1} in the heating and cooling modes, respectively.

This experimental entropy change (ΔS) is significantly larger than the expected entropy variation resulting from the change in spin only value ($\Delta S = R\ln[(2S_{HS} + 1)/(2S_{LS} + 1)] = 13.4$ J mol^{-1} K^{-1} for $S_{HS} = 2$ and $S_{LS} = 0$). The excess of entropy corresponds mainly to the changes associated with the intramolecular Fe – N bond lengths, *ca*. 0.208 Å shorter in the LS than in the HS state. The longer bond lengths of the HS state decrease the interatomic force constants, thereby reducing the corresponding vibrational frequencies. As a result, the number of excited vibrational states experience an abrupt jump with the lattice expansion. However, both thermodynamic quantities are significantly lower than the values obtained by DSC measurements on the non-solvated powder samples of $[Fe(C_{10}H_8N_6)_2](ClO_4)_2$,[14] indicating that the presence of acetonitrile molecules in the crystal lattice, has contributed to decrease the thermodynamic parameters associated with spin state conversion.

5.2.3 Mössbauer Data

^{57}Fe Mössbauer Spectra of $[Fe^{II}(bpp2)_2](ClO_4)_2 \cdot MeCN$ appear in Figure 5.3. At RT the spectrum of this compound seems to be composed of three different quadrupole split (QS) contributions with relatively high QS values, namely Q1, Q2 and Q3. As the temperature decreases however, a quadrupole split component with lower QS values (Q4) starts to appear on the left (lower velocity) branches of the quadrupole split spectra. This component increases its absorption area at the expense of the absorption areas of two (Q1 and Q2) of the three major components observed at RT and becomes dominant at 225 K.

The spectra at all temperatures have quite symmetric quadrupole split absorption lines. Thus in order to fit the spectra of $[Fe^{II}(bpp2)_2](ClO_4)_2 \cdot MeCN$ adequately, we used a set of four different quadrupole split components for measuring temperatures between

300 K and 225 K. The resulting Mössbauer parameters, listed in Table 5.4, indicate that the components Q1, Q2 and Q3 are characterized as Fe^{II} high spin (S=2) states, while component Q4 has quite lower isomer shift (IS) and QS values than those of the other three components. Taking into account the fact that this component has resulted at the expense of the Q1 and Q2 components, we can conclude that it corresponds to an Fe^{II} low spin (S=0) state and that the $[Fe^{II}(bpp2)_2](ClO_4)_2 \cdot MeCN$ compound undergoes a high spin to low spin transition around T_{ST} = 225 K.

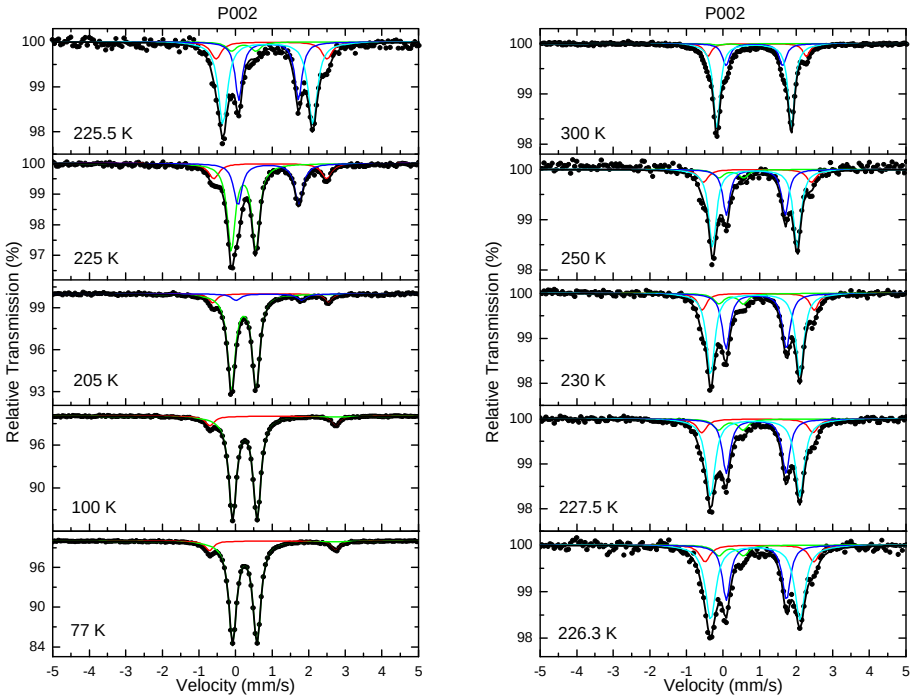

Figure 5.3. ^{57}Fe Mössbauer spectra of $[Fe(bpp2)_2](ClO_4)_2 \cdot CH_3CN$ obtained in the warming mode, after rapid quenching of the sample at 77 K. The colored solid lines represent the quadrupole split components used to fit the spectra: Q4-green, Q3-red, Q2-blue and Q1-aquamarine.

This is confirmed also by the magnetic susceptibility measurements where the $\chi_m T$ values decrease abruptly, from about 3.41 cm^3 K mol^{-1} for temperatures above 225 K, to about 0.10 cm^3 K mol^{-1} below that temperature. However, one would expect the susceptibility to reach low values even closer to zero, as the low spin Fe^{II} state possesses no spin moment. The relatively high value of $\chi_m T$ at this temperature region suggests the presence of another source of spin moment in the sample. In addition a small hysteresis is observed between the ZFC and FC branches indicating the presence of some magnetic interactions between the iron centers.

Table 5.4 ^{57}Fe Mössbauer Spectral Parameters for $[Fe(bpp2)_2](ClO_4)_2 \cdot CH_3CN$, with QS, the quadrupole splitting, IS, the isomer shift (relative to metallic iron at room temperature), Γ/2, the half line-width and Area, the relative absorption area for each component.

T (K)	Component	IS (mm s^{-1})	Γ/2 (mm s^{-1})	QS (mm s^{-1})	Area (%)
300	Q1	0.95	0.11	2.04	68
	Q2	0.96	0.12	1.54	19
	Q3	1.04	0.12	2.69	11
	Q4	0.29	0.16	0.67	2
250	Q1	0.98	0.12	2.32	53
	Q2	1.00	0.12	1.61	29
	Q3	1.04	0.16	2.96	11
	Q4	0.33	0.16	0.67	7
230	Q1	0.99	0.13	2.44	49
	Q2	1.01	0.13	1.65	33
	Q3	1.07	0.14	3.07	11
	Q4	0.33	0.16	0.67	7
227.5	Q1	0.98	0.15	2.45	51
	Q2	1.01	0.13	1.64	31
	Q3	1.05	0.16	3.05	10
	Q4	0.32	0.16	0.67	8
226.3	Q1	0.99	0.17	2.45	52
	Q2	1.02	0.13	1.65	29
	Q3	1.10	0.17	2.98	12
	Q4	0.33	0.16	0.67	7
225.5	Q1	0.99	0.15	2.46	52
	Q2	1.01	0.12	1.63	30
	Q3	1.09	0.17	3.04	12
	Q4	0.33	0.16	0.67	6
225	Q2	1.00	0.14	1.67	29
	Q3	1.05	0.17	3.09	14
	Q4	0.32	0.13	0.67	57
205	Q2	1.00	0.13	1.71	4
	Q3	1.06	0.13	3.14	7
	Q4	0.33	0.13	0.68	89
100	Q3	1.13	0.14	3.45	10
	Q4	0.36	0.12	0.67	90
77	Q3	1.12	0.13	3.45	9
	Q4	0.36	0.13	0.66	91

An important characteristic of all Mössbauer spectra is the relatively stable absorption area value observed for the Q3 component, which seems to be unaffected by the major changes taking place in the other part of the Mössbauer spectra. The IS values of this component correspond to a Fe^{II} high spin (S=2) state but show only the expected variation, with respect to temperature, due to the second order Doppler shift effect.[29] This indicates that this component does not experience a high spin to low spin transition, but probably corresponds to a different secondary phase present in the sample and not to a different iron site of the $[Fe^{II}(bpp2)_2](ClO_4)_2 \cdot MeCN$ system. The presence of this phase, containing high spin Fe^{II} states, is probably responsible for the increased magnetic susceptibility $\chi_m T$ levels found for this sample at low temperatures.

5.2.4 Solid-State Absorption Spectroscopy

The compound shows an obvious change of colour on cooling from yellow to dark-brown when undergoing the transition. Thus, a solid-state absorption spectrum was measured at room temperature (293 K). As can be observed from Figure 5.4, the spectrum shows two weak shoulders at around 313 nm and about 435 nm. These bands are assigned to metal-ligand charge transfer (MLCT) transitions and are responsible for the colour of the compound in its high-spin state. This spectrum also shows a relatively weak band at around 975 nm that can be assigned to the $^5T_{2g} \rightarrow {}^5E_g$ transition, characteristic of the high-spin state.

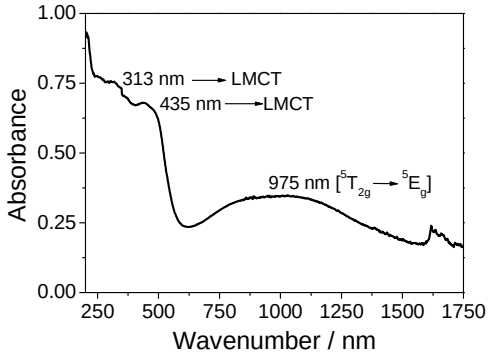

Figure 5.4. UV-Vis spectra of $[Fe(bpp2)_2](ClO_4)_2 \cdot CH_3CN$ at room temperature.

The ligand field parameter can be derived as $10Dq^{HS}$ = 10256 cm^{-1}, which is in the range of values commonly observed for a high-spin compound.[24] On basis of the conditions mentioned before, and considering from X-ray crystal structure determination

that for this Fe^{II} ion the $\Delta r = r_{HS}-r_{LS} \sim 0.208$ Å is found, thus the ligand field parameter for the low-spin state can be inferred from equation (5.1) as: $10Dq^{LS} = 18872$ cm^{-1}, a value expected for a spin-transition compound.[24] It is clear that the range in $10Dq$ over which a spin crossover may occur is rather narrow and should be close to the crossover point of the Tanabe-Sugano diagram.[30] This explains why minor changes in coordination environment or even in the crystal lattice, allow or hinder the spin transition.[24]

5.2.5 Photomagnetic Properties

The photomagnetic behaviour of the single crystalline material is depicted in Figure 5.5. As evidenced by the open circles in panel (a), the material exhibits the LIESST effect[31,32] at 10 K upon irradiation with 530 nm light. Under constant irradiation, the magnetic $\chi_m T$ value saturates at approximately 2.25 cm^3 K mol^{-1}. Subsequent slow heating of the material at a rate of 0.3 K min^{-1} increases the measured $\chi_m T$, which reaches a plateau value of about 3.1 cm^3 K mol^{-1}, indicating a full photo-conversion to the metastable HS state. The observed increase of the magnetic signal at these low temperatures is attributed to the zero-field splitting of the HS Fe(II) ion.[17] Upon further heating, the induced metastable HS state is found to relax back to the LS ground state at T(LIESST) = 90 K, as evidenced by the vanishing of the magnetic signal. The relaxation temperature of the light induced high spin state was established by the corresponding feature in the $\partial\chi_M T/\partial T$ versus T curve (inset Figure 5.5a). The steepness of the relaxation transition confirms the role of cooperative effects in the photomagnetic process. Now in the LS ground state, the material exhibits the hysteretic thermal spin transition upon thermal cycling, reproducing the curve obtained earlier using conventional SQUID magnetometry (Figure 5.2a). In comparison to the previously studied, unsolvated powder material,[17] for which $T_{1/2}\uparrow$ = 203 K, $T_{1/2}\downarrow$ = 199 K and T(LIESST) = 100 K, the crystalline material exhibits a larger hysteresis width, indicating a stronger cooperativity in the solvated crystal. Additionally, in the crystal the thermal spin transition occurs at a higher temperature, while the relaxation temperature of the LIESST state is lower. This expected correlation between an upshift of the thermal spin transition and a simultaneous downshift of T(LIESST) was also previously observed in a series of Fe(II) spin crossover compounds containing 2,6-di(pyrazol-1-yl)pyrazine-like ligands.[17]

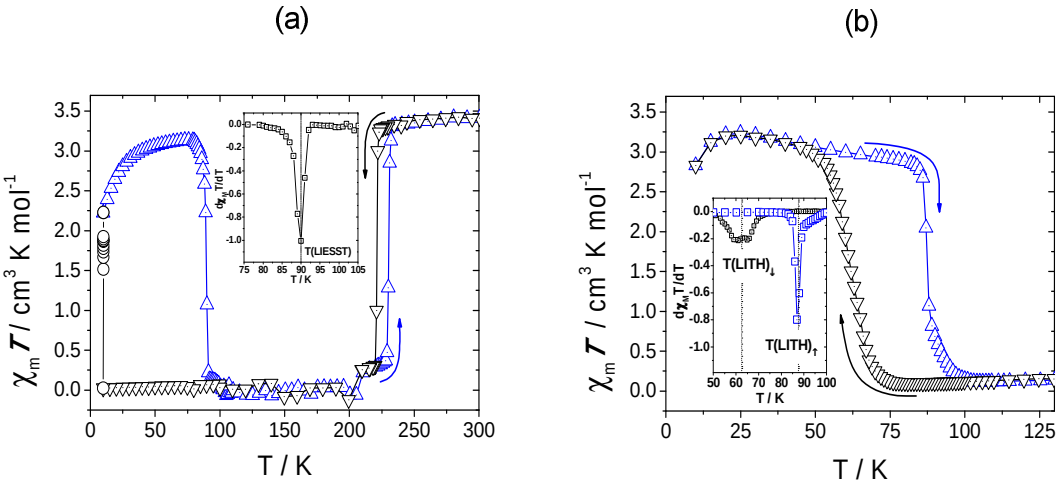

Figure 5.5. Photomagnetic behavior of single crystalline $[Fe(bpp2)_2](ClO_4)_2 \cdot CH_3CN$. (a) LIESST experiment and subsequent thermal cycling. Open circles (○) denote data recorded under constant 530 nm irradiation at 10 K; solid triangles represent data recorded in subsequent heating (Δ) and cooling (∇) modes. The inset shows the derivative of $\chi_m T$ w.r.t. T of the data recorded in the heating run. (b) LITH experiment; All data are recorded under constant 530 nm irradiation. Solid triangles represent data recorded in subsequent cooling (∇) and heating (Δ) modes. Correspondingly, the inset shows the derivative of $\chi_m T$ w.r.t. T of the data from both runs.

Figure 5.5b shows the photomagnetic properties of the crystalline material under constant irradiation. In the so-called Light-Induced Thermal Hysteresis (LITH) experiment, the material is thermally cycled (cooling, then heating) under constant irradiation (530 nm) while its magnetism is monitored.[33] Due to the two competing processes in the material; the photo-excitation prompting the LS to HS conversion (LIESST) on the one hand and the temperature dependent self-accelerated relaxation inducing the opposite transition on the other, the system's magnetic behavior is governed by their relative temperature dependences. At 130 K, all Fe(II) ions are in the LS state, after having undergone the thermal spin transition. Upon subsequent cooldown, the strongly temperature dependent rate of relaxation from the photo-induced metastable HS state becomes progressively smaller. Because the competing rate of LS to HS conversion is relatively temperature independent under constant irradiation, one observes a crossover of regimes; at high temperatures (above ~100 K) the relaxation is dominant, and the system is in the LS ground state, while at low temperatures (below ~ 40 K) the photo-conversion is the most efficient, converting the system to the HS state. In the intermediate temperature region, the two processes are comparable in conversion efficiency. In both in the heating and cooling mode, the cooperativity of the system (the self-acceleration of the HS relaxation)

causes a persistence of the initial state when crossing this intermediate region, which thus induces a thermal hysteresis of approximately 25 K width for single crystalline $[Fe(bpp2)_2](ClO_4)_2 \cdot CH_3CN$. The slightly lower value of $T(\text{LITH})\downarrow$ with respect to T(LIESST) is attributed to a small light-induced heating of the sample during the LITH experiment.

The experimental T(LIESST) value recorded for the title compound may be compared with those previously obtained for other meridional tridentate ligands.[34] It has been shown that a linear correlation between the thermal spin crossover temperature and T(LIESST) holds generally for iron(II) complexes.[35] In particular, for the $[Fe(bpp)_2]X_2$ family,[36] the two physical quantities may be related by the formula: $T(\text{LIESST}) = T_0 - 0.3T_{1/2}$, with T_0 = 150 K. $[Fe^{II}(bpp2)_2](ClO_4)_2 \cdot$MeCN exhibits a thermal spin transition with a hysteretic behavior centered at: $T_{1/2}\uparrow$ = 231 K and $T_{1/2}\downarrow$ = 221 K. Taking $T_{1/2}$ as the mean value of $T_{1/2}\uparrow$ and $T_{1/2}\downarrow$, T(LIESST) of 82 K is expected, in reasonable agreement with the experimental value.

5.3 Concluding Remarks

The spin state switching in $[Fe^{II}(bpp2)_2](ClO_4)_2 \cdot$MeCN, may be considered as being intrinsic. As a matter of fact, it is not triggered by a structural phase transition. The decrease in unit cell volume is about 4.8 %. The lattice parameters contract about 4 % for the *c* axis and by 2 % for the *a* and *b* axis, on going the HS↔LS conversion. The strong cooperativity of the compound is achieved by using intermolecular π stacking interactions as suggested from the single crystal X-ray analysis. This study has established a transition enthalpy and entropy value of (10.8 ± 0.3) kJ mol^{-1} and (46.9 ± 1.3) J $K^{-1}mol^{-1}$ respectively, and are the lowest ever found for iron(II) complexes of 2,6-bis(pyrazol-1-yl)pyridine and its derivatives. We show that the photomagnetic properties originate within the thermal spin crossover history. The optical irradiation of the LS state gives access to a metastable state with a long-lived lifetime. T(LIESST) = 90 K, which is the temperature above which the photomagnetic effect is erased by thermal relaxation. The nature of the photoinduced HS states is illustrated too by the measurements of the LITH loop, under irradiation below T(LIESST). We also found that changes outside the coordination sphere, *i.e.*, intermolecular cooperativity, identity of the counter anion and solvent molecules, result in only small perturbations to the T(LIESST).

5.4 References

(1) (a) Hollingsworth, *Science* **2002**, *295*, 2410. (b) Janiak, C. *J. Chem. Soc., Dalton Trans.* **2003**, 2781.

(2) Gütlich, P.; Garcia, Y.; Woike, T. Photoswitchable Coordination Compounds. *Coord. Chem. Rev*. **2001**, *219-221*, 839-879.

(3) (a) Kahn, O. *Acc. Chem. Res*. **2000**, *33*, 647. (b) Kahn, O.; Martinez, C. J. *Science* **1998**, *279*, 44. (c) Cambi, L.; Szego, L. *Ber. Dtsch. Chem. Ges*. **1931**, *64*, 2591.

(4) O'Connor, C. J. in: Coronado, et al. (Eds.), *Molecular Magnetism*: From Molecular Assemblies to the Devices, 1996, p. 521.

(5) Hauser, A. *Top. Curr. Chem.* **2004**, *234*, 155 and references therein.

(6) (a) Hauser, A. *Chem Phys. Lett*. **1986**, *124*, 543. (b) Hauser, A. *J. Chem. Phys*. **1991**, *94*, 2741.

(7) Decurtins, S.; Gütlich, P.; Hasselbach, M. K.; Spiering, H.; Hauser, A. *Inorg. Chem.* **1985**, *24*, 2174.

(8) Bressler, C.; Milne, C.; Pham, V.-T.; ElNahhas, A.; van der Veen, R. M.; Gawelda, W.; Johnson, S.; Beaud, P.; Grolimund, D.; Kaiser, M.; Borca, C. N.; Ingold, G.; Abela, R.; Chergui. M. *Science* **2009**, *323*, 489.

(9) (a) McCusker, J. K.; Walda, K. N.; Dum, R. C.; Simon, J. D.; Magde, D.; Hendrickson, D. N. *J. Am. Chem. Soc.* **1993**, *115*, 298. (b) Monat, J. E.; McCusker, J. K. *J. Am. Chem. Soc.* **2000**, *122*, 4092.

(10) Gawelda, W.; Cannizzo, A.; Pham, V.-T.; van Mourik, F.; Bressler, C.; Chergui, M. *J. Am. Chem. Soc.* **2007**, *129*, 8199.

(11) Brady, C.; McGarvey, J. J.; McCusker, J. K.; Toftlund H.; Hendrickson, D. N. *Top. Curr. Chem.* **2004**, *235*, 1.

(12) (a) Vankó, G.; Neisius, T.; Molnár, G.; Renz, F.; Kárpáti, S.; Shukla, A.; Groot, F. M. F. de. *J. Phys. Chem.* **2006**, *B 110*, 11647. (b) Vankó, G.; Renz, F.; Molnár, G.; Neisius, T.; Kárpáti, S. *Angew. Chem. Int. Ed.* **2007**, *46*, 5306

(13) Money, A. M.; Evans, R. I.; Elhaïk, J.; Halcrow, A. M.; Howard, A. K. J. *Acta Cryst.* **2004**, *B70*, 41.

(14) Elhaïk, J.; Money, V. A.; Barrett, S. A.; Kilner, C. A.; Evans, I. R.; Halcrow, M. A. *Dalton Trans.* **2003**, 2053.

(15) Pritchard, R.; Kilner, C. A.; Halcrow, M. A. *Chem. Commun.* **2007**, 577.

(16) (a) Buchen, Th.; Schollmeyer, D.; Gütlich, P. *Inorg. Chem.* **1996**, *35*, 155-161. (b) Létard, J.-F. ; Guionneau, P.; Nguyen, O.; Costa, J. S. ; Marcen, S.; Chastanet, G.; Marchivie, M.; Capes, L. *Chem. Eur. J*. **2005**, *11*, 4582.

(17) Money, V. A.; Costa, J. S.; Marcén, S.; Chastanet, G.; Elhaïk, J.; Halcrow, M. A.; Howard,

J. A. K.; Létard, J.-F. *Chem. Phys. Lett.* **2004**, *391*, 273.

(18) (a) Létard, J.-F.; Capes, L.; Chastanet, G.; Moliner, N.; Létard, S.; Real, J.-A.; Kahn, O. *Chem. Phys. Lett.* **1999**, *313*, 115. (b) Marcén, S.; Lecren, L.; Capes, L.; Goodwin, H. A.; Létard, J. -F. *Chem. Phys. Lett.* **2002**, *358*, 87.

(19) (a) Carbonera, C.; Costa, J. S.; Money, V. A.; Elhaïk, J.; Howard, J. A. K.; Halcrow, M. A.; Létard, J.-F. *Dalton Trans.* **2006**, 3058. (b) Létard, J.-F. *J. Mater. Chem.* **2006**, *16*, 2550.

(20) (a) Sugiyarto, H.; Craig, D. C.; Rae, A. D.; Goodwin, H. A. *Aust. J. Chem.* **1994**, *47*, 869. (b) Sugiyarto, K. H.; Weitzner, K.; Craig, D. C.; Goodwin, H. A. *Aust. J. Chem.* **1997**, *50*, 869. (c) Coronado, E.; Giménez-López, M. C.; Gimenez-Saiz, C.; Martínez-Agudo, J. M.; Romero, F. M. *Polyhedron* **2003**, *22*, 2375. (d) Scudder, M. L.; Craig, D. C.; Goodwin, H. A. *CrystEngComm* **2005**, *7*, 642.

(21) Sugiyarto, K. H.; McHale, W.-A.; Craig, D. C.; Rae, A.D.; Scudder, M. L.; Goodwin, H. A. *Dalton Trans.* **2003**, 2443.

(22) Sugiyarto, K. H.; Scuddler, M. L.; Craig, D. C.; Goodwin, H. A. *Aust. J. Chem.* **2000**, *53*, 755.

(23) König, E. *Prog. Inorg. Chem.* **1987**, *35*, 527.

(24) Gütlich, P.; Hauser A.; Spiering, H. *Angew. Chem., Int. Ed. Engl.* **1994**, *33*, 2024.

(25) Munakata, M.; Wu, P. L.; Yamamoto, M.; Kuroda-Sawa, T.; Maekawa, M.; Kawata, S.; Kitagawa, S. *J. Chem. Soc., Dalton Trans.* **1995**, 4099.

(26) Leita, B. A.; Moubaraki, B.; Murray, K. S.; Smith, J. P.; Cashion, J. D. *Chem. Commun.* **2004**, 156.

(27) Stassen, A. F.; Vos, M. de; van Koningsbruggen, P. J.; Renz, F.; Ensling, J.; Kooijman, H.; Spek, A. L.; Haasnoot, J. G.; Gütlich, P.; Reedijk, J. *Eur. J. Inorg. Chem.* **2000**, 2231.

(28) Holland, J. M.; McAllister, J. A.; Lu, Z.; Kilner, C. A.; Thornton-Pett, M.; Halcrow, M. A. *Chem. Commun*. **2001**, 577.

(29) Greenwood N. N.; Gibb T. C.; *Mössbauer Spectroscopy*; Chapman and Hall, London, United Kingdom, 1971.

(30) (a) Tanabe, Y.; Sugano, S. *J. Phys. Soc. Jpn.* **1954**, *9*, 753. (b) Tanabe, Y.; Sugano, S. *J. Phys. Soc. Jpn.* **1954**, *9*, 766.

(31) Decurtins, S.;Gütlich, P.; Köhler, C. P.; Spiering, H.; Hauser, A. *Chem. Phys. Lett.* **1984**, *105*, 1.

(32) Hauser, A.; Jeftic, J.; Romstedt, H.; Hinek, R.; Spiering, H. *Coord. Chem. Rev.* **1999**, *190-192*, 471-491.

(33) Létard, J.-F.; Guionneau, P.; Rabardel, L.; Howard, J. A. K.; Goeta, A. E.; Chasseau, D.; Kahn, O. *Inorg. Chem.* **1998**, *37*, 4432.

(34) Halcrow, M. A. *Coord. Chem. Rev.* **2005**, *249*, 2880.

(35) (a) Buchen, T.; Gütlich, P.; Sugiyarto, K. H.; Goodwin, H. A.*Chem. Eur. J.* **1996**, *2*, 1134.

(b) Money, V. A.; Carbonera, C.; Elhaïk, J.; Halcrow, M. A.; Howard, J. A. K.; Létard, J.-F. *Chem. Eur. J.* **2007**, *13*, 5503-5514.

(36) Halcrow, M. A. *Polyhedron* **2007**, *26*, 3523-3576.

Chapter VI

Light-Induced Bistability in Fe(III) Spin Transition Compounds of 5X-Salicylaldehyde Thiosemicarbazone [X = H, Cl, Br]

Synopsis

Introduction of strong intermolecular π-π stacking interactions leads to the observation of the LIESST effect even for iron(III) spin-crossover (SCO) compounds. This is a necessary but not sufficient condition to have the high spin metastable state trapped of an iron(III) SCO complex through a photoexcitation process. In fact, three novel iron(III) spin transition compounds of substituted salicylaldehyde thiosemicarbazone ligand, have been designed in which strong cooperativity is achieved by using π stacking interactions and hydrogen bonding networks. Both systems, [Fe(Hth5Clsa)(th5Clsa)]·H_2O and [Fe(Hth5Brsa)(th5Brsa)]·$(H_2O)_{1/2}$, exhibit the LIESST phenomenon, whereas [Fe(Hthsa)(thsa)]·H_2O does not. One of a plausible explanation might be that there is no electron withdrawing group incorporated into the 5-position of salicylaldehyde subunit, responsible for the observation of the LIESST effect.

6.1 Introduction

There has been considerable interest in molecular bistability,[1,2] which means the property of a molecular assembly existing under two stable (or metastable) electronic states in a given range of external parameters (light, temperature, pressure, etc.), for the purpose of its application to electronic devices such as thermal sensors, switching units, and information storage media.[3-10] The first example of spin interconversion by light illumination in solid state was observed in Fe(II) spin-crossover compound, $[Fe(ptz)_6][BF_4]_2$, and this was termed "LIESST" (Light Induced Excited Spin State Trapping).[11,12] Indeed a lot of interesting photomagnetic properties have been reported for few SCO Fe(II) complexes,[13-18] the thermally stable LS state gives rise to the metastable HS state by laser irradiation at 10 K or below. In particularly favourable cases, the metastable spin state of the sample may be stable to thermally activated decay at temperatures up to 120 K.[18-20] In SCO iron(II) and iron(III) complexes, the primary driving force governing the spin state transformation is the entropy increase associated with the LS $\leftrightarrow$ HS conversion. This entropy change can be mainly ascribed to differences in metal-ligand bond lengths.[21] Thus, the average bond distance change for SCO iron(II) compounds is about 0.20 Å,[22-24] while the smaller changes of about 0.13 Å, were observed in SCO Fe(III) compounds.[25-28] Figure 6.1 shows the potential wells of the HS and LS states in typical iron(II) and iron(III) SCO compounds. It is, therefore, presumed that the life-time of the photo-induced excited HS state for iron(III) SCO complexes is shorter than that for Fe(II) SCO complexes, because the small energy barrier between the HS and LS states cannot prevent the relaxation of the metastable HS state back to its ground state in SCO iron(III) complexes.[27,29] Note that the occurrences of a transient HS species of the iron(III) complex was initially reported by Lawthers and McGarvey in solution at relatively high temperatures,[26] however, the resulting light-induced states were comparatively short-lived. Although LIESST is unfavourable in SCO iron(III) systems, introduction of strong intermolecular interactions such as π-stacks and hydrogen bonds afford cooperative spin interconversion with large thermal hysteresis and LIESST effects.[30] The first LIESST phenomenon in solid state for an iron(III) system was provided by $[Fe(pap)_2]ClO_4 \cdot H_2O$.[31] It should be noted that this complex exhibits a frozen in effect, *i.e.*, when the Fe(III) complex is rapidly cooled from room temperature down to 5 K, the high spin state is trapped without the spin transition proceeding from high spin to

low spin.[32,33] Single crystal X-ray structure analysis revealed that $[Fe(pap)_2]ClO_4 \cdot H_2O$ showed large structural changes upon SCO compared with that in typical iron(III) SCO complexes [34] and strong intermolecular π-stacks of aromatic rings in pap–were observed. The large structural change upon SCO and strong intermolecular interactions caused strong cooperativity and abrupt spin transition with hysteresis loop. By irradiating into a LS-state absorption band (~ 550), or in a neighbouring metal-ligand charge transfer band, the molecules are switched to the metastable HS state, which absorbs in the near IR, and the species retain up to about 100 K, suggesting an occurrence of LIESST. $[Fe(pap)_2]PF_6 \cdot MeOH$ also showed temperature driven abrupt spin transition, centered at 288 K, with no hysteresis loop, and LIESST was observed below 55 K.[34,35] Another example of LIESST was reported for $[Fe(pap)_2]BF_4 \cdot H_2O$, and for the diluted phases of composition $[Fe_xAl_{1-x}(pap)_2]ClO_4 \cdot CH_3OH$, (x = 0.25, 0.5) – showed a relatively abrupt spin transition upon SCO.[36]

Although the approach, that is, the introduction of strong molecular distortion enables to trap the photo-induced excited state, is now widely applied in the design of Fe(III) complexes with LIESST effects, however, the general requirements for the observation of LIESST for iron(III) are not yet understood, therefore, we focus on the elucidation of the structural and electronic factors involved for observing this phenomenon. In this respect, $[Fe(Hthsa)(thsa)] \cdot H_2O$ (**7**), $[Fe(Hth5Clsa)(th5Clsa)] \cdot H_2O$ (**8**) and $[Fe(Hth5Brsa)(th5Brsa)] \cdot (H_2O)_{1/2}$ (**9**), are designed in which cooperative spin crossover – and an associated expected photo-physical behaviour – are attained by using 5X–salicylaldehyde thiosemicarbazone (X = H, Cl, Br) acting as chelating agents. The cooperativity is even enhanced by the introduction of hydrogen bonding and π-stacking interactions. Such an approach is also motivated by the quasi-absence of Fe(III) LIESST spin transition materials in literature. In summary, it is anticipated that the present study may be a worthwhile contribution towards the elucidation of the Fe(III) LIESST mechanism.

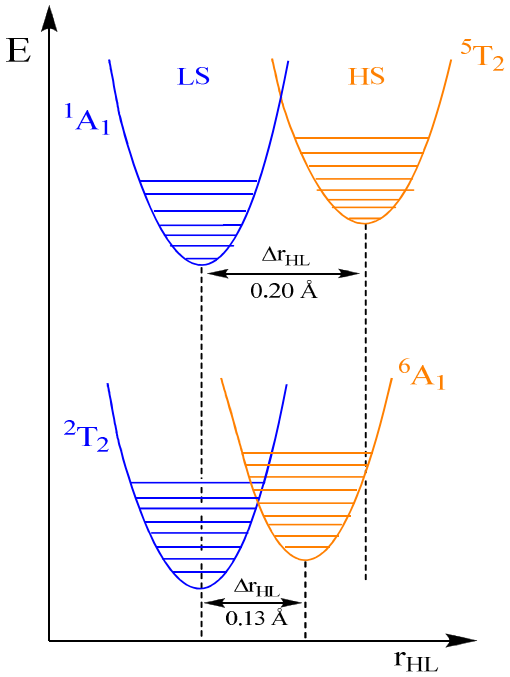

Figure 6.1. Potential wells of HS and LS states. Metal–ligand bond lengths for iron(II) compounds are $\Delta r_{HL} \approx 0.20$ Å and those for iron(III) compounds are $\Delta r_{HL} \approx 0.13$ Å.

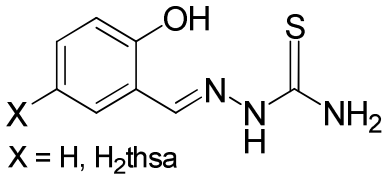

X = H, H_2thsa
X = Cl, H_2th5Clsa
X = Br, H_2th5Brsa

Chart 6.1. Structure of 5X-salicylaldehyde thiosemicabazone ligand.

6.2 Results and Discussion

6.2.1 Crystallographic Studies[1]

Compounds [Fe(Hthsa)(thsa)]·H_2O (**7**), [Fe(Hth5Clsa)(th5Clsa)]·H_2O (**8**) and [Fe(Hth5Brsa)(th5Brsa)]·$(H_2O)_{1/2}$ (**9**) were obtained as microcrystalline powders with cocrystallized water solvent molecules. Powder X-ray diffraction (XRD) patterns were measured for **8** and **9** (HS at room temperature) and **7** (HS at room temperature and LS at 150 K). The crystal structures of 7 and **8** were determined at room temperature (HS).

[1] See chapter 2 for details on the experimental procedures and recipes for compounds presented in this chapter

Table 6.1 Crystallographic Data and *GSAS* Refinement Details for the Structures of [Fe(Hthsa)(thsa)]·H_2O (**7**) and [Fe(Hth5Clsa)(th5Clsa)]·H_2O (**8**) at 293 K.

	7	**8**
Formula	$C_{16}H_{17}N_6O_3S_2Fe$	$C_{16}H_{15}Cl_2N_6O_3S_2Fe$
Formula weight (g.mol^{-1})	461.32	530.21
Temperature (K)	293(1)	293(1)
Calculated density (g.cm^{-3})	1.617	1.698
Crystal system	monoclinic	monoclinic
Space group	$P2_1/n$	$P2_1/n$
Powder colour	dark-brown	dark-brown
a, (Å)	8.9922(5)	9.0070(4)
b, (Å)	18.2972(9)	20.0760(10)
c, (Å)	11.5334(5)	11.4697(5)
β, (deg)	92.744(3)	91.265(3)
Volume (Å^3)	1895.4(2)	2073.5(2)
Z	4	4
Radiation type	1.54056 Å (Cu Kα)	1.54056 Å (Cu Kα)
2θ range (deg)	10-60	10-60
Number of reflections	543	597
Number of atoms	46	46
Number of restraints	106	106
Number of structural refined parameters	151	165
R_p, R_{wp}	0.0474, 0.0611	0.0469, 0.0602

Complex **7** is isostructural to that of **8** and both crystallize in the monoclinic $P2_1$/n space group (Table 6.1) while **9** crystallizes in a monoclinic $P2_1$/c space group. In both systems studied, despite differences in the substituent at the 5-position of the salicylaldehyde moiety, the Fe(III) ion is coordinated by two thiosemicarbazonato ONS ligands (Figure 6.2). The donor atoms of these ligands are located in two mutually perpendicular planes with O and S atoms in *cis* and N atom in *trans* positions. No significant changes in the structure of the organic part of the ligands have been observed. However, examination of the crystal structures of **7** and **8** revealed that the chelating agents are bound to the central atom in two different tautomeric forms: the thione and the thiol tautomers. The thione form is the uninegative ligand and bears a proton at the hydrazinic nitrogen whereas the dianionic thiol tautomer has no hydrogen atom at the hydrazinic nitrogen. Several additional structural features to characterize the ligand form of **7** and **8** can be obtained from the bond distances and angles listed in Table 6.2.

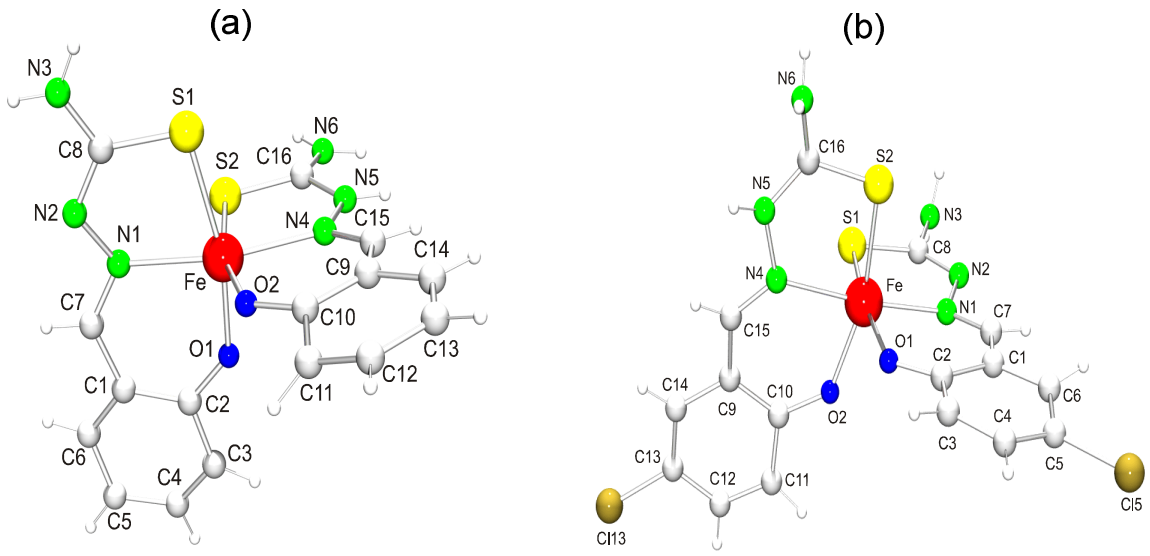

Figure 6.2. A perspective view of: (a) [Fe(Hthsa)(thsa)]·H_2O and (b), [Fe(Hth5Clsa)(th5Clsa)]·H_2O complexes at 293 K, with atom labeling scheme. Water molecules are omitted for clarity.

Table 6.2 Selected Bond Lengths (Å) and Bond Angles (deg) for [Fe(Hthsa)(thsa)]·H_2O (**7**) and [Fe(Hth5Clsa)(th5Clsa)]·H_2O (**8**). Standard deviations in the last decimal place are given in parentheses.

Distance (Å)	**7**	**8**	Angles (deg)	**7**	**8**
Fe – S1	2.370(7)	2.346(13)	S1 – Fe – S2	88.9(2)	94.7(4)
Fe – S2	2.444(7)	2.386(13)	O1 – Fe – O2	93.36(19)	86.7(7)
Fe – O1	1.894(5)	1.902(16)	N1 – Fe – N4	161.9(2)	174.4(6)
Fe – O2	1.927(5)	1.920(17)	S1 – Fe – N1	79.8(2)	79.7(5)
Fe – N1	2.166(6)	2.118(12)	S1 – Fe – O1	165.8(3)	167.4(6)
Fe – N4	2.111(6)	2.210(11)	O1 – Fe – N1	86.1(2)	88.5(6)
S1 – C8	1.708(4)	1.727(12)	O2 – Fe – N1	112.0(3)	100.9(6)
S2 – C16	1.683(4)	1.686(11)	S1 – Fe – N4	98.4(2)	98.9(5)

However, a comparison of **2** (LS, chapter 3) and **7**, **8** (HS), gives us an opportunity to study the structure of the [Fe(Hthsa)(thsa)] and [Fe(Hth5Clsa)(th5Clsa)], units in both spin states in the temperature range 5–300 K. In spite of the difference in spin states between **2** (LS state) at 100 K and **7**, **8** (HS state) at room temperature, the coordination sphere of the iron atoms is similar to each other as well as the packing of the molecules. Comparison of the powder structure in the HS state with that of the single-crystal structure in the LS state will give us information of structural changes accompanying the

spin transition in **7** and **8**. It should be noted that there is a huge difference in bond lengths between HS and LS states. In **2** (LS), the average Fe–O distance is $r_{Fe–O}$ = 1.908(6) Å, the average Fe–N distance is $r_{Fe–N}$ = 1.933(8) Å and the average Fe–S distance is $r_{Fe–S}$ = 2.2462(22) Å. In **7**/**8** (HS), the average Fe–O distance are $r_{Fe–O}$ = 1.9105(10)/1.911(33) Å, the average Fe–N distance are $r_{Fe–N}$ = 2.1385(12)/2.164(23) Å and the average Fe–S distance are $r_{Fe–S}$ = 2.407(14)/2.366(26) Å; this results in average bond length differences of: $\Delta r_{HL,Fe–O}$ = 0.025/0.030 Å, $\Delta r_{HL,Fe–N}$ = 0.206/0.231 Å and $\Delta r_{HL,Fe–S}$ = 0.161/0.120 Å. These differences are due to the difference in the spin states of the [$FeO_2N_2S_2$] core from O_h symmetry, and the average variations in Fe to ligand bond distance are: 0.131/0.127 Å, respectively. It is in the range of what would be expected for typical values of Δr observed for iron(III) SC compounds. It is also important to notice that the changes in the Fe–S and Fe–N bond lengths are much larger than the changes in the Fe–O bond distances. It shows that during the spin transition the iron-ligand bonds may asymmetrically stretch and the thsa/th5Clsa ligands may open up around the iron atom like a pair of scissors.

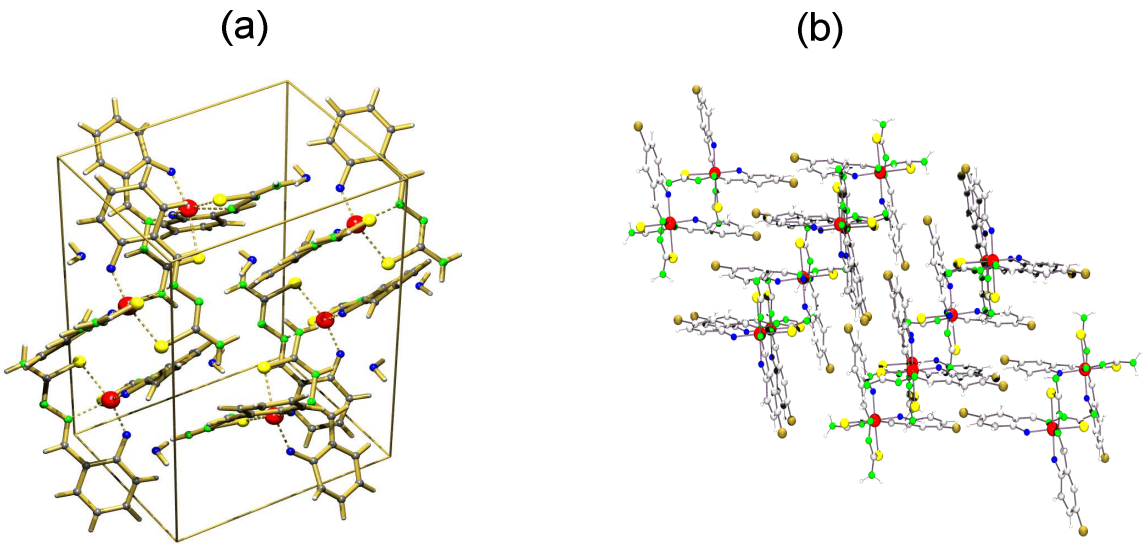

Figure 6.3. (a) Molecular packing arrangement of [Fe(Hthsa)(thsa)]·H_2O. View face A. (b) Projection of the 2D networks of [Fe(Hth5Clsa)(th5Clsa)]·H_2O. View along ZO.

The packing diagram of complexes **7** and **8** at room temperature is illustrated in Figure 6.3. The plane of the thsa/th5Clsa ligands of an iron(III) is parallel to those of the thsa/th5Clsa ligands of the neighbouring iron(III) and stacked with a distance between the planes of 3.63 Å for **7** and 3.61 Å for **8** (Figure 6.4). The close parallel packing of

aromatic rings means that the [Fe(Hthsa)(thsa)] and [Fe(Hth5Clsa)(th5Clsa] units have strong intermolecular π stacking. This interaction, fixing the interplanar distance of the aromatic rings, does not allow the thsa/th5Clsa ligands to move freely. As a consequence, the structural changes of the spin-transition around a iron(III) unit must be followed by a complex rearrangement of the packing with the neighbouring molecules.

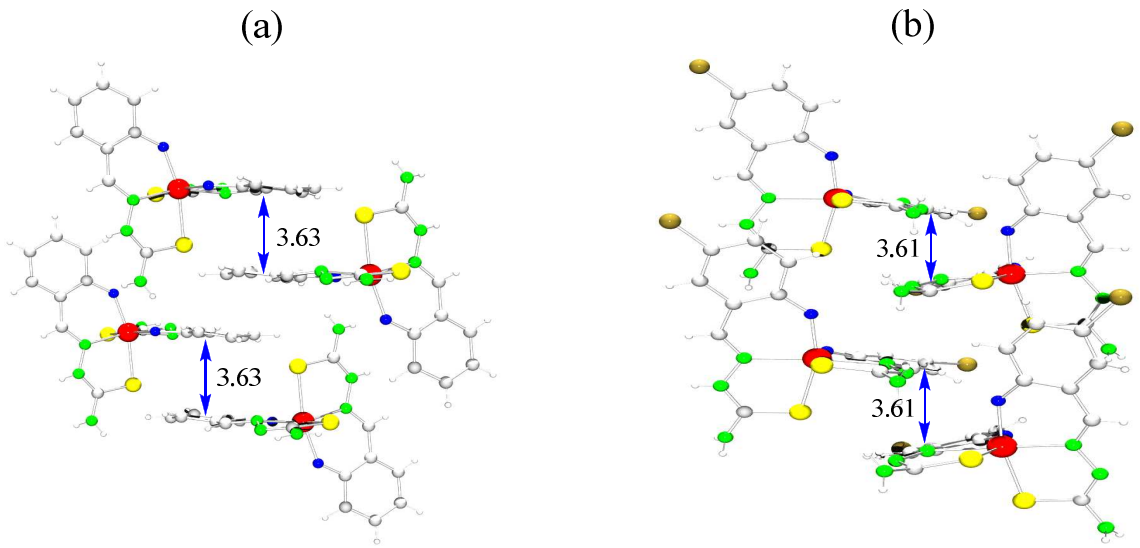

Figure 6.4. π stacking interactions between the complex units for both: (a) [Fe(Hthsa)(thsa)]·H_2O, and (b) [Fe(Hth5Clsa)(th5Clsa)]·H_2O. The interplanar distance is indicated by the double-headed arrow.

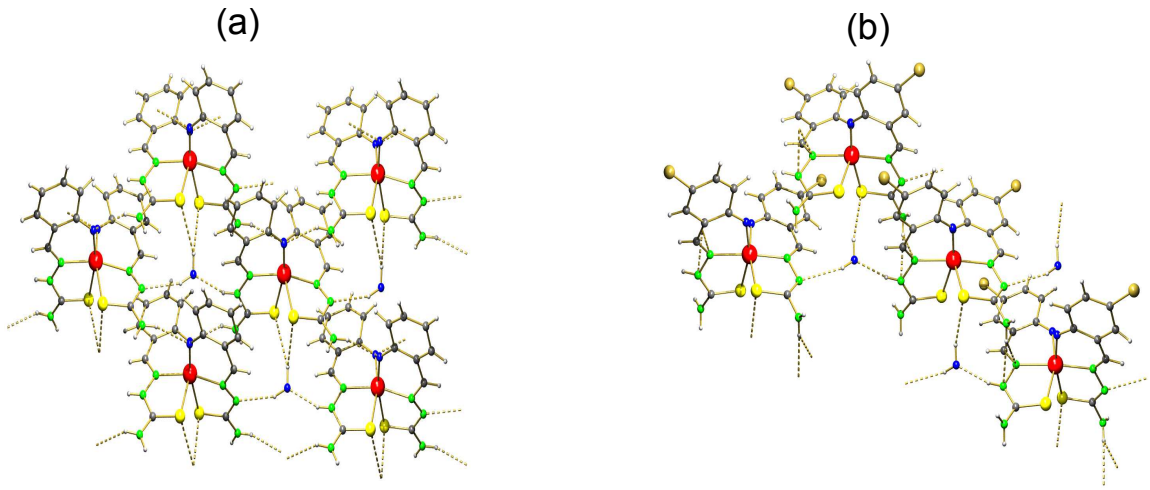

Figure 6.5. View of the asymmetric unit along the YO direction, showing the hydrogen bonding networks for: (a) [Fe(Hthsa)(thsa)]·H_2O, and (b) [Fe(Hth5Clsa)(th5Clsa)]·H_2O. Hydrogen bonds are given as single dotted lines. Unit cell boxes have been omitted for the purpose of clarity.

These stacked units form 2D sheets, with water molecules inserted between the sheets, hydrogen-bonded to three sets of overlapping thsa/th5Clsa ligands around it (Figure 6.5). The molecular assembly of **7** and **8** are close packed, similar to what is observed in $[Fe(pap)_2]ClO_4 \cdot H_2O$.[31] The packing arrangement suggests that strong cooperativity operates in these systems and arises from both: the intermolecular π-π interactions between the nearest thsa/th5Clsa ligands, and the hydrogen bonding networks that serve to propagate the structural information expressed in metal coordination preferences throughout the extended structure.

6.2.2 Magnetism

The magnetic property of $[Fe(Hthsa)(thsa)] \cdot H_2O$ (**7**) is presented in Figure 6.6a as the $\chi_m T$ versus T curve. The $\chi_m T$ value for **7** is equal to 3.80 cm^3 K mol^{-1} at 340 K, which is in the range of the values expected for the HS iron(III) ion. At temperatures below 300 K, a slow cooling experiment revealed that SCO takes place in a two-step manner. The so called "step 1" and "step 2" are centered on temperatures $T_{1/2(S1)}\downarrow$ = 262 K and $T_{1/2(S2)}\downarrow$ = 232 K, respectively. The magnetic behaviour shows that both steps are almost equal in height. The $\chi_m T$ value at the inflection point at around 238 K is 2.25 cm^3 K mol^{-1}. On heating, the $\chi_m T$ value remains practically constant in the temperature range from 100 K to 269 K, then abruptly increases at $T_{1/2}\uparrow$ = 275 K, showing a thermally driven spin transition from LS to the HS state. If the hysteresis widths (ΔT) in step 1 and step 2 are defined as the difference between $T_{1/2(S1)}\downarrow$ and $T_{1/2}\uparrow$, and between $T_{1/2(S2)}\downarrow$ and $T_{1/2}\uparrow$, respectively, they are estimated to be 13 K (step 1) and 43 K (step 2). Additional thermal cycles did not modify the hysteresis loop. It is thought that the wide thermal hysteresis are induced by strong intermolecular interactions in the molecular packing through π–π stacking and/or hydrogen bonding networks between the SCO centres. Although the hysteresis loop in the temperature dependence of the magnetic behavior has been observed in many SCO iron(II) complexes, SCO iron(III) compounds with thermal hysteresis are rare. The first examples of this family of iron(III) Schiff-base type ligand are given by: [Fe(Hthpu)(thpu)] [37] (ΔT = 10 K) and $[Fe(HL)_2]Cl$ [38] (ΔT = 11 K); (where H_2thpu and HL are pyruvic acid thiosemicarbazone and pyridoxal thiosemicarbazone, respectively). Furthermore, it should be noted that this kind of two-step spin crossover in cooling mode only, has not been observed before. In the case of $[Fe(qsal)_2]^+$ systems,[39] for instance, it was shown that these complex cations form two different kinds of π–π

stacking in the qsal ligands, between the quinoline and phenyl rings. The authors therefore simulated the two step spin transition behaviour obtained during the warming run only, by the dinuclear model of Kahn[40] and Real *et al.*[41] in terms of two different kinds of π–π stacking. Detailed discussions and demonstrations are given in reference 39.

The magnetic properties show also that $\chi_m T$ for [Fe(Hth5Clsa)(th5Clsa)]·H_2O (**8**) at room temperature is equal to 4.22 cm^3 K mol^{-1}, which corresponds to what is expected for the HS state in iron(III) compounds (Figure 6.6b). On cooling, the value of $\chi_m T$ drops abruptly around $T_{1/2}\downarrow$= 230 K. The $\chi_m T$ value at 100 K is equal to 0.45 cm^3 K mol^{-1}, representing the low spin state. In the warming mode, an abrupt variation of $\chi_m T$ is observed around $T_{1/2}\uparrow$ = 231 K.

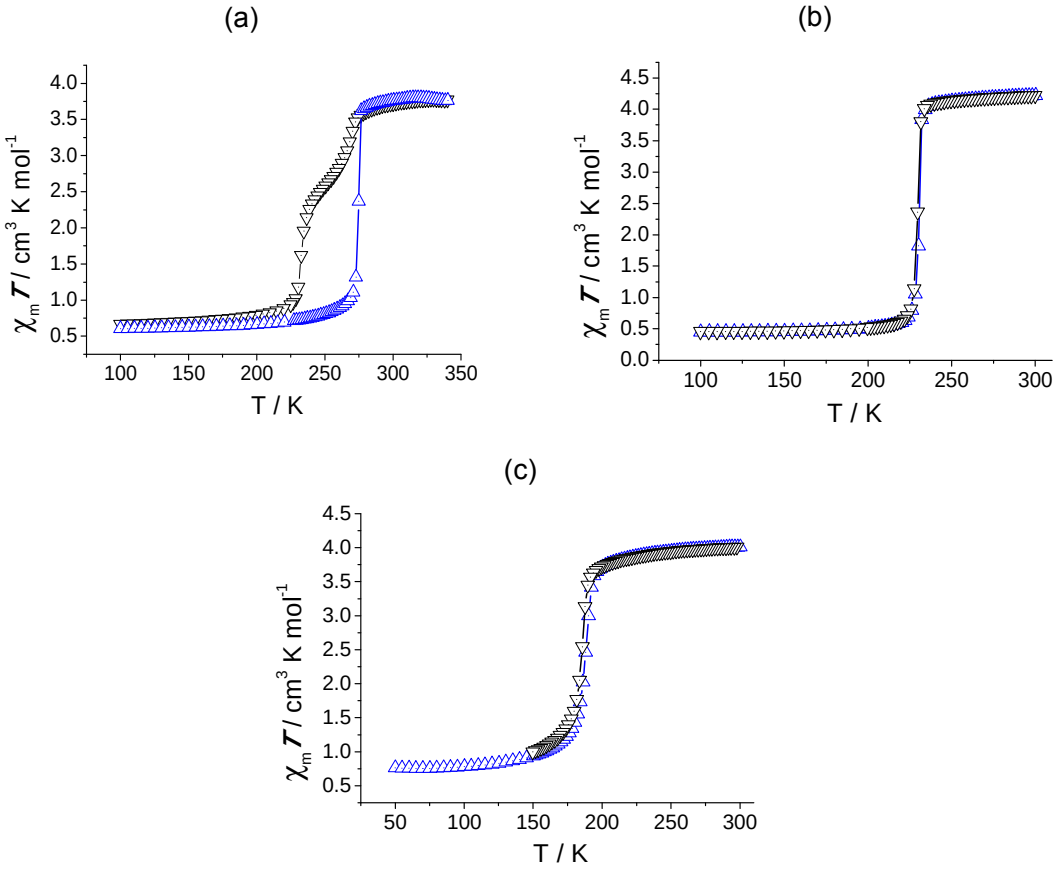

Figure 6.6. $\chi_m T$ vs T plots for: (a) [Fe(Hthsa)(thsa)]·H_2O, (b) [Fe(Hth5Clsa)(th5Clsa)]·H_2O, and (c) [Fe(Hth5Brsa)(th5Brsa)]·$(H_2O)_{1/2}$. Samples were warmed (Δ) and subsequently cooled (∇) in the temperature region 50 – 340 K, at a rate of 2 K min^{-1}.

Compound **9** is a dark green microcrystalline powder, that shows $\chi_m T$ = 4.01 cm^3 K mol^{-1} at room-temperature. This observation is consistent with it being fully populated in a

high-spin, S = 5/2 spin state.[16] Upon cooling, the sample undergoes a fairly abrupt transition to a fully populated S = 1/2 low-spin form. This transition is centred at: $T_{1/2}\uparrow$ = 188 K and $T_{1/2}\downarrow$ = 186 K, and shows a hysteresis loop of 2 K (Figure 6.6c), while for **8**, the hysteresis loop is only 1 K. Additional thermal cycles did not modify the thermal hysteresis loop for both compounds. An important characteristic of this complex system is that, by replacing the hydrogen atom with a halogen group (Cl, Br) at the 5-position on salicylaldehyde unit of the ligand, the cooperative interactions between the spin-changing molecules tend to disappear as the extent of the substituent size increases and thus, shifts the transition to lower temperatures, reflecting increasing stabilization of the HS state. These results clearly support the existence of cooperative elastic interactions between the SCO Fe(III) centers due to the chemical pressure.

6.2.3 Mössbauer Spectroscopy

Characteristic ^{57}Fe Mössbauer spectra of [Fe(Hth5Clsa)(th5Clsa)]·H_2O (**8**) are shown in Figure 6.7. All spectra show quadrupole split absorption lines with absence of any magnetic splitting at all measured temperatures, between 300 K and 77 K. Starting the analysis from the room temperature (300 K) spectrum, it is clear that is dominated by a quadrupole split doublet. However, the two absorption lines of this doublet are rather asymmetric, with the left (lower velocity) absorption line being narrower and longer than the right (high velocity) absorption line.

For bulk samples this feature can be a consequence of several origins. Because the iron ions in the complex are occupying one and only crystallographic site the asymmetry of the absorption lines is due to an asymmetry in the γ-ray recoilless fraction, which is a characteristic of the structure of the compound and is known as the 'Goldanskii-Karyagin effect'.[42]

Apart from the major central quadrupole contribution there is an indication of another minor quadrupole split contribution with higher quadrupole splitting (QS) value at the 300 K spectrum of [Fe(Hth5Clsa)(th5Clsa)]·H_2O compound. This contribution is gradually increasing its relative absorption area as the temperature decreases, at the expense of the absorption area of the lower QS doublet. Below 235 K it is obvious that this minor quadrupole split contribution possesses also an absorption line asymmetry. However in this case the right absorption line is narrower and more intense than the left absorption line, in contrast to the major quadrupole split doublet at RT. In order to distinguish between the two contributions, we will refer to the small QS doublet as the

high temperature (HT) doublet and to the large QS doublet as low temperature (LT) doublet.

To describe the line asymmetry of the two doublets, and following the indication of the possible existence of two different iron neighbour environments, we used a set of four quadrupole split paramagnetic components to fit the corresponding Mössbauer spectra adequately. Two of these correspond to the HT doublet (Q3 and Q4) and the other two to the LT doublet (Q1 and Q2). The resulting Mössbauer parameters are listed in Table 6.3. The isomer shift (IS) of the HT components correspond to high spin (S=5/2) Fe^{III} characteristics, while a drop in the IS values is observed for the components describing the LT doublet, suggesting a spin transition to a low spin (S=1/2) Fe^{III} state.

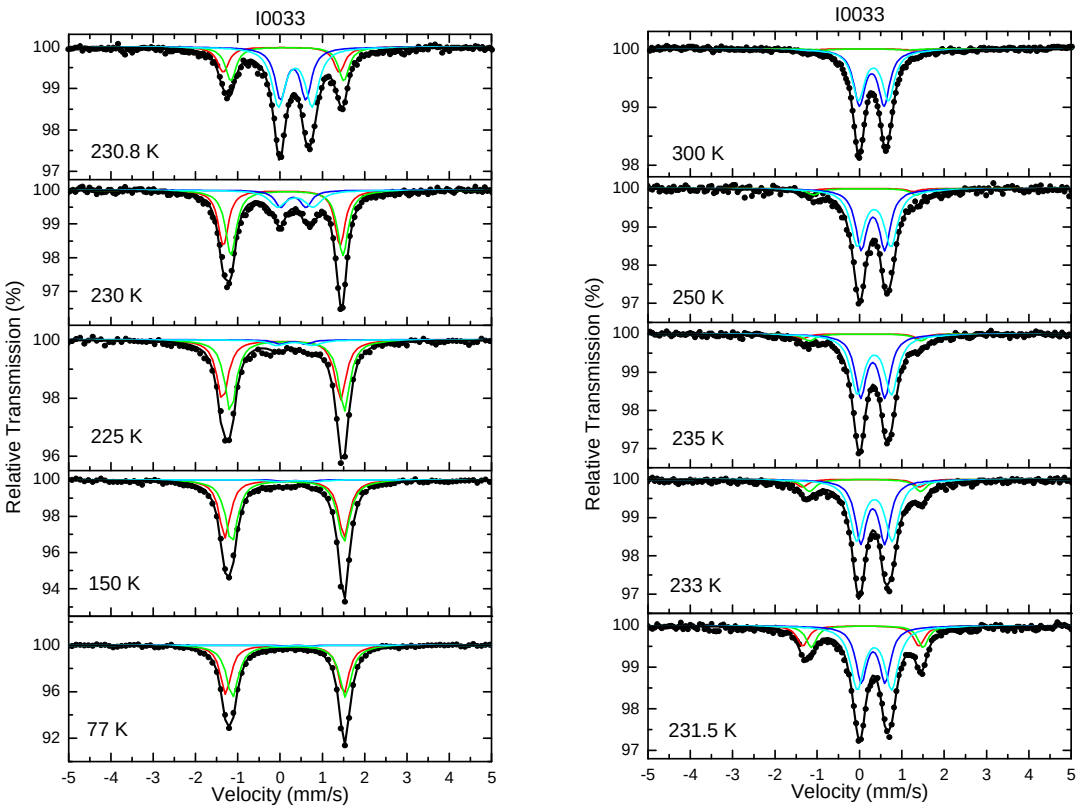

Figure 6.7. Temperature dependence of the ^{57}Fe Mössbauer spectra of [Fe(Hth5Clsa)(th5Clsa)]·H_2O obtained in the cooling mode. The colored solid lines represent the quadrupole split components used to fit the spectra: Q1-green, Q2-red, Q3-blue and Q4-aquamarine.

Indeed, the shape of the spectra changes dramatically below 233 K and at 230 K the spectrum is dominated by the large QS doublet. The magnetic susceptibility measurements indicate also a sharp transition from high to low susceptibility values as

the temperature decreases at the same temperature region. Combining the Mössbauer spectroscopy and magnetic susceptibility results we can confirm that the **8** undergoes a high-spin to low-spin transition as the temperature decreases. The spin transition temperature is estimated from Mössbauer spectroscopy to be around T_{ST} = 231 K.

At lower temperatures the HT doublet is gradually diminished and at 77 K is almost absent. It is worth to notice here that the line asymmetry absorption of the LT doublet consolidates our suggestion of having two different iron neighbour environments in the structure, as this is the expected development for the low spin state, if one admits the existence of the same environments for the high spin state of the compound. Another characteristic of the spectra is the remarkable increase in the recoilless fraction (*f*) as the temperature decreases. The maximum absorption effect, which is directly related to *f* ,[43] increases from about 2 % at RT to about 9 % at 77 K, and this is a consequence of the relative low value of the Debye temperature (Θ_D) resulting from the nature of the bonds between iron and its ligands for this compound.

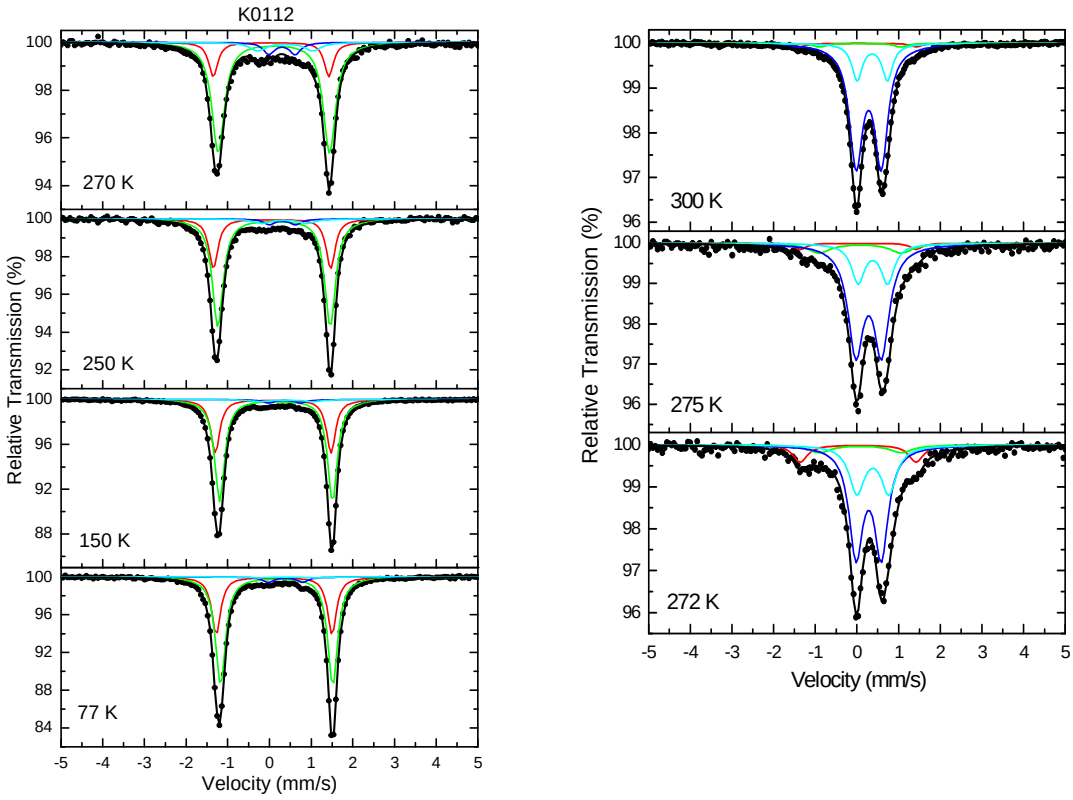

Figure 6.8. Temperature dependence of the ^{57}Fe Mössbauer spectra of [Fe(Hthsa)(thsa)]·H_2O obtained in the cooling mode. The colored solid lines represent the quadrupole split components used to fit the spectra: Q1-green, Q2-red, Q3-blue and Q4-aquamarine.

The compound [Fe(Hthsa)(thsa)]·H_2O (**7**) shows very similar Mössbauer spectra with **8**, which are given in Figure 6.8. As in the case of **8**, at RT the presence of a dominant doublet with relative low QS value is evident. This doublet shows also an absorption line asymmetry. As the temperature descends a new contribution with larger QS value appears and takes the majority of the absorption area of the spectrum below 272 K. The low temperature doublet acquires also an absorption line asymmetry. In order to reproduce this asymmetry we used a set of four quadrupole split components as in the case of [Fe(Hth5Clsa)(th5Clsa)]·H_2O. The IS and QS values resulting from the best fits of the spectra appear in Table 6.4. These values lie in the same range of the corresponding values of **8**, revealing the presence of the Fe^{III} state in the structure of the compound. Thus we can suggest that similar to the first studied case, the Fe^{III} in [Fe(Hthsa)(thsa)]·H_2O compound undergoes a high-spin (S=5/2) to low-spin (S=1/2) transition as the temperature decreases, with the transition temperature estimated at T_{ST} = 271 K. The magnetic susceptibility measurements confirm the above findings as they show a steep drop in the zero field cooled susceptibility values at around 271 K as well. An interesting characteristic of the magnetic susceptibility measurements is the hysteretic behaviour observed between the zero field cooled (ZFC) and field cooled (FC) branches, which indicates that the applied magnetic field in the FC procedure influences the spin transition temperature by shifting it at lower values. This could be due to the presence of some weak magnetic interactions between the iron centres of the compound. A remarkable change in the recoilless fraction is also observed for this compound as the maximum absorption effect increases from ~ 4 % at RT to ~ 17 % at 77 K.

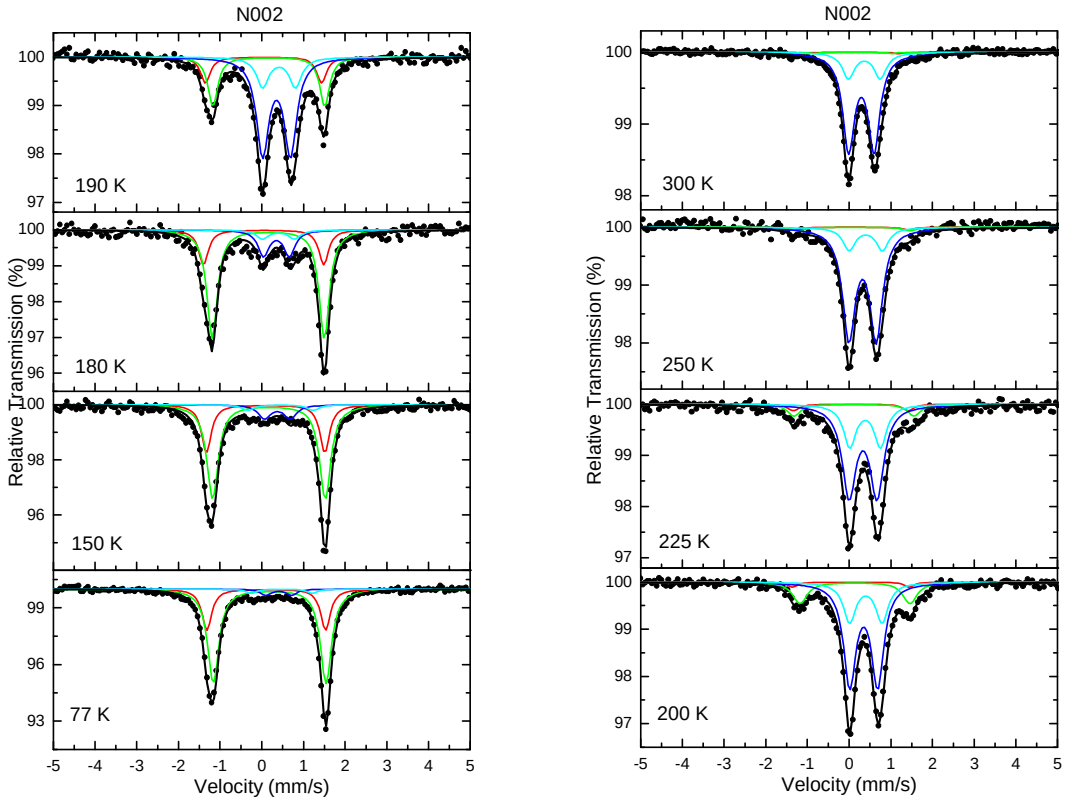

Figure 6.9. Temperature dependence of the ^{57}Fe Mössbauer spectra of [Fe(Hth5Brsa)(th5Brsa)]·$(H_2O)_{1/2}$ obtained in the cooling mode. The colored solid lines represent the quadrupole split components used to fit the spectra: Q1-green, Q2-red, Q3-blue and Q4-aquamarine.

Finally, the Mössbauer spectra of compound [Fe(Hth5Brsa)(th5Brsa)]·$(H_2O)_{1/2}$ (**9**) are also similar to the two previously compounds. The spectra appear in Figure 6.9 and the Mössbauer parameters are listed in Table 6.5.

The asymmetry observed in the Mössbauer spectra of the two former compounds appear also in the spectra of **9**. The Mössbauer parameters values indicate that the metal center is still Fe^{III} and undergoes a spin transition from high (S=5/2) to low (S=1/2) spin states at the temperature region between 200 K and 180 K. However in this case the high spin to low spin transition is not so sharp compared with the two previous cases. This is also confirmed by the magnetic susceptibility measurements which show a more gradual decrease in its values as the temperature decreases in the same region. The recoilless fraction *f* increases also as the temperature decreases, as the maximum absorption effect increases from about 2 % at RT to about 8 % at 77 K.

Table 6.3 ^{57}Fe Mössbauer Spectral Parameters for [Fe(Hth5Clsa)(th5Clsa)]·H_2O, with QS, the quadrupole splitting, IS, the isomer shift (relative to metallic iron at room temperature), Γ/2, the half line-width and Area, the relative absorption area for each component.

T (K)	Component	IS (mms^{-1})	Γ/2 (mms^{-1})	QS (mms^{-1})	Area (%)
300	Q1	0.14	0.16	2.48	1
	Q2	0.24	0.18	1.97	1
	Q3	0.40	0.16	0.59	49
	Q4	0.44	0.17	0.71	49
250	Q1	0.14	0.16	2.48	3
	Q2	0.24	0.18	2.43	5
	Q3	0.42	0.16	0.56	43
	Q4	0.45	0.19	0.79	49
235	Q1	0.14	0.16	2.77	3
	Q2	0.24	0.18	2.63	5
	Q3	0.42	0.16	0.58	43
	Q4	0.46	0.19	0.80	49
233	Q1	0.14	0.16	2.77	5
	Q2	0.24	0.18	2.63	9
	Q3	0.42	0.16	0.57	40
	Q4	0.46	0.19	0.84	46
231.5	Q1	0.14	0.16	2.75	12
	Q2	0.29	0.15	2.64	12
	Q3	0.43	0.16	0.56	32
	Q4	0.46	0.19	0.81	44
230.8	Q1	0.13	0.16	2.75	14
	Q2	0.28	0.15	2.67	18
	Q3	0.42	0.16	0.60	29
	Q4	0.47	0.19	0.79	39
230	Q1	0.14	0.15	2.76	33
	Q2	0.27	0.15	2.65	41
	Q3	0.42	0.16	0.60	11
	Q4	0.47	0.24	0.84	15
225	Q1	0.14	0.16	2.79	42
	Q2	0.28	0.16	2.69	50
	Q3	0.42	0.16	0.60	3
	Q4	0.47	0.24	0.84	5
150	Q1	0.21	0.16	2.82	44
	Q2	0.29	0.17	2.65	52
	Q3	0.49	0.16	0.62	2
	Q4	0.51	0.24	0.88	2
77	Q1	0.22	0.15	2.79	45
	Q2	0.32	0.17	2.67	53
	Q3	0.51	0.16	0.60	1

	Q4	0.54	0.24	0.84	1

Table 6.4 ^{57}Fe Mössbauer Spectral Parameters for [Fe(Hthsa)(thsa)]·H_2O, with QS, the quadrupole splitting, IS, the isomer shift (relative to metallic iron at room temperature), Γ/2, the half line-width and Area, the relative absorption area for each component.

T (K)	Component	IS (mms^{-1})	Γ/2 (mms^{-1})	QS (mms^{-1})	Area (%)
300	Q1	0.14	0.17	2.78	2
	Q2	0.19	0.19	1.95	2
	Q3	0.39	0.19	0.60	77
	Q4	0.48	0.15	0.73	19
275	Q1	0.14	0.17	2.78	3
	Q2	0.19	0.33	1.97	9
	Q3	0.39	0.22	0.62	67
	Q4	0.49	0.19	0.71	21
272	Q1	0.14	0.21	2.78	9
	Q2	0.19	0.33	1.97	7
	Q3	0.39	0.20	0.61	57
	Q4	0.49	0.22	0.76	27
270	Q1	0.15	0.13	2.78	16
	Q2	0.21	0.18	2.68	70
	Q3	0.41	0.16	0.63	7
	Q4	0.49	0.24	1.32	7
250	Q1	0.17	0.13	2.82	26
	Q2	0.22	0.16	2.70	66
	Q3	0.42	0.16	0.63	4
	Q4	0.46	0.24	1.09	4
150	Q1	0.19	0.13	2.78	31
	Q2	0.26	0.14	2.71	64
	Q3	0.47	0.16	0.77	3
	Q4	0.51	0.24	1.26	2
77	Q1	0.22	0.13	2.78	31
	Q2	0.28	0.14	2.70	65
	Q3	0.49	0.16	0.82	3
	Q4	0.53	0.19	1.37	1

Table 6.5 ^{57}Fe Mössbauer Spectral Parameters for [Fe(Hth5Brsa)(th5Brsa)]·$(H_2O)_{1/2}$, with QS, the quadrupole splitting, IS, the isomer shift (relative to metallic iron at room temperature), Γ/2, the half line-width and Area, the relative absorption area for each component.

T (K)	Component	IS (mms^{-1})	Γ/2 (mms^{-1})	QS (mms^{-1})	Area (%)
300	Q1	0.14	0.15	2.29	1
	Q2	0.21	0.15	1.87	1
	Q3	0.40	0.17	0.61	77
	Q4	0.47	0.18	0.77	21
250	Q1	0.15	0.16	2.76	2
	Q2	0.23	0.19	2.68	3
	Q3	0.43	0.18	0.65	79
	Q4	0.50	0.18	0.80	16
225	Q1	0.15	0.16	2.76	4
	Q2	0.23	0.19	2.88	8
	Q3	0.44	0.20	0.67	62
	Q4	0.49	0.18	0.74	26
200	Q1	0.15	0.14	2.80	2
	Q2	0.25	0.21	2.64	15
	Q3	0.45	0.18	0.67	60
	Q4	0.50	0.18	0.78	23
190	Q1	0.15	0.14	2.79	11
	Q2	0.27	0.14	2.69	21
	Q3	0.46	0.18	0.67	52
	Q4	0.52	0.18	0.79	16
180	Q1	0.15	0.14	2.89	18
	Q2	0.26	0.15	2.69	61
	Q3	0.46	0.16	0.62	15
	Q4	0.51	0.18	0.77	6
175	Q1	0.20	0.13	2.81	25
	Q2	0.28	0.17	2.70	56
	Q3	0.48	0.18	0.61	14
	Q4	0.56	0.17	1.33	5
150	Q1	0.20	0.14	2.84	26
	Q2	0.28	0.16	2.71	60
	Q3	0.48	0.18	0.62	10
	Q4	0.56	0.17	1.57	4
77	Q1	0.21	0.14	2.85	25
	Q2	0.30	0.16	2.71	68
	Q3	0.51	0.15	0.62	4
	Q4	0.59	0.15	1.46	3

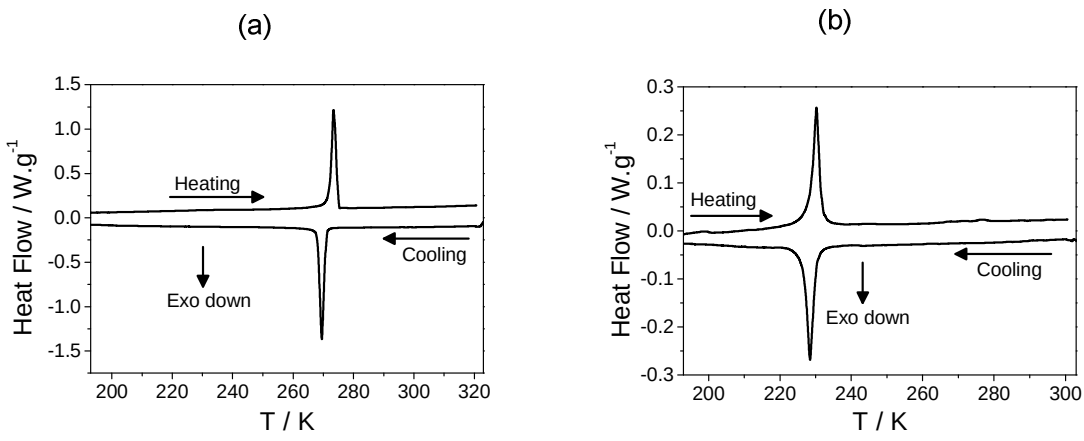

Figure 6.10. Heat flow curves obtained by DSC measurements of: (a) [Fe(Hthsa)(thsa)]·H_2O, and (b) [Fe(Hth5Clsa)(th5Clsa)]·H_2O. Heating and cooling branches are represented by full lines, respectively.

6.2.4 Differential Scanning Calorimetry

In order to obtain additional insight into the nature of the electronic changes revealed by the magnetic and Mössbauer data, differential scanning calorimetry (DSC) measurements were performed in the 188 – 313 K range. Figure 6.10 represents the DSC scan of samples **7** and **8** initiated with cooling, following by heating, with a 2 K min^{-1} rate. The values of the transition temperatures corresponding to the observed thermal anomalies refer to the peak maxima in the DSC scan, and are obtained for the cooling and heating temperature sequences respectively as: $T_c\uparrow$ = 273 K, $T_c\downarrow$ = 270 K for **7** and $T_c\uparrow$ = 230 K, $(T_c)\downarrow$ = 228 K for **8**. Similar scans with different cooling/heating rates produced similar values. In order to deduce the enthalpy and the entropy contents of the transition from the DSC curves, a background contribution has been estimated from a smooth interpolation above and below the transition and finally subtracted from the measured values. The enthalpy estimations are (7.5 ± 0.2) kJ mol^{-1} and (6.4 ± 0.3) kJ mol^{-1} for [Fe(Hthsa)(thsa)]·H_2O and [Fe(Hth5Clsa)(th5Clsa)]·H_2O, respectively. These data correspond to transition entropy values of (27.5 ± 0.3) J mol^{-1} K^{-1} and (27.9 ± 0.9) J mol^{-1} K^{-1}. These entropy gains are larger than the expected electronic entropy value associated with the change in spin state of Fe^{III} from $^2T_2$ to the $^6A_1$ state, Rln(6/2) = 9.13 J K^{-1} mol^{-1}, and indicate a substantial contribution due to the change in the frequencies of the vibrational states coming mainly from the metal-skeletal vibrational modes.[44] However, both thermodynamic quantities (ΔS for **7** and **8**, respectively) are significantly lower than the values obtained by DSC on iron(III) spin crossover complex $[Fe(acpa)_2]PF_6$ [Hacpa =

N-(1-acetyl-isopropylidene) (2-pyridylmethyl) amine][45] indicating that there is an important difference between the excess entropy of an abrupt spin crossover transformation and a gradual type.

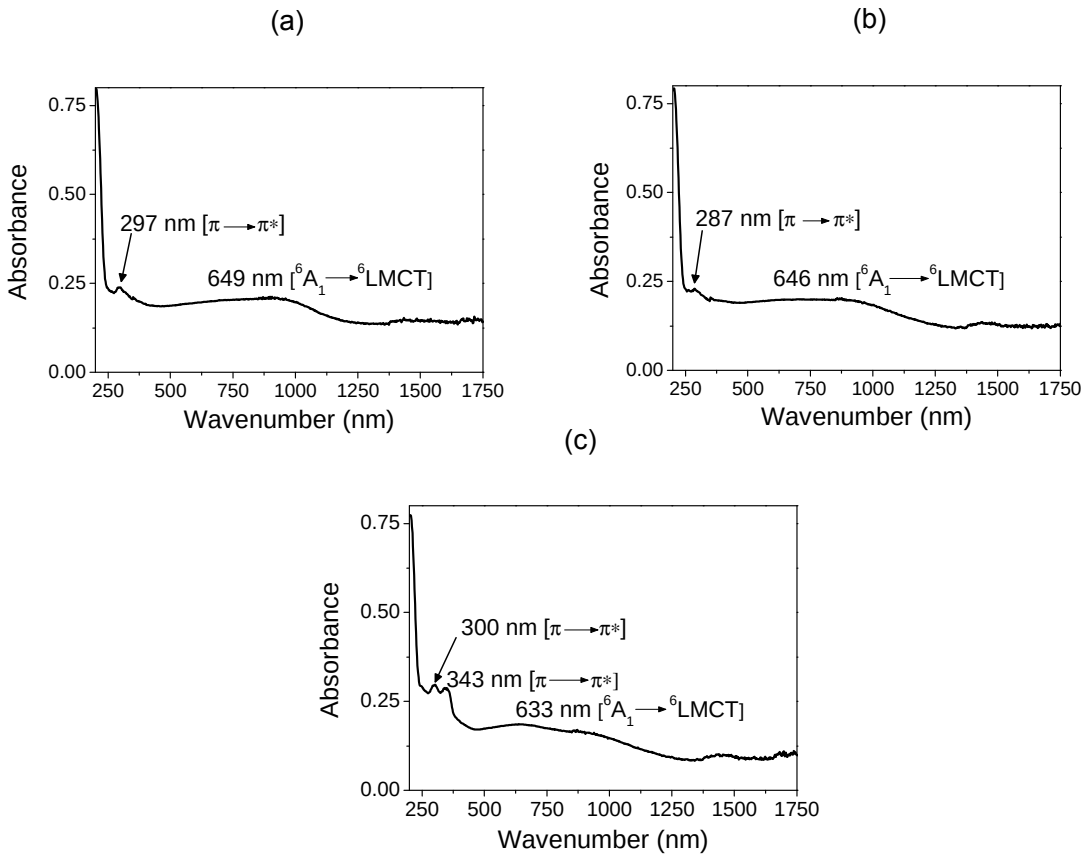

Figure 6.10. Room temperature electronic spectra of: (a) [Fe(Hthsa)(thsa)]·H_2O, (b) [Fe(Hth5Clsa)(th5Clsa)]·H_2O, and (c) [Fe(Hth5Brsa)(th5Brsa)]·$(H_2O)_{1/2}$, in solid state and relative band assignments; LMCT = ligand-to-metal charge transfer mechanisms.

6.2.5 Optical Properties

Ligand Field Spectroscopy: The room temperature electronic spectra of **7**, **8** and **9** in the solid state reported in Figure 6.11, can be interpreted with a good approximation in terms of $\pi \rightarrow \pi^*$ transitions (most common transition is observed in organic compounds with lone pairs and multiple bonds), together with spin allowed ligand to metal charge transfer transitions on the basis of previous studies on iron(III) complexes of Schiff base type-ligands.[46-49] However, the spectroscopic features of iron(III) SCO systems, especially in solid state, have not been subject to extensive studies and at present they are not well understood. The ligand field spectrum of **7**/**8** at room temperature (Figure 6.11a, b) shows an absorption band at *ca.* 649/646 nm and an obscured shoulder at *ca.* 297/287 nm. The

first of these bands is ordinarily observed in the spectra of thermochromic complexes,[50,51] and the second being the signature of thsa/th5Clsa core. Assignments are given in the corresponding Figures. Both absorptions have been observed in the region 500-800 nm and 200-400 nm, respectively. The intensities of these ligand-field bands correspond to what is typically observed for high-spin octahedral d^5 metal complexes.[52,53] This accounts for the dark-brown colour of the microcrystalline powders of **7** and **8**. The high spin state ligand field spectrum of **9** in the solid state is given in Figure 6.11c. Distinct and significant features are observed as compared with the ligand field spectra of **7** and **8**. The high-energy bands at ~ 300 and 343 nm are attributed to $\pi \rightarrow \pi^*$ transition, both of them being the signature of the 5-bromosalicylaldehyde thiosemicarbazone core. The next feature in the spectrum of **9** is the band at *ca.* 633 nm. This band is likely to arise from $^6A_1 \rightarrow {}^6$LMCT transition, characteristic of the high-spin state. A similar band was reported for some $[Fe^{III}_2(Salten)_2(L)](BPh_4)_2$ binuclear complexes in solution with L representing ligands such as 4,4'-azobis-pyridine and its derivatives.[54]

LIESST Effect: LIESST experiments were carried out on powder samples of iron(III) compounds $[Fe(Hthsa)(thsa)]\cdot H_2O$ (**7**), $[Fe(Hth5Clsa)(th5Clsa)]\cdot H_2O$ (**8**) and $[Fe(Hth5Brsa)(th5Brsa)]\cdot (H_2O)_{1/2}$ (**9**). The first example of a photoinduced spin transition for an Fe(III) spin crossover compound in the solid state was observed on $[Fe(pap)_2]ClO_4\cdot H_2O$.[31] It has been reported that a broad band (500–800 nm) in the visible region of the LS iron(III) compound can be attributed to the spin-allowed ligand-to-metal charge-transfer (LMCT) transition. Samples of **8** and **9** were first slowly cooled from room temperature down to 10 K and the $\chi_m T$ versus T plots were recorded. At 10 K, the samples were illuminated at 532 nm for 2 h. The magnetic response of the sample increased rapidly and finally reached a limiting value of: $\chi_m T$ = 1.35 cm^3 K mol^{-1} for **8** and $\chi_m T$ = 3.57 cm^3 K mol^{-1} for **9**. This suggests that the LS fraction of 32 % for **8** and of 90 % for **9** is converted into the photo-induced metastable HS state by illumination. Figures 6.12a and 6.13a show LIESST properties of **8** and **9**, respectively. The $\chi_m T$ value remained constant when the temperature was sufficiently low and decreased on heating. The LIESST temperature, T(LIESST), was determined as the extreme of the $\partial\chi_m T / \partial T$ derivative, and T(LIESST) = 42 K for **8** and T(LIESST) = 55 K for **9**. The critical temperature of the photoinduced high-spin species of **8** (T(LIESST) = 42 K) is lower than that of **9** (T(LIESST) = 55 K). The decrease of T(LIESST) with the increase of $T_{1/2}$ is

expected in the limit of strong vibronic coupling (inverse energy gap law [55]) and is well known in the case of iron(II) spin-crossover compounds. The limit of strong vibronic coupling means that the vertical shift of the LS and HS state potential wells is small, and the horizontal shift is large. The change in the magnetization persisted for periods of at least 6 hours after the illumination was stopped.

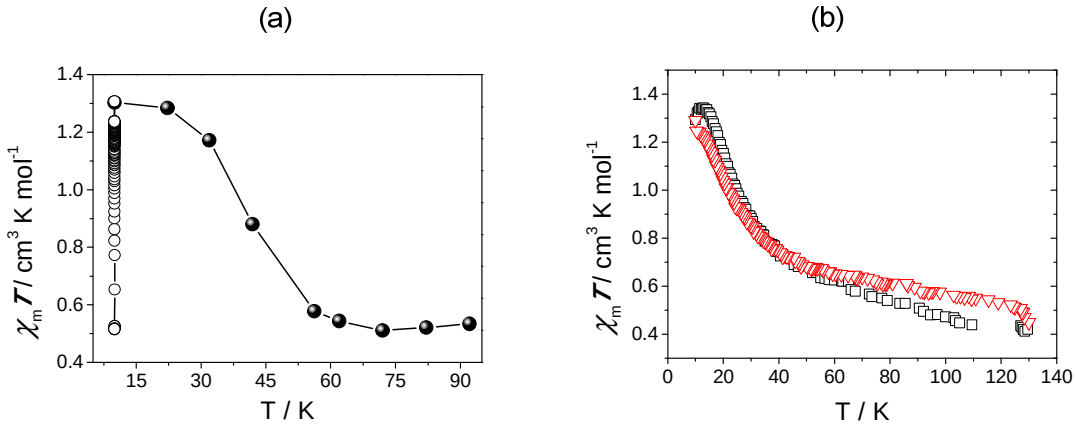

Figure 6.12. Temperature dependence of $\chi_m T$ for [Fe(Hth5Clsa)(th5Clsa)]·H_2O. (a) data recorded with irradiation at 10 K for 2 h (○); data recorded in the warming mode after the light irradiation had been applied for 2 h, then switch off (●). (b) LITH experiments, recorded in the warming (Δ) and cooling (□) runs under constant irradiation. Data were corrected for paramagnetic background, using Pauli/Pascal constants.

As shown for [Fe(pap)$_2$]ClO_4·H_2O, Hayami *et al.*[31,34,35] proposed that the LIESST phenomenon of iron(III) compounds with strong intermolecular interactions such as π–π stacking can be observed. The π electrons in the thsa ligand can be expanded, similar to pap ligand, and [Fe(Hthsa)(thsa)]·H_2O (**7**) might also exhibit optical bi-stability at low temperature. In fact, it appears not to be the case here. An increase in magnetization did not occur when **7** was excited at 10 K. Consequently, the LIESST effect of **7** is not possible even though strong cooperativity operates in this system to prevent the rapid relaxation from happening *via* tunneling regime. A plausible explanation is that, the ligand form of **7** does not bear any bulk halogen substituent at the 5-position on salicylaldehyde unit, which coupled with its electron-accepting tendency, gives rise to increased quantum mechanical tunneling barrier, thus can prevent the photo-induced HS state from relaxing back to its LS ground state until an activation temperature for thermal relaxation is reached.

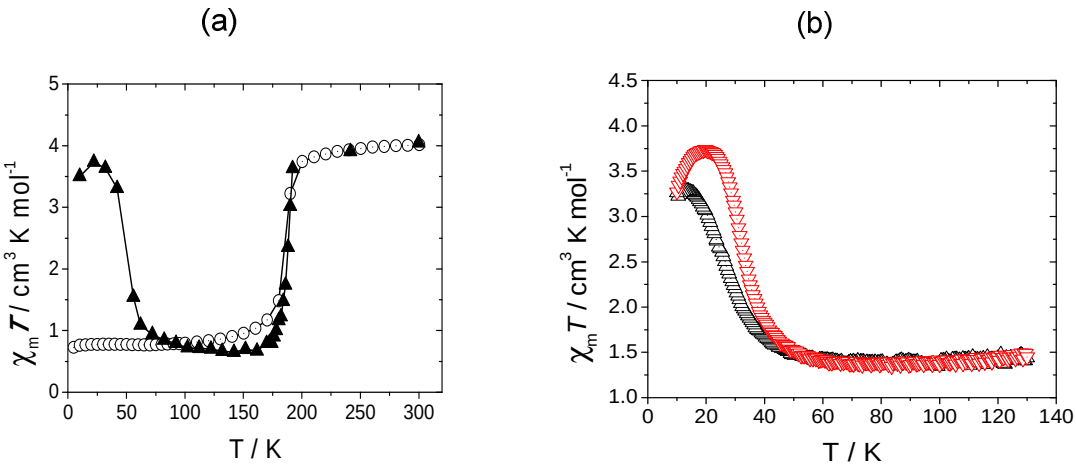

Figure 6.13. Temperature dependence of $\chi_m T$ for [Fe(Hth5Brsa)(th5Brsa)]·$(H_2O)_{1/2}$. (a) data recorded in the cooling mode without irradiation (○); data recorded in the warming mode after the light irradiation had been applied for 2 h, then switch off (▲). (b) LITH experiments, recorded in the warming (Δ) and cooling (∇) runs under constant irradiation. Data were corrected for paramagnetic background, using Pauli/Pascal constants.

An alternative way to study the effect of the cooperativity on the photoexcitation is to monitor the magnetic properties of a spin crossover material under constant irradiation. The competition between the constant photoexcitation and the self-accelerated thermal relaxation process is well known to induce a thermal hysteresis in the region of *T*(LIESST), named Light Induced Thermal Hysteresis (LITH).[56] Figures 6.12b and 6.13b show the LITH loops observed for both compounds under constant irradiation, hysteresis widths for the two compounds are: 4 K for [Fe(Hth5Clsa)(th5Clsa)]·H_2O and 8 K for [Fe(Hth5Brsa)(th5Brsa)]·$(H_2O)_{1/2}$. These data confirm that in all cases the photoinduced high spin phase displays some degree of cooperativity. The nature of such cooperative interactions is purely mechanical.[57] In fact, with increasing halogen size incorporated into the 5-position of salicylaldehyde unit of the ligand, however, the crystal volume do change per atom size increases, and thus the chemical pressure also increases. This results in the observed increasingly more cooperative nature of the photoexcited state for the bromo substituent and its shifted stability towards high thermally activated decay temperatures.

6.3 Conclusions

Iron(III) compounds [Fe(Hthsa)(thsa)]·H_2O (**7**), [Fe(Hth5Clsa)(th5Clsa)]·H_2O (**8**) and [Fe(Hth5Brsa)(th5Brsa)]·$(H_2O)_{1/2}$ (**9**) exhibited abrupt spin transition with thermal hysteresis. Results of the crystal structure analysis showed that, the molecular packing for **7** and **8** are stacked up in neat piles, extended by π– π interactions and hydrogen bonding networks. This suggests that strong intermolecular interactions exist in the molecular assembly. The bond length difference for iron(III) LIESST compound, **8** (Δr_{HL}= 0.127 Å), is similar to that for other iron(III) SCO compounds (Δr_{HL}= 0.130 Å), and is considerably smaller than that for iron(II) SCO compounds (Δr_{HL}= 0.20 Å). We succeeded in observing the LIESST effect of compounds [Fe(Hth5Clsa)(th5Clsa)]·H_2O and [Fe(Hth5Brsa)(th5Brsa)]·$(H_2O)_{1/2}$, whereas [Fe(Hthsa)(thsa)]·H_2O showed no evidence for the LIESST phenomenon when excited into the LS-state absorption band (~ 550 nm). Therefore, the approach, that is, the introduction of strong intermolecular interactions to prevent the metastable high spin state from rapid relaxing back to the low spin state, cannot be widely applied in the design of iron(III) spin crossover complexes with LIESST effects. A striking observation is that there is no electron withdrawing group incorporated into the 5-position of salicylaldehyde subunit, responsible for the observation of the LIESST effect.

However, the influence of a modification of the hydrogen atom with weakly deactivating groups (Cl, Br) at the pendant salicylaldehyde fragment displaces the transition to lower temperatures in the sense of increasing substituent size and thereby, causes a fundamental change in the nature of the transition. This result is in accord with the inverse energy gap law, which predicts for the halogen free compound a much shorter lifetime for the LIESST state even to an extent that the LIESST is no longer observed. Nevertheless **8** and **9** display long-lived metastable lifetimes, as stated above and represent a new example for iron(III) complexes exhibiting the LIESST phenomenon. Further work is currently in progress to study the relaxation mechanisms.

6.4 References

(1) Kahn, O. ; Martinez, C. J. *Science* **1998**, *279*, 44.

(2) Kahn, O. *Chem. Ber.* **1999**, *35*, 24.

(3) Itkis, M. E.; Chi, X.; Cordes, A. W.; Haddon, R. C. *Science* **2002**, *296*, 1443.

(4) Fujita, W.; Awaga, K. *Science* **1999**, *286*, 261.

(5) Niel, V.; Thompson, A. L.; Muñoz, M. C.; Galet, A.; Goeta, A. E.; Real, J. A. *Angew. Chem.* **2003**, *115*, 3890; *Angew. Chem. Int. Ed.* **2003**, *42*, 3760.

(6) Konishi, Y.; Tokoro, H.; Nishino, M.; Miyashita, S. *Phys. Rev. Lett*. **2008**, *100*, 0672061.

(7) Seredyuk, M.; Gaspar, A. B.; Ksenofontov, V.; Galyametdinov, Y.; Kusz, J.; Gütlich, P. *J. Am. Chem. Soc.* **2008**, *130*, 1431.

(8) Kiriya, D.; Chang, H. C.; Kitagawa, S. *J. Am. Chem. Soc*. **2008**, *130*, 5515.

(9) Hayami, S.; Shigeyoshi, Y.; Akita, M.; Inoue, K.; Kato, K.; Osaka, K.; Takata, M.; Kawajiri, R.; Mitani, T.; Maeda, Y. *Angew. Chem*. **2005**, *117*, 4977; *Angew. Chem. Int. Ed*. **2005**, *44*, 4899.

(10) Sato, O.; Iyoda, T.; Fujishima, A.; Hashimoto, K. *Science* **1996**, *272*, 704.

(11) Gütlich, P.; Hauser, A.; Spiering, H. *Angew. Chem*. **1994**, *106*, 2109; *Angew. Chem. Int. Ed. Engl.* **1994**, *33*, 2024.

(12) Decurtins, S.; Gütlich, P.; Köhler, C. P.; Spiering, H.; Hauser, A. *Chem. Phys. Lett*. **1984**, *105*, 1–4.

(13) Chastanet, G.; Létard, J.-F.; Gaspar, A. B.; Real, J. A. *Chem. Commun.* **2001**, 819.

(14) Létard, J.-F.; Real, J. A.; Moliner, N.; Gaspar, A. B.; Capes, L.; Cador, O.; Kahn, O. *J. Am. Chem. Soc.* **1999**, *121*, 10630.

(15) Varret, F.; Boukheddaden, K.; Chong, C.; Goujon, A.; Gillon, B.; Jeftic, J.; Hauser, A. *Eur. Phys. Lett.* **2007**, *77*, 30007-30008.

(16) Decurtins, S.; Gütlich, P.; Koehler, C. P.; Spiering, H. *J. Chem. Soc. Chem. Commun*. **1985**, 430-432.

(17) Poganiuch, P.; Gütlich, P. *Inorg. Chem*. **1987**, *26*, 455-458.

(18) Buchen, T.; Guetlich, P.; Goodwin, H. A. *Inorg. Chem*. **1994**, *33*, 4573-4576.

(19) Buchen, T.; Gütlich, P.; Sugiyarto, K. H.; Goodwin, H. A. *Chem. Eur. J.* **1996**, *2*, 1134.

(20) (a) Wu, C. H.; Jung, J.; Gantzel, P. K.; Gütlich, P.; Hendrickson, D. N. *Inorg. Chem.* **1997**, *36*, 5339. (b) Renz, F.; Oshio, H.; Ksenofontov, V.; Waldeck, M.; Spiering, H.; Gütlich, P. *Angew. Chem.* **2000**, *112*, 3832; *Angew. Chem. Int. Ed*. **2000**, *39*, 3699. (c) Hayami, S.; Gu, Z.-Z.; Einaga, Y.; Kobayashi, Y.; Ishikawa, Y.; Yamada, Y.; Fujishima, A.; Sato, O. *Inorg. Chem*. **2001**, *40*, 3240.

(21) Sorai, M.; Seki, S. *J. Phys. Chem. Solids* **1974**, *35*, 55.

(22) Gütlich, P.; Goodwin, H. A. *Top. Curr. Chem*. **2004**, 233 –235.

(23) (a) Goodwin, H. A. *Coord. Chem. Rev*. **1976**, *18*, 293 –325. (b) Gütlich, P. *Struct. Bonding (Berlin)* **1981**, *44*, 83–195. (c) Gütlich, P.; Hauser, A. *Coord. Chem. Rev*. **1990**, *97*, 1–22. (d) König, E. *Prog. Inorg. Chem*. **1987**, *35*, 527-623. (e) König, E. *Struct. Bonding (Berlin)* **1991**, *76*, 51.

(24) Gütlich, P.; Garcia, Y.; Spiering, H. *Magnetism*: *Molecules to Materials IV*; (Eds.: Miller, J. S.; Drillon, M.), WILEY-VCH: Weinheim, 2003; p. 271.

(25) (a) Maeda, Y.; Oshio, H.; Takashima, Y.; Mikuriya, M.; Hidaka, M. *Inorg. Chem*. **1986**, *25*, 2958-2962. (b) Maeda, Y.; Oshio, H.; Toriumi, K.; Takashima, Y. *J. Chem. Soc. Dalton Trans*. **1991**, 1972-1999. (c) Oshio, H.; Toriumi, K.; Maeda, Y.; Takashima, Y. *Inorg. Chem*. **1991**, *30*, 4252-4260.

(26) (a) Lawthers, I.; MacGarvey, J. J. *J. Am. Chem. Soc*. **1984**, *106*, 4280-4283. (b) Lawthers, I.; McGarvey, J. J. *Chem. Commun*. **1982**, 906.

(27) (a) Schenker, S.; Hauser, A.; *J. Am. Chem. Soc.* **1994**, *116*, 5497-5498. (b) Schenker, S.; Hauser, A.; Dyson, R. M. *Inorg. Chem*. **1996**, *35*, 4676-4682.

(28) Enachescu, C.; Hauser, A.; Girerd, J. J.; Boillot, M. L. *ChemPhys-Chem* **2006**, *7*, 1127.

(29) Hauser, A.; Enachescu, C.; Daku, M. L.; Vargas, A.; Amstutz, N. *Coord. Chem. Rev*. **2006**, *250*, 1642-1652.

(30) Sato, O. *Acc. Chem. Res*. **2003**, *36*, 692-700.

(31) Hayami, S.; Gu, Z. Z.; Shiro, M.; Einaga, Y.; Fujishima, A.; Sato, O. *J. Am. Chem. Soc*. **2000**, *122*, 11569-11570.

(32) Hayami, S., Maeda, Y. *Inorg. Chim. Acta* **1997**, *255*, 181-184.

(33) (a) Ritter, G., König, E., Irler, W., Goodwin, H. A. *Inorg. Chem.* **1978**, *17*, 224-228. (b) Nelson, S. M.; Mcllroy, P. D. A.; Stevenson, C. S.; König, E.; Ritter, G.; Waigel, J. *J. Chem. Soc., Dalton Trans.* **1986**, 991-995.

(34) Juhasz, G.; Hayami, S.; Sato, O.; Maeda, Y. *Chem. Phys. Lett*. **2002**, *364*, 164-170.

(35) Hayami, S.; Hiki, K.; Kawahara, T.; Maeda, Y.; Urakami, D.; Inoue, K.; Ohama, M.; Kawata, S.; Sato, O. *Chem. Eur. J*. **2009**, *15*, 3497-3508.

(36) Hayami, S.; Kawahara, T.; Maeda, Y.; Inoue, K.; Sato, O. *J. Radioanal. Nucl. Chem*. **2005**, *266*, 521-525.

(37) (a) Timken, M. D.; Wilson, S. R.; Hendrickson, D. N. *Inorg. Chem*. **1985**, *24*, 3455-3457. (b) Hayami, S.; Hashiguchi, K.; Inoue, K.; Maeda, Y. *J. Nucl. Radiochem. Sci.* **2004**, *5*, N1–N3.

(38) Mohan, M.; Madhuranath, P. H.; Kumar, A.; Kumar, M.; Jha, N. K. *Inorg. Chem*. **1989**, *28*, 96-99.

(39) Hayami, S.; Gu, Z. Z.; Yoshiki, H.; Fujishima, A.; Sato, O. *J. Am. Chem. Soc*. **2001**, *123*, 11644-11650.

(40) Kahn, O. *Molecular Magnetism*; WILEY-VCH: Weinheim, 1993.

(41) Real, J. A.; Bolvin, H.; Bousseksou, A.; Dworkin, A.; Kahn, O.; Varret, F. Zarembowitch, J. *J. Am. Chem. Soc*. **1992**, *114*, 4650-4658.

(42) Goldanskii, V. I.; Makarov, E. F. *Chemical Application of Mössbauer Spectroscopy*; Academic Press: New York/London, 1968; p. 102.

(43) Greenwood, N. N.; Gibb, T. C. *Mössbauer Spectroscopy*; Chapman and Hall Ltd: London, 1971.

(44) Moliner, N.; Salmon, L.; Capes, L.; Muñoz, M. C.; Létard, J.-F.; Bousseksou, A.; Tuchagues, J. P.; McGarvey, J. J.; Dennis, A. C.; Castro, M.; Burriel, R.; Real, J. A. *J. Phys. Chem. B* **2002**, *106*, 4276.

(45) Sorai, M,; Maeda, Y,; Oshio, H. *J. Phys. Chem. Solids* **1990**, *51*, 941.

(46) Shongwe, M. S.; Al-Rashdi, B. A.; Adams, H.; Morris, M. J.; Mikuriya, M.; Hearne, G. R. *Inorg. Chem.* **2007**, *46*, 9558.

(47) Djukic, B.; Dube, P. A.; Razavi, F.; Seda, T.; Jenkins, H. A.; Britten, J. F.; Lemaire, M. T. *Inorg. Chem*. **2009**, *48*, 699-707.

(48) (a) Shongwe, M. S.; Smith, R.; Marques, H. M.; van Wyk, J. A. *J. Inorg. Biochem.* **2004**, *98*, 199. (b) Shongwe, M. S.; Kaschula, C. H.; Adsetts, M. S.; Ainscough, E. W.; Brodie, A. M.; Morris, M. J. *Inorg. Chem.* **2005**, *44*, 3070.

(49) Grillo, V. A.; Gahan, L. R.; Hanson, G. R.; Stranger, R.; Hambley, T. W.; Murray, K. S.; Moubaraki, B.; Cashion, J. D. *J. Chem. Soc., Dalton Trans*. **1998**, 2341-2348.

(50) Lever, A. B. .P. *Inorganic Electronic Spectroscopy*; 2nd edn.; Elsevier: Amsterdam, 1984; pp.87-90.

(51) Lever, A. B. P. *Inorganic Electronic Spectroscopy*; Elsevier: Amsterdam, 1968.

(52) Sutton, D. *Electronic Spectra of Transition Metal Complexes*; McGraw-Hill, 1968.

(53) McClure, D. S.; Stephens, P. J. *Electronic Spectra of coordination compounds in Coordination Chemistry*; (Edited Martell, A. E.): Van Nostrand Reinhold, 1971.

(54) (a) Hayami, S.; Sato, O.; Inoue, K.; Einaga, Y.; Maeda, Y. *J. Nucl. Radiochem. Sci.* **2002**, *3*, A1-A9. (b) Matsumoto, N.; Ohta, S.; Yoshimura, C.; Ohyoshi, A.; Kohata, S.; Okawa, H.; Maeda, Y. *J. Chem. Soc. Dalton Trans*. **1985**, 2575. (c) Ohta, S.; Yoshimura, C.; Matsumoto, N.; Okawa, H.; Ohyoshi, A. *Bull. Chem. Soc. Jpn* **1986**, *59*, 155.

(55) Hauser, A.; Vef, A.; Adler, P. *J. Chem. Phys*. **1999**, *95*, 8710.

(56) Létard, J.-F.; Guionneau, P.; Rabardel, L.; Howard, J. A. K.; Goeta, A. E.; Chasseau, D.; Kahn, O. *Inorg. Chem*. **1998**, *37*, 4432.

(57) Spiering, H. *Top. Curr. Chem.* **2004**, *235*, 171.

Chapter VII

Design and Preparation of Double Switches

Synopsis

A step forward!!! A novel strategy towards the obtaining of double switches is presented and may enhance the capability of yielding even more efficient switching devices. The synthetic procedure takes advantage of the incorporation of suitable potential spin crossover-active iron(III) and iron(II) fragments within a single solid material.

7.1 Introduction

There is a rapidly growing interest in engineering mixed materials (hybrid systems) where features of the two inorganic components complement each other leading to the formation of new solid-state structures and materials with new composite properties. Some examples of recent interest are molecule-based magnetic materials, which possess synergy or interplay between two or more properties such as electrical conductivity with magnetism[1,2] or spin crossover,[3-7] host-guest solids.[8-10] New inorganic lattice structures are formed, resulting from cooperative interactions between the two systems. In all cases, there is promise of developing new materials with properties not seen in the pure counterparts.

Although there have been as many as 200 spin crossover (SCO) systems reported so far,[11] the ligands are in principle composed of approximately 20 structural units,[12] such as pyrazole, tetrazole, pyridine, pyrazine, 1,10-phenanthroline, phenolate, etc. These basic units possess intermediate ligand-field strengths to generate SCO of a $3d^4$ – $3d^7$ metal ion in a narrow temperature range limit. In the quest for stable systems which display improved characteristics, researchers have combined the units together to build new SCO chelating agents, giving access to a multitude of SCO systems.[12] Interestingly, as soon as the SCO ligand bears active sites which can be tuned through changing the functionality or segment size of the component, it will pave the way for tailoring the electronic and geometric structures of the ligand and eventually the SCO properties. More recently, cobalt(II) tris(bipyridyl) complex cation, has been successfully encapsulated in the Zeolite-Y supercages for the construction of the “ship-in-a bottle” compound,[13] which, for intramolecular reasons,[14] becomes a spin crossover complex – a phenomenon not observed for this ion either in solid state or in solution. In addition to providing structural diversity and unusual magnetochemistry, oxalate-bridged networks were selected as precursors to replace the Zeolite-Y cavities, affording a route to new materials with exchange coupling and SCO effects. A number of inorganic hybrid architectures which couple SCO with ferro- or antiferro-magnetic properties have been described;[15-18] however, to the best of our knowledge, hybrid solids constructed from two distinct switchable transition metal complexes are lacking. Herein, we report a novel strategy towards the obtaining of double switch compounds. The synthetic procedure takes advantage of the combination of the extremely rare **anionic** Fe(III) spin crossover fragment with **cationic** spin crossover entities, the latter may contain either Fe(III) or

another spin switchable transition metal ion. Moreover, the spin crossover entities to be incorporated in the proposed hybrid spin-switching systems can be selected according to their feasibility of displaying the LIESST phenomenon. Such a synergistic effect has not been observed before and the present result opens an exceptional, but very realistic, perspective towards the obtaining of a dual photo-tunable material in which the individual transition metal centers can be photo-activated independently by the interaction with light of a wavelength specific for each photoprocess.

Table 7.1 Crystal Data and Refinement Details of the Structure Determination of $Cs[Fe^{III}(thsa)_2]\cdot 4H_2O$ (**11**) and $[Fe^{II}(bpp1)_2](ClO_4)_2$ (**12**)

	11	**12**
Formula	$C_{16}H_{22}CsFeN_6O_6S_2$	$C_{22}H_{18}Cl_2FeN_{10}O_8$
Formula weight ($g.mol^{-1}$)	647.26	677.21
Crystal system	orthorhombic	monoclinic
Space group	*P*bcn	*C*2/*c*
Crystal colour	dark-green	yellow
Crystal description	block	block
Crystal dimensions (mm)	0.49 x 0.23 x 0.16	0.38 x 0.32 x 0.29
a, (Å)	10.502(2)	14.295(3)
b, (Å)	15.524(3)	9.171(2)
c, (Å)	13.912(3)	20.008(4)
β, (deg)	-	99.596(3)
Volume ($Å^3$)	2268.1(8)	2586.3(9)
Z	4	4
D_{calc} ($g.cm^{-3}$)	1.896	1.739
Temperature (K)	100(1)	100(1)
Radiation (Å)	0.71073	0.71073
μ (Mo Kα) (cm^{-1})	24.77	8.61
F(000)	1284	1376
Number of unique data	2800	2641
Number of data with $[F_o \geq 4.0\ \sigma\ (F_o)]$	2371	2320
$R(F)$[a]	0.0272	0.0387
$wR(F^2)$[b]	0.0716	0.0937
GOF on F^2	1.079	1.093
$\Delta_\rho$max, $\Delta_\rho$min / $e.Å^{-3}$	-0.40, 1.41(12)	-0.56, 0.41(10)

[a] $R(F) = \sum (||F_o| - |F_c||) / \sum |F_o|$ for $F_o > 4.0\ \sigma\ (F_o)$ for observed reflections.

[b] $wR(F^2) = [\sum [w(F_o^2 - F_c^2)^2] / \sum [w(F_o^2)^2]]^{1/2}$ for all data.

7.2 Results and Discussion

7.2.1 Molecular Structure Description[1]

The Anionic Moiety: $Cs[Fe^{III}(thsa)_2]\cdot 4H_2O$ (11). Crystallographic data of **11** were collected at 100 K; selected bond lengths for the structural determination are given in Table 7.1, and structure of $Cs[Fe^{III}(thsa)_2]\cdot 4H_2O$ is shown in Figure 7.1. The asymmetric unit contains half of the formula unit, consisting of four moieties: a half anionic Fe-complex, a half Cs cation and two water solvate molecules. The Fe- and Cs- positions are both located on special positions; a two-fold axis (·2·), meaning only half of the formula unit comprises the asymmetric unit. The orthorhombic unit cell contains four Cs cations, four Fe-complexes and eight water molecules. One water is coordinated to the Cs cation and also the S atom of the ligand is coordinate to the Cs cation. The coordination environment around the Fe(III) atom is formed by two molecules of the tridentate ONS-ligand with the formation of a distorted octahedron $FeS_2N_2O_2$. The donor atoms of the two ONS-ligands are located in mutually normal planes, the S and O atoms being at the *cis*- and the N atoms at the *trans*-positions (Figure 7.1). The geometry of **11** is a strongly distorted octahedron; the angles at an iron atom deviate from 90° by 4-12° and all equatorial planes are deformed noticeably, from about 0.1 to 0.5 Å. The values of the bond lengths are consistent with those typical for high spin iron(III) centre of tridentate ONS-donor set.[19,20]

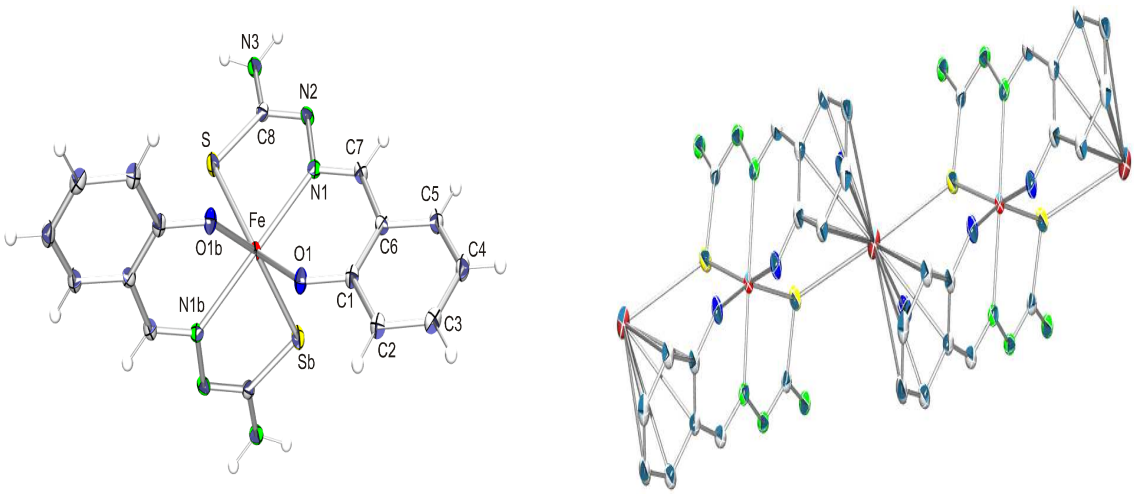

Figure 7.1. ORTEP drawing of $Cs[Fe^{III}(thsa)_2]\cdot 4H_2O$ complex, with atom labeling and view of the 1-D chain structure. Atoms are represented by thermal ellipsoids with 20% probability level. Hydrogen atoms, water molecules, and cesium cation are omitted for clarity.

[1] See chapter 2 for details on the experimental procedures and recipes for compounds presented in this chapter.

Table 7.2 Selected Bond Lengths (Å) and Bond Angles (deg) for $Cs[Fe^{III}(thsa)_2]\cdot 4H_2O$ (**11**) and $[Fe^{II}(bpp1)_2](ClO_4)_2$ (**12**). Standard deviations in the last decimal place are given in parentheses.

Distance (Å)	**11**	Distance (Å)	**12**
Fe – S	2.4088(8)	Fe – N1	2.1678(19)
Fe – O1	1.9681(17)	Fe – N3	2.1592(17)
Fe – N1	2.1799(19)	Fe – N5	2.1992(19)
Cs – S	3.7462(10)	N1 – N2	1.369(2)
Cs – O2	3.0485(19)	N2 – C4	1.397(3)
S – C8	1.743(2)	N3 – C8	1.326(3)
Angle (deg)	**11**	Angle (deg)	**12**
S – Fe – O1	155.28(5)	N1 – Fe – N3	72.33(7)
S – Fe – N1	78.06(5)	N1 – Fe – N5	141.59(6)
O1 – Fe – N1	85.27(6)	N3 – Fe – N3a	155.54(7)
N1 – Fe – N1b	152.86(7)	N5 – Fe – N1a	105.99(7)
S – Cs – Sa	137.61(1)	N3 – Fe – N1a	128.01(7)
O2 – Cs – O2a	77.54(5)	N3 – Fe – N5a	90.17(7)

The Cationic Entity: $[Fe^{II}(bpp1)_2](ClO_4)_2$ (12). A single crystal X-ray analysis of **12** was undertaken at 100 K. Important data collection and refinement parameters are provided in Table 7.1, and selected structural data are given in Table 7.2. ORTEP drawing of the molecular structure is depicted in Figure 7.2, together with the atomic labelling scheme. Similar to the anionic entity, the asymmetric unit of this compound contains an half of the formula unit, consisting of two moieties: a cationic Fe-complex and a perchlorate anion, with the Fe atom setting at special position: at twofold axis (·2·). The monoclinic unit cell contains twelve discrete units, four cations and eight anions moieties. The geometrical configuration of the molecular unit of $[Fe^{II}(bpp1)_2](ClO_4)_2$ contains an octahedral iron(II) center bound equatorially to two ligands through three of the ligands' six nitrogen donor atoms, with an average Fe–N bond distance of 2.1754(18) Å, indicating that the iron(II) is in the high-spin form.[21,22] This central metal ion is strongly distorted away from the D_{2d} structure. The difference is manifest most obviously in the '*trans*' angle N3–Fe–N3a = 155.54(7)°, and in the dihedral angle of 62.23(4)° between the least-squares planes of the two ligands in the cation. This unusual coordination geometry is similar to those exhibited by high-spin $[Fe(L^3Ph)_2][ClO_4]_2$ and $[Fe(L^4)_2][ClO_4]_2$ in the crystal.[23]

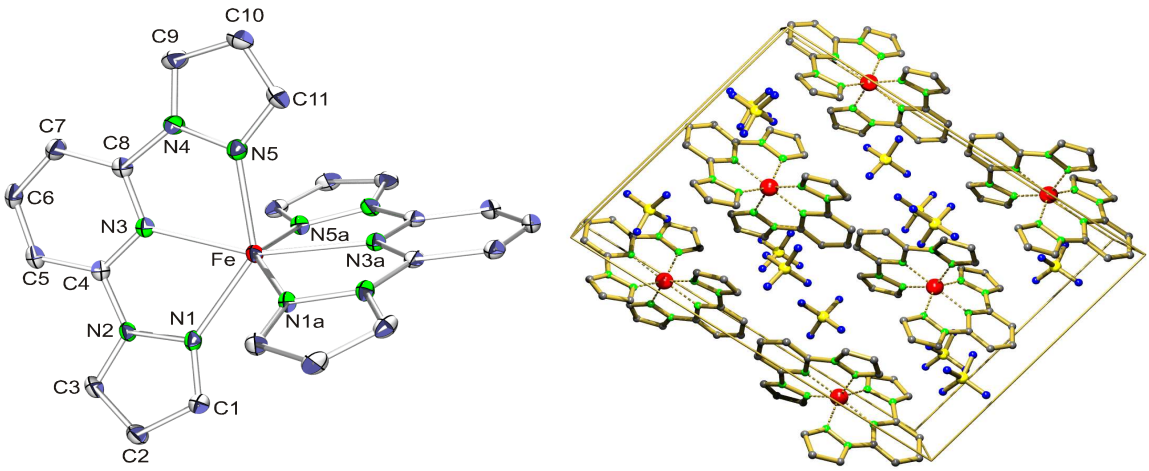

Figure 7.2. ORTEP drawing of $[Fe^{II}(bpp1)_2](ClO_4)_2$ complex , with atom labeling and packing arrangement of the unit cell. Atoms are represented by thermal ellipsoids with 20% probability level. Hydrogen atoms and perchlorate anions are omitted for clarity.

7.2.2 Magnetic Properties of the Anionic Moiety

The magnetic susceptibility measurements of $Cs[Fe^{III}(thsa)_2]\cdot 4H_2O$ in the temperature range 5 – 300 K exhibits a temperature independent effective magnetic moment of 6.03 μ_B (Figure 7.3a), consistent with an S = 5/2 ground term.[24] The spin state of this iron(III) complex is in conformity with the moderate ligand-field strength (ONS donor set). The electron paramagnetic resonance (EPR) spectrum of **11** supports the magnetic observation (Figure 7.3b). The solid state EPR spectrum of $Cs[Fe^{III}(thsa)_2]\cdot 4H_2O$, recorded at 77 K, consists of an intense resonance at $g_\perp = 4.33$ and a very weak one at $g_\parallel = 2.18$, characteristic of an axial distorted high-spin iron(III) complex.[25-27]

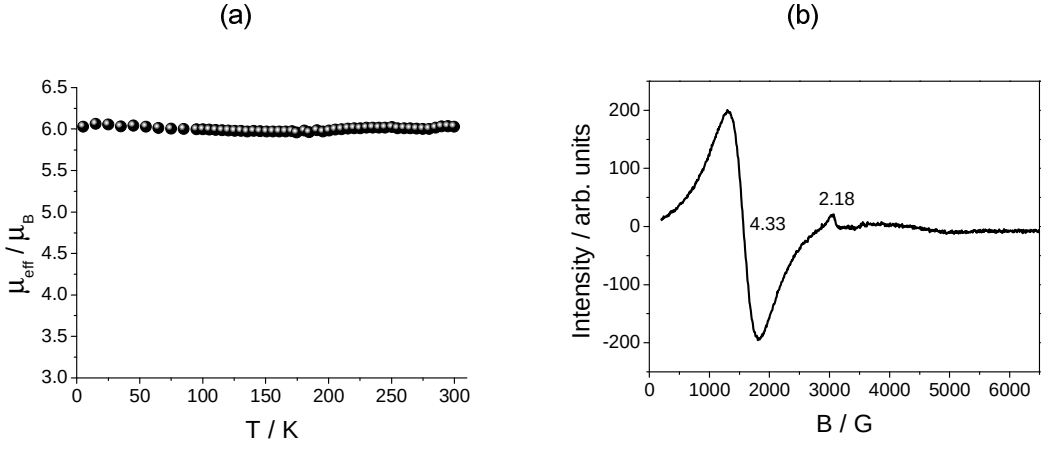

Figure 7.3. Temperature dependence of: (a) the effective magnetic moment (μ_{eff}) for $Cs[Fe^{III}(thsa)_2]\cdot 4H_2O$ and (b) the corresponding solid state EPR spectrum recorded at 77 K.

Table 7.3 ^{57}Fe Mössbauer Spectral Parameters for $[Fe^{II}(bpp1)_2](ClO_4)_2$, with QS, the quadrupole splitting and IS, the isomer shift (relative to metallic iron).

T (K)	Component	IS (mm s^{-1})	Γ/2 (mm s^{-1})	QS (mm s^{-1})	Area (%)
300	Q1	1.02	0.11	2.85	100
150	Q1	1.10	0.11	3.44	100
77	Q1	1.12	0.12	3.53	100

7.2.3 Magnetic Properties of the Cationic Entity

The variation of the effective magnetic moment of $[Fe^{II}(bpp1)_2](ClO_4)_2$ in the solid state has been measured in the 5 – 300 K temperature range. As shown in Figure 7.4a, above 50 K the effective magnetic moment reaches a constant value of 5.21 μ_B, which is close to the experimental spin-only value expected for four unpaired electrons $S = 2$ (5.40 μ_B).[28,29] This behavior clearly shows that complex **12** is in a pure $S = 2$ spin state with no spin crossover and no participation of a minor low spin state fraction. Below 50 K the moment decreases to *ca.* 4.54 μ_B at 5 K, which presumably results from a significant zero-field splitting leading to an unequal population of the Kramer's doublets of the $S = 2$ spin state. The Mössbauer spectra of $[Fe^{II}(bpp1)_2](ClO_4)_2$ are depicted in Figure 7.4b.

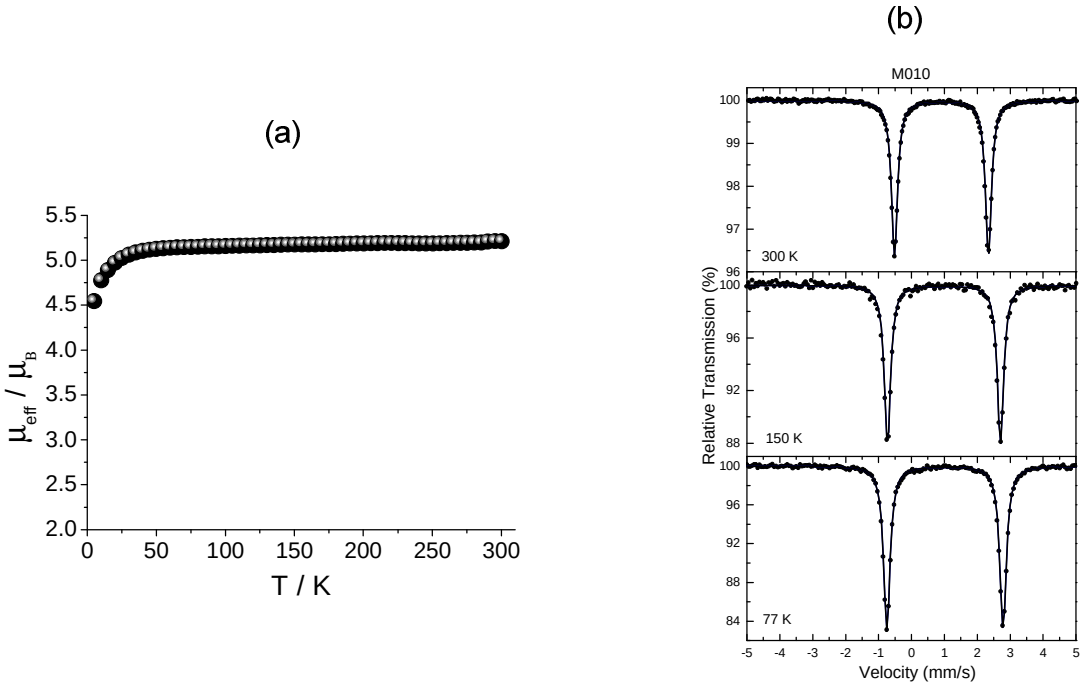

Figure 7.4. Temperature dependence of: (a) the effective magnetic moment (μ_{eff}) for $[Fe(bpp1)_2](ClO_4)_2$ and (b) the corresponding ^{57}Fe Mössbauer spectra.

The spectra are characteristic of a single quadrupole split contribution at all temperatures with no changes observed in their shape. The Mössbauer parameters values resulting from the best fits of these Mössbauer spectra appearing in Table 7.3 indicate that iron(II) in this compound is in the high spin (S=2) state at all temperatures between 300 K and 77 K. This result comes in complete agreement with the effective magnetic moment measurements which show a constant value with no changes in this temperature region.

Table 7.4 C, H, N, S and Fe contents of $[Fe^{III}(thsa)_2]_2[Fe^{II}(bpp1)_2]\cdot CH_3OH\cdot 4H_2O$

Elements	H	C	N	S	Fe
Found (%)	3.63	44.57	20.93	8.77	11.32
Calculated (%)	3.98	45.03	21.01	8.74	11.42

7.2.4 Synthesis and Chemical Composition of the Double Switches

The title compound, $[Fe^{III}(thsa)_2]_2[Fe^{II}(bpp1)_2]\cdot CH_3OH\cdot 4H_2O$, was obtained from aqueous methanol solution with 61.10 % yield. The synthesis method has been chosen based on the solubility of $Cs[Fe^{III}(thsa)_2]\cdot 4H_2O$ which was mainly soluble in water, while the component, $[Fe^{II}(bpp1)_2](ClO_4)_2$, was soluble in methanol. The hybrid complex was obtained as black microcrystalline powder. Attempts to grow single crystals suitable for single-crystal X-ray diffraction analysis so far have been unsuccessful. The material is soluble in dimethylformamide (DMF) and dimethylsulfoxide (DMSO); but insoluble in water and in some common organic solvents like acetone, diethyl ether, ethanol, etc.

The chemical formula of this compound has been extracted from elemental composition, through C, H, N, S and Fe microanalysis. Results yielded the following atomic abundance: $Fe_3C_{55}H_{58}N_{22}O_9S_4$, the content of each element is listed in Table 7.4. Because it was not possible to differentiate between the elemental composition of Fe^{2+} and Fe^{3+} from the bulk analysis, we performed X-ray photoelectron spectroscopy (XPS) measurements. XPS is a versatile surface sensitive analysis technique that can be used for compositional and chemical states analysis.[30] The sample for this measurement was prepared using aluminum foil. The corresponding XPS survey spectrum from the complex powder is displayed in Figure 7.5a. The binding energies of each element were calibrated with the S (2p) peak of the thioamide group at 163.9 eV. In the XPS spectrum of Fe $2p_{3/2}$ after Shirley removal (Figure 7.5b), both Fe^{2+} and Fe^{3+} peaks are found at 708.8 eV and 710.7 eV, respectively; with an Fe^{3+} *shake-up satellite peak* at 712.03 eV; this latter appearing 1.3 eV higher in binding energy, than the Fe^{3+} main line, having 30

% of its intensity.[31] The peak areas are integrated and corrected with atomic sensitivity factors[32] to yield the observed relative intensities for each element, and based on this calibration, a Fe^{2+}/Fe^{3+} ratio was calculated to be *ca.* 0.52 within the uncertainty of the calculations (S.D. = 0.03 for both Fe^{2+}/Fe^{3+}). This ratio is an expected value since the Fe(II) component and Fe(III) fragment are reacting in the 1:2 stoichiometric manner to form the double switch complex, $[Fe^{III}(thsa)_2]_2[Fe^{II}(bpp1)_2]\cdot CH_3OH\cdot 4H_2O$. Moreover, in the wide scan XPS spectrum, the peaks at 533.1, 401.1, 286.0, 228.3 and 163.9 eV were also found, which are assignable to O (1s), N (1s), C (1s), S (2s) and S (2p) respectively. The S (2s) and S (2p) peaks are from the thioamide group of the ligand attached to the Fe(III) metal. With regard to the O (1s) peak, it is impossible to distinguish between the coordinated solvent molecules in the hybrid material lattice and the oxygen atom existing in the Fe(III) fragment. Thus, the XPS results can indeed be of great help for giving the evidence of the chemical composition of the hybrid molecular switch.

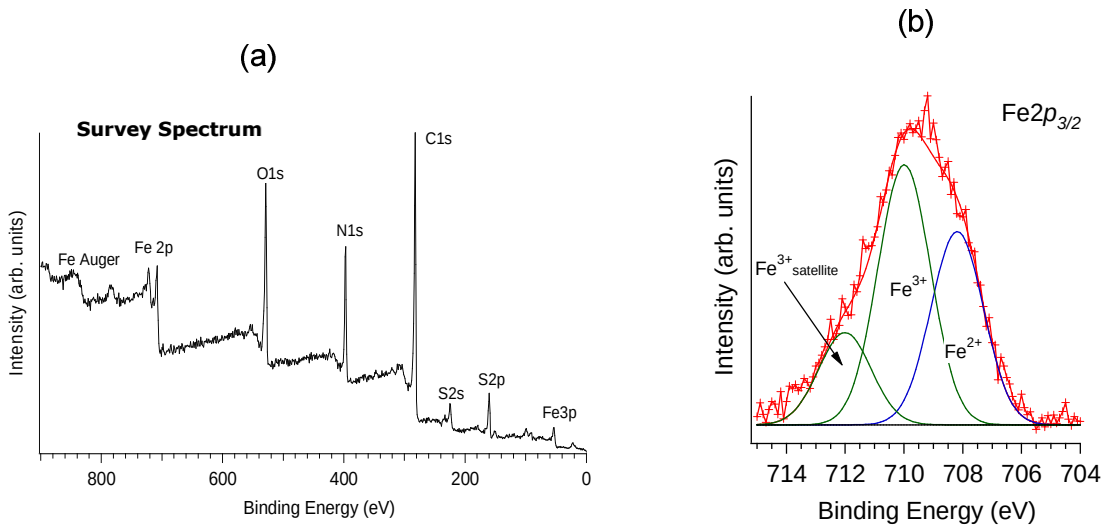

Figure 7.5. (a) XPS survey spectrum of $[Fe^{III}(thsa)_2]_2[Fe^{II}(bpp1)_2]\cdot CH_3OH\cdot 4H_2O$ and (b) Shirley background-subtracted Fe $2p_{3/2}$ spectrum. The Fe^{2+}, Fe^{3+} and Fe^{3+}satellite peaks have been labelled on the spectrum.

7.2.5 Magnetic and Thermal Properties of the Hybrid Spin Switching System

The temperature dependence of the magnetic susceptibility measured for the heating and cooling runs over the range 5 – 310 K for $[Fe^{III}(thsa)_2]_2[Fe^{II}(bpp1)_2]\cdot CH_3OH\cdot 4H_2O$, is shown in Figure 7.6a in the form of $\chi_m T$ vs T, the applied magnetic field being equal to 0.1 T. At 310 K, $\chi_m T$ is equal to 12.28 cm^3 K mol^{-1}, which roughly corresponds to the value expected for three uncoupled iron ions in

100 % high spin state (12.30 cm^3 K mol^{-1}). On lowering the temperature, $\chi_m T$ remains practically constant until 272 K, and then drops abruptly reaching a value of 4.56 cm^3 K mol^{-1} at 200 K. This behaviour is indicative of the interconversion from high- to low-spin state of the two uncorrelated iron(III) sites. The obtained value of 4.56 cm^3 K mol^{-1} lies slightly above the value of 4.30 cm^3 K mol^{-1} calculated for three non-interacting iron ions,[33] and stays constant as the temperature decreases from 200 – 50 K. This is characteristic of 100 % for both one Fe(II) atom in the high spin state and two Fe(III) centers in low spin state. The sharp decrease in $\chi_m T$ to 1.79 cm^3 K mol^{-1} observed as the temperature is lowered from 50 to 5 K (inset of Figure 7.6a), is most likely attributable to zero-field splitting proceeding from the Fe(II) subunit. Thus, $[Fe^{III}(thsa)_2]_2[Fe^{II}(bpp1)_2]\cdot CH_3OH\cdot 4H_2O$ undergoes a thermally-induced abrupt spin transition centered at: $T_{1/2}\uparrow$ = 269 and K $T_{1/2}\downarrow$ = 269 K, with no hysteresis loop. The change of magnetic state in this system mainly concerns the Fe(III) centers, while the Fe(II) ion inherits the same magnetic behaviour observed in its pristine state.

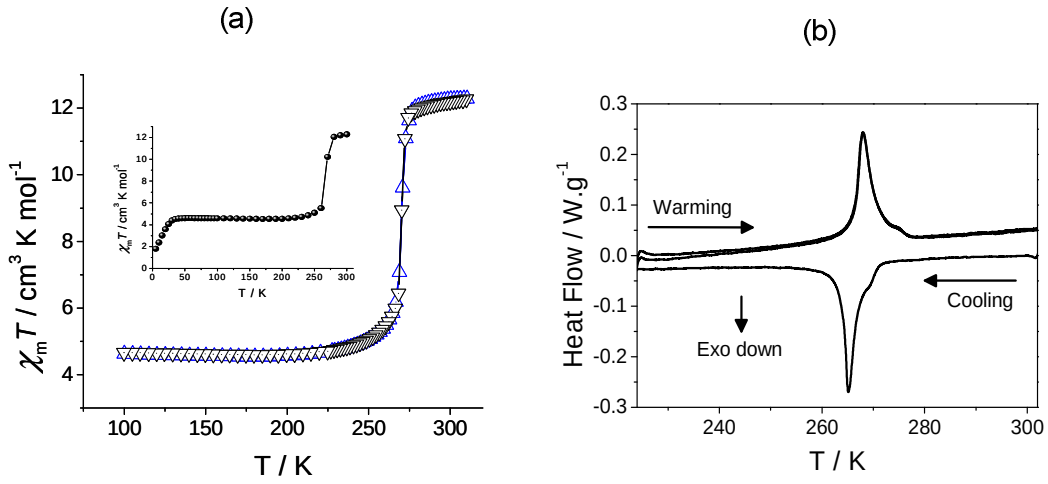

Figure 7.6. Temperature dependence of: (a) the molar magnetic susceptibility ($\chi_m T$) for $[Fe^{III}(thsa)_2]_2[Fe^{II}(bpp1)_2]\cdot CH_3OH\cdot 4H_2O$, as obtained in successive warming (Δ) and cooling (∇) runs; and (b) the corresponding heat flow curves, obtained through differential scanning calorimetry. Heating and cooling branches are represented by full lines, respectively.

The DSC response upon heating and cooling processes is displayed in Figure 7.6b and clearly confirms the spin crossover transition. The measurements shown here were reproduced at a rate of 2 K min^{-1} (for the heating and cooling runs, each), and taken from the third cycle, after carrying out the first and second cycles, at a rate of 10 and 5 K min^{-1},

respectively. The apparent thermal hysteresis width of 3 K ($T_c\uparrow$ = 268 K and $T_c\downarrow$ = 265 K), presumably results from a thermal lag of the device. The excess enthalpy and entropy molar variations connected with the spin crossover transformation were determined as: ΔH = (12.6 ± 0.8) kJ mol^{-1} and ΔS = (47.0 ± 3.3) J K^{-1} mol^{-1}. These thermodynamic parameters deduced are about twice of that observed from the change in spin state of an iron(III) SCO complex, $[Fe^{III}(Hthsa)(thsa)]\cdot H_2O$;[34] suggesting that the obtained values for this hybrid molecular switch, are the contributions arising from the spin states conversion of the two non-equivalent iron(III) atoms. Consequently, the transition from the low-spin level to the high-spin level accompanies increases both in spin multiplicities and in molecular dimensions of the related subunits.[35]

7.3 Conclusions and Outlook

In this chapter, we have described a simple and effective synthetic strategy for double switches systems, using anionic Fe(III) entity and cationic Fe(II) moiety as "building blocks", each having the potential to induce a SCO phenomenon. A new family of molecular magnetic switches has been synthesized in a one-pot reaction. The magnetic susceptibility measurements underscore that the spin crossover transformation is actually such “two-site” transitions, where one site undergoes an almost complete transformation and the other remains totally high spin. This observation is interesting, because normally, the two complex precursors, both in solution and in solid state, retain a high-spin ground state, irrespective of the temperature or the nature of the solvent molecules. However, cooperativity resulting from intermolecular interaction is reflected in the abruptness associated with the spin states conversion. The enthalpy and entropy gains due to the phase transition have been estimated, and precisely account for in terms of the sum of the contributions from the change in spin states of the two non-interacting iron(III) centers.

At this stage of the experiments, no definitive conclusions can be drawn from the magnetic properties of this hybrid spin-switching system. Therefore, comparative studies are required, which will include the mixing of systems in different spin states and, more importantly, the combination of thermally-driven transition compounds exhibiting the LIESST effect. It will be of interest to find out how the well-defined coexistence of spin state does influence the magnetic properties of the hybrid spin-switchable molecular solid.

7.4 References

(1) Coronado, E.; Galán-Mascarós, J. R.; Giménez-Saiz, C.; Gómez-García, C. J.; Ruiz-Pérez, C.; Triki, S. *Adv. Mater.* **1996**, *8*, 737.

(2) Alberola, A.; Coronado, E.; Galán-Mascarós, J. R.; Giménez-Saiz, C.; Gómez-García, C. J.; Romero, F. M. *Synthetic Metals* **2003**, *133-134*, 509-513.

(3) (a) Nakano, M.; Fujita, N.; Matsubayashi, G.; Mori, W. *Mol. Cryst. Liq. Cryst.***2002**, *379*, 365. (b) Takahashi, K.; Kawakami, T.; Gu, Z.-Z.; Einaga, Y.; Fujishima, A.; Sato, O. *Chem. Commun.* **2003**, 2374.

(4) (a) Dorbes, S.; Valade, L.; Real, J. A.; Faulmann, C. *Chem. Commun.* **2005**, 69. (b) Takahashi, K.; Cui, H.-B.; Kobayashi, H.; Einaga, Y.; Sato, O. *Chem. Lett.* **2005**, *34*, 1240.

(5) (a) Faulmann, C.; Dorbes, S.; Bonneval, B. G.; Molnár, G.; Bousseksou, A.; Gomez-Garcia, C.; Coronado, E.; Valade, L. *Eur. J. Inorg. Chem.* **2005**, 3261. (b) Takahashi, K.; Cui, H.-B.; Okano, Y.; Kobayashi, H.; Einaga, Y.; Sato, O. *Inorg. Chem.* **2006**, *45*, 5739.

(6) (a) Faulmann, C.; Jacob, K.; Dorbes, S.; Lampert, S.; Malfant, I.; Doublet, M.-L.; Valade, L.; Real, J. A. *Inorg. Chem.* **2007**, *46*, 8548. (b) Faulmann, C.; Dorbes, S.; Lampert, S.; Jacob, K.; Bonneval, B. G.; Molnár, G.; Bousseksou, A.; Real, J. A.; Valade, L. *Inorg. Chim. Acta* **2007**, *360*, 3870.

(7) Pereira, L. C. J.; Gulamhussen, A. M.; Dias, J. C.; Santos, I. C.; Almeida, M. *Inorg. Chim. Acta* **2007**, *360*, 3887.

(8) Decurtins, S.; Verdaguer, M. *Phil. Trans. R. Soc. Lond. A* **1999**, *357*, 3025

(9) Floquet, S.; Salunke, S.; Boillot, M. L.; Clément, R.; Varret, F.; Boukheddaden, K.; Rivière, E. *Chem. Mater.* **2002**, *14*, 4164.

(10) Decurtins, S.; Schmalle, H. W.; Pellaux, R.; Huber, R.; Fisher, P.; Ouladdiaf, B. *Adv. Mater.* **1996**, *8*, 647.

(11) Bousseksou, A.; Molnár, G.; Matouzenko, G. *Eur. J. Inorg. Chem.* **2004**, 4353.

(12) Gütlich, P.; Goodwin, H. A. (Editors) *Top. Curr. Chem.* **2004**, *233-235*.

(13) Mizuno, K.; Lunsford, J. H. *Inorg. Chem.* **1983**, *22*, 3484.

(14) (a) Tiwary, S. K.; Vasudevan, S. *Chem. Phys. Lett.* **1997**, *277*, 84. (b) Tiwary, S. K.; Vasudevan, S. *Inorg. Chem.* **1998**, *37*, 5239.

(15) Coronado, E.; Clemente-Léon, M.; Galán-Mascarós, J. R.; Giménez-Saiz, C.; Gómez-Garcia, C. J.; Martínez-Ferrero, E. *Dalton Trans.* **2000**, 3955.

(16) Coronado, E.; Galán-Mascarós, J. R.; Gómez-Garcia, C. J. *Mol. Cryst. Liq. Cryst.* **1999**, *334*, 679.

(17) Sieber, R.; Decurtins, S.; Stoeckli-Evans, H.; Wilson, C.; Yifit, D.; Howard, J. A. K.; Capelli, S. C.; Hauser, A. *Chem.–Eur. J.* **2000**, *6*, 361.

(18) Murray, K. S.; Kepert, C. P. *Top. Curr. Chem.* **2004**, *233*, 195.

(19) Padhyé, S.; Kauffman, G. B. *Coord. Chem. Rev.* **1985**, *63*, 127-160.

(20) Zelentsov, V. V. In *Advances in Inorganic Chemistry, 6th ed.;* Spitsyn, V. I., Ed.; MIR Publishers 1983; p 122.

(21) König, E. *Prog. Inorg. Chem.* **1987**, *35*, 527.

(22) Gütlich, P.; Hauser, A.; Spiering, H. *Angew. Chem. Int. Ed. Engl.* **1994**, *33*, 2024.

(23) Constable, E. C.; Baum, G.; Bill, E.; Dyson, R.; Eldik, R. Van; Fenske, D.; Kaderli, S.; Morris, D.; Neubrand, A.; Neuberger, M.; Smith, D. R.; Wieghardt, K.; Zehnder, M.; Zuberbühler, A. D. *Chem. Eur. J.* **1999**, *5*, 498.

(24) Burger, K. *Coordination Chemistry*; *Experimental Methods*, Butterworth: London, 1973.

(25) Palmer, G. In *Iron Porphyrins Part II*; Lever, A. B. P.; Gray, H. Eds.; Addison-Wesley: Reading, MA, 1983; p 43.

(26) Costes, J. P.; Dahan, F.; Laurent, J. P. *Inorg. Chem.* **1990**, *29*, 2448–2452.

(27) Imbert, C.; Hratchian, H. P.; Lanznaster, M.; Heeg, M. J.; Hryhorczuk, L. M.; McGarvey, B. R.; Schlegel, H. B.; Verani, C. N. *Inorg. Chem.* **2005**, *44*, 7414–7422.

(28) Huheey, J. E.; Keiter, E. A.; Keiter, R. L. *Inorganic Chemistry*; *Principles of Structure and Reactivity*, 4th ed.; HarperCollins College Publishers: New York, 1993; 964 p.

(29) Casalot, A. ; Durupthy, A. *Chimie Inorganique*; Cours 2e cycle, Hachette Supérieur: Paris, 1993 ; 395 p.

(30) Briggs, D.; Seah, M. P. *Practical Surface Analysis*; JohnWiley & Sons Ltd., 1990.

(31) Oku, M; Wagatsuma, K.; Konishi, T. J. *Electron Spectrosc. Relat. Phenom.* **1999**, *99*, 277.

(32) Wagner, C. D.; Davis, L. E.; Zeller, M. V.; Taylor, J. A.; Raymond, R. M.; Gale, L. H. *Surf. Interface Anal*. **1981**, *3*, 211.

(33) Hatscher, S.; Schilder, H.; Lueken, H.; Urland, W. *Pure Appl. Chem.* **2005**, *77*, 497–511.

(34) Yemeli Tido, E. W.; Blake, G.; Alberda van Einkenstein, G. O. R.; van Koningsbruggen, P. J. *unpublished results*.

(35) Stoufer, R. C.; Smith, D. W.; Clevenger, E. A,; Norris, T. E. *Inorg.Chem.* **1966**, *5*, 1167.

Summary

This thesis focuses on the synthesis and characterisation of switchable transition metal complexes of thiosemicarbazone based-ligands and 2,6-bis(pyrazol-1-yl) based-ligands. For thiosemicarbazone based-ligands, we used iron(III) as the central atom while for 2,6-bis(pyrazol-1-yl) based-ligands, iron(II) has been used. The dissertation is structured in three main parts presented as follows:

The first part deals with iron(III) complexes of pyridoxal-N-substituted thiosemicarbazone ligand. **In Chapter 3**, the preparation and characterization of two new neutral ferric complexes with desolvation-induced discontinuous spin-state transformation above room temperature are reported. The compounds, $[Fe(Hthpy)(thpy)]\cdot CH_3OH\cdot 3H_2O$ (**1**) and $[Fe(Hmthpy)(mthpy)]\cdot 2H_2O$ (**2**), are low-spin (LS) at room temperature and below, whereas their nonsolvated forms are high-spin (HS), exhibiting zero-field splitting. In these complexes, Hthpy, Hmthpy, and thpy, mthpy are the deprotonated forms of pyridoxal thiosemicarbazone and pyridoxal methylthiosemicarbazone, respectively; each is an O,N,S-tridentate ligand. The molecular structures have been determined at 100(1) K using single-crystal X-ray diffraction techniques. The chemical inequivalence of the ligands was clearly established, for the "extra'' hydrogen atom on the monodeprotonated ligands (Hthpy, Hmthpy) was found to be bound to the nitrogen of the pyridine ring. The ligands are all of the thiol form; the doubly deprotonated chelates (thpy, mthpy) have C-S bond lengths slightly longer than those of the singly deprotonated forms. There is a three-dimensional network of hydrogen bonds in both compounds. The discontinuous spin-state transformation is accompanied with liberation of solvate molecules. Heat capacity data for the low temperature and high temperature phases are revealed. **In Chapter 4**, four novel mononuclear coordination compounds namely: $[Fe(Hthpy)_2](SO_4)_{1/2}\cdot 3.5H_2O$ (**3)**, $[Fe(Hthpy)_2]NO_3\cdot 3H_2O$ (**4)**, $[Fe(H_2mthpy)_2](CH_3C_6H_4SO_3)_3\cdot CH_3CH_2OH$ (**5)** and $[Fe(Hethpy)(ethpy)]\cdot 8H_2O$ (**6)**, (H_2thpy = pyridoxalthiosemicarbazone, H_2mthpy = pyridoxal-4-methylthiosemicarbazone, H_2ethpy = pyridoxal-4-ethylthiosemicarbazone), were synthesized in the absence or presence of organic base, Et_3N and NH_3. Compounds **3** and **4** are monocationic, and were prepared using the singly deprotonated form of

pyridoxalthiosemicarbazone. Both compounds crystallise in the monoclinic system, *C*2/*c* and $P2_1/c$ space group for **3** and **4**, respectively. Complex **5** is tricationic, it is formed with neutral bis(ligand) complex and possesses an interesting 3D channel architecture, the unit cell is triclinic, $P\bar{1}$ space group. For complex **6**, the pH value plays an important role during its synthesis; **6** is neutral and crystallises with two inequivalent forms of the ligand: the singly and the doubly deprotonated chelate of H_2ethpy, the unit cell is monoclinic, *C*2/*c* space group. Notably, in **3** and **6**, there is an attractive infinite three dimensional hydrogen bonding network in the crystal lattice. Magnetic measurements of **3** and **6** revealed that a rather steep spin transition from the low spin to high spin Fe(III) states occurs above 300 K in the first heating step. This transition is accompanied by the elimination of solvate molecules and thus, stabilizes the high spin form due to the breaking of hydrogen bonding networks; compared to **4** and **5**, which keep their low spin state up to 400 K.

The second part studies the optical control of the magnetic behaviour of the newly synthesized materials. **In Chapter 5**, single crystals of the spin crossover compound $[Fe^{II}(bpp2)_2][ClO_4]_2 \cdot MeCN$, (bpp2 = 2,6-bis[pyrazol-1-yl] pyrazine) have been successfully grown. The material displays a complete thermal spin transition with a well-reproducible hysteresis loop of 10 K centred at $T_{1/2}\uparrow$ = 231 K, $T_{1/2}\downarrow$ = 221 K. This is evidenced also from Differential Scanning Calorimetry analysis. The crystal structure has been determined at both 293 K and 100 K, respectively for the high- and the low-spin states. The thermal spin transition takes place without any change of crystallographic phase or space group, which is found to be monoclinic, $P2_1/c$ (with $Z = 4$). The enthalpy and entropy variations connected with the spin state conversion were estimated to be: ΔH = (10.8 ± 0.3) kJ mol^{-1} and ΔS = (46.9 ± 1.3) J $K^{-1}mol^{-1}$, respectively. At low temperatures, the Light-Induced Excited Spin State Trapping and Light-Induced Thermal Hysteresis effects have been observed on the single crystals, through irradiation with 532 nm light. In addition, the discontinuous spin crossover transformation is accompanied by a thermochromic effect in which the crystal changes colour from yellow in the high-spin state to dark-brown in the low-spin state. **In Chapter 6**, iron(III) spin-crossover compounds $[Fe(Hthsa)(thsa)] \cdot H_2O$ (**7**), $[Fe(Hth5Clsa)(th5Clsa)_2] \cdot H_2O$ (**8**) and $[Fe(Hth5Brsa)(th5Brsa)_2] \cdot H_2O$ (**9**) (H_2thsa = salicylaldehyde thiosemicarbazone, H_2th5Clsa = 5-chlorosalicylaldehyde thiosemicarbazone and H_2th5Brsa = 5-bromosalicylaldehyde thiosemicarbazone) have been synthesized and their spin-transition

properties investigated by magnetic susceptibility, Mössbauer spectroscopy and Differential Scanning Calorimetry measurements. The three compounds exhibit abrupt spin transition with thermal hysteresis effect. The more polarizable is the substituent at the salicylaldehyde subunit; the better is the transition at room temperature with an increase degree of cooperativity. Molecular structures of **7** and **8** in the high spin state are revealed. The occurrence of the LIESST phenomenon appeared to be dependant on the substituent at the 5-position on salicylaldehyde moiety. While the compounds with electronaccepting substituent moieties (-Br or -Cl) in the pendant salicylaldehyde exhibit light induced trapped excited high spin state with long-lived metastable lifetimes, that of substituent-free does not, eventhough strong intermolecular interactions (such as hydrogen bonding networks and π-stacking) operate in the system. We have noticed that for the compound **8** at the surface level of photoconversion was less than 35 %. In contrast, compound **9** displays quantitative photoexcitation, such an effect reflects a higher $T_{1/2}$, in regard to the inverse energy gap law introduced by Hauser *et al.*

The last part is devoted to the preparation of hybrid device incorporating switching centres. **In Chapter 7**, the reaction mixture of $Cs[Fe^{III}(thsa)_2]\cdot 4H_2O$, an anionic complex, and $[Fe^{II}(bpp1)_2](ClO_4)_2$, a cationic complex, in a molar ratio of 2:1 in aqueous methanol solution and at room temperature, afforded the hybrid molecular solid with the formula unit, $[Fe^{III}(thsa)_2]_2[Fe^{II}(bpp1)_2]\cdot CH_3OH\cdot 4H_2O$. XPS results have been of great help for giving the evidence of the chemical composition of the hybrid molecular switch. The magnetic susceptibility measurements exhibit a thermally driven interconversion between a low-spin and a high-spin states of the iron(III) centres, while the iron(II) ion conserves the same magnetic behaviour observed in its original state. The DSC response upon heating and cooling processes confirms the phase transition.

Samenvatting

Dit proefschrift is gefocust op de synthese en beschrijving van schakelbare overgangsmetaal complexen van thiosemicarbazon gebaseerde liganden en 2,6-bis(pyrazol-1-yl) gebaseerde liganden. Voor de thiosemicarbazon gebaseerde liganden, gebruikten we ijzer (III) als het centrale atoom, terwijl voor 2,6-bis(pyrazol-1-yl) ijzer(II) is gebruikt. Het proefschrift is opgedeeld in 3 secties die als volgt worden gepresenteerd:

Het eerste deel behandeld ijzer(III) complexen van het pyridoxal N-gesubstitueerd thiosemicarbazon ligand. In **hoofdstuk 3**, worden de bereiding en analyse van twee nieuwe neutrale ferrische complexen met een door oplosbaarheid geïnduceerde discontinue spintoestand overgang gerapporteerd. $[Fe(Hthpy)(thpy)]\cdot CH_3OH\cdot 3H_2O$ (**1**) en $[Fe(Hmthpy)(mthpy)]\cdot 2H_2O$ (**2**), zijn laag-spin (LS) bij kamer temperatuur en daar beneden, terwijl de vormen zonder oplosmiddel hoog-spin (HS) zijn en nul-veld opsplitsing vertonen. In deze complexen zijn, Hthpy, Hmthpy, and thpy, mthpy de gedeprotoneerde vormen van pyridoxaal thiosemicarbazone en pyridoxaal methylthiosemicarbazone, respectievelijk; elk van hen is een O,N,S-tridentaat ligand. De moleculaire structuur is bepaald bij 100(1) K, gebruik makende van één-kristal Röntgen diffractie technieken. De chemische ongelijkheid van de liganden kwam duidelijk naar voren, in het geval van een “extra” waterstof atoom aan de monogedeprotoneerde liganden (Hthpy, Hmthpy), is het ligand gebonden via het stikstof atoom van de pyridine ring. Alle liganden hebben de thiol vorm: de dubbel gedeprotoneerde chelaten (thpy, mthpy) hebben C-S bindingslengtes die net iets langer zijn dan die in de enkel gedeprotoneerde vorm. Er is een drie-dimensionaal netwerk van waterstofbruggen in beide materialen. De discontinue spintoestand overgang gaat samen met het vrijkomen van oplosmiddel moleculen. Warmte capaciteit data van zowel de lage als de hoge temperatuur fase worden gepresenteerd. In **hoofdstuk 4**, werden 4 nieuwe mononucleaire coördinatie materialen gesynthetiseerd: $[Fe(Hthpy)_2](SO_4)_{1/2}\cdot 3.5H_2O$ (**3)**, $[Fe(Hthpy)_2]NO_3\cdot 3H_2O$ (**4)**, $[Fe(H_2mthpy)_2](CH_3C_6H_4SO_3)_3\cdot CH_3CH_2OH$ (**5)** and $[Fe(Hethpy)(ethpy)]\cdot 8H_2O$ (**6)**, (H_2thpy = pyridoxalthiosemicarbazone, H_2mthpy = pyridoxal-4-methylthiosemicarbazone, H_2ethpy = pyridoxal-4-ethylthiosemicarbazone), in de afwezinheid of juist in de aanwezigheid van de basen, Et_3N en NH_3. Materialen **3** en **4** hebben één cation, en werden gemaakt met de enkel gedeprotoneeerde vorm van

pyridoxalthiosemicarbazone. Beide materialen kristalliseren in monokliene systemen met de *C*2/*c* en *P*2_1/*c* spacegroup voor **3** en **4** respectievelijk. Complex **5** heeft drie cationen, het is gevormd met het neutrale bis(ligand) complex en vormt een interessante 3D tunnel architectuur, de eenheidscel is triclien, en *P*$\bar{1}$ de ruimte groep. Voor complex **6**, speelt de pH waarde een belangrijke rol tijdens de synthese; **6** is neutraal en kristalliseert met twee inequivalente vormen van het ligand: het enkel en het dubbel gedeprotoneerde chelaat van H_2ethpy, de eenheidscel is monoclien, *C*2/*c* de spacegroup. Met name in **3** en **6**, is er een interessant oneindig netwerk van waterstof bruggen in het kristal rooster. Magnetische metingen aan **3** en **6** laten zien dat een vrij scherpe spin overgang van laag naar de hoog spin toestand in Fe(III) plaatsvindt boven 300 K in de eerste opwarmingsstap. Deze overgang wordt vergezeld door de eliminatie van oplosmiddel moleculen en dus stabiliseert het de hoog spin vorm door het breken van de waterstof brug netwerken. Ter vergelijking: **4** en **5** behouden hun lage spin toestand tot 400 K.

Het tweede deel bestudeert de optische manipulatie van het magnetische gedrag van de nieuw gesynthetiseerde materialen. In **hoofdstuk 5**, wordt de succesvolle groei van één kristallen van het spin transitie materiaal $[Fe^{II}(bpp2)_2][ClO_4]_2 \cdot MeCN$, (bpp2 = 2,6-bis[pyrazol-1-yl] pyrazine) gepresenteerd. Het materiaal laat een volledige thermische spin overgang zien met een goed reproduceerbare hystereselus van 10 K die gelokaliseerd is bij $T_{1/2}\uparrow$ = 231 K, $T_{1/2}\downarrow$ = 221 K. Deze bevindingen zijn bevestigd door caloriemetrische analyse (Differential Scanning Calorimetrie). De kristal structuur is bepaald bij 293 K en 100 K, respectievelijk voor de hoge en de lage spin toestand. De thermische spintransities gaan niet gepaard met een verandering in kristal structuur of symmetrie groep, deze blijft monoclien, *P*2_1/*c* (met *Z* = 4). De enthalpie en entropie verschillen die gerelateerd zijn aan de verandering in spin toestand zijn geschat op: ΔH = (10.8 ± 0.3) kJ mol^{-1} en ΔS = (46.9 ± 1.3) J $K^{-1}mol^{-1}$ respectievelijk. Bij lage temperaturen, zijn licht geïnduceerde stabilisering van de spin toestand (Light-Induced Excited Spin State Trapping, LIESST) en licht geïnduceerde thermische hysterese geobserveerd in de één kristallen, door middel van bestraling met licht van 532 nm golflengte. Bovendien werd de discontinue spin transformatie gepaard met een thermochromisch effect, waarbij het kristal van kleur veranderd van geel in de hoog spin toestand naar donker bruin in de laag spin toestand. In **hoofdstuk 6**, zijn de ijzer(III) spin transitie materialen $[Fe(Hthsa)(thsa)] \cdot H_2O$ (**7**), $[Fe(Hth5Clsa)(th5Clsa)] \cdot H_2O$ (**8**) en $[Fe(Hth5Brsa)(th5Brsa)_2] \cdot (H_2O)_{1/2}$ (**9**) (H_2thsa = salicylaldehyde thiosemicarbazone,

H_2th5Clsa = 5-chlorosalicylaldehyde thiosemicarbazone en H_2th5Brsa = 5-bromosalicylaldehyde thiosemicarbazone) gesynthetiseerd en hun spin transitie eigenschappen bestudeerd door middel van het meten van de magnetische susceptibiliteit, Mössbauer spectroscopie en de Differential Scanning Calorimetrie. De drie materialen laten een abrupte spin overgang zien met een thermisch hysterese effect. Hoe beter de substituent aan de salicylaldehyde subgroep polariseerbaar is , hoe beter de overgang bij kamer temperatuur is met een toename in de mate van coöperativiteit. De moleculaire structuren van **7** en **8** in de hoog spin toestand zijn bepaald. Of het LIESST effect wel of niet optreed, hangt af van de substituent aan de 5-positie van de salicylaldehyde subgroep. Terwijl de materialen met electron accepterende substituenten (-Br of –Cl) in de hangende salicylaldehyde licht gestabiliseerde aangeslagen toestanden laten zien met langlevende metastabiele toestanden, laten de substituent vrije materialen geen effect zien, hoewel sterke inter-moleculaire interacties (zoals de waterstof bruggen en de π-overlap) aanwezig zijn in dit materiaal. We hebben geconstateerd dat voor materiaal **8** de mate van fotoconversie aan het oppervlak minder dan 35 % was. Materiaal **9**, daarentegen, laat een kwantitatieve foto-excitatie zien. Een dergelijk effect reflecteert een hogere $T_{1/2}$, in verhouding tot de omgekeerd evenredige energie gap wetten die zijn geïntroduceerd door Hauser *et al.*

Het laatste deel is toegewijd aan de preparatie ven hybride spin-schakelbare moleculaire complexen. In **hoofdstuk 7**, heeft het reactie mengsel van $Cs[Fe^{III}(thsa)_2]\cdot 4H_2O$, een anionisch complex, en $[Fe^{II}(bpp1)_2](ClO_4)_2$, een cationisch complex, in een molaire verhouding van 2:1 in een waterhoudende methanol oplossing bij kamertemperatuur geresulteerd in een hybride moleculaire vaste stof met de chemische samenstelling: $[Fe^{III}(thsa)_2]_2[Fe^{II}(bpp1)_2]\cdot CH_3OH\cdot 4H_2O$. XPS resultaten hebben een grote bijdrage geleverd in de onderbouwing van de chemische samenstelling van deze moleculaire schakelbare hybride. De magnetische susceptibiliteit metingen vertonen een thermisch geïnduceerde interconversie van de laag spin toestand naar de hoog spin toestand van de ijzer(III) kernen, terwijl het ijzer(II) ion hetzelfde magnetisch gedrag laat zien in zijn originele toestand. De DSC resultaten voor het opwarmen en het afkoelen bevestigen de aanwezigheid van een fase overgang.

Acknowledgements

Many people have supported and aided to this research project over the last four years, and therefore, I would like to acknowledge all of them for their contributions, even if they were not always merely scientific.

First, I thank my thesis advisor, Dr. Petra J. van Koningsbruggen for giving me the opportunity to carry out my doctoral studies in Groningen and to work on this exciting topic. I also thank her for giving me the unique opportunity to work in Toulouse for a month. Under her guidance, I have developed the skill and knowledge worthy of a Ph.D., and for that I am very appreciative. I started in March 2006 with very little knowledge of the area and almost no research experience. Petra and others put a lot of effort into teaching me the ropes.

I am also very thankful to Prof. Dr. Thomas T. M. Palstra, who has been co-directing this thesis. It is hard to express how much I owe to Thom. Working with him was a true pleasure and a constant motivation. He has made a tremendous impact on the outcome of my research.

I would also like to acknowledge all the members of my Ph.D. committee. I am very grateful to Prof. Dr. Andreas Hauser and Prof. Dr. Ria Broer, who agreed to read, comment and approve this manuscript, despite their busy time schedules. I would also like to thank Prof. Dr. Paul ir H. M. van Loosdrecht not only for his acceptance to become the part of the jury, but also for his interest in my work. Paul has contributed with the photomagnetic properties.

I address all my gratitude to, Lionel Rechignat, Jean-François Meunier and especially Dr. Christophe Faulmann, they all participated in making my stay in Toulouse, an unforgetable memory.

Sincere thanks to Dr. Alex P. Douvalis and Prof. Thomas Bakas from the University of Ionnina in Greece, for their assistance with Mössbauer measurements and their interpretations, without which this thesis would not have been completed.

In addition, I received a great deal of technical help from many members. Thanks to Gert Alberda van Ekenstein, for performing the DSC/TGA measurements. Gert showed perseverance and determination when measuring my samples, and constantly contributed ideas to my work. The crystal structures shown in this thesis would not have been possible without the help of Auke Meetsma. I thank him for his professionalism. A

special thank you goes to Dr. Graeme Blake for his time spent on running, collecting and refining my powder diffraction data. My warmest words are for Jacob Baas. I thank him for his priceless help and teaching me how to handle the SQUID magnetometer. Without you, I wouldn't have gone so far with the results. I am greatly indebted to Dr. Tom Lummen for his free sharing of insights and constructive criticism during my research. You were the springboard between Paul and I, and did all the photomagnetic measurements. I will not forget to thank Dr. Daan van Leusen for his help with the ligands synthesis, Hans van der Velde for performing all the elemental analysis, Dr. Wesley Browne for the UV-Visible and EPR measurements and Régis Gengler for the XPS measurements.

It is a pleasure to acknowledge the members of the Molecular Inorganic Chemistry group, both past and present. The group has always been a delight to work with, nurturing an environment of learning as well as fun, and I have enjoyed their company both in and out of the lab. Most notably, to Dr. Esther Vertelman from whom I almost learn everything, she has been with me at the very first beginning, when I started my Ph.D., and we both share the same supervisor. She really helped me a lot. I will not forget Dr. Edwin Otten, a nice guy, always willing to help and present whenever you need him. Additionally, I would like to thank those with whom I constantly had fruitful discussions and received useful advice: Dr. Marco Bouwkamp, Dr. Kai Schröder, Dr. Itzel Guerrero, Dr. Andy Noble, Nicky Philipp, Tessa Leuning, Niels van Velzen, Siebe van der Veer and Guido Vossenberg. To Anne Arkenbout, I express my sincere gratitude for the work done.

Again I would like to thank my parents Tido Jacques Normand and Magne Agnès Tido for their support and love through the years of my graduate career, as well as my brothers and sisters for their constant encouragement.

I wish to offer special thanks to the Cameroonian community of Groningen. I had a great pleasure to work and interact with you guys over the past years. I was fortunate to have some very good friends outside the laboratory: Marcel and Anne-Marie van der Pol, Marnix and Lentje, Kenneth and Marie Tebo, Berend and Pulchérie, Eric Detsi and Selma, Eric Akum. I look forward to many more wonderful times with them in the years to come. Finally, a special thanks to Héloïse for her love and patience. I could not have written this thesis without your care and support. Thank you.